INVESTIGATION OF ADSORPTION, REACTION AND CONFINEMENT OF MOLECULES IN SINGLE WALL CARBON NANOTUBES

by

Oleg Byl

BS, National Taras Shevchenko University of Kyiv, Kyiv, Ukraine, 1999

MS, National Taras Shevchenko University of Kyiv, Kyiv, Ukraine, 2000

Submitted to the Graduate Faculty of

Art and Sciences in partial fulfillment

of the requirements for the degree of

Doctor of Philosophy

University of Pittsburgh

2005

UNIVERSITY OF PITTSBURGH

FACULTY OF ARTS AND SCIENCES

This dissertation was presented

by

Oleg Byl

It was defended on

November 29, 2005

and approved by

Prof. J. K. Johnson

Prof. D. H Waldeck

Prof. C. S. Wilcox

Prof. J. T. Yates, Jr.
Dissertation Director

INVESTIGATION OF ADSORPTION, REACTION AND CONFINEMENT OF MOLECULES IN SINGLE WALL CARBON NANOTUBES

Oleg Byl, PhD

University of Pittsburgh, 2005

Abstract

Adsorption of simple molecules (CF_4, Xe, CO_2, NO and H_2O) inside single wall carbon nanotubes has been investigated by means of infrared spectroscopy. It was demonstrated that confinement has a profound effect of the IR spectra of the internally adsorbed species. The spectral changes relate to the enhanced binding of the adsorbates to the nanotube interior walls and to the spatial limitations that prohibit formation of bulk-like structures.

It was found that CF_4 exhibits a 15 cm^{-1} redshift in its ν_3 symmetric stretching mode when adsorbed on the exterior surface of closed SWNTs. Adsorption on the nanotube is accompanied by adsorption in the interior in the case of opened SWNTs and the ν_3 mode is redshifted 35 cm^{-1}. In addition it was shown that confined CF_4 does not exhibit LO-TO splitting observed in the bulk phase.

Physisorption of NO inside of carbon nanotubes results in *cis*-$(NO)_2$ dimer formation for almost all adsorbed NO, indicating that confinement shifts the equilibrium according to Le Chatelier's Principle.

In all cases Xe was used as a displacing agent to verify the internal adsorption. It was shown that Xe preferentially adsorbs inside nanotube displacing high coverage CF_4 molecules. The externally bound adsorbates do not form a full monolayer and therefore Xe adsorbs non-competitively on empty external sites.

Confinement of H_2O in the nanotube interior leads to appearance of a sharp mode at 3507 cm^{-1} that is indicative of a weaker hydrogen bond relative to hydrogen bonding in bulk ice. Molecular simulations show that the confined water forms stacked ring structures with bulk-like intra-ring and weaker inter-ring hydrogen bonds.

The spectroscopy studies of adsorption in nanotubes were accompanied by nitrogen volumetric adsorption studies of bulk nanotubes. It was demonstrated that n-nonane can be utilized as a nanotube interior blocking agent.

The oxidation of SWNTs by ozone, followed by heating to remove oxidized carbon atoms as carbon oxides occurs preferentially on the outer surface of bulk samples of nanotubes. The high surface reactivity of O_3 at the outer surface of a bulk nanotube sample causes this effect.

TABLE OF CONTENTS

LIST OF TABLES

LIST OF FIGURES

ACKNOWLEDGEMENTS

The last five years have been the most exiting and dynamic time in my life and I am thankful to many people who have helped me to accomplish my goal.

Most importantly, I would like to thank my advisor Prof. John T. Yates, Jr. for giving me an opportunity to work in his laboratory. I am very grateful to him for continuous support and for his perpetual encouragements in science and life. I believe the momentum I gained under his guidance will be dominant over many years to come.

I am especially thankful to Prof. J. Karl Johnson for fruitful collaboration and many hours of exciting discussions.

I greatly appreciate support from all members of the Surface Science Center. I am thankful to Petro Kondratyuk for being very helpful in my research and for our interesting debates.

I would like to express my sincere thanks to all people from the Department of Chemistry for helping me in whatever problem I had. I thank Bob Muha, Chuck Fleishaker, Dave Emala and Jim McNerney from the electronic shop; Tom Gasmire, Jeff Shicher, Dennis Sicher and Rob Walters from the machine shop; and Bob Greer from the glass shop. Many thanks to Margie Augenstein for her everyday care.

I acknowledge with many thanks the Army Research Office and Aberdeen Proving Ground for financial support of this work.

It would be enormously harder for me to reach this goal without love and support from my wife Ruslana. I am forever indebted to her for all sacrifices she made over this time.

INTRODUCTION

CARBON NANOTUBES – STRUCTURE AND SYNTHESIS

The truly extraordinary property of the carbon atom to arrange with itself in so many ways serves as the basis for existence of a number of carbon structures and a nanotube is one of the most remarkable. Carbon nanotubes were discovered in 1991 by Iijima *(1)* and immediately were recognized as a potential material with exceptional properties for a variety of applications, ranging from reinforcing materials *(2)* to adsorbents *(3)*, to molecular electronic devices *(4)*. The scientific excitement about this particular type of carbon stems from the fact that nanotubes have an ideal tubular structure with molecular size diameters and macroscopic lengths. Carbon nanotube related research has many facets and more information can be found in several books and reviews which have appeared since the their discovery *(3-16)*.

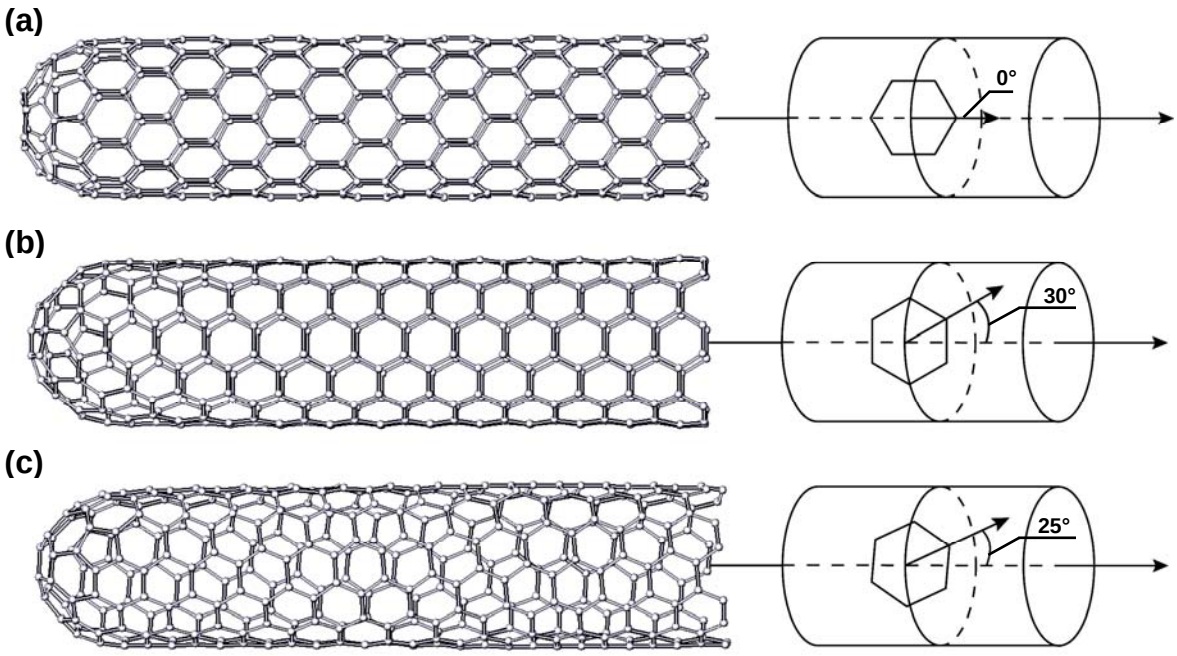

Figure 1. Schematic theoretical models of single walled carbon nanotubes, their hexagons, orientations and cap structure: (a) zigzag (10,0) nanotube, (b) armchair (6,6) nanotube; (c) chiral (7,5) nanotube.

Carbon nanotubes are classified into two main categories: single wall (SWNTs) and multiwall carbon nanotubes (MWNTs). A single wall carbon nanotube can be imagined as a graphene sheet (the hexagonal arrangement of carbon atoms) rolled into a seamless cylinder so the structure is one-dimensional with axial symmetry, and in general exhibiting a spiral conformation, called chirality. Its diameter is of nanometer size and its length can reach several millimeters (*i.e.* length/diameter ratio can be as large as 10^3-10^7) *(17, 18)*. The structure of a carbon nanotube is defined by the orientation of the carbon hexagon relative to the tubular axis. Figure 1 shows three primary configurations of SWNTs with respect to the arrangement of hexagons: armchair, zigzag and chiral.

The first SWNTs observed in 1993 were synthesized by the arc discharge method *(19, 20)*. Since then a number of techniques for SWNT manufacture have been developed and four major synthetic routes can be singled out: 1) arc discharge synthesis *(21)*; 2) laser ablation method *(22)*; 3) chemical vapor deposition (CVD); and 4) catalytic growth in gas phase *(4, 7, 10)*. The last two methods show great promise toward large scale synthesis of SWNTs *(2)*. Now, SWNT synthesis is still an active research field because the manufacturing procedure influences the macroscopic properties of the final nanotube material *(10, 23, 24)*. The main issues which are addressed in SWNTs synthesis research are the nanotube purity from catalysts and other carbonaceous particles, nanotube diameter and length distributions, and the nanotube structural integrity.

The simplest way of specifying the structure of an individual nanotube is the vector model *(5, 12)*. The key point of this model is the chiral vector which is defined as a vector C (OK) in Figure 2 that joins two equivalent points on the original graphene lattice. It can be expressed as:

$$C = n \cdot a_1 + m \cdot a_2 \qquad (1)$$

where a_1 and a_2 are the unit cell base vectors of the graphene sheet, and n ≥ m. It is seen from Figure 3 that for all armchair tubes n = m, while for all zigzag tubes m = 0. Armchair and zigzag nanotubes have achiral structures. All other tubes are chiral and exhibit a spiral symmetry whose mirror image cannot be superposed on to the original one. An arbitrary tube is produced by rolling up the sheet into a cylinder such that the end-point A and the origin O are superimposed. By joining the segment AB to the parallel segment A'B' the 1D tubule unit cell is formed.

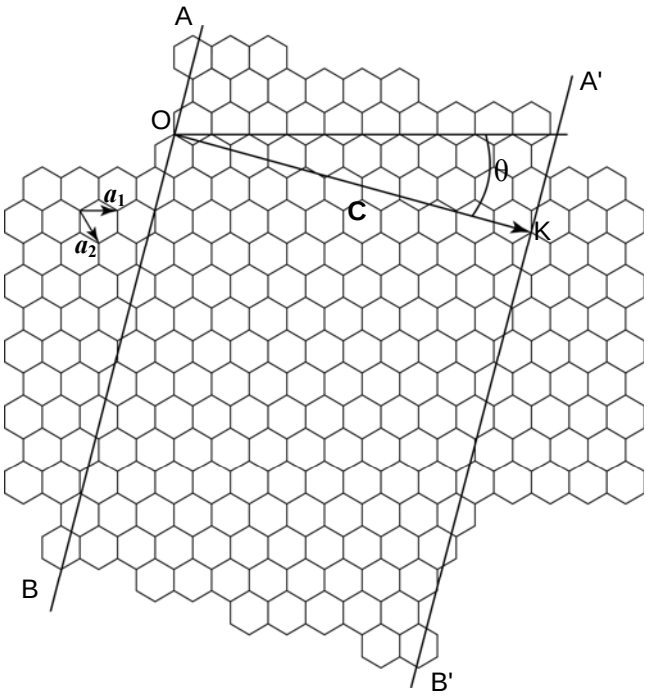

Figure 2. The unrolled honeycomb lattice of a (8, 3) nanotube. OK defines the chiral vector C. The chiral angle θ represents the tilt angle of the carbon atom hexagon with respect to the direction of the nanotube axis. a_1 and a_2 are the unit cell base vectors of the lattice.

Rolling a graphene sheet into a nanotube introduces a strain into the structure that is inversely proportional to the square of the nanotube diameter *(25, 26)* and therefore smaller diameter nanotubes are less stable. This in fact was confirmed by observation of nanotube coalescence and the formation of larger diameter tubules during heating or electron irradiation

(27). The stability of the nanotube tubular geometry relative to a graphene sheet with the same number of carbon atoms is determined by the total energy drop due to elimination of the dangling bonds *(28)*. However when the nanotube diameter is reduced below 6 Å the cylindrical structure becomes less stable than the planar one *(28)*. This was corroborated by an experiment when extremely small (~4 Å) nanotubes were observed only in solid matrices *(29, 30)* or as the inner part of a multiwall carbon nanotube whereas synthesized SWNTs usually have diameters in the 7-20 Å range. Much larger diameter nanotubes (up to 70 Å) were also detected by TEM *(27, 31, 32)* and so far there is no clear indication on the upper limit of a SWNT diameter. The reason for this may be in the increased number of structural defects in a larger diameter nanotube that distorts cylindrical geometry and therefore makes it difficult to classify this structure as a nanotube.

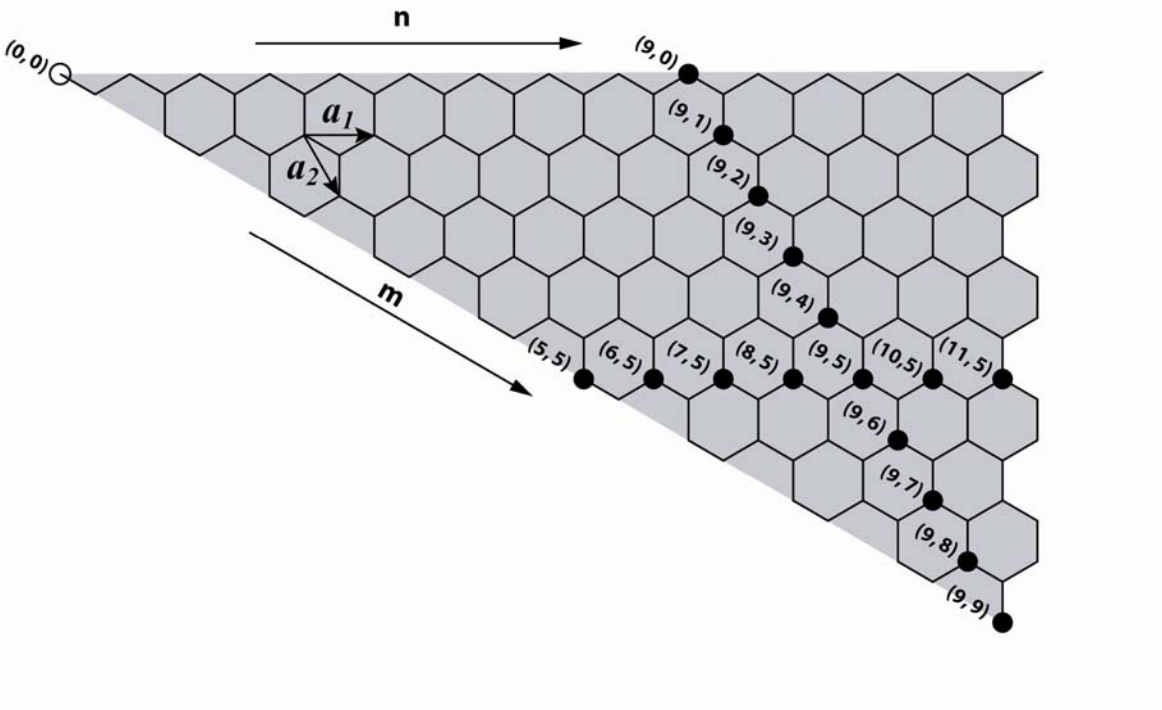

Figure 3. A section of the 2D graphite sheet called 'irreducible wedge' is shown along with the pairs of integers (n, m) which specify the symmetry and electronic properties of the considered single walled carbon nanotube.

Theoretical studies have shown that the physical properties of carbon nanotubes are strongly dependant on tubule diameter *(5, 6)*. Every carbon nanotube, its structure and physical properties can be defined only by a pair of (n, m) integers. The electronic properties of nanotubes strongly depend on the values of (n, m). In general, nanotubes exhibit metallic or semiconducting behavior which is correlated to the pair of (n, m) values in the following way: the nanotube has metallic properties if n – m = 3×integer, whereas it is a semiconductor if n – m ≠ 3×integer. Further information on the nanotube electronic properties can be found elsewhere *(5, 12, 33)*.

The diameter of a SWNT can be calculated from the equation (2):

$$d = a \cdot \frac{\sqrt{3}}{\pi} \cdot \sqrt{n^2 + m^2 + n \cdot m} \qquad (2)$$

where *a* is the nearest-neighbor C-C distance (1.41 Å in graphite). The diameter distribution of SWNTs is of great interest for both theoretical and experimental reasons. However experimental separation of nanotubes of identical structure has not been realized yet and prepared materials contain a distribution of nanotubes diameters and chiralities. Some success in the nanotube diameter distribution has been achieved by changing some parameters of nanotube synthesis *(24, 34-44)*, or by oxidative or acidic purification when small diameter nanotubes are destroyed faster *(45)*. During such treatment, defects are introduced into the nanotube structure *(46)* and when the number of defects per length unit overcomes some critical value the cylindrical structure becomes unstable any more and is destroyed *(47)*. This barrier is lower for small diameter nanotubes because of higher structural strain.

A nanotube material with a uniform diameter distribution is desirable in many fields of potential carbon nanotube applications. The diameter distribution can be sharpened either during the synthesis or in the following treatments. Synthesis of SWNTs in matrices with uniform well defined pores (e.g. in the zeolites designated MCM-31 *(48)*) is a promising way to obtain

nanotubes with uniform diameters. Some success in sharpening the nanotube diameter distribution has been achieved via diameter selective interactions of nanotubes with some agents. For instance, it was demonstrated that some polymers are capable of isolating of certain nanotubes via selective suspension in solutions *(49, 50)*. In addition, nanotube diameter distribution can be changed selectively during oxidation with H_2O_2 when irradiated with the light frequency corresponding to the nanotube absorption maximum *(51)*. However, STM *(52, 53)* and electron diffraction *(54)* studies show that a sharp diameter distribution *(22, 27)* does not necessarily represents the real nanotube material properties since nanotubes with similar diameters may possess different chiralities, i.e. be a mixture of metallic and semiconducting nanotubes.

Separation of metallic nanotubes from semiconducting nanotubes is a very important problem for their application in molecular electronics *(55)*. *Ab initio* calculations indicate that metallic nanotubes are more reactive during wall functionalization *(56)*. This was corroborated by experimental tests and it was shown that semiconducting SWNTs are more inert in the reaction with NO_2^+ ions *(57)*, acids *(58)* and bromine *(59)*. Some separation on macroscale also can be achieved by electrophoresis *(60)*. On the microscale, semiconducting nanotubes can be separated by selective elimination of metallic tubes via resistive heating in an oxidizing gas of a rope composed of mixed nanotubes *(61)*. In spite of the apparent progress in nanotube diameter and chirality selective separation, researchers will need to go a long way before uniform nanotube materials become available in large quantities.

Nanotube length control is another important issue from the application standpoint. The average length of synthesized nanotubes is in the range of 1-100 μm. The production of extremely long (1-4 mm) nanotubes has been also reported *(17, 18)*. Shortening of the as-

synthesized material usually happens during the purification procedure, that result in nanotubes with hundreds of nanometer lengths *(62-65)*. Controlled length reduction of an individual tubule can be achieved by means of a high voltage pulse directed from an STM tip *(66)* which cuts the nanotube wall. Precise cutting of SWNTs also may be achieved by lithographic methods *(67)*.

The large length/diameter ratio aspect allows high flexibility for nanotubes *(68-70)*. Even during careful handling of the nanotube containing materials, spatial fluctuations of mechanical forces are sufficient to cause bending, twisting, or flattening. Nonetheless, deformations caused by these factors are not permanent and the structure can be easily restored as the stress is removed *(68)*.

Purified single walled carbon nanotubes produced in large volumes usually form ropes which are aggregated by axially aligned individual nanotubes attracted to each other by van der Waals forces *(21, 22)*. These ropes can be created during either the synthesis or purification process and may reach centimeters in length *(71, 72)*. An ideal bundle consists of identical nanotubes assembled into a hexagonal macrostructure. The separation between two adjacent tubes should be around 3.4 Å – the interlayer distance in graphite. Indeed, the existence of a 2D lattice formed by SWNTs organized in bundles was determined from XRD analysis of nanotube-containing materials *(73)*. Since nanotube manufacturing techniques available at the moment are not chirality selective, an unlimited number of arrangements are possible for a particular bundle. This may result in a variety of "structural" defects in the bundle such as an increase or decrease of inter-tubular distances and cavity formation. The average bundle length always exceeds the average length of nanotubes in the bundle. Therefore bundles consist of a number of nanotubes stretched along the bundle direction. Bundles can be enlarged by attaching of separate nanotubes on their surface and extending discontinued positions with new tubes. As a consequence of the

bundle elongation and growth, junctions and branching also appear as is shown in Figure 4. All these imperfections may influence the desired property of a nanotube material and therefore dealing with separate tubes is preferred. Due to this, the extraction and stabilization of individual SWNTs or debundling is an important problem. Debundling can be achieved by side wall chemical functionalization *(74)* or non-covalent polymer wrapping *(75)*. Some nanotube applications require highly ordered structures. Alignment of SWNTs can be achieved via dispersing in superacids *(76)*, during CVD synthesis *(77)*, by spinning *(2, 78)*, by application of electric *(79, 80)* or magnetic fields *(81)* or may be liquid flow induced *(82)*.

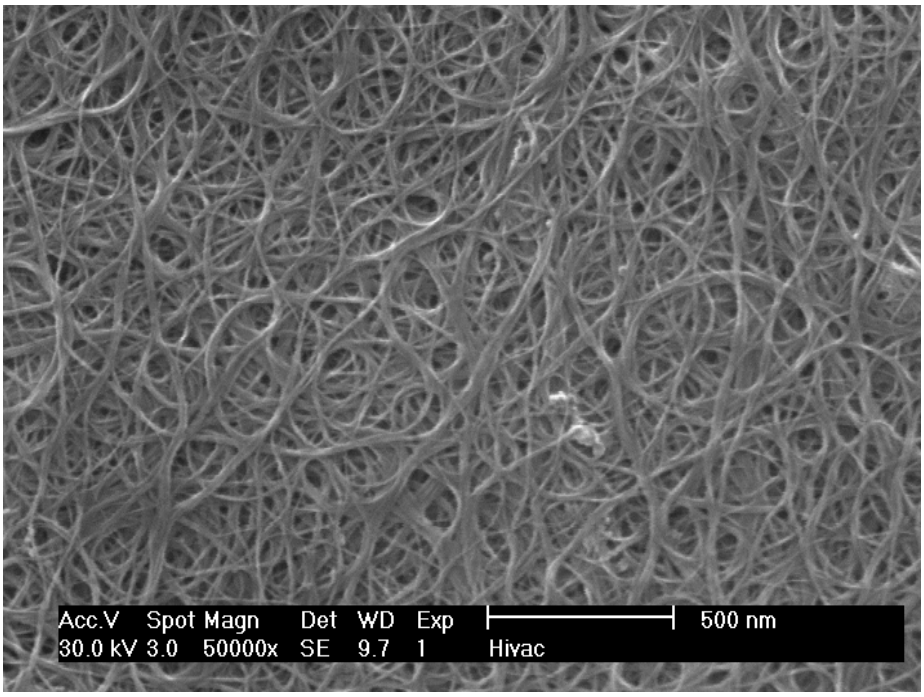

Figure 4. SEM image of single walled carbon nanotubes.

Since as-produced nanotubes contain metallic catalyst particles and other carbonaceous impurities some sort of purification is usually applied to remove these non-nanotube constituents. Nanotubes can be purified via acid treatment and sonication *(83)*, acid treatment and air oxidation *(58)*, high temperature hydrogen treatment *(84-86)*, magnetic filtration and

oxidation *(87)*, surfactant sonication and oxidation *(58, 88)*, functionalization and extraction *(89)*, reaction with sulfur *(90)*, centrifugation *(74, 91)*, oxidation with fluorination of catalyst particles *(92)*, potassium intercalation and wet oxidation *(93)*, by means of chromatography *(94, 95)*, electrophoresis *(96, 97)*, or by selective synthesis *(98)*. Purification procedures usually involve oxidative and acidic treatments, and a mechanical separation. Oxidation is required for burning the less stable non-nanotube carbon materials and for extracting catalyst particles from carbonaceous layers. Non-oxidative acid treatments are applied mainly to dissolve the exfoliated catalyst particles. Nanotube purity is usually evaluated by means of Raman spectroscopy, TEM, SEM, and TGA methods *(50, 99)*.

Any chemically aggressive purification results in defect formation in the nanotube structure. As-synthesized nanotubes are usually terminated by fullerene-like hemispherical caps. Chemical cutting processes involving strong oxidizing agents destroys the end caps leaving nanotubes with open ends *(62, 100, 101)*. In addition the nanotube wall can be attacked as well *(46, 100)* forming openings as were observed by TEM *(102)*. The extensively discussed possibility of formation of point defects, e.g. side wall opening due to carbon atom exclusion or creation of adatom structures was also observed by TEM *(103)*. Oxidative treatment can substantially change the electronic properties of carbon nanotubes, for instance, by transforming semiconducting SWNTs into metallic SWNTs *(104)*. Introduction of pentagon and heptagon defects in a nanotube can transform the nanotube from metallic to semiconducting and vice versa *(105)*. Some defects created for instance by electron irradiation can the trigger formation of intertubular links and formation of nanotube joints *(106, 107)*.

Functionalization, i.e. chemical attachment of a functional group to the nanotube body, is another way for property modification of carbon nanotubes. Functionalization is employed for

nanotube solubility enhancement *(55, 108)*, and optical and mechanical properties modifications *(109)*. It also offers a convenient way for individual nanotube manipulation via debundling of nanotube ropes *(102)*. Several functionalization methodologies have been developed, and all of them employ a highly reactive agent for the attack of the nanotube sidewall *(55)*. Functionalizations via fluorination *(110, 111)*, chlorination *(112)*, thiolation *(113)*, bromination *(59)*, use of free radicals *(114)*, amide/amine *(115, 116)*, hydrogen *(117)*, CO_2 *(108)*. and alkyl species *(108, 118)* have been reported.

The spectral properties of carbon nanotubes are well understood and defined by their chirality and can be modified by defect formation and functionalization. Itkins et al. presented an experimental spectroscopic study of SWNTs from the far-IR to the UV region *(119)*. The UV region is dominated by π-plasmon absorption. Inter-band transitions between van Hove singularities are observed in the near-IR region. Raman spectroscopy within the 200-300 cm^{-1} frequency region can reveal the composition of the nanotube material with respect to chirality. The enhanced intensity of the D-band at 1350 cm^{-1} relative to the 1580 cm^{-1} nanotube phonon mode in the Raman spectra points to a presence of disordered graphitic structures. Mid-IR infrared spectroscopy is used mainly for detection of nanotube functional groups since the inherent nanotube modes have very low intensity in IR spectra. The far-IR region of the SWNT spectrum is dominated by absorption due to the intra-band transitions *(119)* that can be enhanced by defect creation or functionalization of SWNTs.

In conclusion, at present the main structural, electronic, spectroscopic and chemical properties of carbon nanotubes are understood. The production of nanotubes has been scaled up and large quantities of nanotubes can be received at relatively low prices. However the purity

and especially chirality and length homogeneity are yet to be improved so experimental testing of the predicted outstanding properties of carbon nanotubes can be carried out *(120)*.

ADSORPTION PROPERTIES OF SWNTS

The adsorption of gases in carbon nanotubes is a subject of growing experimental and theoretical interest *(3)*. From a practical perspective carbon nanotubes are considered as a promising material for hydrogen storage *(15, 121, 122)* and gas mixture separations *(123-125)*. Due to the high aspect ratio and relatively smooth walls, carbon nanotubes are viewed as an ideal medium for realization of matter in one dimension *(126, 127)*. Single wall carbon nanotubes exhibit a very rich spectrum of adsorption properties. A number of papers appeared in the last decade dealing with some or all aspects of adsorption on SWNTs. Adsorption of small molecules like He *(128-139)*, Ne *(128, 129, 135-137, 140-145)*, Ar *(126, 128, 136, 140, 141, 143, 146-154)*, Kr *(126, 136, 152, 155)*, Xe *(47, 135, 136, 141-145, 151, 153, 156-162)*, N_2 *(124, 149, 163-181)*, O_2 *(124, 146, 165, 169)*, CO *(169, 182)*, CO_2 *(146, 152, 158, 169, 182-185)*, CH_4 *(128, 136, 141-146, 151, 155, 186-190)*, CF_4 *(136, 159, 186, 191, 192)*, CCl_4 *(193-195)*, SF_6 *(136, 159, 184)*, NO_x *(196, 197)*, MeOH *(164)*, C_6H_6 *(164)*, C_xH_y *(188, 194, 198)* and H_2O *(127, 199-223)* has been reported. In many cases interactions of hydrogen and water with nanotubes are considered separately because of the great span of the topic in the first case and a possibility of hydrogen bonding in the second one. A brief overview of H_2 adsorption on carbon nanotubes is given in the Apendix B. Adsorption of water in carbon nanotubes will be considered in detail in Chapter V-1 of this work. In the following description of the adsorption properties of carbon nanotubes we will limit ourselves in most cases only to physisorption, i.e. adsorption without formation adsorbate-adsorbent chemical bonds.

The adsorption properties of carbon nanotube materials may strongly depend on the synthesis, purification and additional treatments. However the majority of the publications admit only a limited number of adsorption sites related to the fact that nanotubes are ordered into

bundles. In a perfect bundle, single walled carbon nanotubes are arranged in a hexagonal array. That gives rise to the four possible adsorption sites for the bundle: outside nanotube surface, groove sites, interstitial channels and nanotube interior, as shown in Figure 5 *(133, 135, 150, 162)*. The adsorption properties of the considered species on every site usually are compared to those on a flat graphite sheet *(135)*.

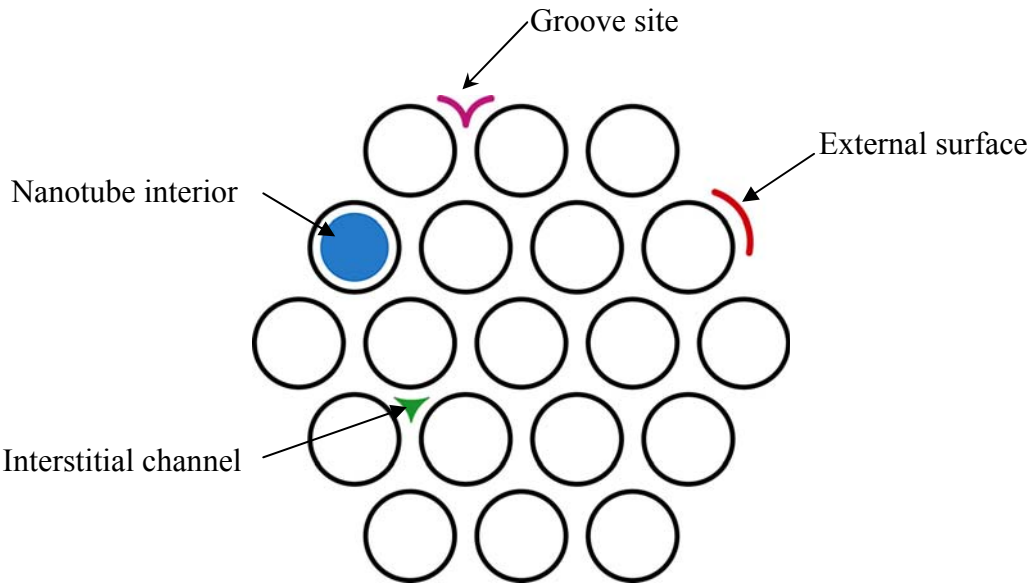

Figure 5. A schematic representation of the four main adsorption sites on an ideal bundle of single wall carbon nanotubes.

A. Adsorption in the Nanotube Interior.

The major interest in adsorption properties of SWNTs is caused by the unique cylindrical geometry of carbon nanotubes. A molecule adsorbed in the nanotube interior experiences stronger binding forces relative to a flat graphitic surface that result from a higher degree of coordination of the adsorbate molecule with the concave nanotube wall *(136)*. Theoretical works *(186)* show that adsorption occurs at some optimal distance from the nanotube wall which is dictated by the adsorbate size and the carbon atom–adsorbate interaction energy. In many instances the distance of 1.7 Å is adopted for the first approximation since it is roughly the half of the interlayer separation for graphite and was shown to be correct for many nanotube samples.

Apparently, the adsorption is prohibited sterically when the molecule or atom diameter exceeds the pore diameter inside a nanotube available for adsorption. The best example for this would be encapsulation of C_{60} first observed by Smith et al. *(224)* by means of TEM. The outer diameter of C_{60} is ~10 Å, a diameter which includes the outer π-electron cloud. So only nanotubes with diameters greater than ~13.5 Å (here again the π-electron thickness inside the SWNT is taken into account) can accommodate C_{60} molecules. A Raman spectroscopy study of different size fullerenes encased in SWNTs conducted by Bandow et al. *(225)* indicates that C_{60}, C_{78}, and C_{84} cannot be encapsulated by nanotubes with diameters smaller than 13.7 Å, 14.5 Å and 15.4 Å respectively. However in comparison to many molecules presently used for testing adsorption properties of carbon nanotubes, C_{60} is a large species. In most cases nanotube diameter distributions start around 8-9 Å giving a 5 Å cylindrical pore as the smallest adsorption site for the nanotube interior when one includes the space occupied by nanotube π-electrons. Thus molecules like Ar (3.40 Å), CH_4 (3.45 Å), Xe (4.10 Å), CF_4 (4.58 Å) or SF_6 (5.25 Å) can easily fit inside most of the nanotubes *(135)*.

It is believed that an adsorbate forms chains in the nanotube interior when the pore diameter is comparable with the adsorbate size. Internally adsorbed species can be found in a deeper potential well if the molecular diameter matches the size of the internal pore *(136)*. In this case an interesting result was reported by Li et al. *(226)*. It was shown that out of two metallocene compounds, bis(cyclopentadienyl) cobalt ($CoCp_2$) and bis(ethylcyclopentadienyl) cobalt ($CoEtCp_2$), the first one could be found in nanotubes of ~10 Å diameter and the second one was observed only in tubes with diameters greater than ~10 Å. Since the ethyl groups possess great flexibility and do not appreciably alter the molecular shape, both molecules have approximately equal molecular sizes. However, when adsorbed inside a nanotube the ethyl

groups allow enhanced interaction of $CoEtCp_2$ with larger tubules whereas ($CoCp_2$) finds a better fit in smaller nanotubes.

Adsorption inside larger diameter tubes proceeds via coating the concave walls at low coverages ("shell phase" formation) followed by filling the central part of the pore, i.e. "axial phase" development *(132, 147, 150)*. To some degree construction of the "shell phase" resembles monolayer adsorption for planar surfaces. Intermolecular interactions in the "shell phase" may initiate construction of different ordered structures with shapes defined by the ratio of the adsorbate size to the pore diameter. Hodak et al. *(227)* have calculated geometries of ordered phases of C_{60} in carbon nanotubes as a function of tube diameter. It was shown that different helical and columnar structures may appear depending on the nanotube diameter. The prediction of helixes inside carbon nanotubes was corroborated by Fan et al. *(228)* by detecting helixes of iodine atoms in SWNTs. The authors also proposed that a difference in helix periods results from the difference in nanotube chiralities. This in turn suggests formation of a commensurate phase of the adsorbate on the concave nanotube wall and was also considered by Green et al. *(229)* for He. On the other hand, it is known the sensitivity of the adsorbate to the atomic structure of the graphite surface is limited only to small size species like H_2 and He *(230)* and that agrees with computations of Simonyan et al. *(160)*. These authors have predicted that Xe atoms confined in nanotube interior are packed into an incommensurate 2D hexagonal lattice. Due to this in many cases the influence of the periodic potential inside carbon nanotubes is omitted and the surface may be considered smooth.

The smoothness of the nanotube interior is also responsible for enhanced diffusivities of light gases in carbon nanotubes *(140, 188, 231)*. Computer simulations predict that the exceptionally rapid transport through nanotubes results from the absence of corrugations in the

nanotube interior. It was shown that the rate of diffusion is independent of nanotube chirality but decreases with nanotube diameter. This effect can be explained by the drop in smoothness of the internal surface as the nanotube size decreases.

Stan et al. *(136)* pointed that the "shell phase" might exhibit dual properties with respect to the dimensionality of the adsorbed species. Thus helium adsorbed at temperatures close to 0 K in a nanotube of diameter 10 Å was predicted to be a 1D system with the specific heat per particle approaching $k_B/2$. At higher temperatures a transition occurs, which converts the system into a 2D phase with the specific heat of k_B. This transition can be described by assuming the quantum behavior of the adsorbent that is characterized by a discrete spectrum of motion in the azimuthal and axial directions. According to Calbi et al. *(230)* the azimuthal excitation temperatures between the two lowest levels are of order 1 K for He and H_2 and 0.1 K for Ne. Therefore the 1D regime in the "shell phase" can be achieved at very low temperatures and only for light particles. This however is not the same for the "axial phase" which appears after the completion of the first layer on the nanotube walls. When the diameter of the formed pore does not considerably exceed the adsorbent size the axial phase will exhibit the properties of a 1D system. For nanotubes with larger diameters and respectively larger pores where the axial phase can be accommodated, development of ordered structures similar to those appearing during the filling of the "shell phase" may be possible *(227)*. Ultimately, for extremely large tubes an adsorbent will fill the pore by capillary condensation (formation of liquid within pores at pressures below the saturation pressure at given temperature) and will exhibit bulk-like properties. Maddox at al. *(149)* performed grand canonical Monte Carlo simulations to study the adsorption of simple fluids in 10-50 Å diameter nanotubes. It was found that argon and nitrogen fill up the interior of a 10.2 Å nanotube at low pressures forming 1D phases. Adsorption in a

47.8 Å nanotube proceeds differently and the tube interior is loaded with an adsorbate via continuous layer formation with consecutive capillary condensation. Thus the capillary condensation occurs in pores with diameters not smaller then few nanometers *(149, 232)*. Importantly, this is above the range of diameter distributions for the majority single wall carbon nanotube samples and therefore usually is not considered.

B. Adsorption in Interstitial Sites

The interstitial channel site appears as a product of the hexagonal arrangement of nanotubes in a bundle as shown in Figure 5. In an ideal bundle this site is formed by three neighboring nanotubes and its size is defined by their diameters. For example, in a bundle composed of only (10, 10) nanotubes with diameters of 13.6 Å the interstitial channels are 6 Å in diameter. However only 2.6 Å diameter pores are available for adsorption since the layer of 3.4 Å is occupied by nanotube π-electrons *(190)*. In this case only small adsorbates like H_2, He or Ne can fit into the interstitial site *(138, 139)*. In reality nanotube bundles are composed of tubules of different diameters, e.g. they are heterogeneous *(233)*. A random distribution of nanotubes in a heterogeneous bundle will undoubtfully result in some number of interstitials large enough to accommodate larger adsorbate molecules that could not fit in a channel composed of equal diameter tubules. Thus Shi et al. *(151)* has found much greater agreement between the theoretical and experimental isosteric heats of adsorption for CH_4, Ar and Xe if adsorption is assumed to occur in heterogeneous bundles, i.e. the largest interstitial channels are available for adsorption. Another way a large molecule can enter an interstitial channel results from expansion of the nanotube bundle lattice. Calbi et al. *(128, 129)* have calculated that interstitial channels can accommodate Ar or CH_4 if 1.94% or 2.19% lattice constant increases, respectively, are allowed. On the experimental side, Muris et al. *(155)* have observed two steps in the isotherms of CH_4 and

Kr and suggested that the first step corresponds to the adsorption in the interstitial channels. This however was rejected by the same group based on their neutron diffraction measurements of methane, argon, oxygen and carbon dioxide on SWNT bundles *(146)*. Instead adsorption in the interstitials of heterogeneous bundles was suggested. Moreover, the authors indicated that nanotubes in a pristine heterogeneous bundle may deform to enhance contact area between neighboring tubules. This consecutively leads to shrinkage of the "imperfect" interstitial channels *(187)*. However, the authors have shown that when a molecule or atom enters the interstitial channel, the neighboring nanotubes locally are pushed apart but remain intact elsewhere. This effect in fact allows stabilization of methane molecules adsorbed in the interstitial channel. The possibility of adsorption in interstitial channels of a homogeneous bundle also was strongly questioned by Migone's group *(145, 162, 189)*. Based on the observation of close percentage increase of binding energies for ^{4}He, Xe, CH_4 and Ne adsorbed on SWNTs relative to planar graphite, and taking into consideration the size of the H_2 molecule (its dynamic molecular diameter is larger than ^{4}He and Ne, but smaller than Xe and CH_4 *(145)*) these authors argued whether even H_2 can adsorb in the interstitial channels. In their later publications though this group seemed to have adopted the model of gas adsorption in interstitial sites of heterogeneous bundles *(148)*.

Due to the tight transverse confinement and extreme axial elongation of interstitial channels the adsorbed matter can exhibit properties of a one-dimensional phase *(137)*. It is well known that no phase transition can occur in a 1D system at temperatures above 0 K. This is because any thermal fluctuation would disrupt any ordering in one dimension *(230, 234)*. However, it was shown that He may form a 1D phase and exhibit an order/disorder phase transition in interstitial channels of homogeneous carbon nanotube bundles in the presence of an

ordering external potential *(234)*. Thus the theoretical calculations indicate that He confined in the carbon nanotube interstitials undergoes a phase transition (though at very low temperatures) due to a weak interaction between molecules in neighboring channels *(130, 230)*. Recently 1D behavior of He adsorbed at low temperatures was observed experimentally by Lasjaunias et al. *(134)* by measuring the specific heat of ^{4}He below 6 K.

C. Adsorption in Groove Sites

The groove sites are created by the pairs of adjacent nanotubes along the outside surface of a bundle. This adsorption site has a trough-like geometry which allows strong coordination to an adsorbed atom or molecule. In the most simplistic approach a species adsorbed in the groove site may be viewed as to interact with two surfaces and therefore its binding energy should be substantially greater than that for a molecule or atom adsorbed on single surface of graphite *(187)*. A number of publications corroborate this assumption. For instance, Williams et al. predicted that the attractive potential for a hydrogen molecule adsorbed in the groove site is ~43% higher than the one for an internally bound H_2 *(235)*. Experimentally Talapatra et al. *(145)* have fount that the binding energies of Xe, CH_4 and Ne adsorbed in the groove site are 75% larger than the corresponding values of these gases adsorbed on planar graphite.

Theoretical calculations of Calbi et al. *(142, 230)* show that filling of a groove site at low temperatures starts with adsorption in the lowest part of the groove along the contact line of two nanotubes and that the adsorbate is lined up in a single-atom (or molecule) strand (called here the original strand). The linear arrangement is caused by the adsorbate-adsorbate attraction and result in greater binding energies with respect to single-species distribution of the adsorbate. The exact position of the adsorbate with the respect to the nanotube walls depend on its size and binding energy as well as the diameters of the nanotubes that form the trough *(126)*. The species

adsorbed in the original strand exhibit properties of a one-dimensional (1D) phase as was computed by Calbe et al. *(141)* and demonstrated experimentally by Talapatra et al. *(153)*. An adsorbate in the 1D phase possesses a great translation freedom in the lateral direction but a large barrier limits intra-groove translations. For example, Ulbricht at al. *(161)* have shown that the energy required for translation of a Xe to the adjacent groove is ~10 kJ/mol. As the chemical potential increases additional strands of the adsorbate appears on both sides of the original chain, but the number of the strands that follow the original one depends on the size and binding energy of the adsorbate. For instance, Ne, Ar and Kr exhibit 3-strand behavior whereas Xe forms 5-strand arrangement. This difference can be explained by lower sensitivity of xenon to the surface corrugations due to its larger diameter and stronger interatomic attraction relative to Ne, Ar or Kr. In any case building of the additional strands gives rise to filling of the external surface. Adsorbate-adsorbate interactions also result in a shift of neighboring strands in the same groove so the atomic arrangement resembles hexagonal packing *(142)*. In addition, these interactions can change molecular orientation with respect to each other. Thus Matranga et al. *(236)* have shown that CO_2 molecules are forced to form a "T-shaped" one-dimensional chain by intermolecular quadrupole-quadrupole interactions. The same behavior for N_2 in the groove site was predicted by Arab et al. *(169)*.

As pressure increases a sequence of other strips builds up until the full monolayer is developed. Beyond this point multilayer condensation begins though construction of the second layer by filling the corrugation of the monolayer formed above the original strand *(142-144, 147)*, and as the number of layers increases this surface nonuniformity disappears *(141)*. The successive strand-like adsorption in the groove site is reflected in theoretical adsorption isotherms by coverage discontinuities or steps. These steps blur with temperature increase due to

site occupation change according to the Boltzman distribution law. In addition the behavior of the adsorbate in the original strand crossed from 1D at low temperature to 3D at higher T *(141)*. The 1D character of the groove site was also explored by Kondratyuk et al. by means of Temperature Programmed Desorption (TPD) *(194)*. It was shown that n-nonane occupies substantially more space that CCl_4 when adsorbed in the groove site than in the nanotube interior. This suggests that a n-nonane molecule unfolds into its linear conformation to enhance the interaction with nanotube walls whereas CCl_4, due to its almost spherical shape, is conformationaly non-specific. This concept was confirmed later by a TPD study of linear alkenes of different lengths of the carbon atom skeleton *(237)*. It was shown that the hydrocarbon occupancy per molecule in the groove site strongly correlates with the molecular length which indicates that the alkanes unfold when adsorbed in groove sites.

D. Adsorption on the External Surface.

The external surface is defined as the convex outside surface of carbon nanotube. In the case of an individual nanotube, adsorbates can reach the external surface around the whole nanotube circumference but in a bundle only the outermost nanotubes can furnish outside surfaces for adsorption and the outside surface of the nanotubes in the core of the bundle is not accessible. Geometrically the external surface in a bundle can be represented by a curved strip of a single sheet of graphite limited from the sides by groove sites. Due to this limitation the capacity of the external site is also dependant on the adsorbate size. This was pointed by Muris et al. *(159)* demonstrating that amounts of CF_4 and SF_6 the adsorbed on the external surface are slightly smaller then that of CH_4.

In some instances groove sites are included in the external surface *(230, 235)*, however, the true convex surface has much different adsorption properties than the groove site and

therefore discrimination between these sites must be made. Adsorption on the external sites at low temperatures starts upon completion of a string of the adsorbed particles in the groove site. Filling of the secondary strings on both sides still may be referred to as adsorption in the groove site even though the adsorbate does not interact directly with two nanotubes, but the potential well created by two adjacent nanotubes still has some depth relative to the external surface *(142)*. The consecutive adsorption on the external surface at low temperatures follows the stripe-like surface filling until monolayer completion. This situation changes if adsorption occurs at higher temperatures when a particle can overcome an energy barrier preventing the transverse motion. Urban et al. *(154)* have shown that as temperature increases the "three-stripe" phase for Ar become unstable and that the probability of finding a particle on the external surface also rises. The authors also demonstrated that the specific heat capacity as a function of coverage peaks at three coverages: (1) upon completion of the groove site; (2) upon completion of the "three-stripe" phase; and (3) upon completion of the monolayer. The specific heat capacity exhibits two peaks at 55 K and 165 K that are due to "three strip" phase $\rightarrow$ monolayer and primary groove strip $\rightarrow$ "three strip" phase transitions.

E. Other Aspects of Adsorption on Carbon Nanotubes

Due to the richness of the adsorption properties of carbon nanotubes the conventional definition of adsorption (enrichment of one or more components in an interfacial layer *(238)*) has to be extended to include distribution over all adsorption sites. Generally, the amount of adsorbed gas (n) by a solid of mass m at equilibrium can be described by the following equation:

$$\frac{n}{m} = f\left(p, T, \varphi(adsorbate - adsorbent)\right) \qquad (3)$$

where p is the equilibrium pressure, T – temperature and $\varphi(adsorbate - adsorbent)$ is a function that describes the nature of adsorbate-adsorbent interactions. Since in most cases determining

this function is the purpose of an investigation, the characterization of an adsorption process can be reduced to finding of the $\frac{n}{m} = f(p,T)$ dependence and fitting the data to a certain model for the adsorption process. By fixing the temperature an adsorption isotherm $\frac{n}{m} = f(p)_T$ can be measured.

Adsorption isotherms can be constructed by using a number of methods though its analysis might be not a trivial task because of the complexity of the nanotube structure. This however can be overcome by working at certain pressure and temperature conditions or application of different probe molecules or atoms. To understand this it is useful to consider an imaginary experiment involving the adsorption of a particular gas on bundles of carbon nanotubes shown in Figure 6.

Here the adsorbent size is arbitrarily chosen so the interstitial sites can be filled (at least the widest ones in case of heterogeneous nanotube diameter distribution) and formation of an axial phase in the interstitial sites is feasible. This however may not be possible if the diameter of the adsorbed species is big, limiting the adsorption only to the nanotube interior, groove sites and the external surface. Moreover adsorption in the internal adsorption site may be prohibited if nanotubes are closed. In that case adsorption in groove sites and on the external surface can be probed. A similar argument was used by Muris at al. *(159)* for explanation of two steps in the isotherms of Xe, CF_4 and SF_6 measured on closed SWNTs. The authors concluded that the first step corresponds to adsorption in the groove site and the second one was assigned to adsorption on the walls of outer nanotubes of the bundles.

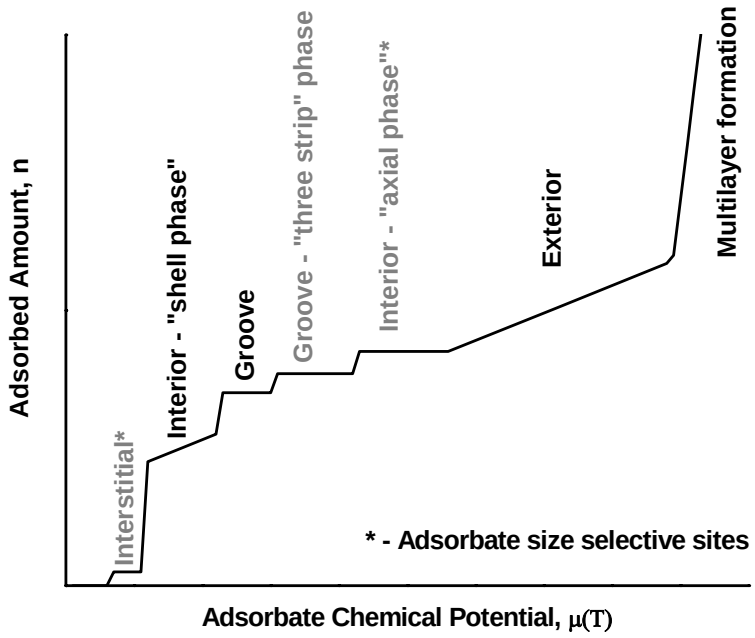

Figure 6. A schematic generalized adsorption isotherm for single wall carbon nanotubes.

The heights of the kinks in the isotherm in Figure 6 correspond to the capacity of a certain adsorption site. First of all, the amount of the adsorbed gas in the nanotube interior is a function of the fraction of opened nanotubes which in turn depends on the preparation technique, purification methods and later treatments. The capacities of the interstitial, groove and external adsorption sited depend on the size and shape of nanotube bundles. Very often bundles are believed to have a perfect hexagonal arrangement (assuming they are homogeneous) but TEM studies show that bundles can acquire different shapes. This however often is neglected with an argument that deviations from perfectly ordered bundles are not significant. From simple geometric considerations a perfect homogeneous bundle possesses the largest number of the interstitial channels and has the lowest external surface and least relative fraction of groove sites. Zambano et al. *(162)* have shown that in ideal nanotube bundles formed of 19, 37, 91, 169 and 217 SWNTs of 13.8 Å in diameter the capacities for Xe of the groove sites and the external

surface are 23% and 77% respectively. From the fact that only two steps were observed in their isotherms the authors also concluded that Xe adsorbs in the groove sites and on the external surface.

By far if all nanotubes are open, the interior of single wall carbon nanotubes is the most capacious adsorption site in a bundle. Comparison of the maximum adsorbate uptake by the nanotube interior and the capacity of the external surface combined with groove sites can be made by considering their geometric surface areas. The geometric specific surface area (GSSA) of a graphene sheet is 1315 m^2/g for one-side adsorption according to simple geometrical calculations of Peigney at al. *(239)*. There is a difference in the geometric specific surface area used in geometrical calculations in ref. *(239)* and specific surface area obtained experimentally for carbon nanotube materials. The latter includes the decrease in the area that appears due to the pore curvature. As a result fewer molecules can fit on the concave surface relative to the flat one. When the nanotubes are arranged into bundles, the internal GSSA does not change but the combined GSSA of the groove sites and nanotube exterior drops as the bundle size increases. For example, nanotube materials composed of closed identical SWNTs ordered into ideal bundles with 7, 19 and 217 tubes would give a GSSA of 751, 484 and 151 m^2/g respectively whereas the internal GSSA remains at the 1315 m^2/g value. A more realistic approach has been adopted by Williams et al. *(235)*. The specific surface area was calculated for adsorption of a spherical probe atom of diameter 2.8 Å in ideal bundles composed of nanotubes 13.6 Å in diameter. The calculations generate the following values for specific surface areas: 783 m^2/g for the nanotube interior independent of bundle size, 1893 m^2/g for the external surface of an individual nanotube, 1275 m^2/g, 818 m^2/g, 505 m^2/g and 358 m^2/g for combined SSA of the groove and external sites of bundles made of 3, 7, 19, 37 tubes. The SSAs of the interstitial site are 12 m^2/g, 31 m^2/g, 45

m^2/g and 52 m^2/g for the same bundles. Independent of the model the total SSA for all bundle types is over 1000 m^2/g, i.e. nanotubes are shown to be able to compete with high surface area carbons. Moreover grand canonical Monte Carlo molecular simulations carried out by Yin *at al. (168)* for adsorption of nitrogen at 77 K on square arrays of open and closed single-wall carbon nanotubes with diameters of 6-30 Å and nanotube separations of 4-30 Å indicate that even higher BET surface areas (in the most favorable structure) of ~3000 m^2/g may be expected. However it is obvious that adsorption inside of nanotubes must be realized in order to reach the highest adsorption capacities (and binding energies) for materials based on single wall carbon nanotubes.

The highest experimental total SSA value for SWNTs was reported by Cince et al. *(163)* and is 1587 m^2/g for the purified sample versus 567 m^2/g for the raw material. The external and internal surfaces make up 909 m^2/g and 678 m^2/g for the purified SWNTs against 382 m^2/g and 194 m^2/g for the raw material. The increase of the internal surface are was related to opening of nanotubes during the acidic treatment and wet oxidation. The enhancement of the external SSA was suggested to be mainly the result of debundling, caused by nanotube dispersing in an organic solvent mixture prior to amorphous carbon removal by the gentle acid treatment and heterogeneous oxidation in wet air. Yang et al. indicated that such treatment enhances SSA by a factor of ~2 relatively to the 861 m^2/g surface area obtained for more "bundled" SWNTs *(167)*. Pierard et al. *(240)* reported that the SSA of SWNTs can be increased to ~ 1500 m^2/g form ~750 m^2/g after 2h of ball-milling. Again the SSA increase was associated with opening of the nanotube interior.

The interior of nanotubes can be made accessible in a variety of ways but all of them related to introduction of defects into the nanotube structure *(241)*. The defects may vary in size and shape but it is believed that in all cases their edges are decorated with functional groups

resulting from after-synthesis treatments. The NEXAFS study by Kuznetsova at al. *(242)* indicates that purification of HiPco single wall carbon nanotubes with HNO_3/H_2SO_4 or H_2O_2/H_2SO_4 mixture produces oxygenated groups with 5.5 – 6.7% ratio of O/C whereas samples not treated with oxidizing acids exhibit an O/C ratio of 1.9%. By combination with IR studies the authors identifies these functionalities as C-O-C bonded moieties as well as carboxylic (-COOH) or quinone (>C=O) C=O groups *(156, 243)*. A number of studies point that these functional groups hamper the adsorption in the nanotube interior. For instance, the TPD investigations of Xe adsorption in SWNTs of 13.6 Å in diameter show that these functionalities block the entry port into nanotube interior and slow down the kinetics of adsorption *(47)*. The blocking oxygenated groups can be removed by heating nanotubes to temperatures above 873 K increasing the effective nanotube capacity to Xe by a factor 280.

In general, adsorbates can enter the internal adsorption site of carbon nanotubes through the opened ends or through defective "ports" on the nanotube walls. Since the untreated nanotubes are closed with hemispherical caps which are less stable then the walls one may think that opening of nanotubes proceeds via reaction of the curved nanotube end caps. However Mawhinney et al. *(46)* have shown that the SWNTs purified by acidic oxidation and heated to 1273 K contain a fractional defect level of ~5.5% of the surface carbon atoms which can not be attributed only to the end caps indicating that adoption in the nanotube interior in fact occurs through both the open ends and through entry ports etched in the carbon nanotube walls.

The blocking properties of functionalities can be used for optimization of adsorption in nanotubes. In another study Kuznetsova at al. have demonstrated that oxygenated groups can be regenerated on SWNTs by utilizing ozone *(157)* as an oxidizing agent. These groups may be destroyed by annealing at 973 K. Successive reiteration of this process causes etching of

nanotubes. It was shown that etching is initially accompanied by an increase of surface defects, reaches some optimal structure for nanotube adsorption, and ends up with total degradation of nanotubes with loss of considerable adsorption capacity. This trend reflects on adsorption of xenon (monitored by means of TPD spectroscopy) and it was shown that xenon coverage can be strongly enhanced by functionality removal by etching. The rate of Xe adsorption into the interior maximizes when the optimal radius of 5-7 Å is reached for openings in the walls of carbon nanotubes.

Another possible application of nanotube functionalities has been explored by Matranga et al. *(184)*. It was demonstrated that small quantities of SF_6 and CO_2 can be locked into the nanotube interior by the oxygenated surface groups and kept there above the desorption temperatures of these gases for some time. The gases were adsorbed a low temperatures and the functionalities were created by exposing the filled nanotubes to ozone. The release of the entrapped adsorbates can be achieved by thermal treatment of nanotubes in vacuum to 700 K. The oxygenated functionalities also may become a source of CO_2 that again can be permanently trapped in the nanotube interior during thermolysis *(183, 236)*. In this case CO_2 was found to be stable inside nanotubes for months and could survive temperature cycling in vacuum from 5 to 700 K *(184)*. The author suggested that the confinement of CO_2 may be related to steric rearrangements of the defects on the nanotube surface and blocking by the undecomposed functionalities.

Surface defects can also serve as adsorption sites in addition to the mentioned sites related to nanotubes themselves. In the IR study of carbon monoxide adsorption on SWNTs Matranga et al. *(182)* have shown that CO adsorbed on acid treated nanotubes exhibits a blue shift relative to the gas phase frequency. The authors concluded that the shift result from CO

molecules that are hydrogen-bound to carboxylic functionalities produced during the treatment. Another phenomenon related to adsorption on nanotube defects has been reported by Kuznetsova et al. *(157)*. The authors carried out a theoretical GCMC calculation of Xe adsorption into the nanotube interior through a hole in the nanotube wall. It was shown that upon complete filling of the nanotube interior, Xe atoms can cluster at the hole on the external surface of the tube and that the probability of cluster formation increases with the strength of the induced dipole moment in Xe cluster atoms created by functionalities on the edge on the hole.

F. Summary

In summary, the adsorption properties of single wall carbon nanotubes are defined by the hollow tubular structure of nanotubes and their ability to form bundles. Four major adsorption sites (outside nanotube surface, groove sites, interstitial channels and nanotube interior) were predicted theoretically and detected experimentally and the nanotube interior is the most capacious and strongly binding adsorption site. All four adsorption sites support formation of 1D structures at certain coverages. Surface defects, carbon atom vacancies or functionalities, play an important role in adsorption in nanotubes and can block or enhance the adsorption or serve as additional adsorption sites on their own. Methods involving temperature programmed desorption, infrared spectroscopy and isotherm measurements are valuable for studying adsorption in and on single wall carbon nanotubes.

PART I

ADSORPTION OF SMALL MOLECULES ON SWNTS - INFRARED SPECTROSCOPY STUDIES

SYSTEM DESCRIPTION

The system employed in the infrared studies of gas adsorption on carbon nanotubes consists of a FTIR spectrometer, a transmission IR cell and a gas handling vacuum line. The IR cell is directly positioned in the sample compartment of the Matteson Research Series FTIR spectrometer. Two types of IR transducers, wide band photoconductive MCT ($D^* = 9\times10^9$ $cm\cdot Hz^{½}\cdot W^{-1}$, 420 – 5000 cm^{-1}) and narrow band photoconductive MCT ($D^* = 3\times10^{10}$ $cm\cdot Hz^{½}\cdot W^{-1}$, 740 – 5000 cm^{-1}), were used depending on the absorption region of interest. The spectrometer and the IR beam pathway were constantly purged with dry N_2 gas from a liquid nitrogen reservoir. The sample and IR beams where aligned by using an infrared viewer and by monitoring the detector response to the position change of the sample before every measurement.

The stainless steel vacuum system (Figure 7) is equipped with a 60 L/s turbomolecular, a 20 L/s ion pump and a zeolite sorption pump. The pressure was measured with an ionization gauge (10^{-10} – 10^{-4} Torr range) and a capacitance manometer (10^{-3} – 10^{3} Torr range). The system base pressure was 10^{-7} Torr after 20 hours of baking out at 430-455K. A UTI 100C quadrupole mass spectrometer was used for leak checking and monitoring of the gas composition in the system. Gas transfer from a container to a glass bulb, purification and dosing has been done entirely on the system gas line. High performance Nupro valves along with copper gasket VCR joints provided leak-proof gas handling.

Figure 8 shows the cell used for transmission IR studies. The cell is connected directly to the gas line and was described in detail previously *(244)*. Either commercial CaF_2 or homebuilt differentially pumped KBr IR windows were used depending on the studied IR region and the window resistance to the dosed gas. The nanotubes were deposited on the surface of a CaF_2 spot produced from CaF_2 powder hydraulically pressed at some pressure into a tungsten sample support grid with second CaF_2 spot used as the reference or directly onto the grid. The grid is

stretched between nickel clamps, which are electrically and thermally connected to copper power leads that enter the cell through a reentrant dewar. In some studies IR spectra were measured on SWNTs deposited on the clean grid. The grid temperature range depends on the employed refrigerant and in case of ℓ-N_2 used in the majority of our studies the temperature range is from 90 K to ~1500 K. Temperature is measured with a type K thermocouple spot-welded to the top of the grid. Thermal control is accomplished electronically using LabView software, permitting accurate temperature programming as well as temperature stability to ±0.2 K.

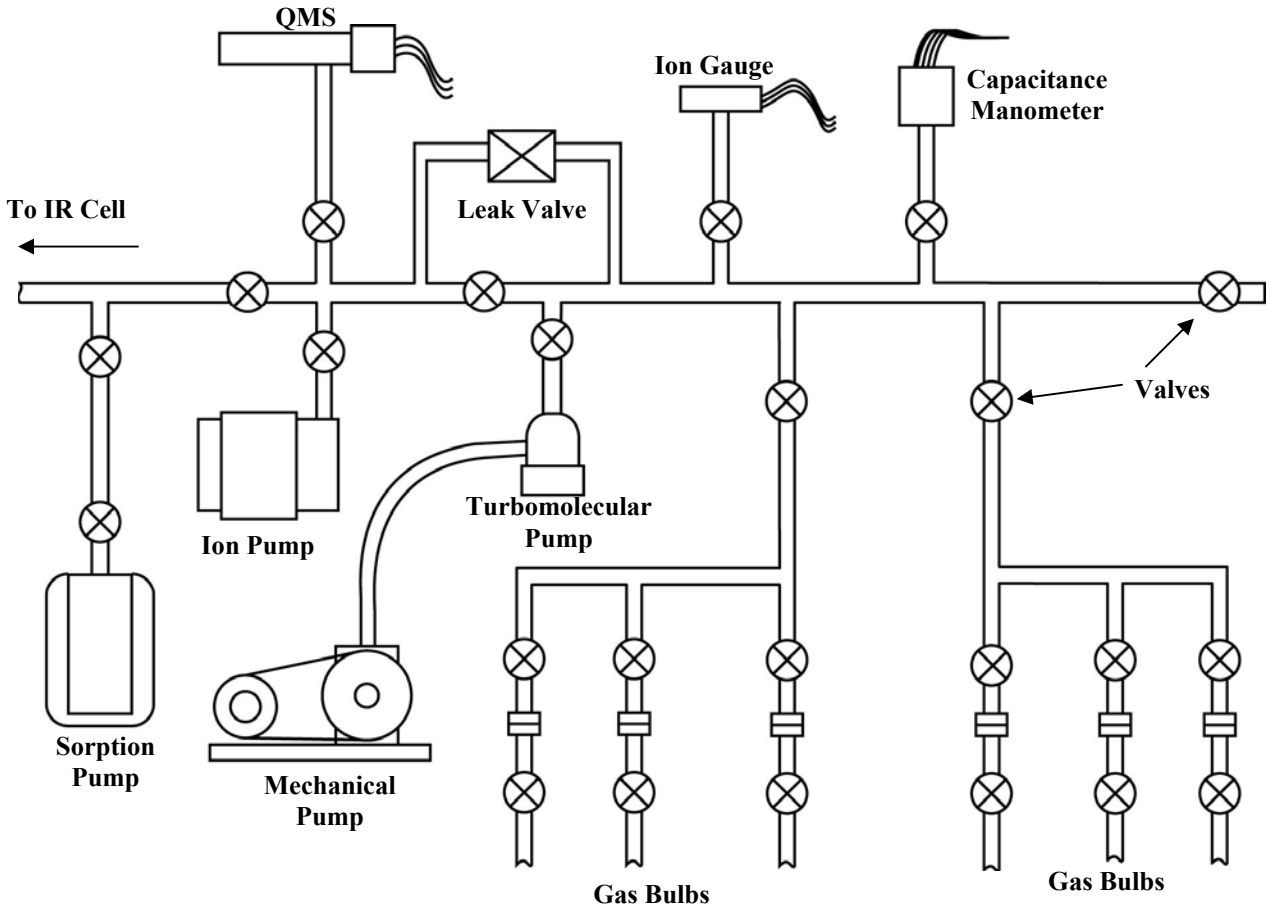

Figure 7. Diagram of the gas line of the system used in the IR studies.

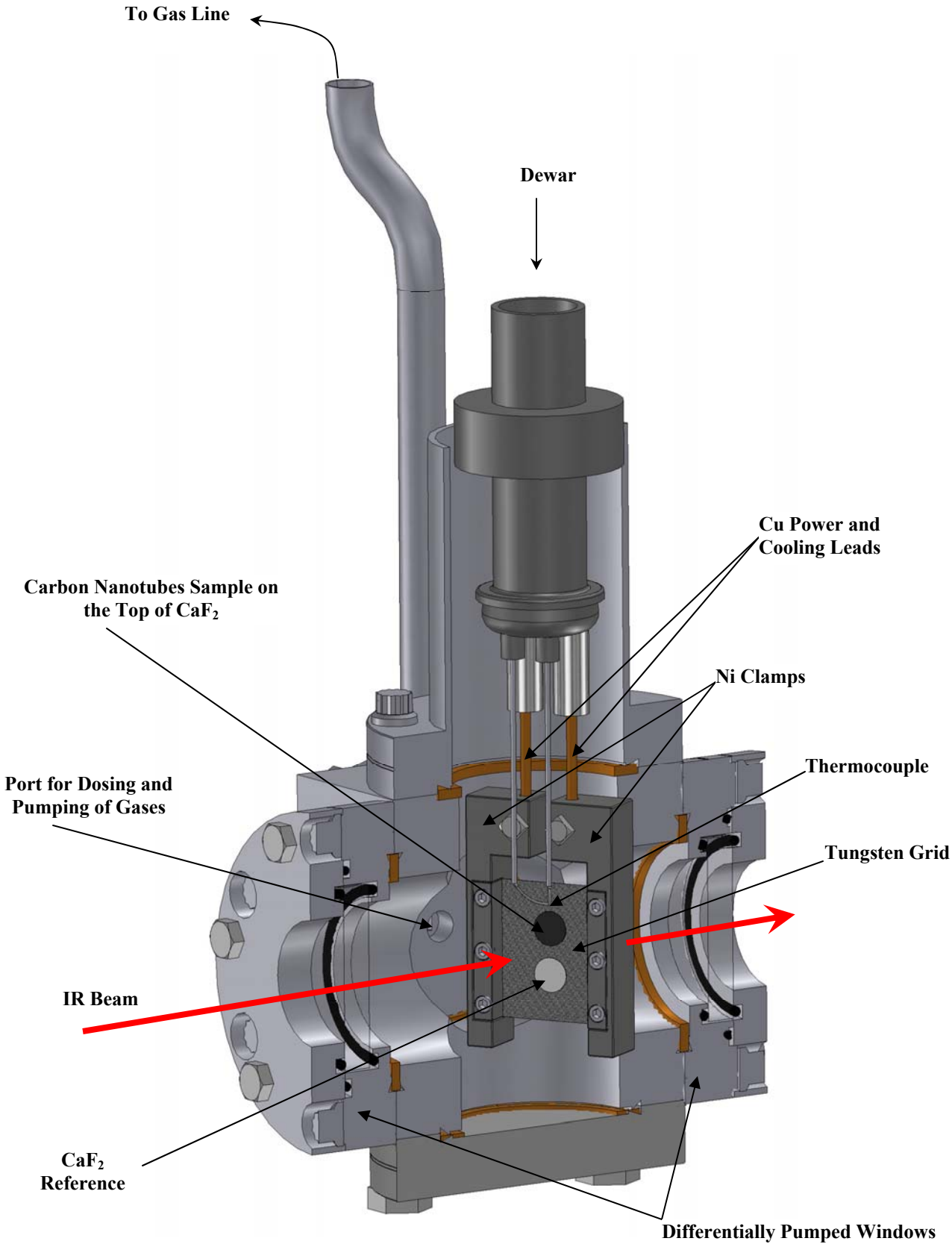

Figure 8. Transmission IR cell cross-section. The sample normal is 30° rotated relative to the IR beam direction.

The highest gas vapor pressure in the cell is defined by the coldest point in the system which is the outer surface of the reentrant dewar and in the case of ℓ-N_2 it is 77 K. The sample temperature at the lowest pressure is always somewhat higher due to imperfect thermal contacts between the parts of the sample holder. However with gas pressure increase the heat transfer from the walls of the cell to the sample enhances causing additional sample temperature rise. When higher gas pressures are required, other refrigerants can be used providing that the investigated temperature regime is high enough. For instance ℓ-O_2 was used in some of these studies. On the other hand if temperatures lower that 90 K required ℓ-He can be employed. Even though the cell was not built to utilize ℓ-He, by using this refrigerant, temperatures as low as ~ 30 K can be reached.

I. ADSORPTION OF CF_4 ON THE INTERNAL AND EXTERNAL SURFACES OF OPENED SWNTS*

I-1. Abstract

Infrared spectroscopy has been used to make the first experimental discrimination between molecules bound by physisorption on the exterior surface of carbon single-walled nanotubes (SWNTs) and molecules bound in the interior. In addition, the selective displacement of the internally bound molecules has been observed as a second adsorbate is added. SWNTs were opened by oxidative treatment with O_3 at room temperature, followed by heating in a vacuum to 873 K. It was found that, at 133 K and 0.033 Torr, CF_4 adsorbs on closed SWNTs, exhibiting its ν_3 asymmetric stretching mode at 1267 cm^{-1} (red shift relative to the gas phase, 15 cm^{-1}). Adsorption on the nanotube exterior is accompanied by adsorption in the interior in the case of opened SWNTs. Internally bound CF_4 exhibits its ν_3 mode at 1247 cm^{-1} (red shift relative to the gas phase, 35 cm^{-1}). It was shown that, at 133 K, Xe preferentially displaces internally bound CF_4 species, and this counterintuitive observation was confirmed by molecular simulations. The confinement of CF_4 inside (10,10) single-walled carbon nanotubes does not result in the production of lattice modes that are observed in large 3D ensembles of CF_4.

* Reproduced in part with permission from O. Byl, P. Kondratyuk, S. T. Forth, S. A. FitzGerald, L. Chen, J. K. Johnson, J. T. Yates, Jr. "Adsorption of CF_4 on the internal and external surfaces of opened single-walled carbon nanotubes: A vibrational spectroscopy study", Journal of the American Chemical Society, 125, 5889-5896, (2003). Copyright 2005 American Chemical Society The theoretical work was performed by L. Chen and Dr. J. K. Johnson and is included here for completeness.

I-2. Introduction

Since the discovery of single walled carbon nanotubes (SWNTs) by Iijima *(19)* and by Bethune et al. *(20)* in 1993 there has been a large interest in their application as sorbents *(145, 153, 155, 159, 164, 165, 190, 196)*. This is due to the deep potential energy well for adsorption in the interior of the nanotube *(136, 160, 186)*. The synthesis of SWNTs normally produces closed structures where each tube is terminated by an end cap, which prevents adsorption within the interior *(5, 8)*. Oxidative chemical treatments *(46, 245)* must be applied to the closed SWNTs to open the end caps in order to access the interior of the nanotubes *(156)*. While oxidation in solution [$HNO_3 + H_2O_2 + H_2SO_4$] has been found to be effective for opening closed SWNTs, we have developed a gas phase ozone oxidation process, which is more easily controlled. This O_3-oxidation procedure has been extensively investigated by IR spectroscopy in previous studies *(243, 246)*. Oxidation can remove the end caps of individual SWNTs as well as producing or enlarging vacancy defects on the nanotube walls. Both carbonyl groups and C-O-C functional groups are known to form at the rims and at defective wall sites by oxidation *(156, 242, 243)*. Heating to 773-1073 K removes these blocking groups (by evolution of CO and CO_2 *(47)*) leaving open entry ports for gas adsorption into the interior *(157)*.

Adsorption in the interior of a nanotube may also be accompanied by adsorption on the exterior surface under appropriate conditions of temperature and pressure *(126, 135, 136, 145, 159, 165, 247)*. This paper provides the first experimental detection of adsorbed molecules on both the interior and exterior sites on opened SWNTs as well as a method for selective displacement of the internally-bound adsorbed molecules. This has been done by working at cryogenic temperatures and observing the adsorbed probe molecule by transmission infrared spectroscopy. It has been found that the vibrational mode observed is red shifted due to

interaction with the nanotube surface. The red shift for interior molecules is larger than the shift for exterior adsorbed molecules.

Confinement of CF_4 in pseudo-one-dimensional condensed structures inside the (10,10) nanotube used here does not result in the production of LO and TO lattice modes observed in 3D clusters of CF_4.

We have employed CF_4(g) as a probe molecule for adsorption on opened single walled nanotubes *(5, 159)*. CF_4 exhibits an intense triply degenerate asymmetric stretching mode at 1282 cm^{-1} *(248)*. Its almost spherical shape and polarizability [3.84 $Å^3$] are similar to that of Xe [4.04 $Å^3$], which was used in earlier experiments *(47, 156, 157, 160)*. The similar properties of CF_4 and Xe make them ideal for interesting adsorbed CF_4 displacement experiments *(249)* to be reported in this work.

I-3. Experimental section

I-3A. Single Walled Carbon Nanotubes

The SWNTs obtained from Professor R. Smalley's group, Rice University, Houston TX, were produced by means of the pulsed laser vaporization technique. The raw material was purified by HNO_3/H_2SO_4 treatment *(250)*. This technique is used to remove foreign carbon impurities and produces oxidized C=O and C-O-C functionalities on the rims and on defect sites in the walls of the SWNTs. These functional groups have been shown to block physical adsorption into the interior of SWNTs and the groups must be removed by heating to ~873 K in order to open the entry ports for adsorption *(157)*. The tube diameter distribution was centered near that of (10,10) SWNTs with a diameter of 13.6 Å, The length distribution was rather narrow with the most probable length of 320 nm. The purified SWNTs are observed by SEM to form long bundles. This material was identical to that used in previous studies *(47, 157)*. The purified

sample of nanotubes was suspended in dimethylformamide (DMF). About 25 μg of SWNTs was used for this study that gave 65 $\mu g/cm^2$ surface density of the sample.

I-3B. Spectral Measurements

Transmission IR spectra were recorded at 4 cm^{-1} resolution with 500 scans for averaging. IR spectra were recorded as follows: (1) SWNTs on a CaF_2 support; (2) CaF_2 support; (3) gas phase thorough the empty grid. In each case spectra were ratioed to background spectra taken without CF_4 in the system.

Prior to each adsorption experiment a background set of spectra was measured. Upon adsorption of CF_4 a second set of spectra was measured and ratioed to the background. Then appropriate differences were taken in order to obtain the spectrum of CF_4 adsorbed on the SWNT sample.

When there is an equilibrium pressure of CF_4 in the cell (mTorr range), slight warming of the sample by thermal conduction through the gas phase occurs. This warming effect is automatically compensated by a slight reduction in heating power to the grid, achieving excellent temperature regulation. A temperature gradient in the gas phase results in a slight gas density gradient as one moves vertically along the sample support grid. Thus, subtraction of the gas phase spectrum (in comparing sample to reference spectra) is incomplete not perfect and a small gas phase CF_4 IR peak at 1282 cm^{-1} results as well as a small contribution at 1297 cm^{-1} (shoulder) and at 1224 cm^{-1} (shoulder) from CF_4 adsorption on CaF_2.

Condensation of CF_4 occurs on the reentrant dewar (dewar temperature = 77 K) resulting in an equilibrium vapor pressure of $CF_4 = 3.3 \times 10^{-2}$ Torr. This is therefore an upper limit of the gas pressure in this experiment. Lower CF_4 adsorption pressures may be achieved by controlled dosing of small quantities of CF_4 gas into the cooled cell.

I-3C. Controlled Oxidation Using Ozone

The SWNT sample was heated in vacuum to 873 K to remove the majority of the oxidized surface functionalities produced by the HNO_3/H_2SO_4 purification process and was then subjected to a series of O_3 exposures, followed by annealing to 873 K in vacuum. This cyclic oxidation/annealing procedure has previously been found to open the SWNTs caps completely and to enhance the adsorption kinetics into the nanotube interior by opening sites on the nanotube walls and rims *(46, 47, 156, 157, 243)*. The cyclic procedure causes etching of the SWNT sample, and samples so treated are designated as etched.

High purity O_3 was prepared and purified in an all glass generator described previously *(251)*. We have found that O_3 prepared in this manner will partially decompose upon admission to a stainless steel vacuum system. This effect may be minimized by prolonged passivation of the stainless steel surface with O_3 at ≅10 Torr pressure. For the experiment shown here, the O_3 treatment was carried out at room temperature in three stages: Stage 1: 30 min at 8 Torr, 298 K; Stage 2: 19 hr at 14.3 Torr, 298 K; Stage 3: 18 hr at 15.5 Torr, 298 K. As we will show, initial ozonization produced functional groups at the entrance to the tubes, thus blocking adsorption of CF_4 into the interior of SWNTs in agreement with previous Xe adsorption studies *(47, 156)*. The SWNTs were then opened by removal of the blocking functional groups through heating to 873 K in vacuum for 30 minutes. This greatly enhanced the ability of the SWNTs to adsorb CF_4.

I-3D. Xe Displacement Experiment

We employed Xe to preferentially displace adsorbed CF_4 from the nanotube interior. This was done by filling the nanotubes with CF_4 at 3.3×10^{-2} Torr and 133 K. Xe was then added in sequential doses and the IR spectra of the adsorbed CF_4 were recorded.

I-3E. Gases

CF_4 (99.9% purity) was obtained in a cylinder from Aldrich Chemical Co. and was used without further purification. Xe (99.995%) was obtained from Matheson in a cylinder and was used without further purification.

I-4. Computational Methods

I-4A. Vibrational Calculations

The vibrational shifts due to adsorption have been investigated theoretically through quantum calculations using the Gaussian 98 software package *(252)*. Gas phase spectra of CF_4 were computed at the levels of LDA theory with the 6-31G basis set. The calculated ν_3-asymmetric stretching mode and ν_4-deformation mode frequencies are 1264 cm^{-1} and 573 cm^{-1}, respectively. Quantitative agreement between spectra calculated from LDA and experiment is not expected since LDA does not accurately account for electron correlation, which would account for much of the binding energy. We are also limited in accuracy by the size of the model nanotube and the size of the basis set we were able to use. The LDA calculations of CF_4 adsorbed in the model nanotube gave the average frequencies for the ν_3 mode and ν_4 mode of 1246 cm^{-1} and 571 cm^{-1}, respectively. We have chosen to use a relatively small basis set (6-31G) in order to make the CF_4-nanotube calculations tractable. The CF_4-nanotube system was modeled by using a small cluster to represent the nanotube. We used three unit cells of a (9,9) SWNT, split the nanotube in half (along the plane of the nanotube axis), and terminated the dangling bonds with hydrogen atoms. The model nanotube fragment contained 40 carbon and 20 hydrogen atoms. The CF_4 molecule was placed a distance of several angstroms from the concave (inside) surface of the nanotube and the position of the CF_4 molecule was optimized, holding the atoms in the nanotube fixed. Once the optimized geometry was found we computed the vibrational

spectrum. The optimization and frequency calculations were performed at the LDA/6-31G level of theory.

I-4B. Adsorption Calculations

We have computed the equilibrium amounts of CF_4 and Xe adsorbed on carbon nanotube bundles as a function of Xe partial pressure from molecular simulations. The Grand canonical ensemble (constant μVT) Monte Carlo (GCMC) method *(253)* was used to calculate adsorption isotherms. The GCMC algorithm consists of three types of moves, namely, translation of a single molecule, creation of a new molecule in the simulation cell, and deletion of a molecule. Moves were attempted randomly with probability 0.2 for translation and 0.4 each for creation and deletion. Simulations were typically equilibrated for 2 million moves, followed by data taking for 1 million moves. The maximum displacement step size was adjusted during equilibration to achieve approximately a 40% acceptance ratio for translations. We have used the Lennard-Jones (LJ) potential to account for all fluid-fluid and fluid-solid interactions. Parameters for Xe were taken from the literature *(254)*. The CF_4 molecule was treated as a single spherical particle. The LJ parameters were derived from viscosity data *(255)* and were previously used in molecular simulations of diffusion in zeolites *(256)*. The carbon parameters were taken from Steele *(257, 258)*. Lorentz-Berthelot combining rules were used for the cross interactions. The LJ potential parameters are given in Table 1 where σ is the molecule diameter in Å and ε is the potential well depth such that ε/k is in units of K, where k is the Boltzmann constant. The use of classical potentials to model the nanotube-fluid interactions precludes the modeling of electronic effects, such as the differences between metallic and non-metallic nanotubes.

Table 1. Lennard-Jones potential parameters used in the simulations.

	Xe-Xe	CF_4 - CF_4	C-C
σ (Å)	4.1	4.66	3.4
ε/k (K)	222.32	134.0	28.0

Table 2. Number and types of nanotubes used in the three different bundles.

Bundle	Number of (8,8) tubes	Number of (9,9) tubes	Number of (10,10) tubes	Number of (11,11) tubes	Number of (12,12) tubes	Average Nanotube Diameter (Å)
1	2	2	10	2	2	13.56
2	4	10	2	2	0	12.35
3	0	0	9	0	0	13.56

Three different nanotube bundles were considered in this work. Two bundles were constructed by randomly placing nanotubes of various diameters in a box and then optimizing the spacing between the nanotubes as described by Simonyan and Johnson*. Each of these two bundles contained 18 nanotubes. The third bundle was a perfect 3×3 array of (10,10) nanotubes. The numbers of each type of nanotube in each bundle are given in Table 2. Using the nomenclature of Table 2, bundles 1 and 2 are representative of heterogeneous bundles, i.e., bundles with a heterogeneous distribution of nanotube diameters. Bundle 3 is a homogeneous bundle since all nanotubes have the same diameter. Experimentally produced nanotubes are heterogeneous. Comparison of simulations on these two classes of bundles will serve to characterize any qualitative differences between adsorption on homogeneous and heterogeneous bundles. Smoothed potentials were used for the nanotubes in the bundles in order to increase the simulation efficiency. See ref. *(160)* for details of the smoothing procedure. We have found that smoothing the potential has no effect on the adsorption isotherms *(160)*. The nanotubes in the simulation cell were all aligned in the *z* direction and the lengths of the nanotubes were about 60

* V. V. Simonyan and J. K. Johnson, in preparation.

Å. The bundle was placed in a parallelepiped simulation cell that was 200 Å on a side in the *x* and *y* directions. Periodic boundary conditions were applied in all directions and the potential cutoff was set to 25 Å. The size of the cell in the x and y directions was large enough so that the bundle was isolated (no periodic image interactions).

I-5. Results

I-5A. Development of CF_4-IR Spectrum upon SWNT Etching by O_3

Figure 9 shows a typical set of IR spectra obtained in these measurements and the results of taking appropriate differences to derive the IR spectrum of CF_4 adsorbed on the SWNT sample. The CaF_2 support exhibits a significant contribution to the composite IR spectrum due to CF_4 adsorption on its surface, as seen in spectrum (b). Additional IR absorbance due to CF_4 is observed for the SWNT sample, supported on CaF_2, as shown in spectrum (a). Subtraction leads to spectrum (c), where contributions from adsorbed CF_4 on the SWNT sample are observed, along with small features due to incompletely compensated gas phase CF_4. The prominent uncompensated gas phase spectral feature is shown as a dashed peak centered at 1282 cm^{-1}.

Figure 10 shows the infrared spectrum of adsorbed CF_4 as increasing amounts of etching take place through repeated exposures to O_3, followed by heating. Three etch cycles are presented. As the etching proceeds, enhanced IR intensity due to adsorbed CF_4 is observed to occur at frequencies below 1275 cm^{-1}.

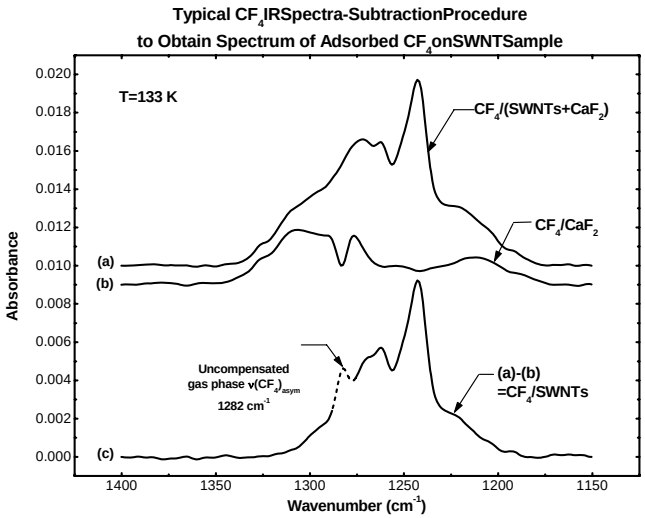

Figure 9. Procedure for spectral subtraction for CF_4 adsorbed at 133 K and 3.3×10^{-2} Torr.

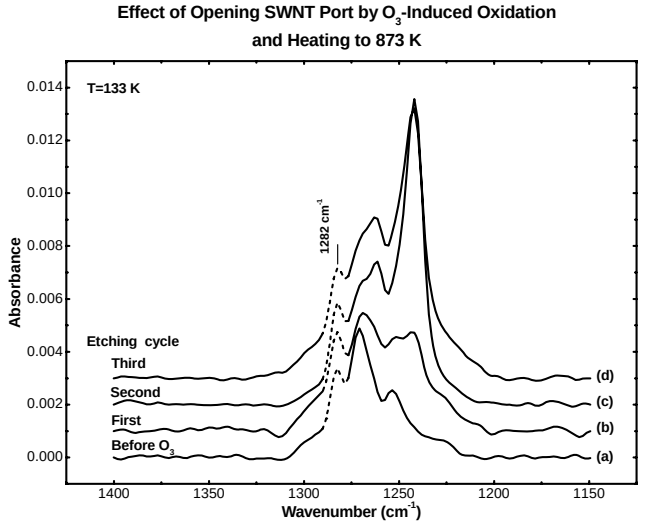

Figure 10. Development of CF_4 IR spectra during cycles of O_3-induced oxidation followed by heating to 873 K for 30 min in a vacuum. $P_{CF_4}=3.3\times10^{-2}$ Torr.

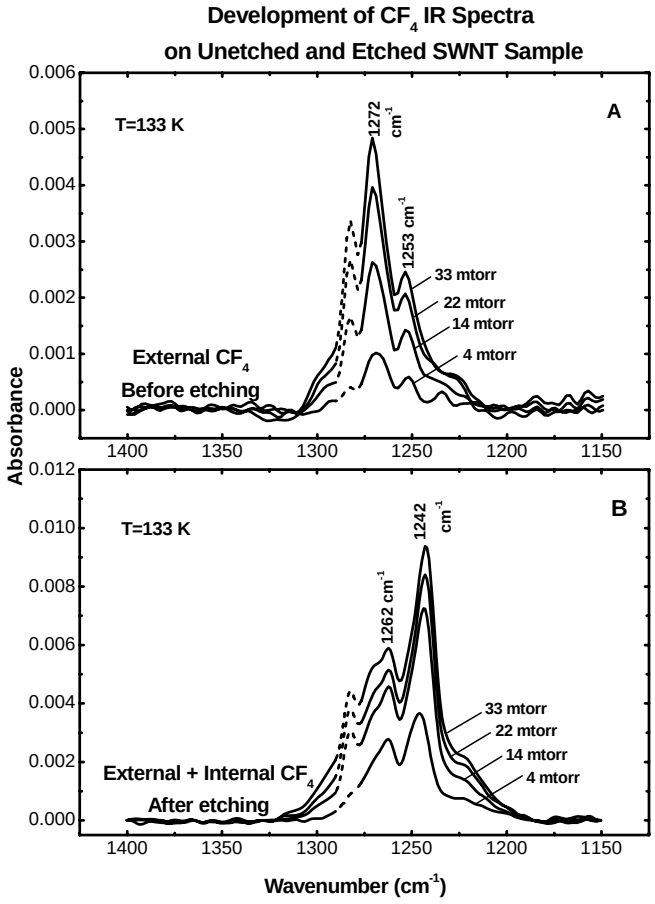

Figure 11. Development of CF_4 IR spectra for (A) external sites and (B) external plus internal sites.

Figure 11 shows a comparison of the development of the IR spectrum of CF_4 for increasing coverage on the SWNT sample before etching by O_3 and after three cycles of etching. Note that the absorbance scales differ by a factor of two for the spectral presentations. The spectra show the effects of increasing equilibrium pressures of CF_4, established at a sample temperature of 133 K. The spectra shown in Figure 11A for the unetched SWNTs contain only two prominent spectral features for adsorbed CF_4 at 1272 cm^{-1} and 1253 cm^{-1}. For the etched SWNT sample (Figure 11B), in addition to the spectral features observed in (Figure 11A), an additional pair of absorption bands are observed at 1262 cm^{-1} and 1242 cm^{-1}. As will be

discussed later, the pairs of bands observed at different frequencies for the unetched and etched nanotubes are due to the Fermi resonance of the strong infrared-active ν_3 mode and the first overtone of the ν_4 mode, designated $2\nu_4$

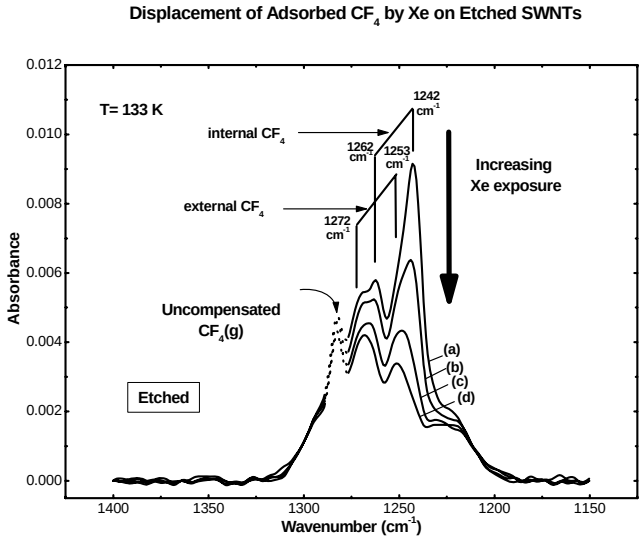

Figure 12. Xe displacement of adsorbed CF_4. The equilibrium Xe pressure was less than 10^{-3} Torr for (a)-(d). The equilibrium $P_{CF_4}=3.3\times10^{-2}$ Torr. for all spectra.

I-5B. Displacement of Adsorbed CF_4 by Xe

The resolution of the overlapping CF_4 spectral features has been experimentally confirmed through the displacement of CF_4 by Xe. Figure 12 shows a high coverage spectrum of CF_4 obtained for the etched SWNT sample. Exposure to Xe at 133 K results in the selective disappearance of two IR bands together at 1262 cm^{-1} and 1242 cm^{-1}. In contrast, the species responsible for the two bands at 1272 cm^{-1} and 1253 cm^{-1} are either not displaced or are more slowly displaced compared to the former band pair. We assign the two bands at 1262 cm^{-1} and 1242 cm^{-1} to CF_4 adsorbed in the interior of the etched SWNT sample, and the two bands at 1272 cm^{-1} and 1253 cm^{-1} to CF_4 species adsorbed externally on the outer SWNT surface. By varying

the sequence of Xe and CF_4 adsorption, it was found that the spectra represent identical equilibrium conditions achieved by gas adsorption in either sequence.

I-6. Discussion

I-6A. Absence of LO-TO splitting in IR spectra of CF_4 on SWNTs.

The ν_3 mode in CF_4 has an exceptionally high infrared intensity *(248)*. This gives rise to a strong transition dipole–transition dipole coupling between ν_3 modes of different CF_4 molecules. As a result longitudinal–transverse optical (LO-TO) splitting appears in the infrared spectra at high volumetric concentrations of oscillators. The splitting is strongly dependent on the arrangement of the oscillators. We have not observed LO-TO splitting in this work implying that the concentration of CF_4 molecules inside of and on the exterior of the SWNT sample is not sufficiently bulk-like to promote lattice mode production.

Figure 13A shows the LO-TO mode splitting evolution in the Raman spectra of CF_4 in an Ar matrix at 84.5 K taken as an example from the work of P. Nextoux *et al. (259)*. More examples of LO-TO splitting in the vibrational spectra of CF_4 in the condensed phase can be found elsewhere *(260-265)*. At a very low concentration of CF_4, spectrum (a), two peaks at 1272 cm^{-1} and 1257 cm^{-1} caused by the Fermi resonance interaction of ν_3 and $2\nu_4$ are observed. The LO-TO splitting is very small in this case and reported to be 1.4 cm^{-1}. In pure condensed CF_4, spectrum (f), LO-TO splitting reaches 75.0 cm^{-1} with the LO band at 1320 cm^{-1} and TO band at 1245 cm^{-1}.

Figure 13B shows the spectrum of CF_4 adsorbed on unetched and etched nanotubes. The close similarity of the IR spectrum of CF_4 adsorbed on SWNTs before etching to the Raman spectra of CF_4 in an Ar matrix at the lowest concentration (see inset in Figure 13B) implies that

there is a similarly negligible amount of LO-TO splitting in the spectra of CF_4 adsorbed on the external surface of nanotubes at these conditions. No evidence for LO or TO modes can be seen.

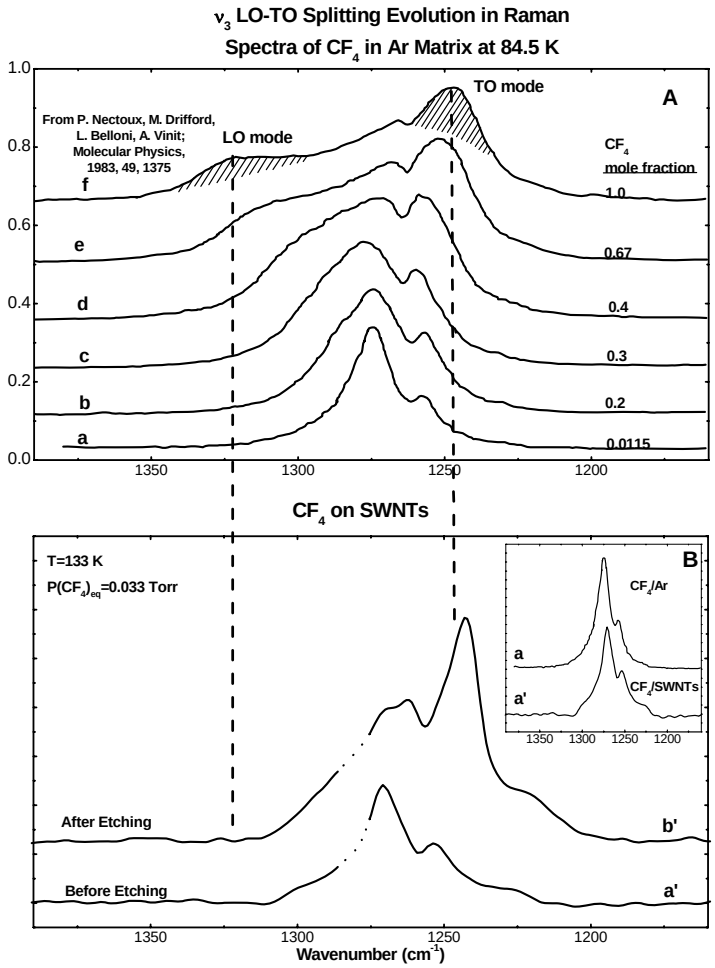

Figure 13. (A) LO-TO splitting evolution in Raman spectra of CF_4 in an Ar matrix at 84.5 K with increasing concentration. (B) Infrared spectra of CF_4 adsorbed at 133 K and 0.033 Torr on unetched and etched SWNTs.

As the nanotubes are etched the internal surface becomes accessible for adsorption. The IR spectra of CF_4 adsorbed on the etched SWNTs (Figure 13B, upper spectrum) contain features from both the external and the internal CF_4. Although the amount of CF_4 adsorbed has increased somewhat compared to unetched nanotubes, the LO mode is not seen and the peak at 1242 cm^{-1} can not be considered to be the TO band because of its sharpness.

Thus, the mean size of adsorbed CF_4 ensembles on the inner and outer surface of the SWNTs must be too small to produce the LO-TO modes characteristic of the condensed phase.

I-6B. Spectra of CF_4 adsorbed on SWNTs.

In vibrational spectroscopy, perturbations between a fundamental and an overtone are frequently encountered, and are known as Fermi resonances *(266)*. In the case of the CF_4 molecule, the Fermi resonance between the ν_3 mode and the first overtone of the ν_4 mode ($2\nu_4$) has been observed in a number of studies *(267-271)*. As a result of the interaction the overtone, usually very weak, borrows intensity from the fundamental band and becomes visible, and at the same time the two bands are shifted further apart. Thus the presence of a Fermi resonance complicates the appearance of the spectrum, so it is often useful to extract the "unperturbed" positions and intensities of the peaks. This was done in the present study in a way similar to that employed in Ref. *(266)*. For the spectra of CF_4 on etched and unetched nanotubes, Lorentzian-shaped profiles of ν_3 and $2\nu_4$ were found that upon numerically calculating the Fermi resonance interaction gave the best fits to the spectra observed.

Figure 14A shows the spectrum of CF_4 on unetched nanotubes, which corresponds to CF_4 adsorbed on the outer surface of nanotubes, and the Lorentzian profiles found for the ν_3 and the $2\nu_4$ energy level distributions. The fit calculated from these two distributions approximates the experimental data well. The presence of the $2\nu_4$ energy level redistributes the intensity of ν_3 in the spectrum creating an additional feature at 1253 cm^{-1} and a "hole" (sometimes referred to as Evans hole in the literature) at 1257 cm^{-1}. Note that for CF_4 molecules bound to the SWNTs exterior, the ν_3 level is located to the higher frequency side of $2\nu_4$.

CF_4 on etched nanotubes should be adsorbed both on the outer surface and the inner surface, made accessible by the etching, whereas the spectrum for unetched nanotubes only

contains the contribution from the outer CF_4. To find the spectrum of only the inner CF_4 one thus needs to subtract the spectrum for the unetched nanotubes from the spectrum for the etched nanotubes. As some of the SWNT surface is destroyed in the process of etching with ozone, the spectrum from the unetched nanotubes has to be multiplied by a coefficient smaller than 1 before the subtraction is carried out. We used a value of 0.75, chosen based on the goodness of the fit to the resulting spectrum. It corresponds to the destruction of 25% of the outer surface during ozonation. Figure 14B shows the spectrum of CF_4 adsorbed on the inner surface of nanotubes resulting from this subtraction and the Lorentzian distributions of ν_3 and $2\nu_4$ that give the best fit to the data. The most striking difference when compared to the external CF_4 distributions (Figure 14A, bottom) is that ν_3 shifts by 20 cm^{-1} to the red (now ν_3 is to the lower energy side of $2\nu_4$), whereas $2\nu_4$ does not change its position. The reason for the shift of ν_3 is the stronger interaction of the molecule with the surface when it is adsorbed in the interior of the nanotube. The LDA calculation also shows that the ν_3 band is much more prone to shift when the molecule's environment changes, than the $2\nu_4$ mode (as judged from the ν_4 fundamental). The calculation indicates that for the CF_4 molecule adsorbed in the interior of the nanotube, the ν_3 mode shifts by about -20 cm^{-1} compared to the gas phase, whereas the shift for ν_4 is only -2 cm^{-1} corresponding to a $2\nu_4$ shift of about -4 cm^{-1}.

This analysis of the experimental spectra shows that the shift for the ν_3-mode of CF_4 compared to gas phase CF_4 is -15 cm^{-1} for CF_4 molecules bound to the nanotube outer surface and -35 cm^{-1} for CF_4 molecules bound in the interior.

Figure 15 shows the addition of the fits for the external and internal CF_4 spectra, resulting in a fit for the total composite spectrum of CF_4 adsorbed on etched nanotubes. The coefficient of 0.75 is employed during addition.

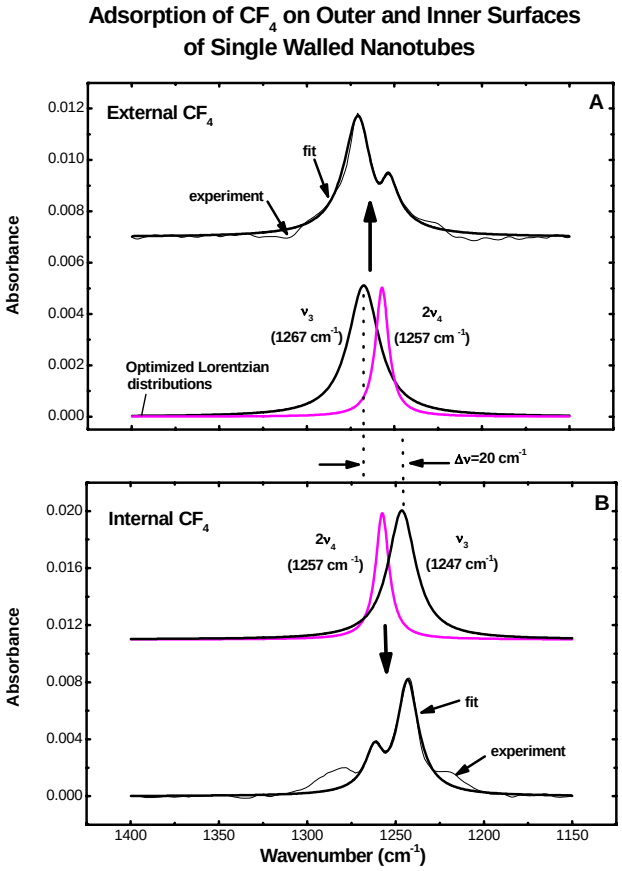

Figure 14. Fermi resonance interaction of the fundamental ν_3 mode with the $2\nu_4$ mode for external and internal CF_4 species on SWNTs. The fit was numerically calculated from the Lorentzian distributions, which were iteratively optimized for the fit to match the experimental spectrum. The interaction strength parameter was allowed to vary slightly to fit the data. It is 6.3 and 7.6 cm^{-1} for unetched (A) and etched (B) samples, respectively.

The shift of the ν_3 mode to lower wavenumbers is in accordance with the redshift often observed for physically adsorbed species and for species bound inside of inert matrixes. The band associated with the smaller ν_3 redshift is assigned to externally-bound CF_4 molecules on this basis as well as on the basis of comparison of CF_4 spectra on etched and unetched nanotubes, and the band associated with the larger wavenumber shift is assigned to internally-bound CF_4, where the interaction would be expected to be larger.

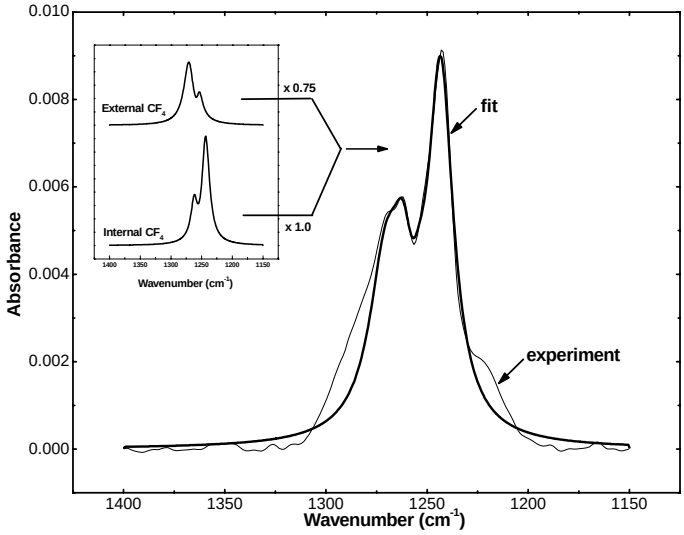

Figure 15. Simulation of combined of external and internal CF_4 spectra on SWNTs.

I-6C. Modeling of Xe Displacement of Adsorbed CF_4 from SWNTs

The displacement of CF_4 by Xe confirms the presence of four IR bands for the adsorbed CF_4 species present on both the exterior and interior sites. It is seen in Figure 12 that Xe preferentially displaces internal CF_4 species causing the bands at 1262 cm^{-1} and 1242 cm^{-1} to disappear first as the Xe coverage is increased. The displacement experiments probe the thermodynamic factors responsible for Xe-CF_4 site exchange under equilibrium conditions, since similar infrared spectra are observed for either order of adsorption of CF_4 and Xe. We know that Xe is thermodynamically favored as an internally bound species compared to CF_4, causing preferential CF_4 displacement by Xe from the SWNT interior. We have performed molecular modeling of CF_4 and Xe coadsorption in order to observe whether preferential CF_4 displacement occurs for the internally-bound CF_4 compared to externally bound CF_4. Classical GCMC simulations were performed at 133 K and a constant partial pressure of CF_4 of 3.3×10^{-2} Torr and various values of Xe partial pressure. Simulations were performed on each of the three model bundles described in Table 2 The results from two simulations on heterogeneous and

homogeneous bundles are shown in Figure 16 and Figure 18, respectively. Simulations on the three different types of bundles are qualitatively similar. In each case Xe begins to adsorb inside the nanotubes, displacing CF_4, at pressures below where there is appreciable Xe adsorption in the grooves on the external surface of the nanotubes. The partial pressure at which Xe begins to displace internal CF_4 is about 10^{-5} Torr. Xenon starts to adsorb on the outside of the nanotubes at about 10^{-4} Torr for the heterogeneous bundle and about 10^{-3} Torr for the homogeneous bundle. It is interesting to note that even after Xe begins to adsorb on the outside of the nanotubes, very little CF_4 is displaced by the Xe, even at the highest Xe partial pressure simulated (10^{-2} Torr). This observation agrees with the experimental results showing that the CF_4 modes associated with adsorption inside the nanotube disappear in a facile manner, while the IR peaks for external adsorption are not substantially attenuated by Xe adsorption. The reason for this can be easily seen by observing snapshots of the simulation. Figure 19 shows snapshots for adsorption on exterior sites of bundle 3 at Xe partial pressures of 10^{-3} (left) and 5×10^{-3} (right) Torr, both with a CF_4 partial pressure of 3.3×10^{-2} Torr. Note that at the lower Xe partial pressure there are a number of CF_4 molecules (shown in red) but only one Xe atom (blue). Note also that CF_4 does not fill all the available external sites at this pressure. Hence, at the higher pressure (right) we observe a dramatic increase in the concentration of Xe atoms in the groove sites, while the number of CF_4 molecules remains almost constant. The first Xe atoms to adsorb onto the external sites simply occupy empty sites rather than replacing CF_4 molecules. At pressures higher than those sampled experimentally, Xe does displace CF_4 on the external sites. This explains why external CF_4 species responsible for the bands at 1272 cm^{-1} and 1253 cm^{-1} persist at all experimental Xe doses

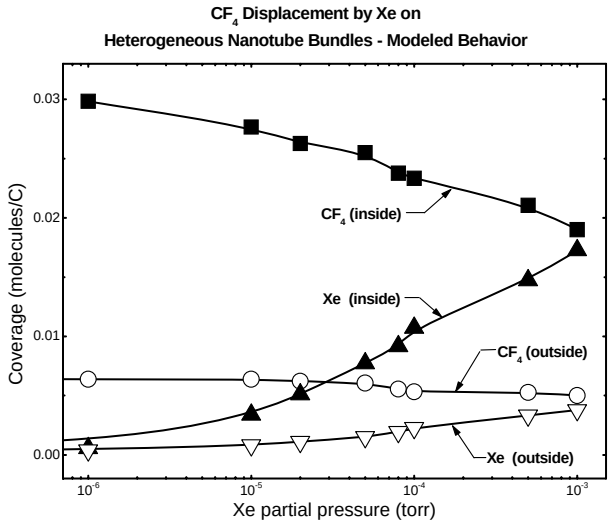

Figure 16. Simulated equilibrium adsorption uptake of CF_4 and Xe (per carbon atom) on heterogeneous nanotube bundle 1 (see Table 2) at 133 K as a function of Xe partial pressure. The CF_4 pressure is held constant at 3.3×10^{-2} Torr. Squares (circles) represent the loading of CF_4 molecules inside (outside) the nanotubes and up triangles (down triangles) represent Xe adsorption inside (outside) the nanotubes. Lines are drawn to guide the eye. The estimated statistical errors are of the order of the symbol size.

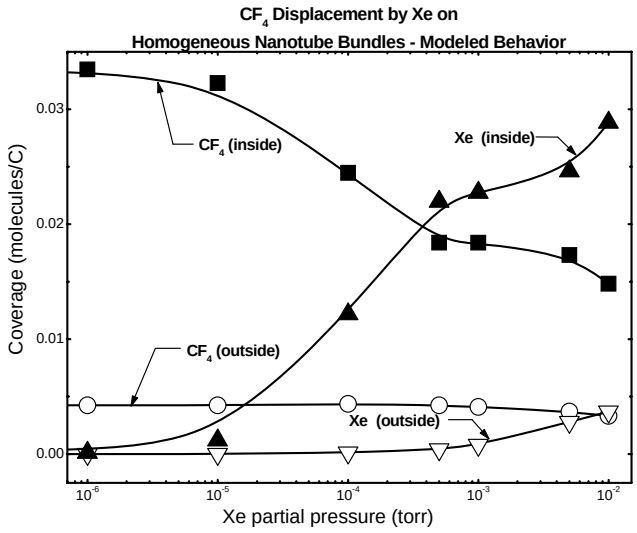

Figure 17. Simulated equilibrium coverage of CF_4 and Xe (expressed per carbon atom) on homogeneous nanotube bundle 3 (see Table 2) at 133 K as a function of Xe partial pressure. The CF_4 pressure is held constant at 3.3×10^{-2} Torr. The symbols are the same as in Figure 16. The lines are drawn to guide the eye.

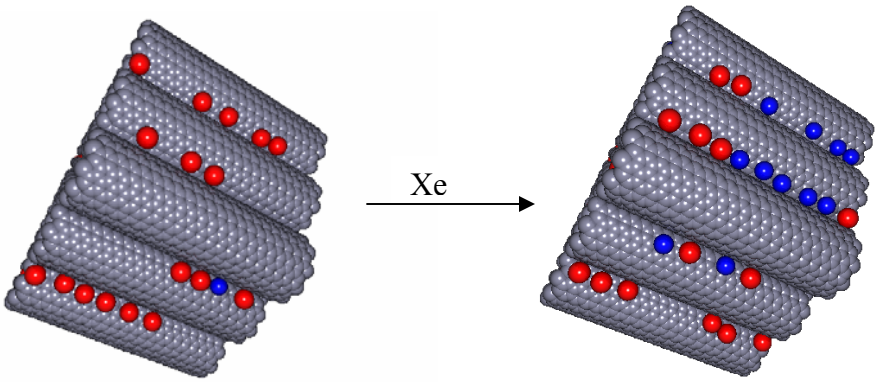

Figure 18. Simulation snapshots for CF_4-Xe coadsorption on the external groove sites at a Xe partial pressure of 10^{-3} Torr (left) and 5×10^{-3} Torr (right). In both cases the CF_4 pressure is 3.3×10^{-2} Torr. Note that the number of Xe atoms (blue) increases dramatically with increasing Xe partial pressure, while the number of CF_4 molecules (red) decreases only slightly.

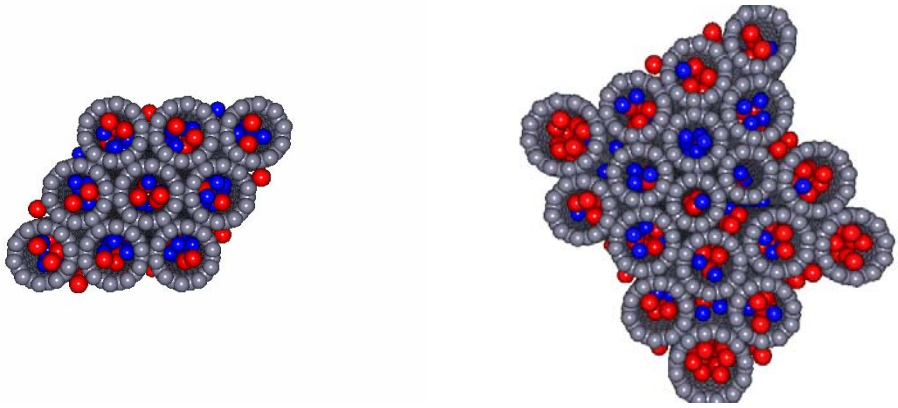

Figure 19. Simulation snapshots for CF_4-Xe coadsorption on homogeneous bundles (left) and on heterogeneous bundles (right). Note that the interstitial channels in the homogeneous bundle are too small to allow adsorption of either Xe or CF_4. The interstitial channels in heterogeneous bundles, such as bundle 1 from Table 2 shown here (right) have some larger interstitial channels that allow adsorption of Xe and CF_4

Molecular simulations show that Xe and CF_4 only adsorb inside the nanotubes and on the external groove of the perfectly packed homogeneous bundles (bundle 3). The interstitial channels in homogeneous bundles of (10,10) nanotubes are too small to allow adsorption of either gas. However, the heterogeneous bundles do not pack perfectly and hence have a few larger interstitial sites for gas adsorption. Simulation snapshots from homogeneous and

heterogeneous bundles are shown in Figure 19. Most of the interstitial channels in the heterogeneous bundle (left) are too small to accommodate adsorption of either Xe or CF_4. However, there are a few interstices that are large enough to facilitate Xe adsorption, but not CF_4, and other channels that are large enough to accommodate either molecule. This explains why the heterogeneous bundles (Figure 16) exhibit external Xe adsorption at lower pressures than the homogeneous bundles (Figure 17). Adsorption in the interstitial channels is counted as external site adsorption so that the upturn in external Xe site adsorption shown in Figure 17 is a result of Xe inside the interstitial channels. We expect that the nanotube bundles studied experimentally behave more like the heterogeneous bundles than the perfectly packed bundles, giving rise to some interstitial adsorption.

I-7. Summary

The following results have been obtained in our study of CF_4 adsorption on unetched SWNTs and etched SWNTs:

(1) The adsorption of CF_4 on SWNTs at 133 K occurs on two adsorption sites: internal and external. On closed SWNTs, CF_4 adsorbs only on the external sites, whereas on opened SWNTs, CF_4 adsorbs on both external and internal sites.

(2) Adsorbed CF_4 on external sites of SWNTs manifests itself by two IR bands, at 1272 cm^{-1} and 1253 cm^{-1}. CF_4 adsorbed on internal sites exhibits two bands at 1262 cm^{-1} and 1242 cm^{-1}. The presence of two bands in both cases results from the Fermi resonance of the strong infrared-active ν_3 fundamental with the first overtone of the ν_4 mode.

(3) The larger shift from the gas phase frequency of the ν_3 mode of internal CF_4 (shift = -35 cm^{-1}, -2.7%) compared to the external CF_4 (shift = -15 cm^{-1}, -1.2%) is due to the stronger interaction of CF_4 with the interior walls of SWNTs.

(4) Xe preferentially displaces CF_4 adsorbed inside of SWNTs as observed both experimentally and in equilibrium simulations.

(5) The confinement of CF_4 inside of the (10,10) single walled nanotube in pseudo one-dimensional structures does not result in production of LO and TO lattice modes characteristics of large 3D ensembles of CF_4 in crystallized CF_4.

I-8. Acknowledgements

We gratefully acknowledge the Army Research Office for the support of this work. We also acknowledge support from Dr. Chris Karwacki at the Aberdeen Proving Ground. We thank Wei Shi for helpful discussions. We also gratefully acknowledge the suggestions of an anonymous reviewer regarding the spectroscopic interpretation of our results Simulations were performed at the University of Pittsburgh's Center for Molecular and Materials Simulations.

II. DIMENSIONAL EFFECTS ON THE LO-TO SPLITTING IN CF_4*

II-1. Abstract

The development of longitudinal optical-transverse optical (LO-TO) modes in CF_4 has been studied experimentally and theoretically as a function of dimensionality. Infrared absorption experiments for CF_4 adsorbed on single-walled carbon nanotubes indicate a lack of LO-TO splitting at low coverage and a gradual appearance of LO-TO modes as the coverage of CF_4 on the nanotubes is increased. We have performed density functional perturbation theory calculations for the vibrational frequencies, IR absorption spectra, and phonon density of states for CF_4 in 1, 2, and 3 dimensions. The calculations demonstrate that LO-TO splitting in 1D is qualitatively different from that computed for 2D or the bulk. The magnitude of the splitting in 1D is about half that computed for the bulk and the LO mode is very weakly blueshifted in 1D. We predict that the phonon density of states changes dramatically as the dimensionality of the crystal is changed. This prediction can be tested experimentally by inelastic neutron scattering. We conclude that LO-TO splitting can be used as a probe to identify 1D states of matter.

* Reproduced with permission from W.-L. Yim, O. Byl, J. T. Yates, Jr. and J. K. Johnson "Dimensional Effects on the LO-TO Splitting in CF_4: First-Principles and Infrared Absorption Studies", Journal of the American Chemical Society, 127, 3198-3206, (2005). Copyright 2005 American Chemical Society. The theoretical work was performed by Dr. Wai-Leung Yim and Dr. J. Karl Johnson and is included here for completeness.

II-2. Introduction

The study of one-dimensional (1D) states of matter has recently enjoyed a significant burst of activity thanks to the discovery of single-walled carbon nanotubes (SWNTs) *(130, 137, 138, 142, 144, 153, 189, 272-276)*. SWNTs are 1D structures constructed by rolling a single graphene sheet into a tube. The diameters of SWNTs are typically on the order of 1 nm, while the lengths can be many micrometers *(277, 278)*. SWNTs are known to self-assemble on to a 2D hexagonal lattice to form bundles containing tens to hundreds of individual tubes. Perfectly packed bundles of SWNTs provide three possible sites for gas adsorption that could result in an effective 1D state of matter. These sites are the interior of the nanotube (endohedral site), the interstitial channel (formed where three tubes meet), and the exterior groove site (formed where two tubes meet on the surface of the bundle). There is evidence for simple gases adsorbing in 1D groove and endohedrial sites *(47, 138, 144-146, 153, 156, 157, 159, 161, 190, 191, 197, 276, 279-281)*. However, there is little direct evidence of how the 1D environment affects the properties of the adsorbed gas *(134, 282)*.

We have recently studied the adsorption of CF_4 on SWNT bundles through a combination of experimental IR and molecular modeling *(191)*. CF_4 has an intense IR absorption peak at 1281 cm^{-1} for the ν_3 asymmetric stretching mode. In the IR spectrum of liquid CF_4, the absorption peak of the ν_3 mode is split into a doublet separated by about 70 cm^{-1}. This splitting is due to dynamic dipole interaction. There is a large electronegativity difference between carbon and fluorine that generates a considerable dynamic dipole resulting from the distortion of the CF_4 tetrahedron. This dynamic dipole in turn interacts with the neighboring CF4 molecules and perturbs their vibrational frequencies. This phenomenon is analogous to the longitudinal optical-transverse optical (LO-TO) splitting in ionic crystals, for example, NaCl, where the LO mode

leads to a blue-shift in the vibrational frequency, while the TO mode leads to a redshift. LO-TO splitting of CF_4 has been previously studied in the bulk *(248, 259, 264, 283)* and on the surface of ice *(261, 262)*

Our previous experimental IR study failed to find any evidence of LO-TO splitting for CF_4 adsorbed on SWNT bundles *(191)*. It is not clear from the experiments whether the absence of LO-TO splitting is due to the low concentration of CF_4 adsorbed on the SWNTs or due to the one-dimensional nature of the phonon modes of CF_4 adsorbed inside the SWNTs and in the groove sites. Atomistic simulations of adsorption at the experimental temperature of 133 K and pressure of 0.033 Torr predicted that the CF_4 density inside the SWNTs would be close to that of liquid CF_4, *(191)* implying that CF_4 concentration is not the reason for the absence of LO-TO splitting. It is therefore interesting to ask whether the absence of LO-TO splitting for CF_4 adsorbed on SWNTs is a signature of the 1D nature of the adsorbed phase.

In this work, we have studied LO-TO splitting both theoretically and experimentally. We have used density functional theory (DFT) to study the lattice dynamics and IR absorption of CF_4, varying both the dimensionality and the concentration of the CF_4 phase. We have experimentally measured the IR spectra of CF_4 adsorbed on SWNTs as a function of coverage. The combined theoretical and experimental studies give a detailed picture of the development of LO-TO splitting as the concentration of the adsorbed gas is increased.

Previous work indicates that CF_4 preferentially adsorbs in the groove and the internal sites at low coverage *(191)*. The groove sites allow only a 1D line of CF_4 molecules to adsorb at low coverage, with the molecules confined by the strong solidfluid potential of the groove site. The CF_4 molecules adsorbed inside the nanotubes are not confined to a line, but are adsorbed against the inside walls of the nanotubes, forming a quasi-1D environment. At higher CF_4

coverage, multilayers of CF_4 appear on the external surface of the nanotubes, giving rise to a bulklike phase. We have experimentally probed a wide range of coverages of CF_4 on SWNTs through control of the temperature and pressure of the system. We find that LO-TO splitting is clearly observed from IR experiments at higher coverages, while LO-TO splitting cannot be observed experimentally at low coverages. Our DFT calculations address the issue of whether LO-TO splitting can occur in 1D and quasi-1D environments.

II-3. Computational Methods

We have performed three types of calculations relating to the IR spectra of CF_4.

First, we have computed the vibrational frequencies of CF_4 for bulk, gas phase, 1D chains, and CF_4 adsorbed on SWNTs from the direct force constant approach using VASP *(284-286)*. Second, we have computed IR intensities (absorption) from density functional perturbation theory (DFPT) using the PWscf package *(287)* combined with the method of Balan and co-workers *(288)* Last, we have computed the phonon density of states (PDOSs) and their corresponding dispersion relations in the first Brillouin zone from DFPT using PWscf. All calculations utilized the nonrelativistic local density approximation (LDA). This level of theory was used previously by us to study the vibrational modes of CO_2 on SWNTs *(185)*. The DFPT calculations were carried out for CF_4 in the 3D bulk solid, the 2D solid consisting of one, two, and three layers, and 1D chains. The effect of the nanotubes was not explicitly included in the DFPT calculations.

II-3A. Vibrational frequency of adsorbed CF_4 in the groove site and internal adsorption site

We have carried out VASP calculations using Vanderbilt's ultrasoft pseudopotentials (USPP) *(289)*. In the following sections the results computed using VASP are denoted by LDA/USPP. The cutoff energies for the wavefunction and augmentation charge were set to 424.5

eV and 975.2 eV, respectively. The vibrational frequencies were calculated by the direct force constant approach *(290)*. Calculations were performed for CF_4 on metallic (10,10) and semiconducting (17,0) SWNTs, in the groove site and interior of the nanotube. These two types of SWNTs have diameters similar to those observed for SWNTs produced by laser ablation *(22)*.

Adsorption of CF_4 on the metallic (10,10) SWNTs was simulated using a supercell having two primitive unit cells of the (10,10) SWNT, giving a supercell length of 4.9 Å. For CF_4 inside the (10,10) SWNT, CF_4 and SWNT are put into a hexagonal cell of 22.1 Å × 21.9 Å × 4.9 Å, giving a separation between the adjacent tubes of about 8.4 Å. For the CF_4 in the groove site, a rectangular supercell of 16.3 Å × 24.3 Å × 4.9 Å was used. One primitive unit cell was used for the (17,0) nanotube, giving a supercell length of 4.2 Å. Internal adsorption in the (17,0) SWNT used a hexagonal cell of 22.3 Å × 22.3 Å × 4.2 Å. Groove site adsorption used a rectangular supercell of 16.3 Å × 24.3 Å × 4.2 Å. The k-space integration used 1×1×6 **k** meshes in all cases.

The vibrational frequency of gas phase CF_4 at the Γ point was calculated using LDA/USPP. The gas phase was approximated by placing a single molecule into a cubic box 15.0 Å on a side.

II-3B. Phonon calculations for CF_4 in different dimensionalities

The PWscf calculations used norm-conserving pseudopotentials generated by the Troullier-Martins scheme *(291)* for carbon and fluorine atoms, using the fhi98PP pseudopotential package *(292)*. A high cutoff energy of 80 Ry was chosen for the pseudopotentials. The k-space integration used 3x3x3 **k** meshes for 3D and 1D models, and 3x3x1 **k** meshes for 2D slab models. The LDA PWscf calculations are denoted by LDA/NCPP in the following sections.

Table 3. Vibrational frequencies of gas-phase CF_4

Vibrational mode[a]	ν_1	ν_2	ν_3	ν_4
Degeneracy	1	2	3	3
LSDA/6-31G[b]	--	--	1264	573
LDA/NCPP[c]	884	407	1218	597
LDA/USPP[d]	908	423	1238	611
Experiment[e]	909	435	1281	632

[a] ν_1= symmetric stretching; ν_2= symmetric bending; ν_3= asymmetric stretching; ν_4= asymmetric bending. [b] LDA calculations of Byl et al.*(191)*. [c] This work, calculated from PWscf. [d] This work, calculated from VASP. [e] Previous experimental work of Byl et al.*(191)*

We have modeled orientationally ordered structures of CF_4 to reduce the computational demands in the DFT and DFPT calculations. It is known that orientational disordering broadens the LO and TO bands without greatly affecting the overall splitting patterns *(264, 283)* The crystal structure of the CF_4 solid in phase II (orientationally ordered) has four CF_4 molecules per unit cell with space group C2/c *(293)*. LDA calculations show a potential minimum with a^*/a_0 at 0.95, where a* is the optimized lattice parameter and a_0 is the experimental result. This 5 % discrepancy is in the acceptable range, when compared with the previous LDA calculations for the Xe crystal, which had 4 % deviation in lattice parameters from experimental results *(294)*. We note that most functionals used in DFT cannot account accurately for weak interactions that are due to electron correlation *(295-300)*. New methods have been developed to deal with van der Waals interactions within DFT *(297, 301-305)*. However, we use the LDA formalism because it has been shown to be reasonably accurate for selected cases involving graphene systems *(306, 307)*. We expect LO-TO splitting to be described relatively well by LDA because

the dynamic dipole interactions are mainly electrostatic in nature, which can be treated by LDA relatively accurately.

We have also considered CF_4 molecules in a body-centered cubic (bcc) cell, in order to study the space group effect on the LO-TO splitting. It is reasonable to choose a bcc Bravais lattice for CF_4, since SiF_4, a larger group IV tetrafluoride, packs in a bcc lattice *(308, 309)*.

The gas phase CF_4 was modeled within LDA/NCPP using a single CF_4 molecule in a bcc cell. $\mathbf{\Gamma}$ point sampling in **k** space integration was used. The length of the lattice vector was set to 20.0 Å, which was long enough to avoid intermolecular interactions.

Gas phase vibrational frequencies for CF_4 computed from various methods are shown in Table 3, along with the experimental frequencies. LDA calculations universally underestimate the vibrational frequencies of the different modes compared with experiment. However, we are interested in shifts of the frequencies rather than absolute values. We expect the qualitative trends to be accurate, although the absolute frequencies are underestimated.

II-3C. IR absorption calculations for CF_4 in different dimensionalities

The coupling between an incident radiation wave vector and the phonon wave vector of a solid is only effective when $\boldsymbol{k} \sim \boldsymbol{q}$, where $\boldsymbol{k}$ is the radiation wave vector and $\boldsymbol{q}$ is the phonon wave vector. Because the IR wavelength is much longer than the lattice constants, IR absorption occurs when $\boldsymbol{k} = \boldsymbol{q} \rightarrow 0$. In this work, we employed the method of Balan *et al*. *(288)* to calculate the IR spectra of condensed CF_4 for $q \rightarrow 0$. The average adsorbed power is given by

$$W(\omega) \propto \omega \,\mathrm{Im}[\varepsilon(\omega)] \qquad (1)$$

where ω is the frequency, $\varepsilon(\omega)$ is 1/3 of the trace of $\vec{\varepsilon}(\omega)$, the dielectric tensor of the sample. The low frequency dielectric tensor $\vec{\varepsilon}(\omega)$ can be calculated by the using the vibrational

frequencies and Born effective charge tensors, *(310)* which were obtained from the DFPT method.

II-4. Experimental Section

Purified SWNTs produced by the laser vaporization method were used in this study. The same batch of nanotubes was used in our earlier experiments and a detailed characterization of the sample can be found elsewhere *(47, 156, 157, 191, 243)*.

A sample of SWNTs was deposited from a DMF suspension onto one of two CaF_2 supporting spots pressed into a tungsten grid. The second CaF_2 spot was used as a reference. The tungsten grid was connected to massive Ni clamps fastened to Cu wires that served as power leads and provided thermal contact with the refrigerant. The sample temperature was controlled by an alumel-chromel thermocouple welded to the top of the grid. The nanotubes were ozonized at 303 K in three cycles, lasting 5 minutes each. The initial O_3 pressures were 21.8, 16.6 and 21.1 torr, for each cycle, respectively. A detailed description of the transmission IR cell and experimental setup can be found elsewhere *(191)*.

Both ℓ-N_2 and ℓ-He were used to cool the sample. The sample was heated to 133 K when ℓ-N_2 was used in the IR cell Dewar flask. Liquid He was used to achieve lower temperatures by transferring it from a ℓ-He Dewar flask to the IR cell Dewar flask via an evacuated double-walled transfer tube. Helium evaporated at the outlet of the transfer tube, due to poor insulation, producing a cold gas at ~28 K. The sample was heated to 36 K to avoid temperature fluctuations.

CF_4 (Aldrich Chemical Co., 99.9% purity) was dosed into the IR cell from the gas line. The highest possible pressure of a gas in the IR cell is defined by the sublimation pressure at the coldest point in the system, which is Dewar flask. When ℓ-N_2 was used as a refrigerant the saturation pressure was 0.033 torr and less than 10^{-5} torr when He was used. For the higher

temperature (ℓ-N_2), gas dosed into the IR cell quickly reached a steady state, giving an effective equilibrium between the gas in the cell at a pressure of 0.033 torr and the gas adsorbed on the nanotubes at 133 K. In contrast, when He was used as a refrigerant gas dosed into the cell rapidly condensed on both the Dewer flask (at ~28 K) and the sample (36 K). The mobility of the condensed CF_4 molecules at these low temperatures was extremely low, so that steady state was not achieved over the time of the experiment. An unknown fraction of each dose of CF_4 gas adsorbed on the sample and a constant increase of condensed CF_4 on the sample was observed with each dose. Hence, the ℓ-N_2 experiments could only produce a low coverage of CF_4 on the nanotubes, due to desorption of the gas from the sample, while the low temperature experiments produced macroscopically thick layers of CF_4 adsorbed on the sample.

Transmission IR spectra were measured with a Mattson Research Series FTIR spectrometer equipped with a wide band MCT detector. All spectra were recorded at 4 cm^{-1} resolution with 500 scans for averaging.

II-5. Results and Discussion

II-5A. LO-TO Splitting in Bulk CF_4

Our main goal is to determine if LO-TO splitting can occur in confined systems, specifically 1D, quasi-1D, and 2D systems. We first show that our IR absorption and PDOS calculations reliably predict the behavior of bulk CF_4. Nectoux *et al.* have measured the Raman spectra of CF_4 dissolved in argon at mole fractions ranging from 10^{-2} to 1 *(259)*. At low concentrations the CF_4 molecules are well separated and the Raman spectrum does not display any LO-TO splitting, as seen from the data in Figure 20a, bottom curve. The LO-TO splitting develops gradually as the concentration of CF_4 increases, as seen by comparing the curves in Figure 20a. A very similar trend can be seen from the LDA/NCPP calculations, presented in

Figure 20b and Figure 20c. The computed IR absorption spectra of the ν_3 mode for bulk CF_4 in a bcc lattice are shown in Figure 20b. The lattice spacing was varied from $a/a_0 = 1.4$ to 1, where a_0 is the equilibrium lattice spacing. At the largest lattice spacing (bottom curve in Figure 20b) the TO and LO peaks are located at 1200 and 1245 cm^{-1}, respectively, giving a splitting of 45 cm^{-1}. The calculated splitting at the equilibrium lattice spacing (top curve in Figure 20b) is 116 cm^{-1}, compared with the experimental value of 65 cm^{-1} (top curve, Figure 20a). Thus, the magnitude of the splitting computed from DFPT is about twice that observed in experiments, but the trends from the calculations are in qualitative agreement with experiments (compare Figure 20a and Figure 20b). Note that the experimental Raman spectra show a peak at about 1258 cm^{-1} that is due to Fermi resonance with the first overtone of the ν_4 mode; this effect is not included in the calculations.

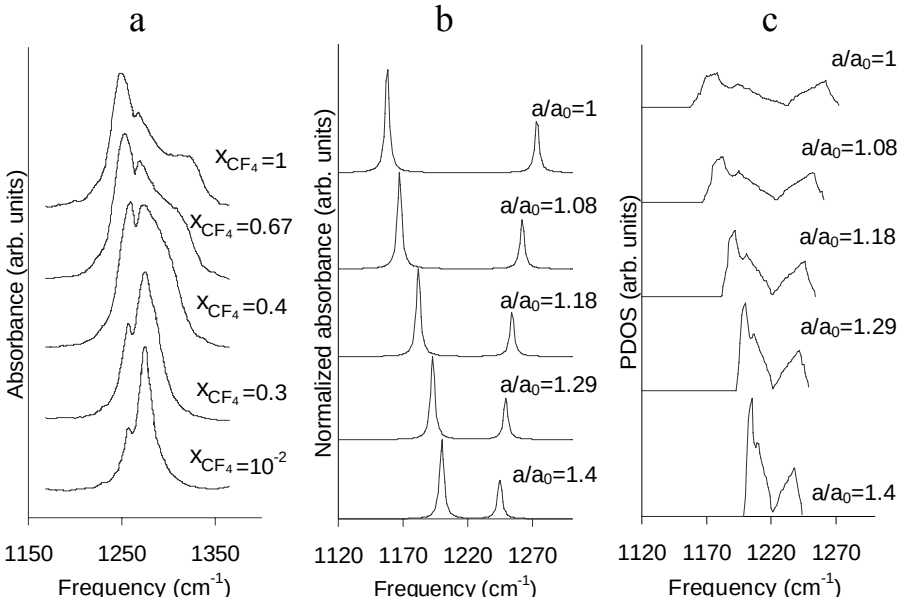

Figure 20. LO-TO splitting of bulk CF_4 as a function of concentration. a) Experimental Raman spectra for CF_4 dissolved in Ar at different mole fractions. Data from Nectoux *et al. (259)* b) The IR absorption for bcc CF_4 computed from density functional perturbation theory as a function of lattice spacing. c) The computed phonon density of states for bcc CF_4 as a function of lattice spacing.

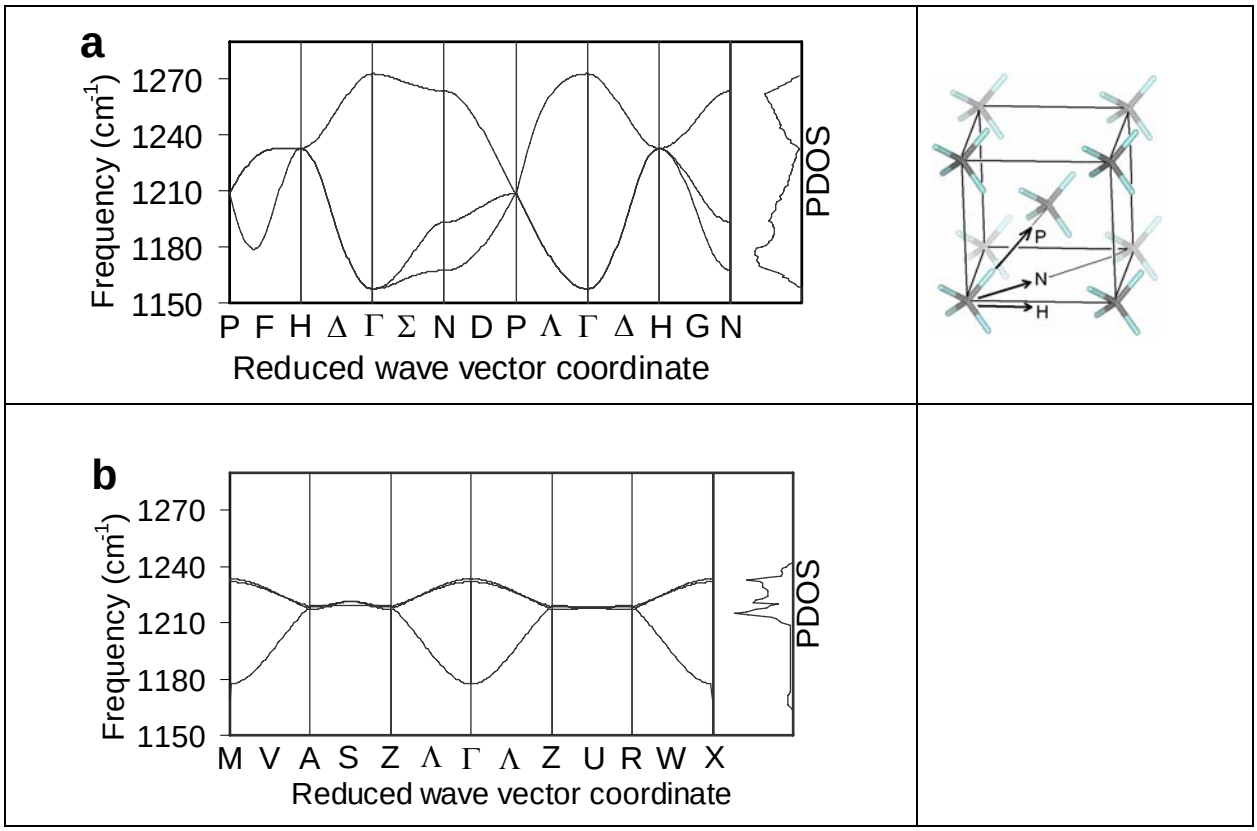

Figure 21. a) Phonon dispersion curves for bulk CF_4 (body-centered cubic lattice); b) Phonon dispersion curves for 1D CF_4 packed along the molecular C_3 axis.

Phonon density of states computed for bulk CF_4 as a function of lattice spacing are presented in Figure 20c. The intensity of PDOS is not directly proportional to the IR/Raman intensity because the former involves the vibrational motions at different values of the wave vector ***k*** over the entire first Brillouin zone. In contrast, the IR and Raman intensities result from vibrational motions at the **Γ** point of the first Brillouin zone. Therefore, the PDOS is not a direct measure of the observable LO-TO splitting in experiments, but it does provide additional information on CF_4 vibrations. We see that the PDOS develops in a way that is qualitatively similar to the experimental Raman spectra as the concentration of CF_4 is increased, either through decreasing the lattice constant (Figure 20c) or increasing the mole fraction (Figure 20a). As stated above, the low-temperature structure of CF_4 is C2/c. We have used a bcc lattice in the calculations presented in Figure 20 for computational efficiency. We have computed the PDOS

for the C2/c crystal structure and have found that the results are very similar, in accord with the experimental observation that the Raman spectra of CF_4 in the solid and liquid phases are very similar, with both exhibiting LO-TO splitting *(264)*.

Phonon dispersion relations can provide additional insight into LO-TO splitting. The calculated phonon structure of bulk bcc CF_4 (Figure 21a) shows that the TO modes are doubly degenerate at the **Γ** points (lower frequency) and that the LO mode is nondegenerate (higher frequency). The band valley at 1233 cm^{-1} in the PDOS is due to the dispersion at **H** (0.0, 1.0, 0.0), where the coordinates of the k point in real space are reported in the parenthesis. The vibrational motion is triply degenerate at the two special k points, **H** (0.0, 1.0, 0.0) and **P** (0.5, 0.5, 0.5). This is because these two k points are at the vertices of the first Brillouin zone, at which the vibrational motions of CF_4 are totally out-of-phase, resulting in the absence of LO-TO splitting.

The phonon dispersion relations (Figure 21a) indicate that the TO band depends on the intra-layer and inter-layer CF_4 interactions. The inset in Figure 21a shows the special k point directions relative to the bcc lattice. The phonon at **N** (0.5, 0.5, 0.0) contributes to the PDOS intensity around 1168 cm^{-1} and 1193 cm^{-1}; the phonon dispersion from **P** (0.5, 0.5, 0.5) to **H** (0.0, 1.0, 0.0) contributes to the PDOS intensity around 1179 cm^{-1}. For the TO dispersion long **P-H**, there exists a minimum in the phonon dispersion curves located at the k point (0.35, 0.65, 0.35), which is almost parallel to the direction of the C-F bond pointing from one (110) layer to another. Moving from **P** to **H**, the dynamic dipole is not cancelled out and the dipolar interaction leads to TO coupling between different layers. As shown in the inset of Figure 21a, the plane spanned by **Γ-P** and **Γ-N** is parallel to the (110) CF_4 layer and the phonon dispersion along **P-H** is pointing out of the (110) layer. So these intra-layer and inter-layer phonon interactions result

in the TO band in the PDOS spectra. The phonon dispersion along **Γ-N** contributes to the PDOS of LO band around 1261 cm^{-1}. The IR absorption and PDOS calculations presented here represent, to our knowledge, the first example of LO-TO splitting for molecular solids computed from first principles.

II-5B. One-Dimensional Systems

We have computed vibrational frequencies from the direct force constant approach to complement the IR intensity and PDOS of calculations in order to study vibrational modes in 1D chains of CF_4 molecules. The ν_3 vibrational frequencies calculated from LDA/USPP and LDA/NCPP for linear CF_4 chains are summarized in Table 4, and the corresponding vibrational motions are schematically illustrated in Figure 22. Lattice parameters of 4.4 and 4.9 Å were used; the former corresponds to the optimized 1D structure for CF_4 aligned along the C_3 axis and the latter is the lattice spacing for two primitive unit cells of a (10,10) SWNT. Comparing the ν_3 frequencies in Table 3 and Table 4, we see that one of the modes is redshifted (softened) and two modes are blueshifted (hardened) for molecules in the 1D chain compared with the gas phase. The frequency shift from the gas phase for each mode is given in parentheses in Table 4. The shifting of the frequencies in the 1D chain is consistent with LO-TO splitting. The in-phase C-F stretching along the packing axis softens the ν_3 mode (M1 in Figure 22a and Table 4), while the C-F stretching perpendicular to the packing axis hardens the ν_3 mode (M2 in Figure 22b and Table 4). Both LDA/NCPP and LDA/USPP show the same trends. Similar results were obtained for a linear CO_2 chain, *(185)* where the asymmetric CO_2 stretching mode is softened compared with the gas phase value. The softening of the modes can be explained by the electrostatic interaction between the dynamic dipoles (Figure 22a), where the dynamic dipoles are parallel to the electric field lines. The in-phase stretch is therefore energetically stabilized. For the ν_3

vibrations perpendicular to the packing axis, the dynamic dipole generates an opposing electric field on the neighboring dynamic dipole (Figure 22b), leading to mode hardening. Our calculations predict that the LO-TO splitting in a 1D chain is between 30 to 55 cm^{-1}. Taking the convention that the softened mode is the TO mode, there is one TO mode and two nearly degenerate LO modes for a linear chain of CF_4 molecules. We note that the LO modes are only weakly blueshifted, with shifts ranging from 1 to 15 cm^{-1}. In contrast, the mode in the TO region is shifted by about 30 to 50 cm^{-1}, with the larger redshift corresponding to the smallest lattice spacing. Hence, the LO-TO splitting is qualitatively different in a 1D chain compared with the bulk, where the LO modes are blueshifted by 56 cm^{-1} and the TO modes are redshifted by 60 cm^{-1}. We note that results from LDA/NCPP and LDA/USPP calculations are in quantitative agreement.

Table 4. ν_3 vibrational frequencies of CF_4 in 1D chains. The LDA/NCPP results were computed from DFPT at the Γ point. The LDA/USPP calculations utilized the direct force constant approach. The first three calculations are for isolated 1D chains. The bottom four rows are for CF_4 molecules in groove or internal sites in either (10,10) or (17,0) SWNTs. In all cases the CF_4 molecules are packed along their C_3 symmetry axis. The vibrational shifts from the gas phase frequency (from Table 3) are shown in parentheses for each mode.

Vibrational mode	M1 (Along the packing axis)	M2 (Perpendicular to the packing axis)	
LDA/NCPP (z=4.4 Å)	1177 (-41)	1232 (14)	1233 (15)
LDA/USPP (z=4.4 Å)	1188 (-50)	1242 (4)	1245 (7)
LDA/USPP (z=4.9 Å)	1207 (-31)	1239 (1)	1241 (3)
LDA/USPP (10,10) groove	1204 (-34)	1227 (-11)	1243 (5)
LDA/USPP (17,0) groove	1185 (-53)	1234 (-4)	1246 (8)
LDA/USPP (10,10) inside	1204 (-34)	1234 (-4)	1230 (-8)
LDA/USPP (17,0) inside	1186 (-52)	1241 (3)	1237 (-1)

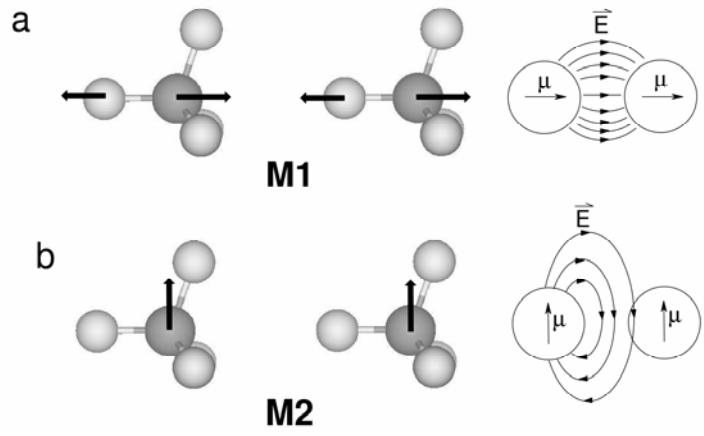

Figure 22. Schematic diagram of the interactions between the dynamic dipoles at the Γ-point. a) ν_3 vibration along the packing axis; b) ν_3 vibrations perpendicular to the packing axis.

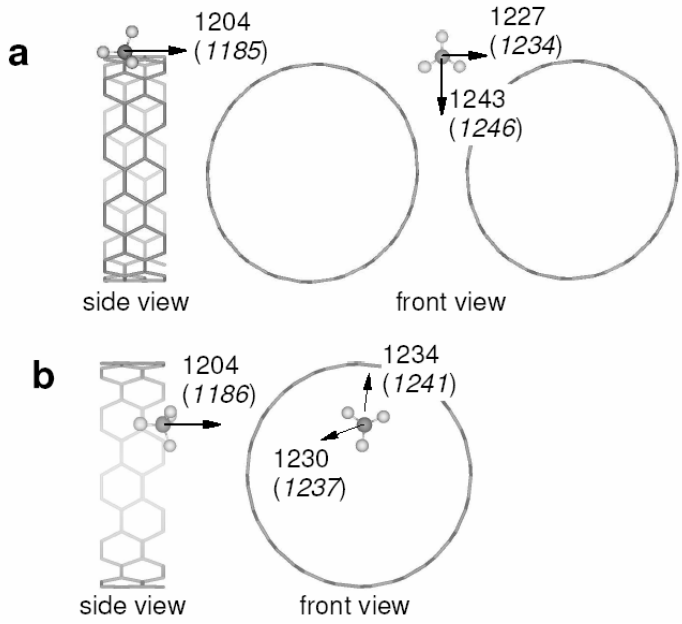

Figure 23. ν_3 vibrational modes of CF_4 calculated from VASP. a) CF_4 in the groove site; b) CF_4 on the SWNT interior site. The vibrational frequencies are given in cm^{-1}. The numbers without parentheses are for CF_4/(10,10) SWNT. The numbers in parentheses are for CF_4/(17,0) SWNT.

The previous calculations considered 1D chains of CF_4 molecules in free space. In reality, the molecules are adsorbed in SWNT groove and internal adsorption sites. The ν_3 vibrational frequencies for a 1D chain of CF_4 in the groove and internal sites of both (10,l0) and (17,0) SWNTs are shown in Figure 23 and Table 4. Only the frequencies have been computed because the number of atoms in the supercells of these systems precluded IR intensity and PDOS calculations. We see from Table 4 that the M1 modes for molecules in the groove site and inside the nanotubes have about the same redshifts (34-53 cm^{-1}) as molecules in a 1D chain without the nanotube. However, the M2 modes for molecules in groove and internal sites are no longer all blueshifted. Five of the M2 modes are slightly redshifted (1-11 cm^{-1}) and three modes are blueshifted by a small amount (3-8 cm^{-1}). We also note that the TO mode for CF_4 on the (17,0) tube is more strongly redshifted than on the (10,10), both for groove and internal sites. This is because the lattice spacing along the tube axis is substantially smaller for the (17,0) tube, giving stronger CF_4-CF_4 coupling. The results for the vibrational calculations are qualitatively similar for CF_4 adsorbed on the (10,10) and (17,0) nanotubes, when the differences in the lattice spacing are taken into account. This indicates that the conductivity of the nanotube does not have a substantial effect on the vibrational modes of a weakly adsorbed species. The overall effect of the nanotubes on the ν_3 modes is to reduce the blueshift of the M2 modes, while leaving the M1 mode virtually unchanged. Groove site adsorption for both the (10,10) and (17,0) nanotubes splits the near-degeneracy of the M2 modes compared with the isolated 1D chains and chains adsorbed inside the nanotubes. Thus, while it can be said that LO-TO splitting does occur for 1D chains in both free space and in nanotubes, the character and magnitude of the splitting are very different from that observed in the bulk.

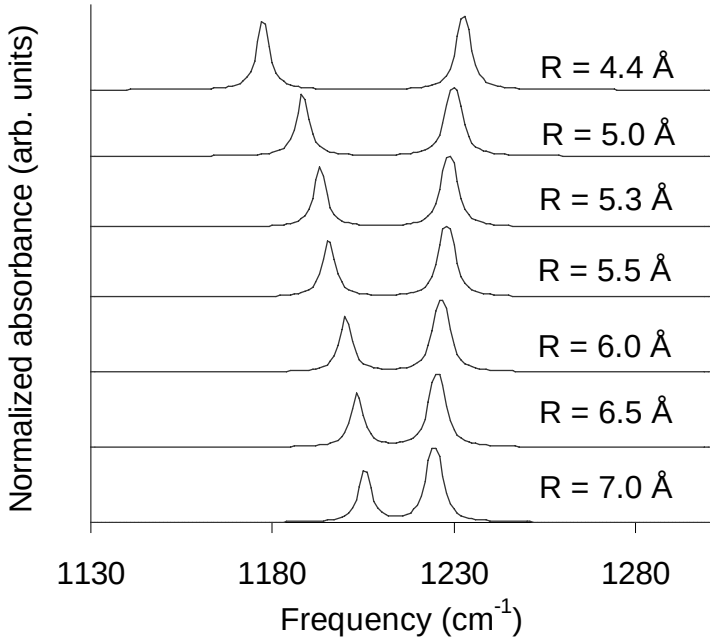

Figure 24. Computed IR absorbance for a 1D in-line chain of CF_4 molecules aligned along their C_3 axes. The lattice spacing increases from the top curve to the bottom curve with the spacing, R, shown on each curve.

The best comparison between calculated and experimental IR spectra would be for realistic geometries of CF_4 molecules adsorbed on the groove and internal sites of $SWNT_S$. Unfortunately, the linear response calculation using PWscf are prohibitively difficult for such systems. We have therefore attempted to mimic the effect of concentration and packing geometry by performing LDA/NCPP calculations for the IR absorbance for a linear chain of CF_4 molecules varying the distance between the molecules, and by considering CF_4 molecules packed into a zigzag geometry. The former calculations mimic the effect of low coverages of CF_4 molecules in the groove site, as observed from classical Monte Carlo simulations *(191)*. The latter calculations model the effects of non-linear packing of CF_4 molecules inside the nanotubes, also observed in classical adsorption simulations *(191)*.

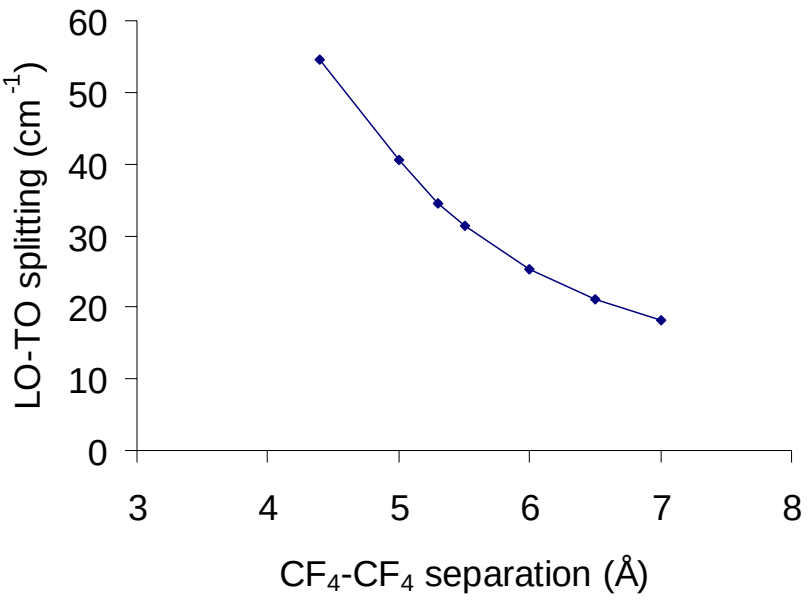

Figure 25. The calculated LO-TO splitting as a function of the CF_4-CF_4 separation for the 1D chain IR spectra shown in Figure 24.

The IR absorbance for a single chain of CF_4 molecules at different values of the distance between the molecules is plotted in Figure 24. The CF_4 molecules are packed along the C_3 axis, although similar results are observed for packing along the C_2 axis. The distance between the molecule centers is given for each curve. The top curve is for a close-packed optimized structure, where the molecules are 4.4 Å apart. Note that the LO-TO splitting is about 55 cm^{-1} for the close packed structure and that the splitting decreases to about 18 cm^{-1} when the CF_4 molecules are spaced 7.0 Å apart. The close-packed splitting in 1D is less than half the splitting calculated for the bulk bcc phase of about 116 cm^{-1} (see Figure 20). The LO-TO splitting as a function of CF_4 separation is plotted in Figure 25. It is obvious from this plot that the splitting drops dramatically with an increase in nearest-neighbor distance. The average nearest-neighbor distance for CF_4 molecules adsorbed inside the nanotubes at the experimental conditions of 133 K and 0.033 torr is about 5.3 Å, as determined from Monte Carlo simulations *(191)*. This average spacing would

result in LO-TO splitting of about 35 cm^{-1} according to Figure 25. The splitting observed experimentally in bulk CF_4 is 65 cm^{-1} *(259)*, roughly half that predicted in our calculations. If the splitting is overestimated in all our calculations then the 1D chains with neighboring CF_4 distances greater than about 5.5 Å may not appear to have LO-TO splitting because the two peaks would be merged. This implies that it would not be possible to observe LO-TO splitting from CF_4 adsorbed in the groove sites, since the concentration of molecules is predicted to be quite low *(191)*.

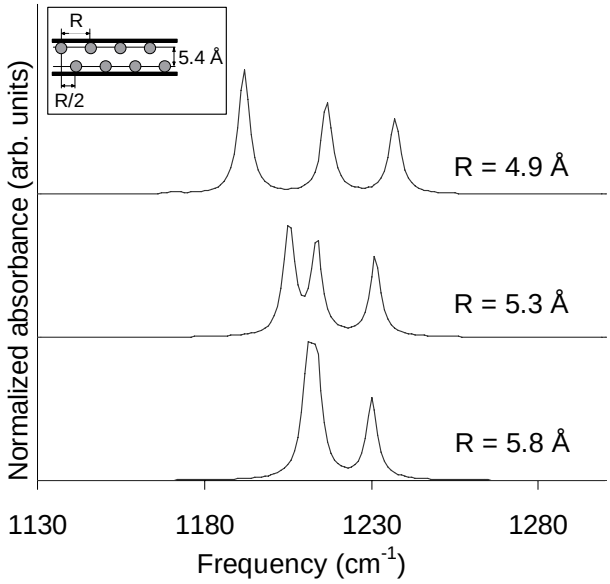

Figure 26. Calculated IR absorbance for a 1D zigzag chain of CF_4 molecules. The lattice spacing along the chain axis is increased from the top curve to the bottom curve.

We have computed the PDOS and phonon dispersion relations for the 1D linear chain geometry as a complement to the IR absorbance calculations. From Figure 21b it can be seen that LO-TO splitting does indeed occur for the linear CF_4 chain at the **Γ** point; the splitting is evident from the spread between the low frequency band and the two high frequency bands near the **Γ** point. The **Γ-Z** direction in Figure 21b points along the chain axis. Note that the high frequency LO mode is composed of two nearly degenerate bands, in agreement with both the IR frequency

and absorption calculations. The most striking feature of Figure 21b is that the PDOS is very low around the TO region, at about 1180 cm^{-1}, as can be seen by comparing the PDOS curve on the right axis of Figure 21b with the dispersion curve. The low PDOS in the TO region does not translate into low IR absorbance, as can be seen from Figure 24, where the TO absorption is about equal to that of the LO mode.

The 1D chain is a reasonable approximation for the geometry of molecules adsorbed in the groove sites. Model calculations have shown that CF_4 molecules adsorbed inside SWNTs adopt a geometry that is closer to a zigzag 1D chain. The IR absorbance of CF_4 molecules confined to a zigzag configuration is plotted in Figure 26. The geometry of the 1D zigzag chain is shown in the inset of Figure 26. The heavy lines represent the wall of the nanotube. The two length scales defining the geometry are also shown in Figure 26. The distance perpendicular to the zigzag axis was held fixed at 5.4 Å while the distance between molecules along the axis was varied from a close-packed distance of 4.9 Å to 5.8 Å. The zigzag structure gives a simulated IR spectrum containing three peaks, one TO peak at about 1190 cm^{-1}, a LO peak at about 1240 cm^{-1}, and a gas-phase-like peak at 1217 cm^{-1}. The two peaks at lower frequency quickly merge with increasing CF_4-CF_4 distance, as can be seen from the bottom curve in Figure 26. These calculations for the zigzag phase agree with the pure 1D chain calculation in that the LO-TO splitting decreases rapidly with increased adsorbate-adsorbate spacing. The zigzag phase, however, indicates that additional peaks will occur for off-axis packing, possibly giving rise to broadening. These features would serve to mask the appearance of the LO-TO modes in experiments.

II-5C. LO-TO Splitting in 1, 2, and 3D

In this section we compare IR absorption spectra for CF_4 in 1D chains, in 2D structures (monolayer and multilayers), and in the 3D bulk crystal. The calculated spectra are given in Figure 27. We have normalized the intensity in all the absorption calculations so that the number of CF_4 molecules being irradiated is the same in different structures. Note that this is different from experiments, where higher coverages will lead to a larger IR signal according to Beer's law. The LO-TO peaks are not sensitive to the relative orientation of adjacent CF_4 molecules because CF_4 packed along its C_2 axis and along its C_3 axis show similar results.

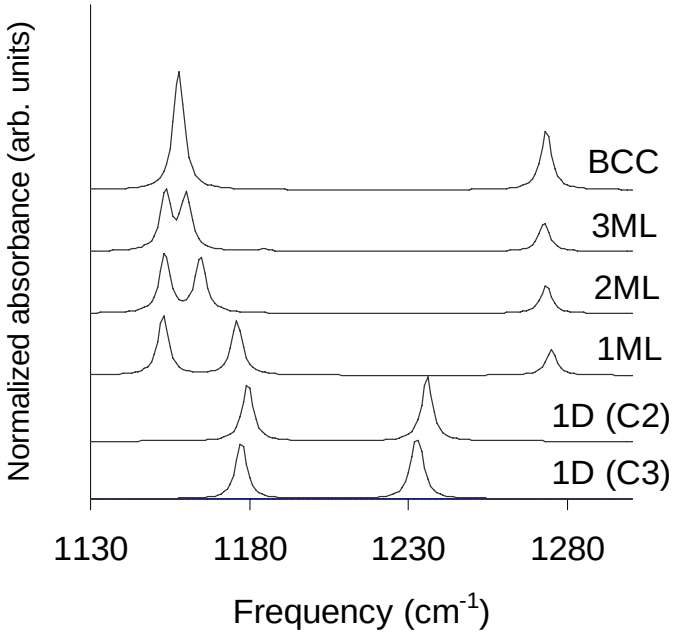

Figure 27. Calculated IR absorption spectra. a) bulk CF_4 (body-centered cubic lattice); b) 3 ML CF_4; c) 2 ML CF_4; d) 1 ML CF_4; e) 1D CF_4 packed along the molecular C_2 axis; f) 1D CF_4 packed along the molecular C_3 axis.

The 2D structures have two TO modes and one LO mode, in contrast to the 1D chains, which have one TO mode and two LO modes. The calculated IR spectra clearly show that the two TO modes are split in the monolayer (1ML curve) and that the two peaks merge as the number of layers increase (2ML and 3ML curves in Figure 27). The splitting is due to anisotropy

in the 2D structure. The TO mode in the bulk (bcc curve in Figure 27) is doubly degenerate. The absorption intensity grows slowly from 1 ML, 2 ML to 3 ML. The TO band has larger intensity because there are 2 TO modes and 1 LO mode, i.e. the absorbance ratio is about 2:1 for TO:LO in the bulk.

The ν_3 vibrations parallel to the slab have lower frequencies, analogous to the vibrational mode aligned along the 1D chain; it follows that the 2D geometry has two TO modes because there are two in-plane directions. For the ν_3 mode in the out-of-plane direction, the dynamic dipoles are coupled repulsively to their nearest neighbor, giving a shift to higher frequency, analogous to the motions shown in Figure 22b. Hence, one of the LO modes becomes a TO mode in going from 1D to 2D. One of the LO modes in 1D gradually becomes a TO mode as lines of 1D chains are brought together to form a 2D slab. There is also another qualitative difference in the LO-TO splitting between 1D and 2D systems. The LO mode in 1D is only slightly blueshifted, whereas it is strongly blueshifted in the 2D and 3D systems, as can be seen by comparing the curves in Figure 27.

The PDOS for the systems shown in Figure 27 are presented in Figure 28. The PDOS for 1D chains packed along the C_3 and C_2 axis are shown in Figure 28 as curves f and e, respectively. The PDOS are qualitatively similar for both packings, both show very low density of states in the TO region and considerably higher density of states in the LO region, with a broad plateau region of low PDOS separating the two. In going from 1D to 2D (Figure 28d) we see that the LO PDOS is decreased and the PDOS in the TO region is increased and broadened.

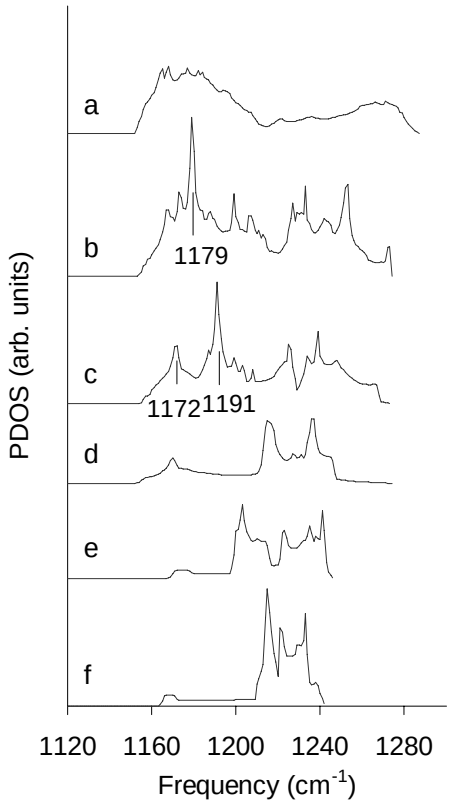

Figure 28. a) PDOS of bulk CF_4 in C2/c structure; b) PDOS of 3 ML of CF_4; c) PDOS of 2 ML of CF_4; d) PDOS of 1 ML of CF_4; e) PDOS of CF_4 in a linear chain packed along the molecular C_2 axis; f) PDOS of 1D CF_4 packed along the molecular C_3 axis.

The change in lattice dynamics due to adding a second layer to the 2D monolayer can be seen by comparing Figure 28d and Figure 28c. A new characteristic peak appears at 1191 cm^{-1}, corresponding to layer-layer interactions. This characteristic peak is between the LO band, which ranges from 1230 cm^{-1} to 1253 cm^{-1}, and the small TO shoulder at 1172 cm^{-1}. The PDOS at the TO band becomes larger as the number of layers is increased, as can be seen by comparing curves d, c, and b in Figure 28, which correspond to the monolayer, bilayer, and trilayer, respectively. The PDOS of the 2D structures become increasingly like the PDOS of the bulk CF_4, shown in Figure 28a, as the number of layers is increased.

II-5D. Experimental Results

Figure 29 shows the IR spectra of CF_4 adsorbed at 133 K and 0.033 torr on etched and unetched SWNTs. A doublet with peaks at 1253 cm^{-1} and 1272 cm^{-1} is observed in the spectrum of CF_4 adsorbed on the unetched SWNTs. This results from the Fermi resonance of the fundamental ν_3 mode and the first overtone of the ν_4 mode. The ν_4 overtone is not included in any of the calculations. The more intensive ν_3 mode is located in the higher frequency range relative to the overtone of the ν_4 mode. The frequencies of these bands can be extracted by the Fermi self-deconvolution method described previously *(191)* and are located at 1267 cm^{-1} and 1257 cm^{-1}, respectively, for the ν_3 fundamental and the first overtone of ν_4 mode. This doublet is assigned to CF_4 molecules adsorbed in the groove sites of SWNT bundles.

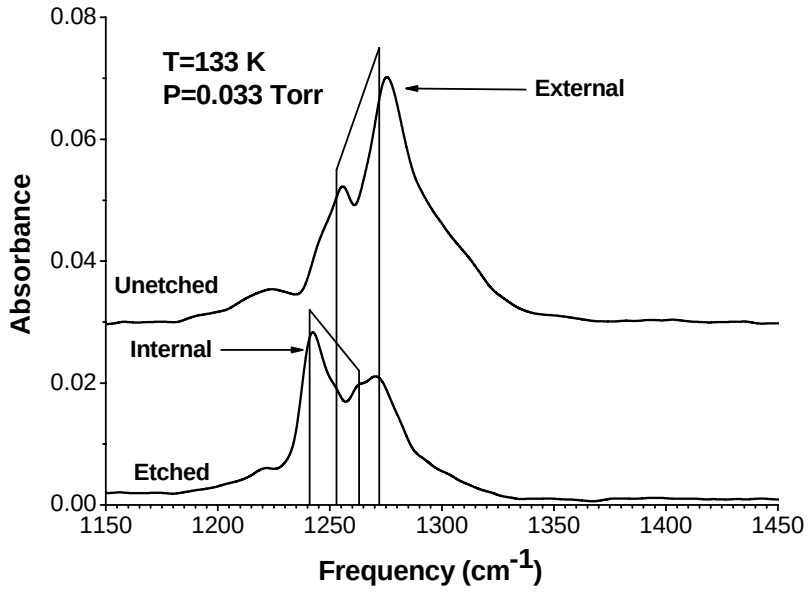

Figure 29. Experimentally measured IR spectra for CF_4 adsorbed on SWNTs at 133 K and a pressure of 0.033 torr.

The internal sites become available for adsorption upon etching of the SWNTs. The IR spectrum of CF_4 on the etched tubes has a doublet with peaks at 1263 cm^{-1} and 1241 cm^{-1} in

addition to the doublet observed for the unetched SWNTs. This doublet is assigned to CF_4 adsorbed in the nanotube interior. Based on the intensity ratio, the fundamental ν_3 mode is believed to be shifted greater than the overtone and is located in the lower frequency region. The Fermi self-deconvolution analysis gives the frequencies of the ν_3 and $2\nu_4$ modes at 1247 cm^{-1} and 1258 cm^{-1}, respectively. Adsorption in the nanotube interior is accompanied by stronger adsorbate-adsorbent interaction due to the deeper potential well inside of nanotubes. This caused softening of vibration motion and higher redshift of the band. The degree of softening depends on the transition dipole moment that is much greater for the ν_3 mode than for $2\nu_4$ mode; therefore, the ν_3 mode is more redshifted.

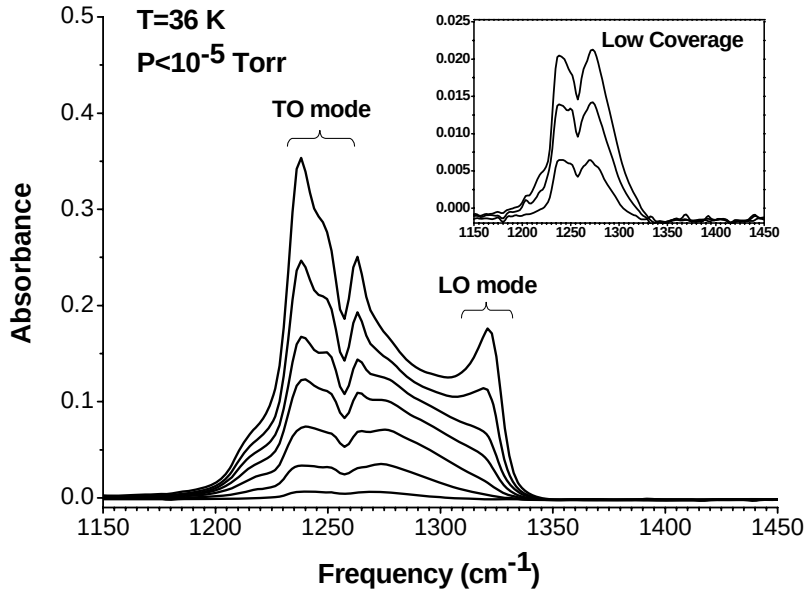

Figure 30. Experimentally measured IR spectra for CF_4 adsorbed on SWNTs at 36 K. The coverage is increased from the bottom curve to the top.

Figure 30 shows the IR spectra of CF_4 adsorbed on etched SWNTs at 36 K. At low coverages the spectral profile resembles the profile of IR spectra of CF_4 adsorbed at 133 K; two families of peaks are observed that may be attributed to overlapping of two doublets observed at

higher temperatures. However, as the coverage increases a peak at ~1239 cm^{-1} starts to appear followed by developing of a less intense and broad shoulder at 1320 cm^{-1} that shifts to higher frequency with increasing coverage. At very high coverages these two bands are observed at 1238 cm^{-1} and 1321 cm^{-1} and can be assigned to TO and LO modes, respectively, detected for condensed phases of CF_4. Thus, CF_4 at low coverages presumably adsorbs in the groove sites and partially inside of nanotubes since the low temperature limits diffusion on the surface. As the coverage increases, larger clusters of CF_4 appear, forming increasingly thick layers on the surface of the SWNTs. The appearance of LO-TO splitting coincides with the increase in CF_4 coverage.

II-6. Conclusions

We have presented the first set of comprehensive *ab initio* calculations for LO-TO splitting in systems of differing dimensionality. We have computed vibrational frequencies, IR absorption, and the phonon density of states for CF_4 in one, two, and three dimensions. We have studied how LO-TO modes develop as the dimensionality is changed. There are two LO modes and one TO mode for an in-line 1D chain of CF_4 molecules. In contrast, 2D structures have one LO mode and two TO modes. One of the 1D LO modes becomes an in-plane TO mode in going from 1D to 2D. The phonon modes for 1D chains and 2D sheets have a relatively low density of states in the TO region. The TO PDOS are developed through interlayer interactions as can be seen by comparing monolayer, bilayer, trilayer, and bulk lattice structures.

We have measured IR spectra of CF_4 adsorbed on samples of unetched and etched SWNTs at 133 K and 0.033 torr. No LO-TO splitting was observed. We also measured IR spectra at 36 K over a wide range of coverages and found that LO-TO splitting developed gradually as the coverage was increased.

Our calculations demonstrate that LO-TO splitting does, in principle, occur for CF_4 molecules confined to 1D, both in linear and zigzag chains. The question then is why LO-TO splitting cannot be observed in experiments at low coverages of CF_4 on SWNT samples. The calculations indicate that there are dramatic qualitative differences between LO-TO splitting in 1D and 2 or 3D. Specifically: (1) the splitting is much smaller for 1D and quasi-1D structures at close packing than for the bulk (Figure 27), (2) the LO modes are very weakly blueshifted, and (3) the nanotubes and packing disorder introduce additional peaks and shift the LO modes to lower frequencies (Table 4 and Figure 26). Therefore, LO-TO splitting for 1D and quasi-1D systems cannot be observed experimentally from the somewhat broad experimental peaks (see Figure 29 and Figure 30). The IR frequencies show that the ν_3 modes in 1D are redshifted, but not strongly blueshifted. When the nanotubes are included in the frequency calculations the blueshifted frequencies almost entirely disappear (Table 4). This is in qualitative agreement with the experiments, which show absorption in the redshifted region but not at higher frequencies at low coverages (Figure 30, inset). The LO peak observed in the IR absorption and PDOS calculations shifts to higher frequencies as the coverage increases from 1D to 2D (Figure 27 and Figure 28). This is also in qualitative agreement with experiments (Figure 30).

We note that the computed LO-TO splitting for bulk CF_4 is too large compared with experiments by about a factor of two. This is likely the result of inaccuracy of the exchange-correlation functional. We performed limited calculations with two different generalized gradient approximations, namely PBE *(311)* and PW91 *(312)*, but the results were not an improvement over the LDA calculations. We assume that the LO-TO splitting in all our calculations is over-predicted. Therefore, the true splitting in 1D systems could be much smaller than our

calculations indicate, giving another reason for the lack of observed LO-TO splitting in the experiments.

Note that we have only included a single CF_4 molecule in the supercell of most of our calculations and we have ignored the effect of the nanotube on the IR absorption and PDOS. Inclusion of multiple CF_4 molecules would have allowed us to investigate orientational and packing effects that are lacking in this study. These effects may have given us a better understanding as to why LO-TO splitting is absent in the experiments. Nevertheless, there is enough qualitative agreement between experiments and calculations to allow us to conclude that while LO-TO splitting is formally present in 1D systems, in practice it cannot be observed.

The calculated PDOS for 1D, 2D, and 3D structures show substantial differences, as can be seen from Figure 28. The density of states in the TO region is very small for 1D and 2D monolayer structures. The PDOS in the TO region increase dramatically with the addition of mutilayers, while the LO PDOS both increase and shift to higher frequencies. These theoretical predictions should be tested experimentally by inelastic neutron scattering.

We propose that LO-TO splitting can be used as a sensitive marker for identifying one-dimensional states of matter. The qualitative changes in the vibrational spectrum and PDOS for CF_4 as a function of dimensionality make the ν_3 mode an excellent probe of the effective dimensionality of adsorbed molecule. Our results agree with those of Devlin et al., who have previously proposed the use of ν_3 spectroscopy as a probe for 2D surface structure *(261, 262)* It should be possible to use other molecules that display LO-TO splitting, such as CCl_4, HCN, *(313, 314)* or meta-nitroaniline *(315)* as probes of the effective dimensionality of an environment.

II-7. Acknowledgments

We gratefully acknowledge the Army Research Office for the support of this work. Computations were performed at the Center for Molecular and Materials Simulations at the University of Pittsburgh and at the U.S. Army Research Laboratory Major Shared Resource Center through a Department of Defense High Performance Computing challenge grant.

III. ADSORPTION AND DIMERIZATION OF NO INSIDE OF SWNTS*

III-1. Abstract

The physical adsorption of NO on purified single walled carbon nanotubes was investigated at low temperatures by means of transmission infrared spectroscopy. Ozone treatment followed by annealing was used as a method of opening the entry ports for adsorption into the interior of the nanotubes. The IR spectra show that NO which is adsorbed inside of nanotubes exists exclusively in its dimer form, with no infrared bands of the monomer visible at a sensitivity level of 5 mole % NO. The internally adsorbed NO dimer species observed is *cis*-$(NO)_2$ with ν_1(symmetric) = 1853 cm^{-1} and ν_5(asymmetric) = 1754 cm^{-1}. Introduction of Xe into the system leads to selective displacement of the internally-bound *cis*-$(NO)_2$ dimer. A large spectroscopic red shift of the symmetric [-0.80%] and the asymmetric [-1.96%] modes for *cis*-$(NO)_2$ adsorbed inside of nanotubes (relative to gas phase *cis*-$(NO)_2$) points to the strong interaction of the dimer with the nanotube interior. The enthalpy of dissociation of the adsorbed dimer molecule is 15.1±0.7 kJ/mol.

* Reproduced with permission from O. Byl, P. Kondratyuk, J. T. Yates, Jr. Adsorption and Dimerization of NO Inside Single-Walled Carbon Nanotubes – an Infrared Spectroscopic Study. Journal of Physical Chemistry B 107(18), 4277-4279 (2003). Copyright 2005 American Chemical Society.

III-2. Introduction

Single walled carbon nanotubes possess excellent adsorption properties due to their high specific surface area and to the enhancement of adsorption energy in their interior *(136)*. In addition, based on modeling, it is expected that confinement effects will cause the dimerization of NO within the nanotubes under thermodynamic conditions which do not favor dimerization under non-confined conditions *(316)*. Indeed, it is known that the enhancement of dimerization occurs in the micropores of activated carbon particles, where more than 98 % of NO is found to be in the dimer form at 298 K *(317)*.

NO exists almost entirely in the dimeric form in the condensed phase *(318)* but only about 1% of the molecules in the gas phase are in the dimer form at its boiling point (121 K and 760 Torr) *(319, 320)*. A number of NO dimers may coexist in the condensed phase and *cis*-$(NO)_2$ is the most stable of the dimers *(321)*. However, adsorbed NO may exist in its monomer form if there are binding sites where the NO-surface interaction is strong enough to prevent dimerization *(322)*.

In this work we report studies of the adsorption of NO in opened single walled nanotubes using transmission FTIR spectroscopy to discriminate *cis*-$(NO)_2$ dimers from other dimer forms and to investigate the presence of NO monomers at cryogenic temperatures.

III-3. Experimental section

The SWNTs were obtained from Professor R. Smalley's group, Rice University, Houston TX. They were produced by means of the pulsed laser vaporization technique and purified by HNO_3/H_2SO_4 treatment *(250)*. The tube diameter distribution was centered near that of (10,10) SWNTs with a diameter of 13.6Å. The length distribution was rather narrow with a most

probable length of 320 nm. This material was identical to that used in our previous studies *(47, 157, 191)*.

All spectra were recorded at 4 cm^{-1} resolution with 1000 scans taken for averaging. CaF_2 pressed into a 7 mm diameter spot on a tungsten grid was used as the support material for the nanotubes of ~50 μg mass. An additional spot of CaF_2 was used as a reference to subtract the infrared absorbance of NO adsorbed on the support itself from the spectrum of the nanotube sample and its support. The experimental setup was described elsewhere *(191)*.

As NO often contains appreciable amounts of impurities, the NO gas used in the experiments was purified in the following manner *(323)*: NO from a cylinder (Matheson) was first frozen at liquid nitrogen temperature (77 K) in a glass bulb, and then the liquid nitrogen was replaced with liquid oxygen (90 K). Then the NO was allowed to slowly distill into another evacuated bulb, which was cooled with liquid nitrogen. This permitted the separation of NO from less volatile compounds such as NO_2 and N_2O. Two cycles of purification were carried out, resulting in NO that showed almost no traces of impurities in its infrared spectrum.

The single walled nanotubes were opened by oxidation with ozone gas at 300 K, followed by annealing in vacuum at 863 K *(191)*. This procedure produces opened segments of SWNTs as shown by earlier studies of the ozonation/annealing process *(47, 156, 157)*. Because of the relatively fast rate of destruction of ozone in the stainless steel IR cell containing the SWNT sample, four cycles of ozonation were carried out with initially 63 % pure ozone at about 19 Torr total pressure. The procedure for preparing and storing high purity O_3 is given in ref. *(251, 324)*.

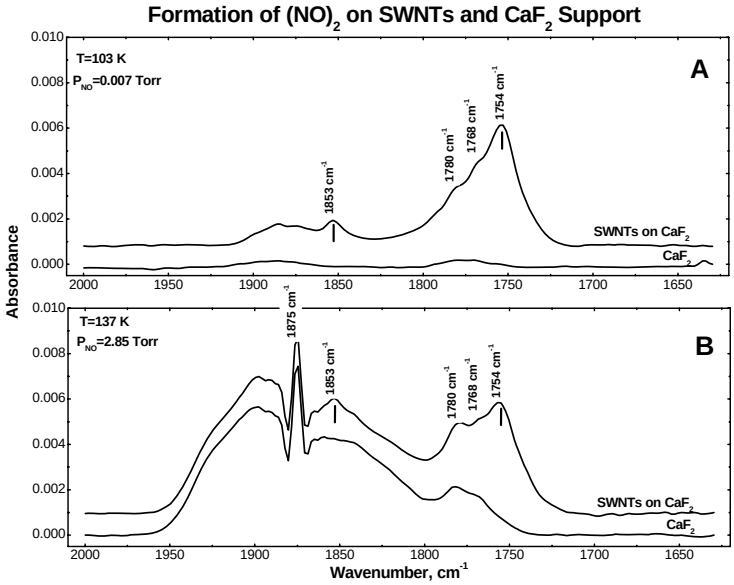

Figure 31. Formation of $(NO)_2$ on SWNTs and CaF_2 support: (A) 103 K and P_{NO}=0.007 Torr; (B) 137 K and P_{NO}=2.85 Torr.

III-4. Results and Discussion

III-4A. Infrared Spectra of *cis*-$(NO)_2$ Adsorbed in the Interior of SWNTs

Figure 31 shows two typical pairs of spectra taken under the same conditions through the sample containing adsorbed NO dimers and the bare CaF2 reference. The spectra shown in Figure 31A were taken at 103 K and an NO pressure of 0.007 Torr. Figure 31B shows the same spectra at 137 K and an NO pressure of 2.85 Torr. It can be noticed that the bands at 1754 cm^{-1} and 1853 cm^{-1} are only observed in the spectra taken of the SWNTs and not in the CaF_2 reference spectra. Furthermore, these bands are weaker in the spectrum taken on nanotubes which have not been opened by the ozone/annealing treatment (not shown). These bands are assigned to $(NO)_2$ diemer species adsorbed in the nanotube interior as will be shown. Bands at 1768 cm^{-1} and 1780 cm^{-1} are present in both the spectra of the nanotubes and the CaF_2 reference, but their intensities are higher in the nanotube spectrum. We believe that the 1768 cm^{-1} and 1780 cm^{-1} bands originate

from $(NO)_2$ species on sites which are not present in the nanotube interior. The spectra in Figure 31B also involve contributions from NO(g), centered at 1875 cm^{-1}, where the P, Q and R branches are observed.

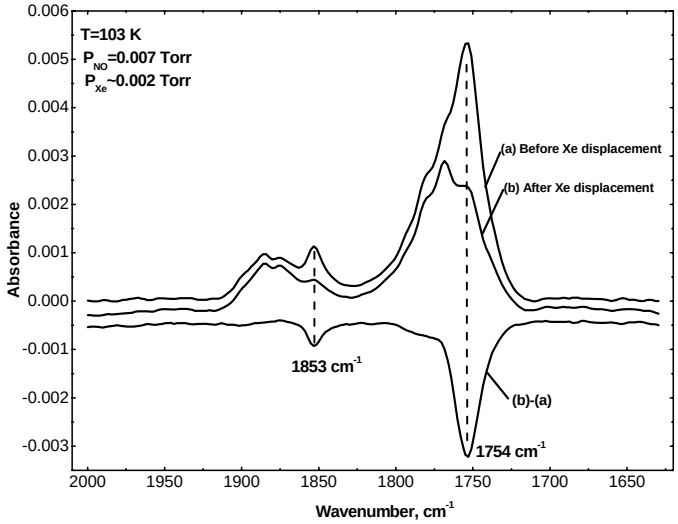

Figure 32. Xe displacement of *cis*-$(NO)_2$ adsorbed on SWNTs at T = 103 K and P_{NO} = 0.007 Torr. $P_{Xe} \approx$ 0.002 Torr

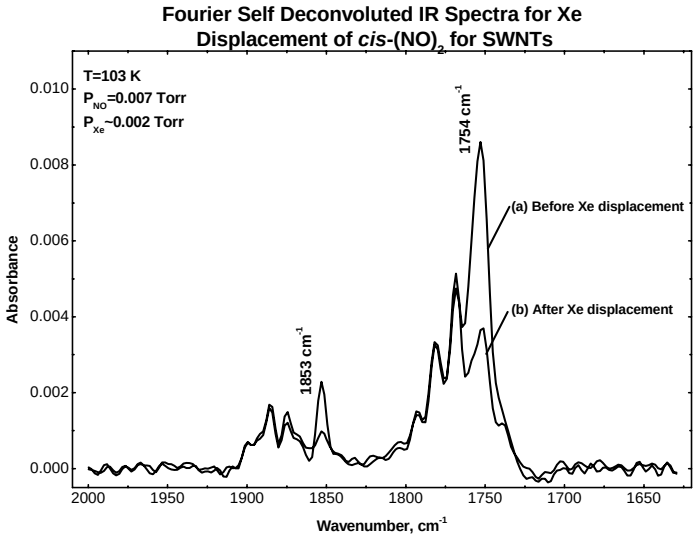

Figure 33. Fourier self deconvolution of adsorbed *cis*-$(NO)_2$ infrared spectra before and after Xe displacement.

Table 5. Vibrational Frequencies of *cis*-$(NO)_2$ Adsorbed on Various Carbon Surfaces and Gas Phase *cis*-$(NO)_2$.

Surface	$\nu_1(NO)_2$ (sym)	$\nu_5(NO)_2$ (asym)	References
graphite film	1863 cm^{-1}	1768 cm^{-1}	*(325)*
diamond film	1866 cm^{-1}	1767 cm^{-1}	*(325)*
C_{60}	1858 cm^{-1} 1853 cm^{-1}	1765 cm^{-1} 1755 cm^{-1}	*(326)*
SWNTs (interior)	1853 cm^{-1}	1754 cm^{-1}	this work[a]
gas phase	1868 cm^{-1}	1789 cm^{-1}	*(319, 320)*

[a] The comparison with gas phase *cis*-$(NO)_2$ frequencies indicates that the red shift for ν_1(sym, 1853 cm^{-1})=[-0.80%] and the red shift for ν_5(asym, 1754 cm^{-1})=[-1.96%].

Xenon, which adsorbs strongly in the interior of SWNTs *(160)* has been shown to preferentially displace other molecules which have been preadsorbed in the nanotube interior *(191)*. We carried out a similar displacement experiment with NO adsorbed on the nanotubes. The result of $(NO)_2$ displacement by Xe is shown in Figure 32 and Figure 33. Figure 33 shows the original spectral data along with a difference spectrum and Figure 33 shows Fourier self deconvoluted spectra enhancing the resolution of the spectral features (GRAMS/AI software, Galactic Inc.). Only the two bands, at 1754 cm^{-1} and 1853 cm^{-1}, significantly decrease after the addition of Xe, as may be seen from the difference spectra shown in Figure 32 and in the comparison deconvoluted spectra shown in Figure 33. Taking into account this fact we assigned these bands respectively as the ν5 (asymmetric stretch) and the ν1 (symmetric stretch) modes of *cis*-$(NO)_2$ adsorbed in the interior of SWNTs*(319, 320, 327)*. This assignment is supported by the assumption that a molecule adsorbed inside a nanotube should experience a relatively strong interaction with the curved walls. Thus a comparatively strong spectroscopic red shift may be expected in the IR spectra, which is indeed observed. A comparison with the frequencies

observed for *cis*-$(NO)_2$ adsorbed on exterior carbon surfaces *(325, 326)*, and *cis*-$(NO)_2$ in gas phase is presented in Table 5.

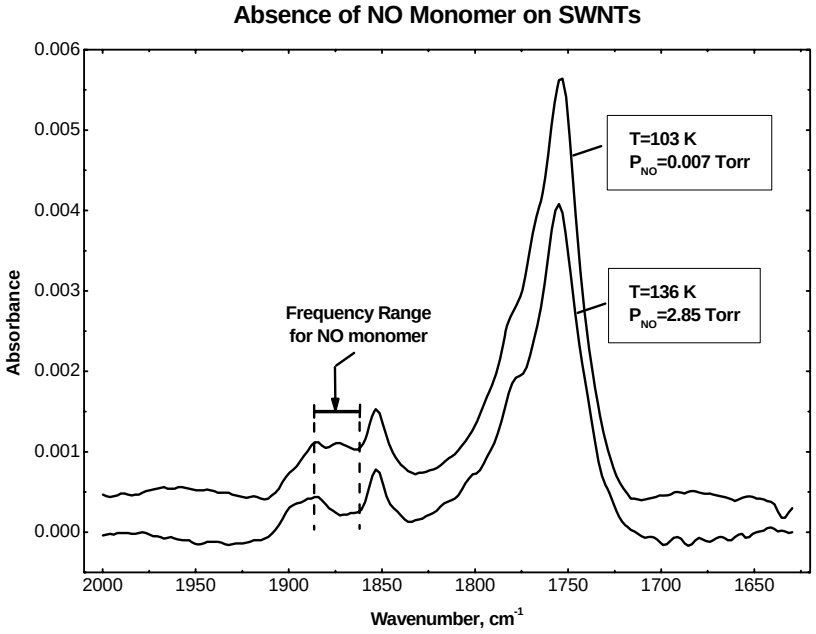

Figure 34. Evidence of absence of NO monomer on SWNTs. Spectra were obtained following NO adsorption by subtraction of the spectrum on CaF_2 from the spectrum on SWNTs and CaF_2

III-4B. NO Monomer Studies

NO in its monomeric form absorbs at 1875 cm^{-1} in the gas phase *(319, 320)*. Figure 34 shows the spectra of NO adsorbed on SWNTs at two different temperatures and NO pressures with the spectra of NO adsorbed on the bare CaF_2 reference subtracted. In the case of the 136 K – spectrum, the pressure was adjusted to 2.85 Torr to obtain approximately the same intensity of *cis*-$(NO)_2$ as in the spectrum taken at 103 K. It is remarkable that the profiles of both spectra are very similar. The close similarity between the spectra at two temperatures and two NO pressures in Figure 34 indicates that no detectable monomeric NO is produced by working at higher pressure and temperature in the temperature range 103 K – 136 K. Like the experiment shown in Figure 32, Xe displacement experiments at 2.85 Torr and 136 K (not shown) indicate that the

amount of monomer displaced by Xe is not greater than the level of noise in the 1875 cm^{-1} region. Using the relative IR absorption coefficients for NO and *cis*-$(NO)_2$ measured elsewhere *(328, 329)*, we estimate that the maximum mole percent of adsorbed NO monomer is less than 5 % at 2.85 Torr and 136 K[*].

III-4C. Thermal Dissociation of Confined *cis*-$(NO)_2$.

We investigated the dependence of the IR spectra of adsorbed *cis*-$(NO)_2$ on the temperature under equilibrium conditions at constant NO pressure as shown in Figure 35. This experiment permits the construction of a van't Hoff plot which allows the measurement of ΔH^o for the change in state occurring. This method has been successfully employed in other infrared studies of reversibly-bound adsorbed species *(331)*. A strong temperature dependence for the 1754 cm^{-1} band is observed, and a similar dependence is also found for the 1853 cm^{-1} band. The van't Hoff plot is shown as an insert, and yields $\Delta H^o = 15.1 \pm 0.7$ kJ/mol for the depletion of *cis*-$(NO)_2$ adsorbed in the nanotube interior. The dissociation energy for the *cis*-$(NO)_2$ dimer, given in the literature ranges from 7.6 kJ/mol to 15 kJ/mol *(316, 318)*, suggesting that the process being witnessed is the conversion of internally-bound *cis*-$(NO)_2$ to NO(g) by the breaking of the N-N bond in the dimer *(319, 320)*. During this dissociation process, no absorbance due to the formation of adsorbed NO monomer is observed in the 1875-1862 cm^{-1} region, consistent with the results of Figure 34. Thus, considering both the experiments of both Figure 33 and Figure 34, to within the sensitivity limits of the infrared measurement, adsorbed NO does not exist at

[*] The ratio of the monomer absorption coefficient to the dimer ν_1 mode absorption coefficient varies from 64 (L. Krim; *J. Mol. Struct.* 471, 267 (1998)) to 0.5 (B. J. Howard, A. R. W. Mckellar; *Mol. Phys.* 78, 55 (1993), R. Kometer, F. Legay, N. Legaysommaire, N. Schwentner; *J. Chem. Phys.* 100, 8737 (1994)).We believe that such a large range may result from changes in the NO dimer geometry which depend on the medium. In this paper the lowest ratio of the monomer to the ν_1-dimer mode absorption coefficients ratio (0.5) was used for calculation of the maximum possible mole fraction of NO monomer.

significant levels in equilibrium with adsorbed *cis*-$(NO)_2$ in the interior of the SWNTs over the temperature range 103 K – 136 K.

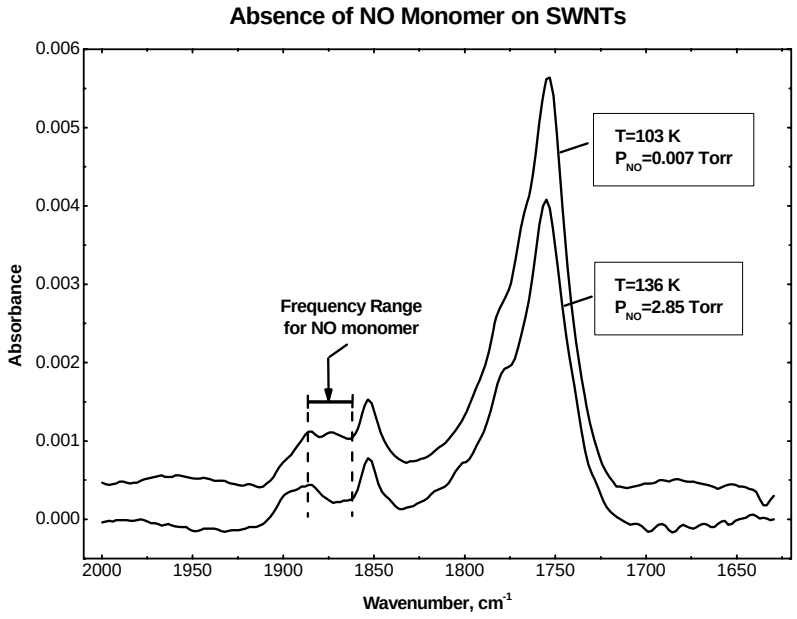

Figure 35. Equilibrium temperature dependence of IR spectra on SWNTs for NO adsorption in the temperature range of 103-114 K at P_{NO}=0.007 Torr.

III-4D. Comparison with Theoretical Calculations

These results disagree with recent calculations of the NO – $(NO)_2$ equilibrium ratio for adsorption in the interior of SWNTs *(316)*. The calculations show that while *cis*-$(NO)_2$ dimers are preferred, there is an equilibrium between dimers and monomers inside nanotubes in the temperature and pressure range studied here. Under the most favorable conditions of our experiment for monomer formation (T = 136 K, P_{NO} = 2.85 Torr), where adsorbed NO was not detected by infrared spectroscopy at a sensitivity level of 5 mole %, the calculations indicate that the equilibrium mole fraction of NO should be about 70 mole %.

III-5. Summary

The following results have been obtained in our study of NO adsorption on opened (10,10) single walled nanotubes:

(1) NO adsorbed on nanotubes exists predominantly in its *cis*-dimer form, exhibiting two vibrational modes: the ν_1 (symmetric) N=O stretching mode at 1853 cm^{-1}; and the ν_5 (asymmetric) N=O stretching mode at 1754 cm^{-1}.

(2) Small absorbances observed at 1780 cm^{-1} and 1768 cm^{-1}, which appear as shoulders on the dominant band at 1754 cm^{-1}, may be due to a small fraction of *cis*-$(NO)_2$ dimers present on other types of sites in the SWNT samples supported on CaF_2.

(3) Xe has been shown to displace *cis*-$(NO)_2$ for the interior of the SWNTs, in agreement with previous experiments where this displacement effect has also been observed.

(4) NO monomer, adsorbed on SWNTs, is not observed in equilibrium with *cis*-$(NO)_2$ dimers in the range of temperature (103 K – 136 K) and pressure (0.001 Torr – 2.85 Torr) employed. The limit of accuracy of the infrared spectroscopic measurements is 5 mole % NO.

(5) The dissociation at equilibrium of internally adsorbed *cis*-$(NO)_2$ dimers occurs to produce NO(g) in the temperature range 103 – 136 K with a $\Delta H^o = 15.1 \pm 0.7$ kJ/mol, consistent with the known dissociation energy of the dimer.

III-6. Acknowledgements

We gratefully acknowledge the Army Research Office for the support of this work. We also acknowledge support from Dr. Chris Karwacki at the Aberdeen Proving Ground.

IV. VIBRATIONAL BEHAVIOR OF ADSORBED CO_2 ON SWNTS*

IV-1. Abstract

We present theoretical and experimental evidence for CO_2 adsorption on different sites of single walled carbon nanotube (SWNT) bundles. We use local density approximation density functional theory (LDA-DFT) calculations to compute the adsorption energies and vibrational frequencies for CO_2 adsorbed on SWNT bundles. The LDA-DFT calculations give a range of shifts for the asymmetric stretching mode from about -6 cm^{-1} to -20 cm^{-1} for internally-bound CO_2, and a range from -4 cm^{-1} to -16 cm^{-1} for externally-bound CO_2 at low densities. The magnitude of the shift is larger for CO_2 adsorbed parallel to the SWNT surface; various perpendicular configurations yield much smaller theoretical shifts. The asymmetric stretching mode for CO_2 adsorbed in groove sites and interstitial sites exhibits calculated shifts of -22.2 and -23.8 cm^{-1}, respectively. The calculations show that vibrational mode softening is due to three effects: (1) dynamic image charges in the nanotube; (2) the confining effect of the adsorption potential; (3) dynamic dipole coupling with other adsorbate molecules. Infrared measurements indicate that two families of CO_2 adsorption sites are present. One family, exhibiting a shift of about -20 cm^{-1} is assigned to internally-bound CO_2 molecules in a parallel configuration. This type of CO_2 is readily displaced by Xe, a test for densely populated adsorbed species, which are expected to be present on the highest adsorption energy sites in the interior of the nanotubes. The second family exhibits a shift of about -7 cm^{-1} and the site location and configuration for these species is ambiguous, based on comparison with the theoretical shifts. The population of the internally-bound CO_2 may be enhanced by established etching procedures that open the entry

* Reprinted with permission from W.-L. Yim, O. Byl, J. T. Yates, Jr. and J. K. Johnson, "Vibrational behavior of adsorbed CO_2 on single-walled carbon nanotubes", Journal of Chemical Physics, 120, 5377-5386, (2004), Copyright 2004 American Institute of Physics. The theoretical work was performed by Dr. Wai-Leung Yim and Dr. J. Karl Johnson and is included here for completeness.

ports for adsorption, namely, ozone oxidation followed by annealing in vacuum at 873 K. Xenon displacement experiments indicate that internally bound CO_2 is preferentially displaced relative to the -7 cm^{-1} shifted species. The -7 cm^{-1} shifted species is assigned to CO_2 adsorbed on the external surface based on results from etching and Xe displacement experiments.

IV-2. Introduction

The adsorption of simple gases on single walled carbon nanotubes (SWNTs) has been studied experimentally for the past several years *(47, 138, 139, 144, 145, 153, 155-157, 159, 161, 162, 181, 189-191, 279, 332, 333)*. The interest in these materials stems from the 1-dimensional porosity, high surface area, and strong adsorption energies theoretically possible in pure carbon nanotubes *(126, 135, 142)*. The adsorption properties of SWNTs may be useful for devices such as gas sensors *(334-340)* and selective adsorption *(123, 196, 341)*. In this paper we examine the adsorption of CO_2 on SWNTs both experimentally and through first principles density functional theory (DFT). Understanding the adsorption of CO_2 on SWNTs is necessary for potential uses of SWNTs in separations applications because CO_2 is both a respiratory gas and the single most important green house gas.

There have been only a few studies of CO_2 adsorption on carbon nanotubes. Zhao *et al*. have studied the adsorption energies of several small gases, including CO_2, on SWNTs and bundles using local density approximation (LDA)-DFT *(307)*. They found adsorption energies in the range of -2 to -2.5 kcal/mol on different nanotubes. Rivera, McCabe, and Cummings used classical potential models to simulate the vapor-liquid equilibrium of H_2O and H_2O/CO_2 mixtures confined inside a large SWNT *(342)*. Cinke and coworkers have measured adsorption isotherms of CO_2 on SWNTs and activated carbon from 273 to 473 K and pressures up to 900 Torr *(343)*. They found that SWNTs adsorb nearly twice as much CO_2 as an activated carbon with similar surface area. Cinke *et al*. also present *ab initio* calculations of CO_2 interacting with small graphene clusters, chosen to represent SWNTs and graphite. Most of the calculations were performed with a single benzene molecule as a surrogate for the carbons. Use of such small cluster models allowed Cinke and coworkers to use high levels of theory, including second order

Møller-Plesset perturbation theory (MP2) and coupled clusters with single, double, and perturbational triple excitations (CCSD(T)). However, the interaction energy was found to be very sensitive to the size of the graphene cluster used, so that these calculations do not adequately address the binding of CO_2 to real graphite or real nanotubes. Matranga *et al*. have very recently studied CO_2 trapped inside SWNT bundles as a result of heating the nanotubes, causing the decomposition of oxygen containing functional groups *(236)*. They also studied the energetics and geometries of adsorbed and trapped CO_2 through classical molecular simulations. In addition, they presented measurement of IR spectra of CO_2 adsorbed on bundles of closed SWNTs and complementary classical simulation isotherms.

In this paper, we present an extensive set of DFT calculations for the energetics, geometries, and vibrational shifts of CO_2 adsorbed on the external and internal surfaces of an isolated (10,10) carbon nanotube and in the groove and interstitial sites of a perfect hexagonal bundle of (10,10) carbon nanotubes. We also present experimental IR spectra of the asymmetric stretch mode of CO_2 adsorbed on SWNTs bundles before and after the nanotubes have been opened by gas phase ozone oxidation *(157, 243)*. Dosing of the sample with Xe gas is used to selectively displace CO_2 after it is adsorbed, following previous work in which Xe was shown to preferentially displace adsorbed CF_4 in the internal SWNT sites *(191)*.

IV-3. Computational Methods

We have chosen to use periodic calculations to model the nanotubes and bundles because the nanotubes investigated in the experiments have a most probable length of 3200 Å *(47)*. Either empirical potential models or first principles methods could be used to compute the intra- and inter-molecular interactions of CO_2-SWNT systems. We are primarily interested in vibrational frequency shifts of CO_2 in the adsorbed phase and therefore we adopt first-principles quantum

mechanical methods in our calculations. This means that we are obliged to use DFT or Hartree-Fock theory, since these are the only periodic *ab initio* methods widely available. In principle, one could instead choose to model the SWNTs as clusters. In that case, one could invoke more accurate methods, such as MP2 or CCSD(T). However, as seen in the study of Cinke *et al. (343)*, one can only use unreasonably small clusters in practice, due to the very large basis sets required and the unfavorable scaling of these high-level quantum mechanical techniques.

It has been shown that DFT cannot account accurately for dispersion interactions within either the LDA or generalized gradient approximations *(295-298, 344)*. Several methods for improving the performance of DFT for computing dispersion interactions have been proposed *(295, 297, 301-303)*. However, none of these methods is in common use and most have not been adapted to periodic systems. Thus, at present we have no method available to us for accurately computing the dispersion interaction energies and vibrational frequencies of CO_2-SWNT systems. Nevertheless, there have been several recent studies showing that use of LDA-DFT can produce fairly accurate binding energies and geometric properties for weakly bound systems *(307, 345, 346)*. The agreement between experiment and LDA-DFT must be seen as a result of a fortuitous cancellation of errors, so that application of LDA-DFT to all weakly interacting systems is not advisable. We were encouraged to use LDA-DFT by the good agreement between experimental data and LDA-DFT calculations for the CO_2-graphite adsorption energy *(307)*.

The adsorption energies, geometries, and vibrational frequencies of CO_2 adsorbed on (10,10) carbon nanotubes have been calculated using density functional theory within the local density approximation. We define the adsorption or binding energy as

$$\Delta E = E(\mathrm{CO_2} + \mathrm{SWNT}) - E(\mathrm{SWNT}) - E(\mathrm{CO_2}) \qquad (4)$$

where $E(CO_2 + SWNT)$ is the energy of the total system (gas and nanotube), $E(SWNT)$ is the energy of the SWNT system and $E(CO_2)$ is the energy of the isolated (gas phase) CO_2 molecule. This definition means that a negative adsorption energy corresponds to an energetically bound species.

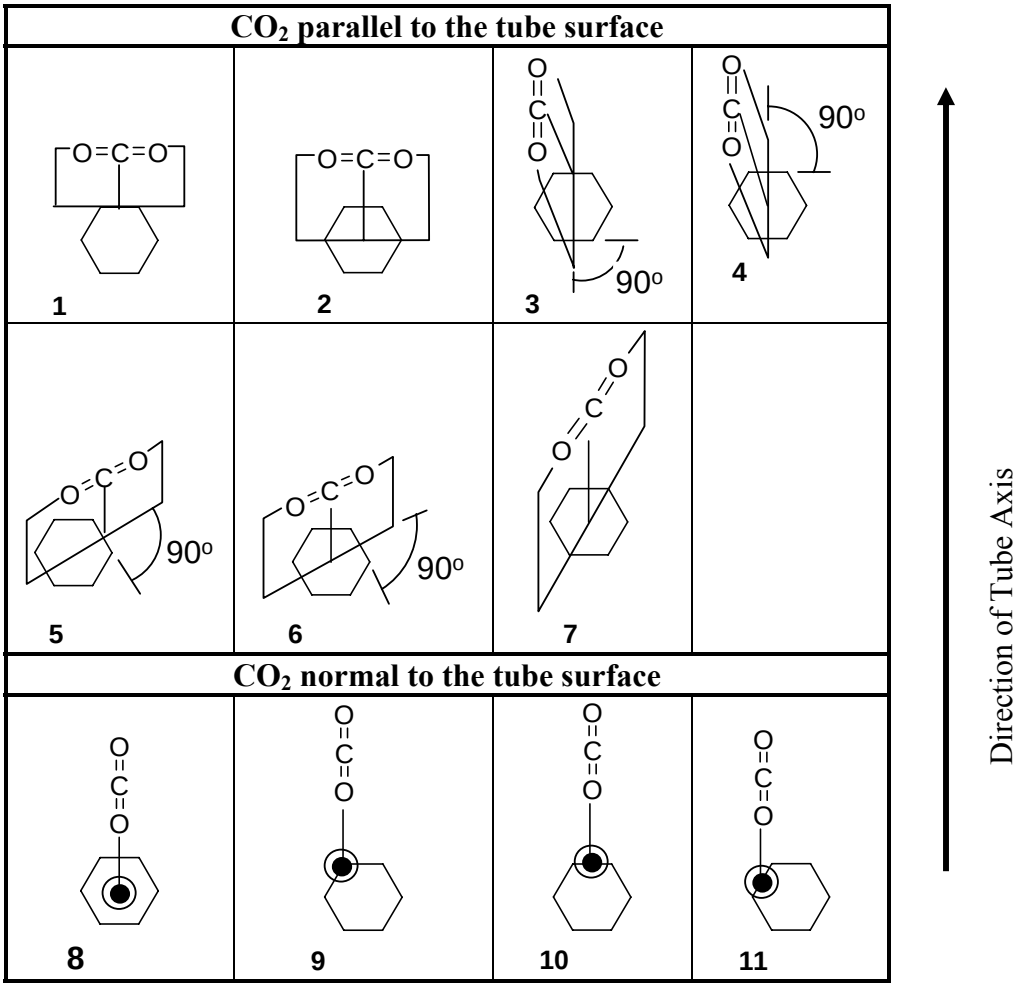

Figure 36. Schematic of different orientations of CO_2 adsorbed on the surface and inside a (10,10) nanotube.

The Vienna Ab Initio Simulation Package (VASP) was used to perform the calculations on periodic systems *(284-286, 347)*. Vanderbilt ultrasoft pseudopotentials were used for carbon and oxygen atoms. Two planewave basis sets, I and II, were tested. The cutoff energies were 269.9 and 395.7 eV for I and II, respectively. Augmentation charge cutoff energies were 553 and 928 eV for I and II, respectively. Neither basis set included d functions. The atomic positions

were optimized using the conjugate gradient minimization method. Both the SCF and ionic relaxation convergence thresholds were set to 10^{-4} eV. For the CO_2-SWNT calculations, two irreducible k-points generated by the Monkhorst-Pack method from a 1×1×3 grid, were used in the k-space sampling *(348)*. Three different periodic geometries were considered. In the first case, adsorption of CO_2 on an isolated (10,10) carbon nanotube was modeled by placing a CO_2 molecule and a (10,10) SWNT in a hexagonal periodic cell with lattice parameters $a = b = 22$ Å and $c = 7.3$ Å, where the c axis is parallel to nanotube axis. This c axis corresponds to 3 primitive unit cells of a (10,10) SWNT. Carbon dioxide was placed at various starting positions inside and outside of the nanotube and the position of the CO_2 molecule was optimized holding the nanotube coordinates fixed. Eleven different adsorption configurations were identified for the CO_2 molecule adsorbing on the internal and external nanotube surfaces. These adsorption geometries are summarized in Figure 36. In the second case, CO_2 adsorbed in groove site of a SWNT bundle was modeled by using an orthogonal cell, with $a = 16.3$ Å, $b = 24.3$ Å, and $c = 7.3$ Å. In the third case a perfect SWNT array was modeled using a hexagonal cell, with the tube-tube distance optimized both with and without CO_2 in the interstitial sites. The optimized parameters are $a = b = 16.6$ Å for the pure tubes, and $a = b = 16.7$ Å for tubes with interstitial CO_2. The effect of adsorbate-adsorbate interactions was studied in all three types of geometries by performing additional calculations in a supercell consisting of 5 primitive unit cells of the (10,10) SWNT. The corresponding lattice parameter is $c = 12.2$ Å for this case. Both adsorption energies and CO_2 vibrational frequencies were computed for both the 3 and 5 unit cell cases for all the lying down geometries, configurations **1-7** in Figure 36, and also the groove and interstitial sites. Γ point integration was used to reduce computational cost of the vibrational

frequency calculations for the larger supercells. Test calculations showed that frequencies were virtually identical from the Γ point and 1×1×3 k-point grid calculations in the large supercell.

The CO_2 vibrational frequencies were calculated by using the direct force constant approach *(290)*. The Pulay-corrected Hellmann-Feynman forces of the optimized and distorted geometries were calculated from VASP. In a distorted structure, the atomic displacement was set to 0.02 Å in *x*-, *y*-, and *z*-directions. The dynamical matrix was only constructed for the CO_2 molecule in order to reduce the computational cost. The frequency shifts were computed by subtracting the frequency of an isolated CO_2 molecule from the frequency of the adsorbed CO_2 molecule, where both calculations were performed in the same size supercell, using the same energy cutoff, and the same k-point grid. Structural and vibrational parameters of gas phase CO_2 were also calculated from LDA using the Gaussian 98 package *(252)* for comparison.

IV-4. Experimental section

A transmission infrared cell *(244)* was connected to a stainless steel vacuum system equipped with a 60 l/s turbomolecular pump and a 20 l/s ion pump. The base pressure was ~ 10^{-7} Torr, and the pressure was measured with an ionization gauge or with a capacitance manometer with a combined range of 10^{-9}-10^{3} Torr. Gaseous CO_2 was admitted to the cell and condensed on the reentrant Dewar at 90 K (ℓ-O_2) used to cool the sample. The upper CO_2 equilibrium pressure was 3×10^{-5} Torr.

Single walled carbon nanotubes, produced by laser vaporization, were obtained from Professor R. Smalley's laboratory (Rice University) after purification and cutting by oxidizing acid treatment and suspension in dimethylformamide (DMF). *(250)* It was shown that this technique produces SWNTs with a diameter distribution centered near that for (10,10) tubes at 13.6 Å. The most probable length of these tubes is 3200 Å, and the purity was reported to be

>90% *(47, 349)*. The SWNTs were deposited onto CaF_2 spots hydraulically pressed into a high transparency tungsten grid by dropping a known volume of the SWNT-DMF suspension onto the CaF_2 support and evaporating the solvent at 120ºC. Two different SWNT samples were studied in this work; the masses of the samples were 19 and 36 μg.

The grid was clamped with a Ni clamp, which conducted electrical power for heating as well as conducting heat away to the support Dewar. Programmed grid heating could be carried out using LabView software over the range 100 – 1500 K, with an accuracy of about 0.2 K, using a type K thermocouple for temperature measurement of the grid. CO_2 (Valley National Gases—99.25%) and Xe (Matheson—99.995%) were used without further purification.

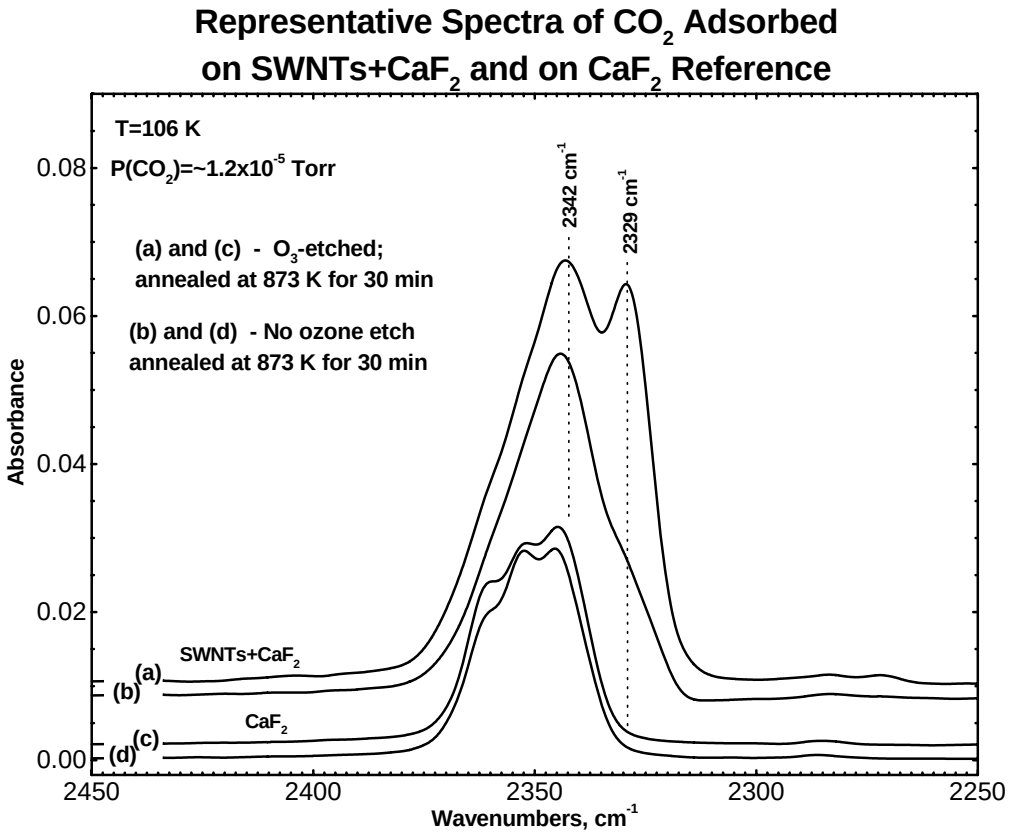

Figure 37. Infrared spectra of CO_2 adsorbed on etched and unetched SWNTs deposited on CaF_2.

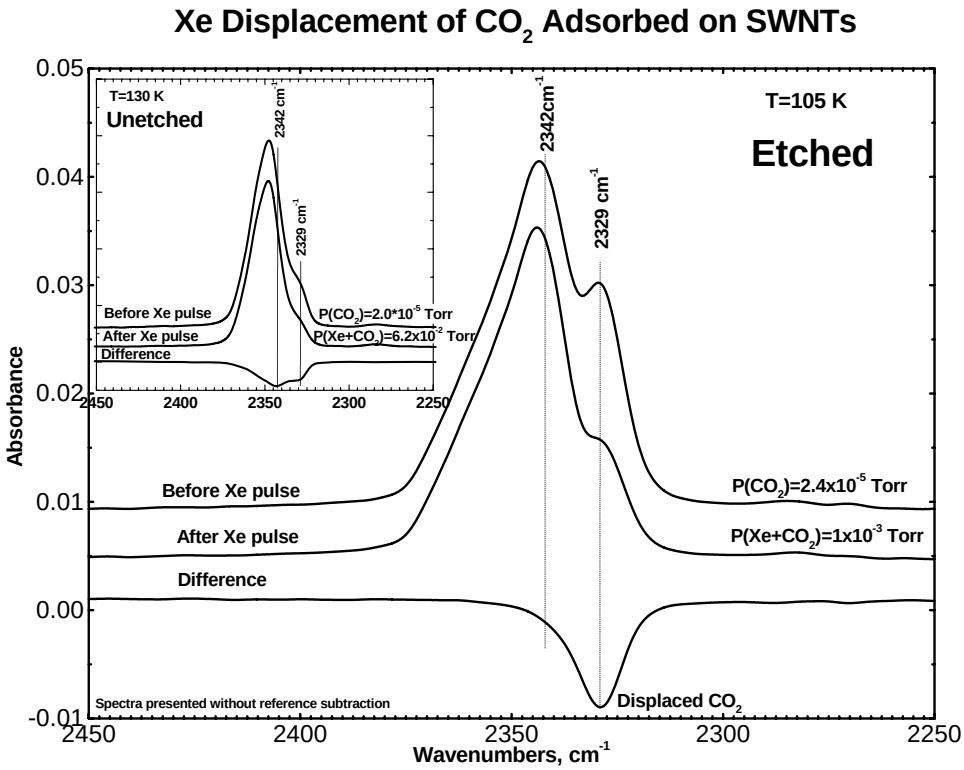

Figure 38. Xe displacement of from SWNT samples at low Xe partial pressure (inset – experiment on unetched SWNT sample at high partial pressures of Xe).

The SWNT sample was evacuated at 10^{-7} Torr pressure. IR spectra were measured with a Mattson Research Series FTIR spectrometer using a wide band MCT detector using 500 - 2000 scans. The spectral resolution was 4 cm^{-1}. Spectra taken on the deposited SWNT sample (not shown) have IR bands indicating the presence of carbon-oxygen functionalities (major bands at 1740, 1680, and 1250 cm^{-1}). These bands almost entirely disappear after annealing the SWNTs to 873 K as reported previously, *(243)* indicating the removal of the C-O functionalities. A well-known nanotube phonon mode at 1580 cm^{-1} is revealed after removal of the C-O functionalities. Ozone treatment, followed by annealing in vacuum, has been shown to result in opening the sidewall and end regions giving more facile entry of adsorbates into the nanotube interior *(157)*.

In the experiments shown here the SWNTs were ozonized to different levels. The IR spectra shown in Figure 37 and Figure 38 were measured on the 19 μg sample after three ozonation/annealing cycles involving 16.8, 17.7 and 32.5 Torr O_3 with 10 minute treatments at 303 K.

IV-5. Results and Discussion

IV-5A. Theoretical Studies

a. Structural and Vibrational Properties of CO_2

The structural properties and vibrational spectra of gaseous CO_2 were determined at the LDA level of theory in VASP. These parameters are compared with LSDA results computed from Gaussian type basis sets in Gaussian 98. As shown in Table 6, the structural parameters are sensitive to the size of the basis set (Gaussian) or energy cutoff (planewave). The C-O bond length calculated from the 6-311G(d) basis set is closer to the experimental value than that calculated from the 6-31G(d) basis set. Comparing the results from the 6-311G(d) and 6-311G(2d,p) calculations indicates that the addition of polarization functions does not affect the C-O bond length. As can be seen from Table 6, the C-O distance computed from LDA/II is 1.165 Å, which is only 0.4% longer than the experimental value. This prediction is very close to the LSDA/6-311G(2d,p) value. The C-O distance computed from LDA/I is 5.4% longer than the known value.

We now examine the gas phase vibrational spectra of CO_2 as computed from VASP and Gaussian98. Since the harmonic frequency is a second-order response property that can be affected by unoccupied states, the calculated asymmetric mode stretching frequency is sensitive to the presence of polarization functions. The frequency is found to decrease by 19 cm^{-1} when additional (d,p) functions were added to the basis set (see Table 6). LDA-DFT using the larger

energy cutoff, LDA/II, gives an asymmetric mode stretching frequency of 2409.0 cm^{-1}, which is closest of any of the calculated values to the experimental value of 2349 cm^{-1}. The frequency computed from LDA/I is substantially too high at 2424.6 cm^{-1}. LDA/II is also more accurate than LDA/I for the symmetric stretching and the bending frequencies. We use the LDA/II energy cutoff in the following calculations based on the good agreement between LDA/II and experiments for both geometries and frequencies.

Table 6. Optimized structural parameters and vibrational frequencies of CO_2.

	C-O distance (Å)	Sym. str.	Bend	Antisym. Str.
LSDA/6-31G(d)	1.171	1359.4	624.5	2459.0
LSDA/6-311G(d)	1.162	1364.6	650.9	2461.0
LSDA/6-311G(2d,p)	1.162	1355.7	655.7	2442.0
LDA/I [a]	1.223	1306.5	568.9	2424.6
LDA/II [b]	1.165	1327.1	647.8	2409.0
Expt.[c]	1.1600	1333	667	2349

[a] Planewave calculation with cutoff energy = 269.9 eV;
[b] Planewave calculation with cutoff energy = 395.7 eV;
[c] Ref [CRC Handbook of Chemistry and Physics (3rd Electronic Ed.)]

b. CO_2 on a Graphene Layer: Energetic and Vibrational Properties

In order to test the accuracy of our LDA-DFT approach, we have modeled the zero coverage (low pressure) limit adsorption of CO_2 on graphite by computing the adsorption of CO_2 on a single graphene sheet. The supercell contained 50 C atoms; the dimensions were $a = b =$ 12.2 Å and c=16 Å, where the c direction is perpendicular to the graphene plane. The k-point mesh was 2×2×1. The binding energy and vibrational frequencies were computed for CO_2 adsorbed on the surface, for configurations both parallel and normal to the graphene surface. It is well known that the dispersion interaction for CO_2 parallel to the surface (lying down) is substantially larger than that for CO_2 normal to the surface, because the former configuration has a much larger contact area between CO_2 and the graphene surface. The calculated binding energies are -3.4 kcal/mol for lying-down CO_2 and -1.4 kcal/mol for CO_2 normal to the surface.

The energy of the lying down configuration is in good agreement with the previously computed DFT value *(307)* and the experimental value of -4.1 kcal/mol *(350)*. We have also used gradient corrected (GGA) DFT with the PW91 functional *(312)* to compute the lying down configuration of CO_2 on a graphene sheet. The adsorption energy from GGA-DFT is only -0.7 kcal/mol. The accuracy of several different GGA functionals for rare-gas dimers has been evaluated by other groups *(297-299)*. The GGA functional was found to have a profound impact on the calculated binding energies, but the overall trend is that these methods underbind. This is certainly the case for our GGA-DFT calculations of the CO_2-graphite system.

The vibrational frequency of the CO_2 asymmetric stretching mode for CO_2 adsorbed on a graphene surface was calculated to be 2393 cm^{-1}. In order to compute a frequency shift for the adsorbed CO_2 we computed the frequency of CO_2 in the same supercell, using the same energy cutoff and k-point grid, but without the graphene sheet. This gave a vibrational frequency of 2402 cm^{-1}. Note that the gas phase frequency reported in Table 6 is 2409 cm^{-1}. The difference between these two values is due to the use of different supercells and k-point meshes. The calculated shift between gas phase and CO_2 adsorbed on the graphene surface is -9 cm^{-1} and agrees well with the experimentally measured shift of -8 cm^{-1} (from 2349 cm^{-1} in the gas phase to 2341 cm^{-1} for CO_2 on graphite) *(351)*. Note that the frequency shift is in better agreement with experiment than the absolute frequencies, since subtraction of the frequencies results in some cancellation of errors.

Given that the adsorption energy and frequency shift for CO_2 on a graphene surface matches the experimental data with reasonable accuracy, we expect that CO_2-nanotube calculations to be similarly accurate. The main difference between these two forms of carbon is that the curvature and periodicity of the nanotube will affect the electronic distribution and the

polarizability of the nanotube, which in turn will modify the CO_2-nanotube interactions. The LDA-DFT method is able to account for the electronic effects in an accurate way, giving qualitatively reasonable adsorption energies and vibrational frequencies.

IV-5B. Adsorption Energies of CO_2 on Nanotube Surfaces

Ozone treatment and thermal annealing are known to generate entry ports to the interior of the nanotubes *(46, 47, 156, 157, 191)*. It is therefore necessary to consider internal adsorption sites in our calculations. Eleven different CO_2 orientations were considered for adsorption on the interior and exterior of a nanotube. These are shown in Figure 36. The optimized parameters are given in the supporting information.

a. CO_2 on the Exterior and Interior of a Nanotube

The adsorption energies of CO_2 on the external and internal surfaces of a (10,10) SWNT are given in Table 7. For the lying down configurations, the closest separation between CO_2 molecules in the adjacent cells (as in configuration **3**), is 5 Å for the supercell containing with 3 nanotube unit cells. This close proximity could result in substantial adsorbate-adsorbate interactions. Classical simulations indicate that end-on configurations are unlikely to occur due to unfavorable quadrupole-quadrupole interactions; pairs of CO_2 molecules are more likely to adopt T or slipped T configurations *(236)*. For configurations where the CO_2 axis is perpendicular to the nanotube surface, the CO_2-CO_2 interactions are expected to be much weaker. We have therefore calculated the binding energies and vibrational frequencies using a supercell containing 5 nanotube unit cells for all the lying down configurations (configurations **1**-**7** in Figure 36). The binding energies are very similar for both supercells (see Table 7), indicating that the 5 Å separation is sufficient for converging the adsorption energies to the low coverage limit.

Table 7. Adsorption energies for CO_2 on the interior and exterior of a (10,10) SWNT, in the groove site and in the interstitial site of a bundle of (10,10) SWNTs and on a graphene surface. The adsorption energy is defined by Eq. (4).

Strucutre	ΔE(kcal/mol)		ΔE(kcal/mol)	
	Interior[a]	Exterior[a]	Interior[b]	Exterior[b]
1	-4.0	-2.2	-3.9	-2.2
2	-3.6	-2.3	-3.5	-2.3
3	-3.8	-3.2	-3.9	-3.3
4	-3.4	-2.2	-3.5	-2.2
5	-4.1	-3.0	-4.0	-3.0
6	-3.6	-2.3	-3.6	-2.2
7	-3.6	-2.1	-3.5	-1.8
8	-1.7	-1.6	--	--
9	-1.8	-0.9	--	--
10	-1.7	-1.0	--	--
11	-1.8	-0.9	--	--
Groove	-5.0		-5.0	
Interstitial	-5.1		-5.1	
Graphene	-3.4			

[a] Supercell consisting of 3 SWNT primitive unit cells.
[b] Supercell consisting of 5 SWNT primitive unit cells.

The adsorption energy is larger for interior adsorption than on the exterior of the nanotube, as would be expected due to the curvature of the nanotube; the interior sites present more nearest-neighbor carbon atoms to an internally adsorbed CO_2 molecule than the exterior sites. Likewise, the adsorption energy of CO_2 on the interior of the nanotube is larger than on the graphene surface, which in turn is larger than on the exterior of the nanotube. The LDA calculations predict the correct trend in binding energy, notwithstanding the fact that DFT does not correctly describe van der Waals interactions. The largest binding energies are found for configurations where CO_2 is adsorbed lying down on the SWNT surfaces. The maximum values are -4.1, -3.4, and -3.2 kcal/mol for the nanotube interior, graphene surface, and nanotube exterior, respectively. The adsorption energies for CO_2 configurations normal to the nanotube surface are much smaller than for the lying-down configurations. For binding configurations **8**-

11 on the interior of the nanotube the adsorption energies for end-on CO_2 range from -1.7 to -1.8 kcal/mol. The adsorption energies for lying down CO_2 range from -3.4 to -4.1 kcal/mol. Note that configurations **10** and **11** are very similar. CO_2 is over a C-C bond center in both cases; the difference being the angle that the C-C bond makes with the nanotube axis, namely, 90° for **10** and 30° for **11**.

Among these 11 different orientations, the van der Waals interaction is largest for CO_2 centered above the C-C bond. In configurations **3** and **5**, the carbon atom of CO_2 lies above the C-C bond on the nanotube surface, which favors the quadrupole-quadrupole interactions, leading to slightly larger physisorption energies. The next largest interaction energy is for the carbon atom of CO_2 located above the center of a hexagonal carbon ring of the nanotube, as in configurations **4**, **6**, and **7**. The recent theoretical work by Cinke *et a. (343)* claimed that CO_2 has the lowest energy when it is located on top of the center of a hexagonal ring. We believe that their prediction is an artifact of using small cluster models.

We note that the long-range van der Waals interaction is underestimated by LDA-DFT, because the attraction falls off faster than the known r^{-6} limit. We therefore expect that the adsorption energies predicted here are underestimated because of effective neglect of interactions with atoms in neighboring nanotubes and farther away on the same nanotube.

b. CO_2 in the Groove and Interstitial Sites

As noted above, CO_2 adsorbed in the interstitial site caused an increase in the *a* and *b* lattice parameters for a perfect SWNT array of 0.1 Å. This small relaxation is similar to that predicted for H_2 adsorbed in a nanotube interstitial site, where a dilation effect only increased the *a* and *b* lattice parameters by 1% *(128, 129)*. This agreement is reasonable because H_2 and CO_2 have similar van der Waals radii when CO_2 is adsorbed with its molecular axis parallel to the

interstitial channel. The physisorption energy of CO_2 in the interstitial site is found to be -5.1 kcal/mol, which is larger than CO_2 on the nanotube interior at -4.1 kcal/mol. For CO_2 in the groove site, the physisorption energy is found to be -5.0 kcal/mol, which is comparable to that in the interstitial site. The binding energy of CO_2 in the groove site and interstitial sites are larger than those at the exterior and interior of nanotube walls because in the groove and interstitial sites, the CO_2 molecule interacts with two or more nanotube surfaces, which compensates the loss of binding energy due to the curvature. The groove site adsorption energy is larger than inside the nanotubes, consistent with model calculations for Ar, Kr, and Ne *(126)*. We note, however, that model calculations indicate that CO_2 will not adsorb in interstitial channels of perfect bundles *(236)*.

IV-5C. Vibrational Frequencies of Adsorbed CO_2

The vibrational frequencies of CO_2 adsorbed on the external and internal SWNT surfaces were calculated for all the structures listed in Figure 36. The frequency shifts for the asymmetric stretching mode were calculated relative to the computed gas phase value of 2409.0 cm^{-1} for the smaller supercell and 2408.4 cm^{-1} for the larger supercell; the results are listed in Table 8.

The effect of adsorbate-adsorbate interactions on the asymmetric stretching frequency can be seen by comparing the frequency shifts for a given CO_2 orientation in the smaller and larger supercells, also reported in Table 8. Under periodic boundary conditions the dynamic dipoles of CO_2 molecules in neighboring supercells are moving in phase and interacting with each other, which further softens the stretching mode. One would therefore expect that adsorbate-adsorbate coupling effects are more pronounced when the CO_2 axis makes a smaller angle with the nanotube axis (configurations **3**, **4**, **7**). This is true for configuration **3** on the nanotube exterior and interior; the adsorbate-adsorbate interactions soften the asymmetric

stretching mode by 3 cm^{-1} for CO_2 adsorbed on the external surface, and 2 cm^{-1}on the internal surface. The next largest effect is for configuration **7**, giving shifts of 1.5 and 2 cm^{-1} for external and internal adsorption, respectively. However, configuration 4, which like configuration **3** has CO_2 in an end-to-end configuration, does not show any adsorbate-adsorbate softening on the external surface, and a shift of only 1 cm^{-1} on the internal surface of the nanotube. The reason for this unexpected result is not clear. For the CO_2 axis transverse to the nanotube axis, the concentration effect is very small due to the larger CO_2 separation (7.3 Å). Also note that the electrostatic interaction between the dynamic dipoles is not as effective in the transverse direction as in the end-to-end direction. This can be observed for configurations **1** and **2**. We have not computed concentration effects for CO_2 adsorbed perpendicular to the nanotube surface because the effect is expected to be very small.

As can be seen from Table 8, CO_2 molecules adsorbed in different configurations have surprisingly large differences in their vibrational frequency shifts. Generally speaking, the magnitude of the shifts increase with increasing adsorption energy. CO_2 on the exterior or interior of nanotubes would be most likely to adsorb in the most energetically favorable sites. For configurations **8-11**, the CO_2 axis is normal to the nanotube surface and hence these configurations have smaller adsorption energies relative to lying-down configurations. The vibrational frequency shifts are also smaller for configurations **8-11**, ranging from about -4 cm^{-1} to -7 cm^{-1} for adsorption on the exterior of nanotube and ranging from about -1 cm^{-1} to -8 cm^{-1} for internal adsorption.

Table 8. Shifts in the asymmetric stretching mode frequency of adsorbed CO_2 relative to gaseous CO_2. Units are cm^{-1}.

Structure	Frequency shift [a]		Frequency shift [a]	
	Interior[b]	Exterior[b]	Interior[c]	Exterior[c]
1	-13.7	-12.3	-13.2	-12.0
2	-13.7	-8.9	-13.4	-8.7
3	-18.0	-17.9	-15.2	-15.6
4	-18.1	-13.3	-18.1	-12.3
5	-20.9	-14.6	-20.0	-13.5
6	-16.9	-11.9	-15.9	-11.4
7	-16.4	-13.3	-14.9	-11.2
8	-1.2	-6.6	--	--
9	-7.7	-4.0	--	--
10	-5.9	-4.5	--	--
11	-5.7	-4.5	--	--
Groove	-23.2		-22.2	
Interstitial	-26.8		-23.8	

[a] Frequency shift = Frequency (CO_2 on nanotube) – Frequency (gas phase CO_2).
[b] Supercell consisting of 3 SWNT primitive unit cells, with a calculated asymmetric mode stretching frequency of CO_2 (g) of 2409.0 cm^{-1} in the same supercell.
[c] Supercell consisting of 5 SWNT primitive unit cells, with a calculated asymmetric mode stretching frequency of CO_2 (g) of 2408.4 cm^{-1} in the same supercell.

The carbon atom in CO_2 for configurations **1**, **3** and **5** is located above the center of the C-C bond, while for configurations **2**, **6**, **7** and **8**, the CO_2 carbon lies above the center of a hexagon. As stated above, the binding energies are larger for CO_2 above the C-C bond and the shifts are also seen to be larger. For CO_2 adsorbed on the interior of a nanotube, configuration **5** has the largest magnitude adsorption energy at -4.0 (-4.1) kcal/mol in the larger (smaller) supercell. The calculated shift is -20.0 (20.9) cm^{-1} in the larger (smaller) supercell. Note that the adsorption energies for configurations **3** and **4** increase in magnitude with increasing supercell size. This is because the end-on CO_2-CO_2 interactions give unfavorable quadrupole-quadrupole interactions. When CO_2 is oriented at an angle with respect to the nanotube axis the quadrupole-quadrupole interaction is more favorable.

We have also calculated the vibrational frequency shifts for CO_2 in the groove and interstitial sites. In the groove site, a shift of -23.2 cm^{-1} is observed for the smaller supercell, while the larger supercell is shifted by 1 wavenumber less. A shift of -23.8 (-26.8) cm^{-1} was found for CO_2 in the interstitial site using the larger (smaller) supercell. The concentration effect on the shift is consistent with that seen for configuration **3**. The trend of the shifts computed from LDA-DFT is generally reasonable, with larger shifts corresponding to stronger binding with the nanotube surfaces.

In addition to the binding energies, the magnitude of the shifts may be affected by the polarizability at different adsorption sites. The CO_2 asymmetric stretching motion generates an instantaneous dipole, which induces an image dipole on the nanotube surface. The image dipole thus formed would generate a field interacting with the CO_2 molecule, leading to a redshift of the asymmetric stretching frequency. At the nanotube surface, the π-bonding is arranged parallel to a cylindrical shell, resulting in a larger image dipole for CO_2 adsorbed with its axis parallel to the surface. CO_2 adsorbed normal to the surface will result in a relatively smaller image dipole, giving rise to smaller redshifts. The calculated frequency shifts are consistent with this simple picture of frequency shifting (see Table 8).

In an attempt to compare our calculated frequency shift with experimental data we have computed a simple Boltzmann average of the vibrational frequency shifts according to

$$\left\langle \Delta\nu \right\rangle_B = \frac{\sum_i \exp\left(\frac{-E_i}{kT}\right)\Delta\nu_i}{\sum_i \exp\left(\frac{-E_i}{kT}\right)} \qquad (2)$$

where $\left\langle \Delta\nu \right\rangle_B$ is the Boltzmann average of the vibrational frequency shift, E_i and $\Delta\nu_i$ are the adsorption energy and the vibrational frequency shift of the *i*-th configuration, *k* is the

Boltzmann constant, and T is the absolute temperature. Considering only the lying down configurations and using the results from the larger supercells, the Boltzmann average shift for CO_2 inside the nanotube is -17 cm^{-1} at 100 K. For CO_2 on the exterior of nanotube, the Boltzmann average shift is -15 cm^{-1}. The Boltzmann averages of the shifts on the interior and exterior are very similar. This is probably due to errors in the calculated adsorption energies and frequency shifts, coupled with an incomplete basis set of adsorption sites. Note that a small error in the adsorption energy could result in a large error in the calculated value of $\langle \Delta \nu \rangle_B$. If we instead consider only the two largest shifts for internal and external adsorption, we compute average shifts of -19 and -14 cm^{-1}, for internal and external adsorption, respectively. Note that the shift for groove site adsorption is very similar to that for internal adsorption. Hence, the calculations roughly indicate a shift of about -20 cm^{-1} for both groove site and internal adsorption and a slightly smaller shift of about -15 cm^{-1} for adsorption of CO_2 on the external surface of the nanotube.

IV-5D. Experimental Results

Figure 37 is a plot of representative spectra of CO_2 adsorbed on the SWNTs and the CaF_2 support [spectra (a) and (b)] and on the bare CaF_2 reference [spectra (c) and (d)]. Spectra (b) and (d) are typical for the unetched sample and reference, whereas the (a) and (c) sets were measured after ozonolysis followed by thermal treatment. The enhancement of the intensity at 2329 cm^{-1} is the only noticeable change in the spectra after ozonolysis of the SWNTs and CaF_2; the reference spectra are virtually unchanged. The enhancement in absorbance for the ozonized tubes points to the large increase of the adsorption site capacity associated with the 2329 cm^{-1} mode. According to previous studies O_3 treatment followed by annealing at the elevated temperatures (called etching) opens entry ports in nanotube walls, making internal adsorption possible *(46, 157)*. On

this basis and according to the xenon displacement experiment (discussed later) the band at 2329 cm^{-1} may be assigned to CO_2 adsorbed inside nanotubes. The large redshift also corroborates the assignment since a CO_2 molecule inside the nanotubes experiences strong interaction with the nanotube wall. The modeling also indicates that CO_2 inside a SWNT has a higher redshift than CO_2 adsorbed on the external surface.

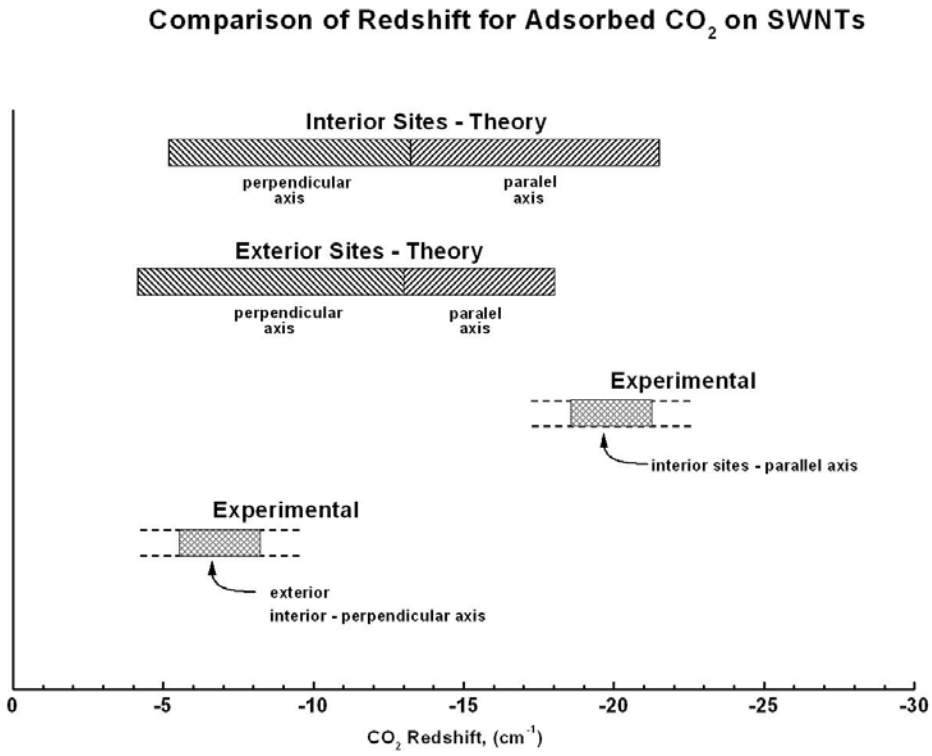

Figure 39. Comparison of the experimental and theoretical results for the adsorption of CO_2 in SWNTs.

By comparison of the spectra for CO_2 adsorption on the nanotubes plus the CaF_2 support (Figure 37, spectra a and b) with the spectra for CO_2 on the CaF_2 support alone (spectra c and d), we observe that the CaF_2 reference spectra cannot be simply subtracted from the SWNT + CaF_2 spectra. This may be due to blocking of CaF_2 sites by the nanotubes or to differences in the thickness of the CaF_2 support spots. Despite this limitation, spectral features due to CO_2 adsorption on the SWNTs may readily be seen at ~ 2329 cm^{-1} and ~ 2342 cm^{-1}.

It is known that Xe readily displaces species adsorbed in the nanotube interior under certain conditions *(191)*. Figure 38 shows the displacement of CO_2 by Xe for the etched sample at low Xe partial pressure. The band at 2329 cm^{-1} exhibits the largest decrease in absorbance after the introduction of Xe, with a smaller decrease also visible near the 2342 cm^{-1} band. At these conditions, Xe may preferentially occupy the nanotube interior displacing CO_2 *(191)*. The Xe displacement test confirms the assignment of the 2329 cm^{-1} band as being due to the CO_2 adsorbed in the nanotube interior. At higher Xe partial pressures the band at 2342 cm^{-1} reveals diminished intensity in addition to the band at 2329 cm^{-1}. This effect is observed for etched as well as unetched samples; an example of an unetched SWNT sample is shown in the inset to Figure 38. A relatively small redshift of the 2342 cm^{-1} band points to a less-strong CO_2 molecule–nanotube interaction. According to Fastow *(351)* CO_2 adsorbed on graphite exhibits a mode at 2341 cm^{-1}. The agreement in frequency may be fortuitous and should not be considered as a basis for identifying graphite in the SWNT sample.

IV-6. Comparison of Theoretical and Experimental Results

Figure 39 summarizes the theoretical and experimental measurements of the redshift for the asymmetric stretching mode of CO_2 adsorbed on various sites on the SWNT bundles investigated in these studies. Generally speaking, both theory and experiment indicate that CO_2 adsorbed inside a SWNT exhibits larger redshifts than CO_2 adsorbed on the external surface. Interstitial sites give even larger redshifts, but the LDA-DFT calculations of adsorption in the interstitial sites may be due to overbinding, as classical simulations indicate that fairly large interstitial sites, due to packing defects, are required to adsorb CO_2 and other molecules of comparable size *(151, 236)*. We therefore do not consider the interstitially bound CO_2 to be important in comparing with experiments. The experimental results detect two classes of CO_2

molecules with shifts of -20 cm^{-1} and -7 cm^{-1}. We believe, on the basis of the Xe displacement experiments as well on the magnitude of the redshift that the 2329 cm^{-1} band (shift = -20 cm^{-1}) is due to internally-bound CO_2. Its relatively high binding energy suggests that these sites will be densely filled with CO_2 at equilibrium and extensive Xe displacement will occur from the filled interior sites according to statistical modeling carried out previously for another molecule adsorbed in the interior of SWNTs *(191)*. The 2342 cm^{-1} band (shift = -7 cm^{-1}) is less easy to assign; it could be indicative of an externally-bound or an internally-bound standing-up CO_2 molecule or a CO_2 molecule bound in a parallel configuration on an external site as shown in Figure 36, configuration **2**.

The main discrepancy between the experimental and simulation results is that experiments indicate that the average shift of all external sites, including groove sites is on the order of -10 cm^{-1}, whereas LDA-DFT calculations predict a shift of about -22 cm^{-1} for groove site adsorption. Matranga et al. also assigned a roughly -10 cm^{-1} shift to groove site adsorption *(236)*. Note that CO_2 near full coverage does not appear to adsorb parallel to the groove site, but is expected to adopt a T-shaped configuration *(236)*. Therefore, the end-to-end configurations considered in the LDA-DFT calculations performed here may not represent the actual situation very well. Hence, the groove site shifts could be substantially overestimated in our LDA-DFT calculations.

IV-7. Summary

We have shown from first principles calculations that the frequency shift of the asymmetric stretch mode of CO_2 adsorbed on SWNTs is due to a combination of three factors: (1) the static binding energy with SWNT surface; (2) the creation of an induced dipole on the SWNT in response to the dynamic dipole of CO_2; and (3) adsorbate-adsorbate interactions. The

adsorption energies and frequency shifts are sensitive functions of the orientation of the CO_2 molecule relative to the surface of the SWNT. CO_2 adsorbed parallel to the surface of the nanotube exhibits much larger adsorption energies and frequency shifts compared with CO_2 adsorbed with its axis perpendicular to the surface. We further note that the registry of the CO_2 molecule with the SWNT surface is important. Configurations with the C atom of CO_2 over the bond-center of a C-C bond in a nanotube give larger adsorption energies and larger frequency shifts compared with configurations where the C atom of CO_2 is over a hexagon center. The binding energies and to some extent the frequency shifts are affected by quadrupole-quadrupole interactions from CO_2 molecules in the periodic cells. End-to-end periodic arrangements of CO_2 generally give increased adsorption energies with increasing supercell size. The opposite is true for configurations that are similar to the slipped-parallel configuration, that is known to be the ground state of the gas phase CO_2 dimer.

Experimental IR spectra reveal two broad asymmetric mode features for CO_2 adsorbed on opened nanotubes. One peak center corresponds to a shift of -20 cm^{-1} and the other with a shift of about -7 cm^{-1} from the gas phase frequency. There is general agreement between calculations and experiment that the -20 cm^{-1} shift is due to CO_2 adsorbed inside the nanotube. Xe displacement experiments and O_3 etching experiments are consistent with this interpretation. On the other hand, the smaller redshift observed in experiments is more difficult to assign, but is probably due to adsorption on the external surface and perhaps also to CO_2 adsorbed in less favorable configurations, such as perpendicular to the surface.

IV-8. Acknowledgements

We gratefully acknowledge the Army Research Office for the support of this work, as well as Dr. Chris Karwacki at the Aberdeen Proving Ground. Computations were performed at

the Center for Molecular and Materials Simulations at the University of Pittsburgh and at the US Army Research Laboratory Major Shared Resource Center through a Department of Defense High Performance Computing challenge grant.

V. WATER CONFINEMENT IN SWNTS[*]

V-1. Abstract

We present the first experimental vibrational spectroscopy study providing direct evidence of a water phase inside single wall carbon nanotubes that exhibits an unusual form of hydrogen bonding due to confinement. Water adopts a stacked-ring structure inside nanotubes, forming intra- and inter-ring hydrogen bonds. The intra-ring hydrogen bonds are bulk-like while the inter-ring hydrogen bonds are relatively weak, having a distorted geometry that gives rise to a distinct O-H stretching mode. The experimentally observed infrared mode at 3507 cm^{-1} is assigned to vibrations of the inter-ring OH-groups based on detailed atomic-level modeling.

[*] Reproduced in part with permission from the Journal of American Chemical Society, submitted for publication. Unpublished work copyright 2005 American Chemical Society. The theoretical part of his work was performed by Dr. Wai-Leung Yim, Dr. Jinchen Liu and Dr. J. Karl Johnson and is included here for completeness.

V-2. Introduction

Confined matter on the nanometer scale differs significantly from bulk matter *(232)*. Widespread interest exists in the structure of confined water *(127, 209, 352-356)*, in its degree of hydrogen bonding *(219, 354, 357)*, and in proton transfer through "water wires" *(358, 359)*. The special properties of confined water can influence molecular transport inside membrane pores *(360, 361)*. Water transport through molecular size pores is a very active research field where the nanotube can offer a new insight. Hummer at al. *(352, 359, 362-364)* investigated water transport through narrow pores of (6,6) carbon nanotubes by means of MD simulations. They have shown that water molecules enter and empty the nanotube interior in a concerted manner so at any time the nanotube is filled with a single chain of H_2O molecules. The transport though the nanotube is stochastic but the participating water molecules exhibit strong co-orientation with single side attachment to the bulk phase. Fragmented water chains in the nanotube interior are rare since hydrogen bond rupture is energetically unfavorable. In general the single file transport of water molecules is governed by hydrogen bonds between the chained water molecules. Similar results also have been reported by others *(358, 365)*.

Adsorption of water into the nanotube interior is an intriguing problem because the nanotube interior similarly to any carbon material should exhibit hydrophobic properties but on the other hand nanotube interior can provide deeper potential well for adsorbed species due to higher coordination to the concave walls. Early experimental studies of Dujargin at al. *(199)* indicate that any substance with surface tension less than 200 mN/m can be drawn into the inner capillary of nanotubes, i.e. water is expected to be adsorbed into a nanotube. Recent microscopy investigations clearly show that the internal nanotube walls are wettable by liquid water *(200, 201)*. However these studies were carried out on large diameter (2-5 nm) nanotubes where the

confinement effects probably are not as strongly pronounced as in the case of nanotubes with the pore diameter around 1 nm.

In a series of publications Koga et al. *(127, 202-205)* have reported the results of *ab initio* and molecular dynamics simulation of water confinement in single wall carbon nanotubes less than 2 nm in diameter. The MD calculations indicate that at temperatures below ~280 K and pressures above 50 MPa the confined H_2O forms n-gonal structures formed of stacked rings. The rings are formed of n number of water molecules that depends on the nanotube diameter, e.g. the square ring structures (n = 4) are found in (13,0) and (14,0) nanotubes and pentagonal, hexagonal and heptagonal rings (n = 5, 6 and 7) are characteristic for (15,0), (16,0) and (17,0) tubes *(127, 203)*. Each water molecule (except those in the edge rings) in these phases is four coordinated, i.e. satisfies the "bulk ice rule". The *ab initio* calculations of these authors show that among all possible arrangements of n-gonal structures the most stable are those with collateral orientation OH bonds in the columns and alternative orientation of columns relative to each other *(202)*. This forces circular orientation of OH groups within the ring plane to alternate as well producing an ABAB stacked ring geometry. Theoretical predictions indicate that in the pentagonal water structure the axial (inter-ring) hydrogen bond should be weaker than the in-plane (intra-ring) hydrogen bond. This prediction is based on density functional theory calculations of the effective charges on the atoms and on calculated charge densities. In the case of the hexagonal structure more types of hydrogen bonds were found with strengths that fill the range of those observed for the pentagonal structure. The offered explanation states that water molecules are more distorted from the bulk tetrahedral arrangement when in the hexagonal rather than in the pentagonal structure. This also results in lower stability of smaller H_2O hexagonal clusters relative to their

pentagonal counterparts; however the difference vanishes in the case of infinitively long structures *(204)*.

It was shown that as the temperature increase or the pressure drops, the n-gonal formations melt with a discontinuous change in water volume and in potential energy per molecule in the case of hexagonal and heptagonal structures signifying the first order phase transition, and with a continuous transformation from solid-like to liquid-like states in the case of pentagonal and square structures. The occurrence of the first order phase transition for wider nanotubes was explained in terms of the abrupt symmetry change with temperature and is related to filling of the center of the nanotube interior (axial phase formation) at higher temperatures whereas smaller tubes do not allow formation of the axial phase.

The predictions of n-gonal water structures have been confirmed by X-ray studies by Maniva at al. *(206, 207)*. In the most recent study the authors carried out an experiment with nanotubes of different average diameters. They observed peak developments in the diffractograms at lower temperatures that were assigned to solid water inside nanotubes. These peaks appear as a result of crystallization of liquid water into stacked ring structures. The inverse dependence of the liquid-solid transition temperature on the nanotube diameter followed the theoretical predictions as well *(127)*.

NMR studies of Ghosh et al. *(208)* show that water solidifies inside nanotube interior below 235 K. Since the relaxation time of ice is larger than that of liquid water only non-frozen water can be monitored by NMR spectroscopy. The authors observed two features in the spectra that were assigned to liquid water confined in the nanotube interior. The assignment was based of the assumption that water interacts with groove sites and the external surface similarly to plane graphite and no suppression of the melting point was observed for water adsorbed on the

surface of graphite. The two peaks were proposed to originate from the liquid "axial" and "shell" phases of water confined in the nanotube interior. The liquid-solid transition proceeds through the disappearance of the liquid "axial phase" first followed by crystallization of the "shell phase".

Recently Kolesnikov at al. *(209)* have presented a theoretical (MD) and experimental neutron diffraction and inelastic neutron scattering (INS) studies of H_2O confinement in ~14±1 Å SWNTs. The nanotube interior filling with water was carried out through the exposure of SWNTs to H_2O at 110°C, pumping out the excess of water at +45°C and cooling the sample to 10 K. The author assumed that upon reaching the 11.3% H_2O/SWNTs mass ratio only the nanotube interior was filled with water. From INS data vibrational spectra were obtained which show a shift of the OH stretching mode of the confined water to higher frequencies relative to bulk ice. This shift was attributed to weakening of the hydrogen bonds due to formation of n-gonal H_2O structures inside nanotubes as predicted by Koga et al. *(127)*. In addition the authors have suggested that water can form the "axial phase" at low temperatures as well.

Molecular dynamic computations by Marti & Gordillo *(210-221)* for liquid water confined in carbon nanotubes at 298 K or higher and density of 1 g/cm^3 indicate that the average number of hydrogen bonds is lower for the confined water relative to the bulk phase. The average number of H-bond drops with nanotube diameter decrease For instance, the average values of H-bonds for water structures in (12,12), (10,10), (8,8) and (6,6) tubes are 3.0, 2.9, 2.8 and 1.8 respectively whereas the correspondent value for bulk water is 3.7 *(219)*. It was also shown that the smallest (6,6) nanotube can furnish only a single chain of water molecules, a (8,8) nanotube is able to accommodate two H_2O molecules in the plane perpendicular to the tube axis, and a (10,10) nanotube is wide enough for development of the "axial phase". The analysis of the

transverse distribution of hydrogen bonds show that the percentage of H-bonds drops near the wall of nanotube because of the impossibility of finding an H_2O molecule in that direction. The authors also obtained infrared spectra of confined water in the mentioned nanotubes. The most important feature was a peak observed between 3640 and 3690 cm^{-1} *(213)*. It was assigned to the antisymmetric component of the bulk stretching frequency which appears due to ~20% of OH groups not participating in the hydrogen-bond network. The frequency of this vibration approaches the bulk value for larger diameter nanotubes and its intensity becomes dominant for the smallest tube. Theoretical comparison of the properties of water confined in carbon nanotubes and in corresponding diameter structureless tubes points to the absence of influence of nanotube wall atomicity. Therefore the nature of the confinement effect is solely geometric in the case of water.

Adsorption of water at room temperature was investigated by Ellison et al. *(222)* by means of IR spectroscopy. It was shown that water adsorbs in the carbon nanotube interior in a state similar to that of the bulk with extensive hydrogen bonding which is in contrast to the predictions by Marti & Gordillo *(220)*. The conclusion about the internal adsorption was based on 1) the fact that water was retained in the studied nanotube sample for a few days, and 2) on the similarity of the room temperature IR spectra with the 9 K INS spectra in the work of Kolesnikov et al. *(209)*. The authors also indicated that a small percentage of water reacts with the nanotubes producing C-O and C-H groups, however, in the latter case no C-H stretches were observed.

Overall it seems that there is a general agreement that water can enter the hydrophobic nanotube interior. The confined H_2O exhibits a depressed melting point as a result of confinement but retains all its properties related to formation of hydrogen-bond networks. The

liquid phase of the confined water is similar to the bulk but the crystalline phase strongly deviates due to formation of stacked ring structures. A number of workers indicated that the hydrogen bonds in the confined water are weaker than those in the bulk. However to best of our knowledge there was no direct study of frozen water structures confined in the nanotube interior. Water adsorbed in the nanotube interior can form very long chains due to the tubular character of carbon nanotubes. In this sense water confined inside nanotubes can be considered as an intermediate between small water clusters and bulk water, both immensely studied. Hydrogen bond strength, orientation and its influence on the overall stability is the core problem in many studies.

Here we review some of the most relevant works related to vibrational spectroscopy of the water clusters. An individual H_2O molecule exhibits two OH stretching modes in the gas phase: symmetric at 3655 cm^{-1} and asymmetric at 3756 cm^{-1}. These modes experience strong shifts when involved in hydrogen bonding and analysis of the new modes provides one of the most insightful means for their characterization *(366)*. Formation of water clusters is driven by the entropy drop of the whole system due to the formation of hydrogen bonds. In bulk ice each water molecule is tetrahedrally coordinated, simultaneously donating and accepting two hydrogen atoms into the network. However, this arrangement is not possible for water agglomerates of finite sizes and therefore is the reason for a variety of shapes for small water clusters which reflects on the vibrational spectra in the OH stretching mode. Thus Zwier et al. *(367)* have shown that 8 water molecules cluster into a cube as predicted previously by Jordan's group *(368)*. Three types of OH vibrations were detected: "free OH" vibration at 3713 cm^{-1}, OH stretching mode that belongs to double H-atom donor-single acceptor in the ~3450 – 3550 cm^{-1} region and the OH stretching mode of single donor-double acceptor in the 3050 – 3200 cm^{-1}

region. This study is also in accord with their previous studies of smaller water clusters *(369, 370)* as well as with other computations *(371)*.

Vibrational spectroscopy studies of large water clusters of known size (20-2000 average number of water molecules) as been done by Anderson et al. *(372)*. Similarly to the studies of small water clusters the authors observed three main area of vibrational activity regardless of the mean cluster size. The vibrations of "free" OH groups, double donor-single acceptor, and single donor-double acceptor were observed at 3718 cm^{-1}, 3550 cm^{-1} and 3200 cm^{-1} respectively. A band at 3400 cm^{-1} that shifts to lower frequencies with increasing cluster size and temperature was attributed to 4-coordinated water molecules.

Devlin et al. *(373-375)* have conducted a systematic research of the vibrational properties of the surface of solid water. It was found that upon condensation from the gas phase amorphous water forms. This phase can be characterized by dangling from the surface "free" OH-groups that belong to double donor-single acceptor water molecules and can are observed at 3693/3100 cm^{-1} (symmetric/asymmetric modes, the assignment disagrees with most theoretical and experimental works as well as with vibrations of individual molecules and probably should be reversed). This mode disappears upon annealing that leads to bulk crystallization and surface rearrangement to maximize the number of hydrogen bonds. Thus even though the water molecules in the bulk may have the ideal tetrahedral coordination, the surface of such crystals is disordered. The authors also reported vibrations of double donor-single acceptor at 3560/3330 cm^{-1} and vibration of double donor-double acceptor in the second layer at 3440/3240 cm^{-1} *(376)*.

Experimental vibrational spectroscopy studies of 4-coordinated or double donor-double acceptor water molecules with distorted hydrogen bonds is complicated due to the much greater similarity of these species to the bulk molecules. In this instance theoretical simulations are

especially helpful. Lee et al. *(377)* performed *ab initio* computation of clusters of 12 water molecules and found that 4- and 6-membered stacked ring structures are the most stable. Furthermore they carried out calculations of the vibrational spectra of these clusters and obtained frequency shifts for double donor double acceptor water molecules with respect to the frequencies of a free water molecule. The shifts range within 262-269 cm^{-1} and 310-443 cm^{-1} for asymmetric and symmetric stretching modes. Correspondingly, these modes should be observed in the 3494-3487 cm^{-1} and 3345-3212 cm^{-1} ranges in the experimental spectra. Similarly, Fanourgakis et al. *(378)* have reported simulations of IR spectra of $(H_2O)_{20}$ clusters. As in the previous case, the 4- and 5-membered stacked ring structures were found to be among the most stable clusters. However, this calculation predicted the frequency of the asymmetric vibration of 4-coordinated water molecules to be at ~3317 cm^{-1}.

In relation to water confinement in the nanotube interior the information on vibrations of 4-coordinated water molecules is very important. When adsorbed inside nanotubes at low temperatures water forms extremely long n-gonal structures and therefore all molecules may be considered 4-coordinated and identical to each other. Bai et al. *(204)* predicted that stacked pentagonal ring structures have two non-equivalent hydrogen atoms. This may lead to two different hydrogen bonds which can be detected by means of IR spectroscopy.

To-date there has not been any direct experimental confirmation of the predicted weaker hydrogen bonds. In this work we report the first observation of a distinct sharp vibrational mode at 3507 cm^{-1} that is unambiguously ascribed to water inside nanotubes. The assignment is based on the effect of blocking the nanotube interior with n-nonane. Our calculations are the first to directly link the structure of the water inside the nanotubes to the specific vibrational feature observed at 3507 cm^{-1}, predicted from both *ab initio* and classical simulations.

V-3. Experimental section

In this study nanotubes were deposited directly onto a tungsten grid which was then inserted into a vacuum-IR cell *(244)*. Ozonization was carried out in two 5 min cycles with 17.2/18.1 Torr and 17.3/18.2 Torr initial/final O_3 pressures respectively. The nanotubes were then annealed at 873 K for 30 min to remove the functionalities formed during the ozonization procedure. The resulting opening of the nanotubes was tested by CF_4 adsorption before and after the etching.

The experiment for H_2O diffusion into the nanotube interior was carried out as follows: (1). Water vapor was condensed to form amorphous ice on the outer geometric surface of the nanotubes at 123 K. At this temperature, diffusion of water into the interior of the nanotubes is severely kinetically restricted; (2). After the deposition and condensation, the sample was heated to 187 K and immediately quenched back to 123 K at a rate (in both directions) of 1 K/s; (3). Consecutive annealing and cooling cycles led to gradual removal into vacuum of both condensed ice and water adsorbed inside the nanotubes. Figure 40 shows a series of spectra for five heating/cooling cycles, and it is observed that a monotonic increase occurs in the ratio of the singular OH absorbance at 3507 cm^{-1} to the integrated associated OH absorbance at lower frequencies as the coverage of water decreases.

Liquid He was used to decrease the sample temperatures for testing H_2O diffusion inside nanotubes at very low coverages. The sample temperature was set within the range of 30 - 45 K and a small amount of H_2O was dosed. Then the sample was heated to 153 K and cooled back to the initial temperature with a 1 K/s rate in both directions. Infrared spectra were measured before and after the heating. Figure 41 clearly shows the absence of the 3507 cm^{-1} mode before annealing.

To probe the internally bound water we utilized adsorbed n-nonane to block interior sites in the SWNTs. Figure 42 shows pairs of IR spectra of water condensed on SWNTs with and without n-nonane blocking of the interior sites. In each case the sample containing adsorbed H_2O was annealed at 183 K. N-nonane was condensed on the nanotubes at 123 K and then the sample was heated to 283 K for 15 minutes and cooled back to 123 K causing blockage of SWNT interior sites. In a second experiment without n-nonane, water was condensed at 123 K then heated and cooled to 183 K several times with a rate of 1 K/s. The figure shows the 4^{th}, 5^{th} and 6^{th} annealing cycles for experiments both with and without n-nonane blocking. All spectra were taken at 123 K. Separate desorption kinetics measurements have shown that internally-bonded n-nonane will remain in the nanotube interior at 283 K *(194)*.

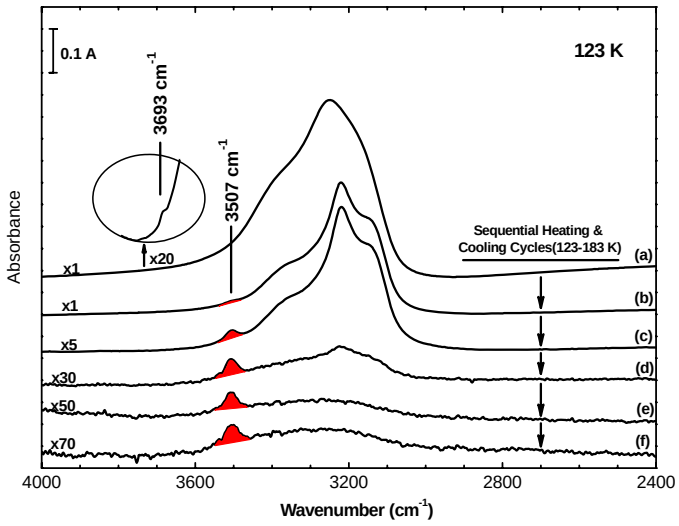

Figure 40. Changes in the IR spectra of H_2O condensed on single walled carbon nanotubes on heating in vacuum.

V-4. Results and Discussion

Figure 40a shows the infrared spectrum in the OH stretching region following condensation of H_2O at 123 K on the outer geometric surface of the nanotubes. The 3693 cm^{-1}

mode corresponds to the "free OH" groups dangling at the surface of the amorphous ice. These groups disappear upon annealing due to surface reconstruction. Spectra (b) through (f) show the consecutive changes which occur as programmed heating to 183 K, followed by quenching to 123 K, occurs (both at 1 K/s rate). The annealing enhances water mobility resulting in H_2O diffusion into the nanotube interior as well as water desorption into vacuum, decreasing the overall amount of condensed water. The development of a high frequency isolated OH vibrational mode at 3507 cm^{-1} was observed in addition to associated OH features in the 3000 cm^{-1} – 3450 cm^{-1} region.

Figure 41 shows the IR spectra for water condensed at medium and very low H_2O coverages on SWNTs measured before and after the first annealing cycle. In both cases we observe the appearance of a relatively sharp 3507 cm^{-1} mode after annealing. The change of the spectra in the 3000 cm^{-1} to 3600 cm^{-1} range, measured for the medium H_2O coverage (Figure 41A), indicates that water, initially condensed in an amorphous phase on the outer surface of the SWNTs, crystallizes upon annealing. Figure 41B shows that the 3507 cm^{-1} mode is not present in the spectra of condensed water before annealing. This indicates that the 3507 cm^{-1} mode originates form a structure that appear only at temperatures when water molecules posses higher surface mobility and can diffuse in the nanotube interior.

The assignment of the 3507 cm^{-1} mode to the internally-bound H_2O is based on the effect of n-nonane blocking of the nanotube interior when it is adsorbed below 283 K. At this temperature n-nonane is trapped in the nanotube and prevents water from diffusing into the nanotube interior. Figure 42 demonstrates that n-nonane almost completely eliminates the mode at 3507 cm^{-1}. This clearly shows that the 3507 cm^{-1} mode originates form the water phase

confined inside nanotubes. D_2O was employed to verify the observation of the singular OH stretching mode; an analogous mode was observed at 2595 cm^{-1}.

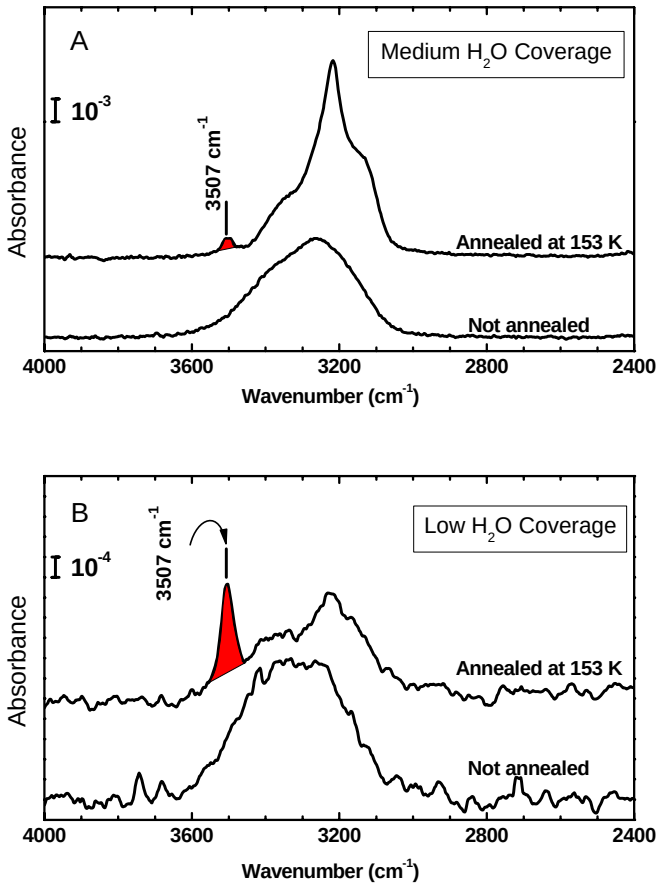

Figure 41. Appearance of the 3507 cm^{-1} OH stretching mode following diffusion of H_2O into the nanotube interior at medium (A) and low (B) coverages.

The vibrational spectroscopy of condensed water indicates that the higher the degree of involvement of a water molecule into the hydrogen bond network, the lower the frequency of the OH-stretching modes *(266, 379)*. In the gas phase spectrum unbound H_2O molecules exhibit antisymmetric ν_3 and symmetric ν_1 stretching modes at 3756 cm^{-1} and 3657 cm^{-1}, respectively *(266)*. A high frequency 'free OH' stretching mode at 3693 cm^{-1} was observed by us (Figure 40) for dangling hydrogen atoms on the surface of ice nanocrystals at low temperatures as reported

by others *(376)*. This mode disappears as the ice nanocrystals are annealed above 140 K due to reconstruction on the ice surface that involves the formation of strained surface hydrogen bonds *(380)*.The OH modes of water molecules are red-shifted when the molecule is entrapped in a matrix and does not participate in H-bonding at all or participates only as a proton acceptor to form a hydrogen bond *(266, 370)*. For a proton donor water molecule, the stretching frequency of the OH bond involved in the H-bond network is much more strongly red-shifted relative to the group not involved in the H-bond *(266, 370)*.

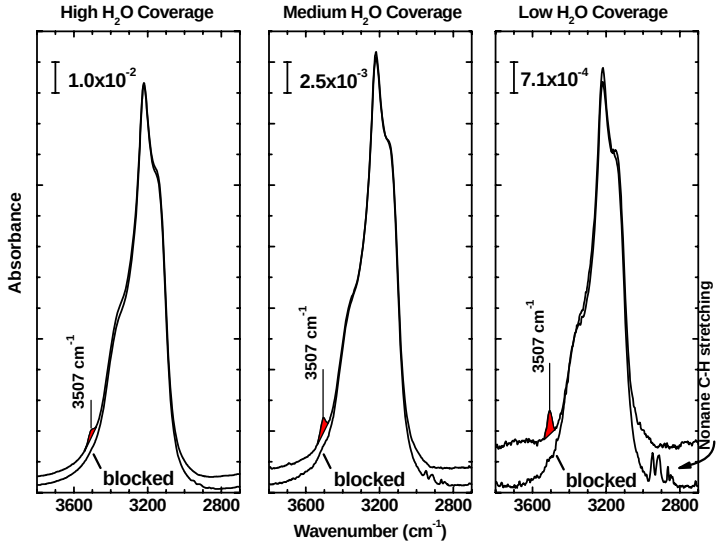

Figure 42. Blocking of the nanotube interior by n-nonane preadsorption. The absorbance scale for the middle and right spectra are 1/4 and 1/14 of the scale in the spectra on the left hand side.

One might think that the 3507 cm^{-1} mode observed inside nanotubes is caused by OH groups not directly hydrogen bonded but highly red-shifted by the confining environment. This would require a large red-shift of between 150 cm^{-1} and 250 cm^{-1} from the 'free-OH' stretching frequency. It is known that confined molecules inside SWNTs exhibit small red-shifts *(185, 191, 197)*, and that the interaction of the benzene π cloud with the OH group of a water molecule in a cluster produces a red-shifted mode in the 3636-3657 cm^{-1} range *(370)*. We have computed the

red-shift for a single H_2O inside a (10,10) SWNT from *ab initio* density functional theory *(284, 286)*. The maximum calculated shift is 30 cm^{-1}. We therefore conclude that only hydrogen bonding could cause the red-shift of the free OH frequency down to 3507 cm^{-1}, thereby excluding interactions of OH groups with the nanotube interior as being the cause of the 3507 cm^{-1} mode.

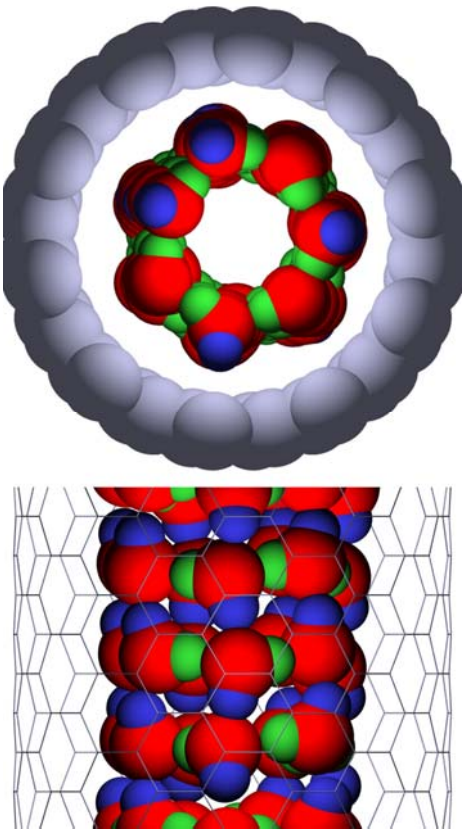

Figure 43. Snapshot from a molecular simulation of water adsorbed inside a (10,10) SWNT at 123 K. (A) End view. (B) Side view. Red spheres represent oxygen atoms, blue spheres are hydrogen atoms that are hydrogen bonded to adjacent rings (inter-ring), and green spheres are hydrogen atoms involved in intra-ring hydrogen bonds. The lines in (B) represent the carbon-carbon bonds of the SWNT.

Our molecular modeling results indicate that the 3507 cm^{-1} mode is due to the distortion of the hydrogen bond angles of fully hydrogen-bonded water that is confined inside the nanotubes. We have used the SPC/E potential model *(381)* for Monte Carlo simulations of H_2O

in various SWNTs. Details of the simulations are given elsewhere*. The water molecules are found to order into ring structures at low temperatures. The number of water molecules in a ring at a given temperature and pressure is dictated by the diameter of the nanotube. For example, rings composed of 5 H_2O molecules are formed in an (8,8) SWNT, whereas rings containing 7 H_2O molecules are formed in a (10,10) SWNT. The rings stack to form a structure that is essentially fully hydrogen bonded. A snapshot of H_2O in a (10,10) nanotube at 123 K is shown in Figure 43.

Water adopts a stacked-ring structure inside nanotubes, forming intra- and inter-ring hydrogen bonds. The stacked ring structure can be seen in Figure 43B. The intra-ring hydrogen bonds are bulk-like while most of the inter-ring hydrogen bonds are relatively weak, having a distorted geometry that gives rise to a distinct OH stretching mode. This is illustrated in Figure 44A where the distribution of hydrogen bond angles, measured as the O-O-H angle, θ, are reported for bulk amorphous ice and H_2O inside a (10,10) SWNT, both at 123 K. The probability density for amorphous ice (black line) has a single maximum at $\theta \approx 6°$, whereas H_2O inside a (10,10) nanotube (red line) has a distribution of hydrogen bond angles that exhibits a maximum at $\theta \approx 5°$ and a shoulder at higher angles. We have analyzed the inter- and intra-ring hydrogen bonds separately and found that the intra-ring hydrogen bond angles (green line) are similar to those of bulk amorphous ice, with a mode at $\theta \approx 5°$. However, the inter-ring hydrogen bond angles (blue line) are very different from the bulk. The probability density $P(\theta)$ for inter-ring hydrogen bond angles has a Gaussian shape, with a maximum at about 17°. The unusually large hydrogen bond angles are caused by H_2O confinement in the nanotube.

* O. Byl et al., submitted to the Journal of American Chemical Society, On-line Supporting Materials.

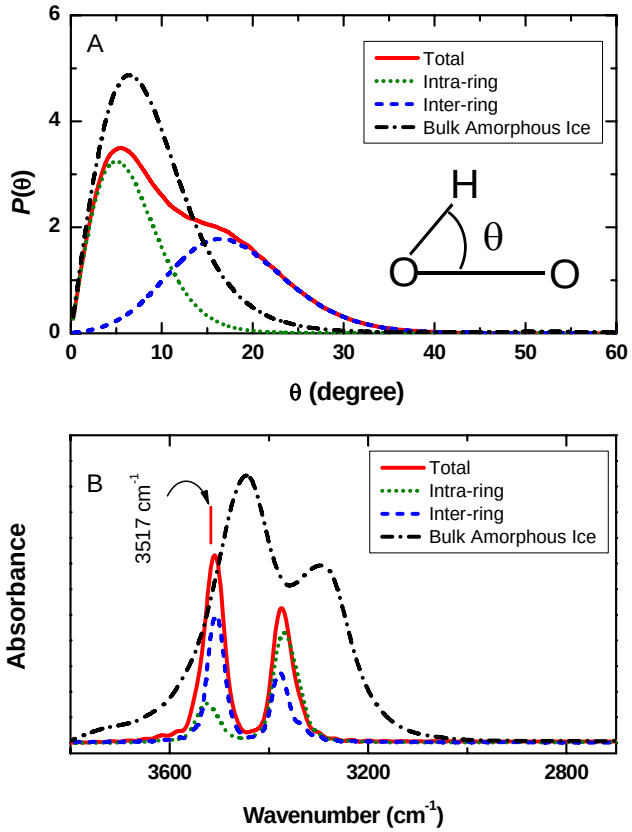

Figure 44. Characteristics of hydrogen bonding in amorphous ice and H_2O inside a (10,10) SWNT computed from molecular simulations. (A) Hydrogen bond angle (O-O-H) distribution computed from Monte Carlo simulation for bulk amorphous ice (dash-dot black line) and for H_2O in a (10,10) SWNT (solid red line). The intra-ring hydrogen bond angles are plotted as the dotted green line, the inter-ring hydrogen bond angles are represented by the dashed blue line, and the red line is the sum of the green and blue lines. The inset shows the definition of the O-O-H angle θ. (B) The IR spectra for bulk amorphous ice (dash-dot black line) and for H_2O in a (10,10) SWNT (solid red line) computed from molecular dynamics simulations. The IR spectrum computed for intra-ring O-H stretching is plotted as the dotted green line and the inter-ring spectrum is the dashed blue line. Note that sum of the green and blue lines is not equal to the total spectrum (red line) because of cross correlations.

We deduce that the sharp IR mode at 3507 cm^{-1} for H_2O inside the nanotubes seen in Figure 40 and Figure 41 is generated by the unusual inter-ring hydrogen bonds. This assignment is verified by classical molecular dynamics simulations and quantum mechanical density functional theory calculations. Molecular dynamics (MD) using a classical water potential has been used previously to compute IR spectra of bulk and confined water *(213)*. We present IR

spectra computed from MD simulations for bulk amorphous ice and for H_2O inside a (10,10) nanotube in Figure 44B. Two distinct modes are observed, one with a frequency of about 3370 cm^{-1}, which lies in the range of hydrogen-bonded OH groups. The other mode is at about 3517 cm^{-1}, which corresponds closely with the experimentally observed mode at 3507 cm^{-1}. We have computed the IR spectrum for intra-ring OH stretching (green line) and for inter-ring OH stretching (blue line). The mode at 3517 cm^{-1} is almost entirely due to inter-ring OH stretching. Similar results are observed for water adsorbed in a (8,8) SWNT, both for the bond angle distribution and the IR spectra.

We have computed the IR frequencies and intensities for the rings of water molecules using first-principles planewave periodic density functional theory *(287)*. Details of the calculations are given elsewhere[*]. The calculations for rings containing 7 H_2O molecules give two O-H modes, one at 3167 cm^{-1} and another at 3567 cm^{-1}. The 3167 cm^{-1} mode corresponds to intra-ring O-H stretching modes while the 3567 cm^{-1} mode is due to inter-ring O-H stretching. Calculations for rings of 5 H_2O molecules give similar results. Hence, our classical Monte Carlo and MD simulations with model potentials give results that are in qualitative agreement with first-principles calculations. All three calculations strongly support the assignment of the experimentally observed 3507 cm^{-1} mode to distorted inter-ring O-H stretching modes.

V-5. Summary

In summary, we have found that H_2O molecules confined inside of SWNTs form ring structures that involve hydrogen bonds of two types. Hydrogen bonds within the ring structure exhibit frequencies like those found in bulk H_2O and O-O-H angles near 5°. Hydrogen bonds formed between neighboring rings exhibit an unusual stretching frequency at 3507 cm^{-1} and are

[*] O. Byl et al., submitted to the Journal of American Chemical Society, On-line Supporting Materials.

associated with larger O-O-H angles near 17°. The strained angles and unusual IR mode are a direct result of water confinement.

V-6. Acknowledgements

We gratefully acknowledge the Army Research Office for the support of this work. We also thank Professor K. D. Jordan for useful discussions of the results of this work.

PART II

NANOTUBE BULK MATERIAL CHARACTERIZATION – N_2 ADSORPTION VOLUMETRIC STUDIES.

INTRODUCTION

Understanding of the adsorption properties of an adsorbent is the ultimate goal of any adsorption study. For practical purposes an adsorbent can be characterized in terms of it specific surface area, total pore volume and pore size distribution. These characteristics can be obtained form an adsorption isotherm, i.e. the function of the adsorbed material excess on pressure. To measure an isotherm the adsorbent is incrementally dosed with an adsorbate and the adsorbed amount and the equilibrium pressures are measured at a constant temperature. The choice of the adsorbate is related to the a priori knowledge of the adsorbate-adsorbent interactions, desired pressure range and availability of the liquid adsorbate as a refrigerant. Nitrogen satisfies these criteria the best and therefore it is used vastly for routine adsorption properties characterizations of various materials.

In this study N_2 was used to estimate the bulk adsorption properties of single wall carbon nanotubes. Since carbon nanotubes can potentially substitute other carbons as adsorbents the choice of the adsorbent was dictated by the extensive number of reports of various adsorbents where nitrogen used as an adsorbate.

Adsorption isotherms are measured by Quantachrome Autosorb 1 MP instrument in automatic regime. A nanotube sample after preadsorption treatments is placed into a measuring tube and connected to the measurement port of the apparatus. The tube is partially immersed into a bath with ℓ-N_2 and the instrument keeps the constant level of ℓ-N_2 by adjusting the position of the bath. The volume of the sample tube is measured automatically prior every run. Each point is obtained by allowing a known amount of gas into the tube followed by monitoring the pressure drop. If the final pressure does not change within a certain preset time and pressure range and does not differs from the target pressure value more than a given tolerance the point is accepted and the adsorbed amount is calculated from the pressure drop and the volume of the sample tube.

In this way the adsorption part of the isotherm can be collected. The desorption part is measured by sequential pumping out of know volumes of the adsorbate with the same validation procedure.

VI. ETCHING OF CARBON NANOTUBES BY OZONE – A SURFACE AREA STUDY*

VI-1. Abstract

The oxidative etching of single walled carbon nanotubes (SWNTs) is useful for opening the end caps and the sidewalls of the nanotubes to provide access to the interior. We have studied the effect of successive treatment of SWNTs by 95 % pure O_3(g), which is a powerful and convenient oxidizing agent. The surface area of the SWNTs was measured following exposure to O_3(g) at 300 K and also following heating to 1073 K in vacuum to decompose the oxidized groups on the nanotubes, a procedure called etching. This O_3-induced etching process was observed by scanning electron microscopy and by transmission electron microscopy and the kinetics of the process was studied gravimetrically. It was found that O_3 attack occurs preferentially on the outermost geometric surface of the conglomerate sample of the nanotubes as a result of the high efficiency of O_3 to react in a few collisions with the nanotube surface. Ozone-induced etching causes the loss of pores in the 20 Å diameter range as observed by nitrogen adsorption at equilibrium by DFT analysis.

* Reproduced with permission from O. Byl, J. Liu, J. T. Yates, Jr.; Etching of Carbon Nanotubes by Ozone – a Surface Area Study. Langmuir 21(9), 4200-4204 (2005).

VI-2. Introduction

Single walled carbon nanotubes (SWNTs) have attracted much attention in recent years as a prominent sorption material *(5)*. This is due to their unique cylindrical shape with tubular diameters of a few nanometers and with two- to four orders of magnitude higher tube lengths compared to diameter. The interior region of nanotubes offers a deep potential well for physical adsorption *(46, 47, 156, 157, 191, 195, 197, 243)*. This geometry provides an ideal example of microporous material.

As produced, SWNTs are closed by hemispherical fullerenelike caps *(8)* that restrict gas adsorption in the nanotube interior *(181, 382)*. The high reactivity of the fullerenelike caps to oxidizing agents may be employed to open SWNTs, activating them as adsorbents.

Individual SWNTs normally form bundles of different shapes and sizes bound together by van der Waals forces *(22)*. In such bundles usually four types of adsorption sites are considered *(159, 165, 307)*: (1) the nanotube interior; (2) the interstitial regions, formed by three or more nanotubes in contact inside of a bundle; (3) the groove sites produced by two adjacent nanotubes on the exterior surface of the bundles; and (4) the outer nanotube convex surface. The interior and interstitial sites fall into the category of micropores.

Bundles of nanotubes can also form larger agglomerates. This results in the appearance of mesoporous voids as observed in a number of studies giving a type-I and type-IV combination isotherm *(163, 164, 175-177)*.

The analysis of nitrogen adsorption isotherms is the classic method that gives information on the specific surface area (SSA) and porosity of high specific surface area solids *(383)*. The Brunauer-Emmett-Teller (BET) method is widely accepted for surface area determination; however its applicability to nanotubes is questioned *(174)*. Nonetheless the BET method is

frequently chosen as a way to compare surface areas of nanotubes and other sorbents *(164, 175-177)*. At present only idealized models of nanotube assemblies have been considered theoretically whereas real materials may involve complicated structures *(168, 174)*. In addition nanotubes in many cases may have appreciable amounts of defects that distort the tubular geometry and affect the adsorption *(157)*. Impurities can also substantially alter nitrogen adsorption isotherms.

The maximum geometric specific surface area for the nanotube interior is 1315 m^2/g according to a simple model *(239)*. The highest SSA to date was measured by Cinke et al. as 1587 m^2/g *(163)*. In all cases some kind of chemical activation is required to enhance the SSA of nanotubes.

In this paper, we present a study of nitrogen adsorption on single walled carbon nanotubes. Ozone was utilized as the oxidative agent to modify the nanotube adsorption properties *(46, 157, 191, 197, 243)*. The BET surface area was measured following oxidation by O_3, and again following annealing in vacuum. Scanning electron microscopy (SEM) and transmission electron microscopy (TEM) imaging was carried out to observe the morphology changes of the material.

VI-3. Experimental section

VI-3A. Single Walled Carbon Nanotubes

Single walled carbon nanotubes were obtained from the Liu group, Duke University, and were prepared by a CVD method using a Fe/Mo catalyst supported on alumina aerogel. Briefly, an alumina boat which was loaded with a certain amount of catalyst was placed into a quartz tube. The tube was heated to 850°C under Ar flow; then the Ar flow was shut off and CO was

introduced at 850ºC. After 40 minutes growth time the gas was switched back to Ar and the system was cooled to room temperature.

The product (100 mg) was mixed with 5 mL of HF(aq) (52%) and 15 mL of distilled water to dissolve the alumina support. It was stirred for 18 h and then HF was removed. The sample still contained many metal particles coated by carbon layers. To further purify the product, it was heated in a 15% air/Ar mixture at 440ºC for 1 h, and then washed in 5 mL of concentrated HCl(aq) (37%) to dissolve the metal particles formed during the oxidation process. The final purified product consists mainly of SWNTs in bundle form, which agglomerate into adherent sheets of material. TEM images show that the sample still contains a small amount of amorphous carbon. Thermogravimetric studies indicate that the purified SWNTs also contain a small amount of metal oxide. The material remaining after full combustion in air is less than 5% of the original weight.

VI-3B. O_3 Generation and Purity Control

O_3 was produced and purified in an all-glass generator described elsewhere *(251)*. To remove oxygen that continuously forms as O_3 decomposes, a freeze-pump-thaw method with liquid nitrogen on a small glass appendage tube was used just before each exposure. Fractional distillation between 77 K and 130 K (pentane/ℓ-N_2 slush) was used to separate impurity CO_2 from O_3, with CO_2(s) remaining in the 130 K trap while O_3(s) was collected at 77 K. This procedure yielded 95-98% pure ozone as determined by IR studies of the gas in a glass cell with KBr windows.

The purity of O_3 was verified by IR spectroscopy of the gas at each step. For calibration, the O_3 pressure (5-60 Torr) versus integrated absorbance (900-1300 cm^{-1} range) was carefully

measured for the most thoroughly purified O_3 sample. The measured IR absorptivity was found to be within the range found in the literature for pure ozone *(384)*.

VI-3C. Nanotube Oxidation and Annealing Procedure

SWNTs were treated in an all-glass-quartz system illustrated in the Figure 45. The pressure was measured with a MKS capacitance manometer type 107 (10^{-3}-10^{3} Torr range). Vacuum annealing was carried out in a quartz tube under 10^{-2}-10^{-3} Torr vacuum.

An 11 mg sample of purified nanotubes was weighed by difference (accuracy ± 0.0001 g) into a small quartz thimble equipped with small hooks used for mechanical transfer from the O_3 treatment chamber, through air, into a modified quartz BET measurement tube which is also used for annealing. The 270 cm^3 O_3 treatment chamber was of wide bore, and this geometry was found to be necessary to avoid large O_3 concentration gradients, retarding the reaction kinetics and leading to irreproducible results. Ozone (93 - 97 %) treatment was carried out at 22.5 Torr and 300 K for 10 minutes. The thimble was then transferred to a 12 mm quartz measurement tube and vacuum annealed for 1 hour at 523 K. An isotherm at 77.3 K was then measured using N_2. Then the sample was vacuum annealed at 1073 K for 1 hour, and a second N_2 isotherm was measured. To increase accuracy, the volume of the standard measurement tube was decreased by inserting a 10 mm diameter glass rod. The O_3-etching cycle was repeated 6 times causing considerable loss of nanotube mass due to oxidation. The zeroth cycle was carried out as above, omitting the O_3 treatment. To expedite the experiments, most of the N_2 isotherms were acquired in the range P/P_0 = 0.05 - 0.30 where linearity is usually observed in the linearized BET equation.

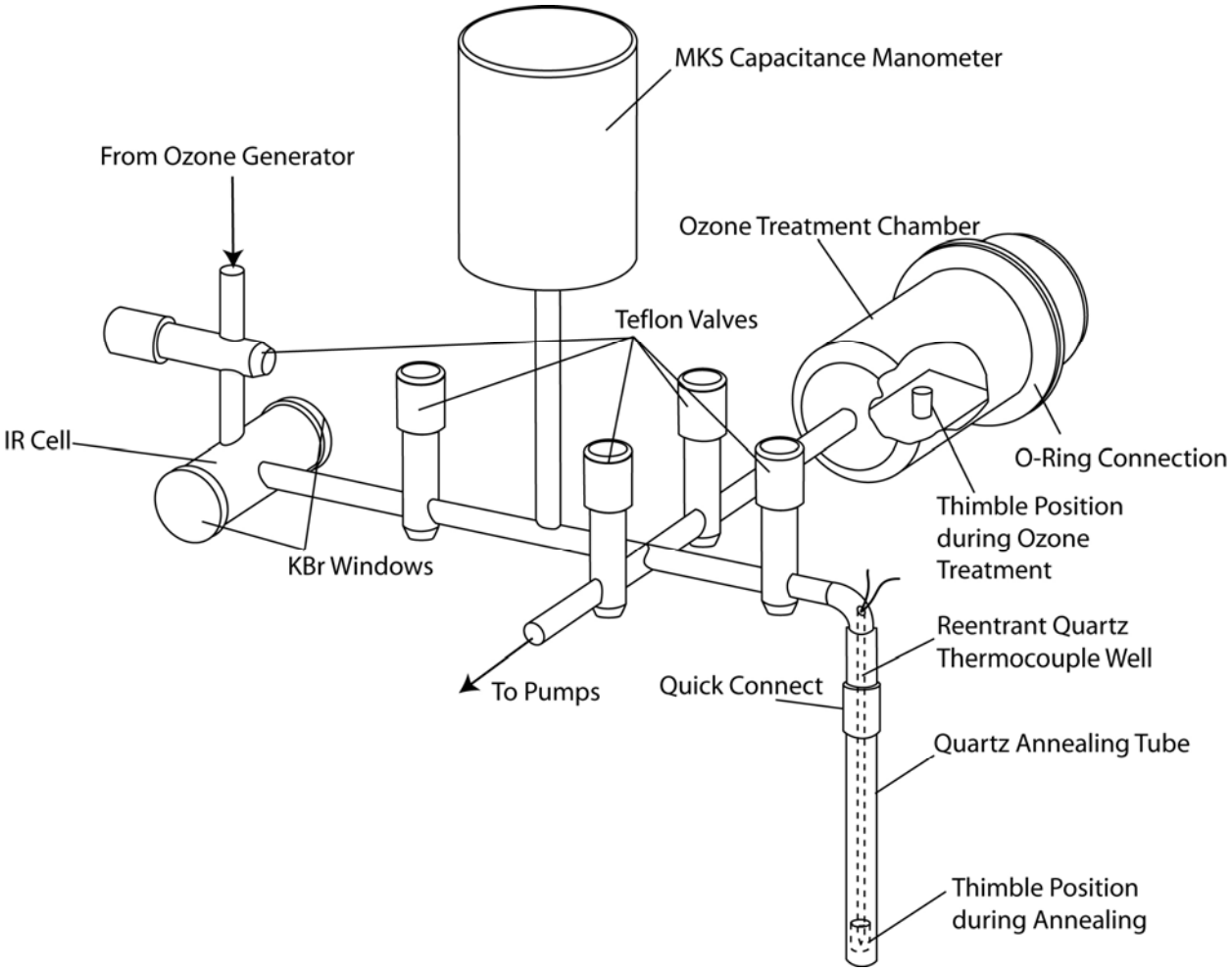

Figure 45. A schematic representation of the glass vacuum system used for ozone purification and control, nanotube oxidative treatment with O_3, and high temperature annealing.

VI-3D. Surface Area and Pore Size Distribution Measurements

Isotherms were measured on a Quantachrome Autosorb 1 MP instrument. N_2 (99.999% pure) and He (99.999% pure) were used. In addition to surface area measurements, the pore size distribution was estimated applying a Nonlinear Density Functional Theory (NDFT) kernel supplied by Quantachrome as a part of their software package. The distribution was calculated by fitting the experimental isotherm with a sum of theoretical isotherms that were computed for the carbon slit pore model. The details of this computation are described elsewhere *(232, 385,*

386). In this paper we present the pore volume histograms and cumulative pore volumes versus pore sizes.

VI-3E. SEM and TEM Imaging

Scanning electron microscopy was carried out on a Philips XL-30 field emission scanning electron microscope operated at 20 kV. The sample was deposited directly onto a sticky carbon film. Images were recorded with up to 100,000 magnification.

A JEOL 2000-FX scanning transmission electron microscope operated at 200 kV equipped with Gatan CCD camera and software to record the images was used. The maximum nominal magnification was 850,000. Nanotube samples were dispersed in dimethylformamide, deposited onto a copper grid and outgassed at room temperature before imaging.

VI-4. Results and Discussion

Figure 46A and Figure 46B show SEM images of an untreated nanotube sample at different magnifications. One can observe at low magnification that the nanotubes form micron size flakes (microflakes) of different sizes that agglomerate into large fragile sheets (macroflakes) that were also observed by Shaffer et al. *(387)*. The microflakes are composed of bundles of nanotubes which may be resolved at high magnification. No appreciable amount of catalyst was detected for the untreated nanotubes. TEM images show the presence of some amorphous carbon. After O_3 treatment and annealing to 1073 K the initial millimeter-size macroflakes are greatly reduced in size and their integrity is broken, exposing many pores resembling a dry clay desert (Figure 46C). No nanotube bundles are observed on the surface on the etched material. A higher magnification image (Figure 46) of the O_3-etched material shows a large amount of catalyst particles composed of iron, molybdenum and oxygen according to our

EDX studies. These particles may be initially covered with carbon layers; they exfoliate during the oxidation and accumulate on the surface of the flake.

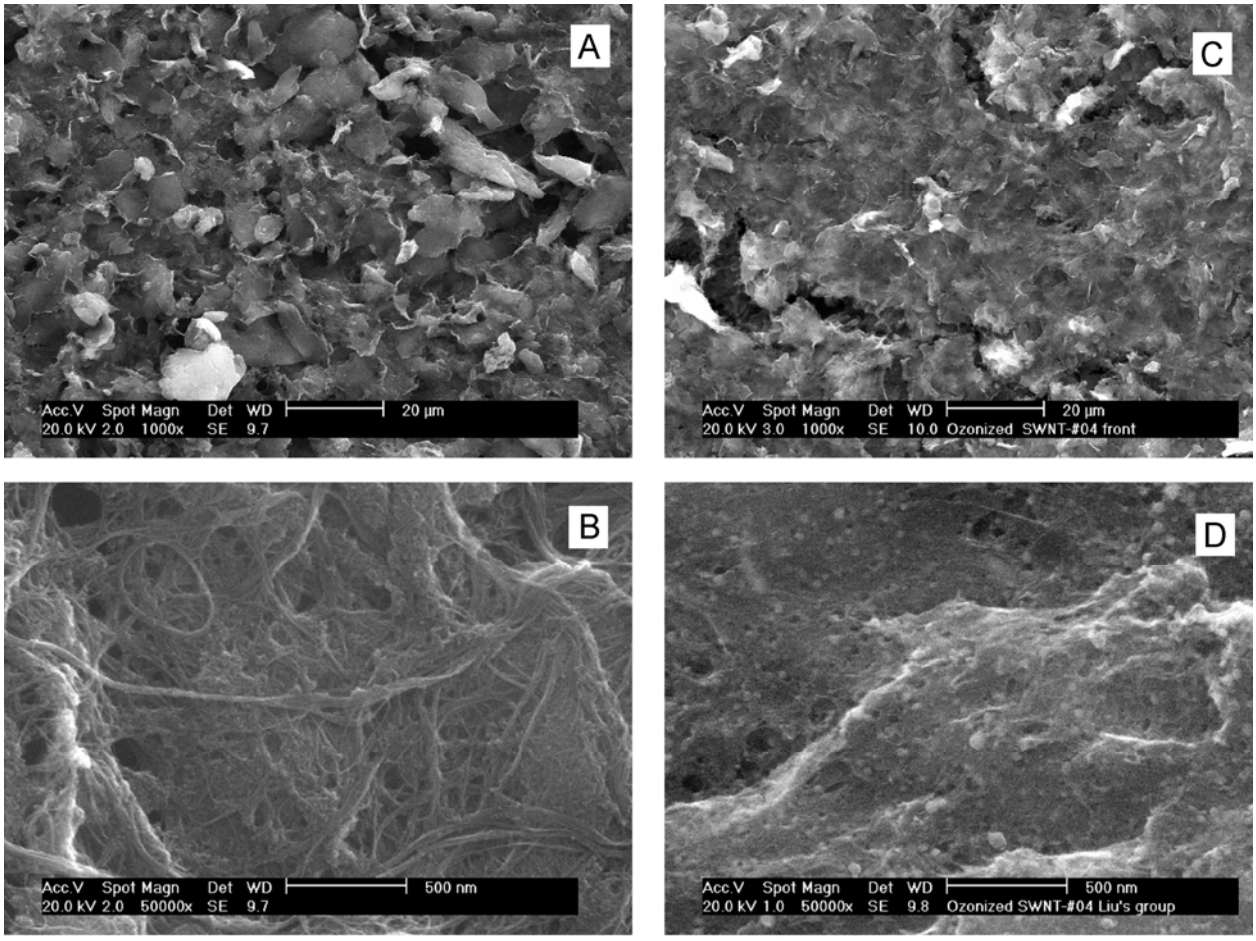

Figure 46. Representative SEM images of nanotubes: (A) and (B): before O_3-etching; (C) and (D): after O_3-etching.

Figure 47A shows the mass decrease upon etching of the nanotubes in six sequential O_3 etching experiments. The pairs of bars refer to mass measurements after O_3 treatment and vacuum annealing at 523 K, and then after annealing to 1073 K. It is observed that mass loss occurs after each O_3 treatment for both annealing temperatures, and CO(g) and CO_2(g) are evolved at both temperatures *(243)*. It is noted that a linear dependence of nanotube mass is found for the points measured after the 523 K vacuum annealing, as shown by the straight line fitted to the dark bars associated with the 523 K vacuum annealing after O_3 treatment.

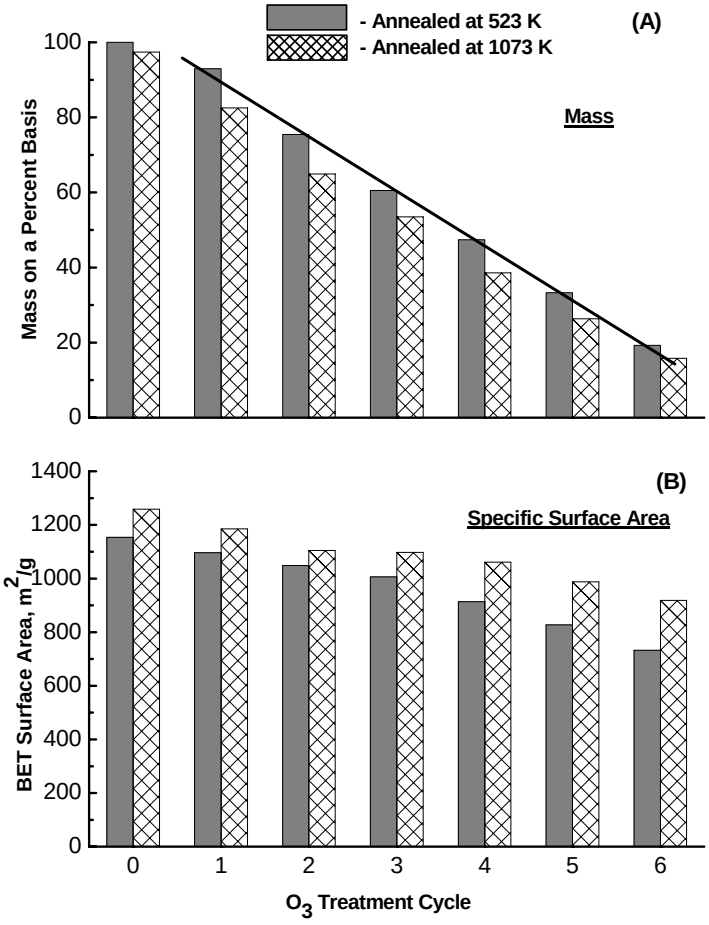

Figure 47. (A) Nanotube mass; (B) BET surface area changes upon each oxidation/annealing cycle. Each cycle was carried out with 10 min ~95% O_3 treatment at an initial pressure of 22.5 Torr and outgassing at 10^{-2} Torr and 523 K for 1 h (filled bars – the first step) and then annealing at 10^{-2} Torr and 1073 K for 0.5 h (crossed bars – the second step). The zeroth cycle represents masses and surface areas of nanotubes not treated with O_3.

Figure 47B shows the BET specific surface area per gram upon etching. Each O_3 treatment cycle causes a slight loss in the ***apparent*** SSA of the nanotubes. It may be seen that the ***apparent*** SSA increases up to 25% when the O_3-treated sample (annealed to 523 K) is further annealed to 1073 K.

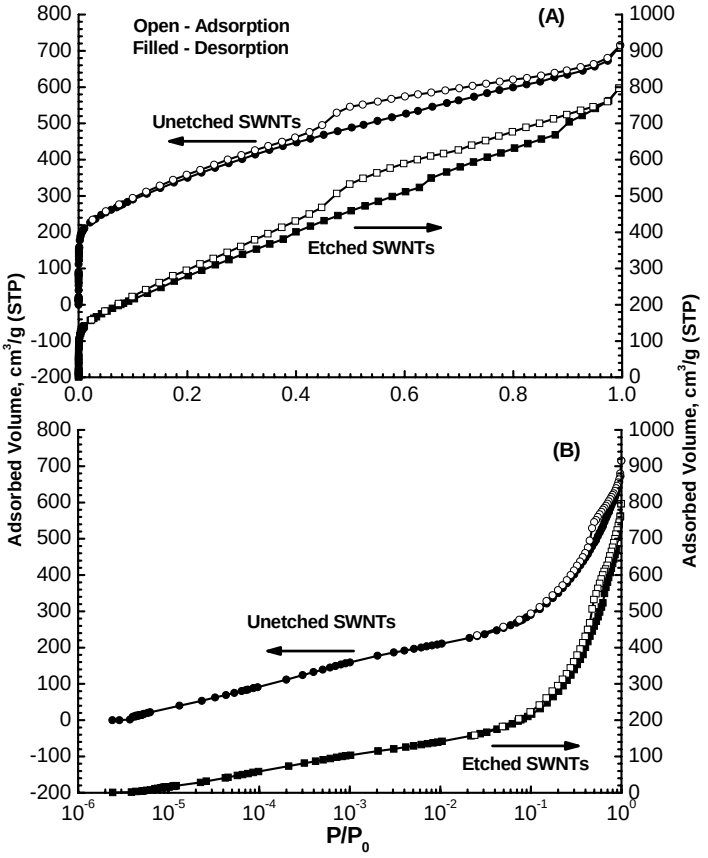

Figure 48. Representative nitrogen adsorption-desorption isotherms for unetched and O_3-etched nanotubes at 83% mass loss. (A) linear P/P_0 scale; (B) semilog P/P_0 scale.

Figure 48A and Figure 48B show two isotherms for untreated nanotubes and extensively O_3-etched nanotubes with 83% mass loss. In both cases the samples were annealed at 1073 K. Hysteresis is observed for both isotherms indicating the presence of mesopores. Moreover the hysteresis is greater for the O_3-etched nanotubes indicating higher content of mesopores in the etched sample. In both cases the hysteresis loop almost closes at about 0.42 relative pressure. The hysteresis does not close up completely for either sample. This may be related to the swelling of bundled structures upon adsorption that traps nitrogen molecules and delays desorption at lower pressures.

As shown in Figure 48A and Figure 48B the initial part of the isotherm became somewhat reduced after etching. Figure 48B demonstrates that the amount of the adsorbed nitrogen is noticeably lower in the low relative pressure region. This region is representative of adsorption in micropores, which are the internal adsorption sites inside the nanotubes.

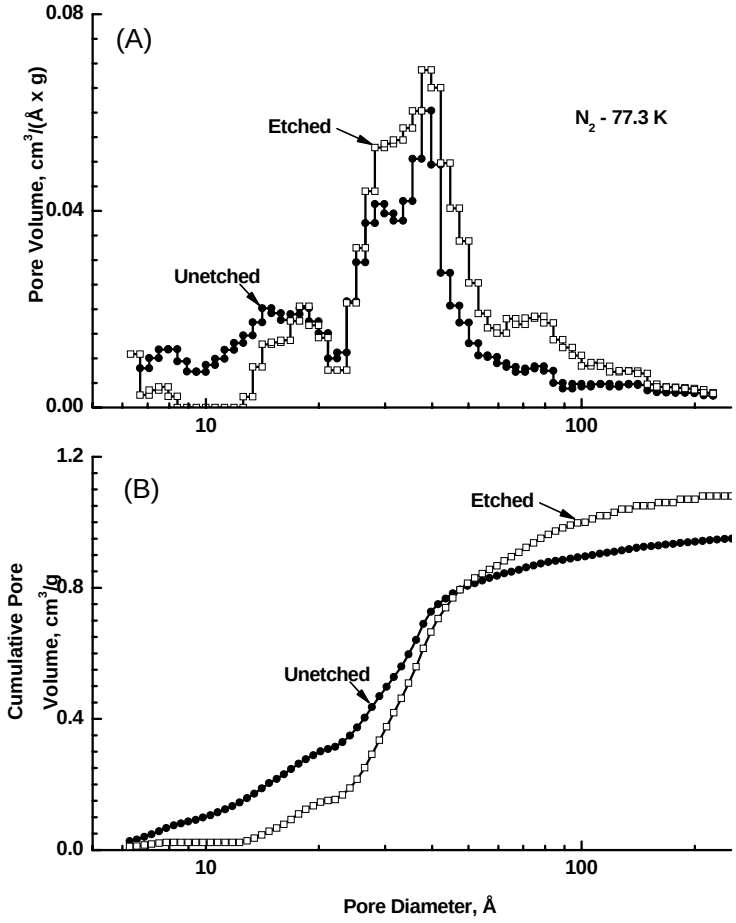

Figure 49. (A) NLDFT (a carbon slit pore model) pore size distribution according to volume; (B) cumulative volume increase with pore size.

Figure 49A shows the pore size distribution derived from the isotherms based on NLDFT computations for the carbon slit pore model. For nanotubes with cylindrical pores the adsorbate-surface interaction should be greater than for a flat surface *(179)*. Therefore the calculated pore sizes represented in Figure 49A and Figure 49B are somewhat underestimated. Nonetheless the

obtained distribution gives qualitative information about changes in pore distributions upon O_3-etching. Both Figure 49A and Figure 49B show that the contribution of smaller micropores in the volume distribution drops after etching. This is partially due to the destruction of the SWNTs eliminating their individual internal adsorption sites. It is noticeable that the pore size distribution of small mesopores (20 - 70 Å diameter) does not change appreciably or increases slightly. This type of pores can not be related to large nanotubes since they have not been detected by TEM. The most probable source of this mesoporosity may be some kind of carbonaceous agglomerates fused from destroyed nanotube fragments and amorphous carbon produced upon annealing.

VI-5. Discussion

It has previously been established that O_3 is a powerful oxidizing agent for nanotubes at 300 K. Geng et al. *(382)* showed by means of transmission electron microscopy that acidic purification of SWNTs leads to removal of fullerenelike cap of nanotubes and enhances nanotube adsorption capacity. Both purification in acidic mixtures or reaction with O_3 produces both C=O and C-O-C functional groups, and that these groups may be destroyed by heating to about 1100 K, yielding CO(g) and CO_2(g) as it was shown by IR *(243)* and near-edge X-ray absorption fine structure *(242)* spectroscopy studies. The removal of these functional groups leads to the enhancement of the kinetics of adsorption into the nanotubes *(156)*. Both the end caps and the walls of the nanotubes are opened by oxidative etching with O_3 *(46)*.

Figure 47A shows that the mass of the nanotubes decreases linearly with the O_3-treatment time over a wide range of mass. This observation indicates that the kinetics of oxidation are independent of the surface area of the nanotube sample. A model to explain these kinetics involves the reaction of O_3 only at the ***geometrical*** outer surface area of the conglomerate sample

of nanotubes present in the reactor. As the quantity of nanotubes decreases significantly, the geometrical area of the exposed sample remains constant causing the oxidation rate to remain constant. Highly reactive ozone gas molecules are consumed with a small fractional penetration into the bulk of the nanotube sample due to their rapid reaction at or near the geometrical surface. A schematic picture of this process is shown in Figure 50.

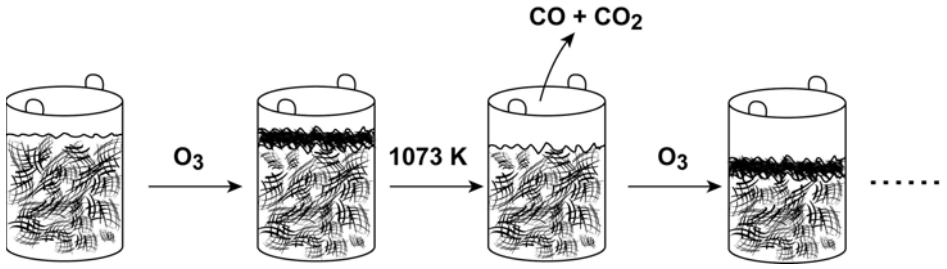

Figure 50. Schematic of O_3-etching of agglomerated SWNT sample, showing preferential reaction on the outer geometric surface of the sample.

Figure 47B shows that the ***apparent*** specific surface area of the nanotube sample decreases slightly during the O_3-etching process. Over the 6 cycle etching process the decrease in specific surface area is 27%, while the decrease in mass (Figure 47) is 83 %. The SWNT sample contained ~5% of inert catalyst material, and as etching take place, the fraction of inert catalyst material will rise and the ***apparent*** specific surface area will therefore decrease. The rate of decrease of the apparent specific surface area can be completely explained by the presence of the catalyst initially at a 5% level. The measurements shown in Figure 47B are consistent with a model in which little or no nanotube material deep in the conglomerate is etched by O_3 causing the reaction to be confined to the geometrical outer surface of the sample.

Upon extensive etching reaction with O_3, when over 80 % of the nanotube material has been consumed, it would be expected that the residual nanotube material will be partially etched because of the finite depth of the reaction zone at the geometrical surface. This has in fact been observed in the studies of the N_2 adsorption isotherms, where the isotherms and the pore size

distributions derived from the isotherms differ slightly following extensive etching, as seen in Figure 48 and Figure 49. Figure 49 clearly shows that extensive etching leads to a reduction in the pore volume below about 20 Å diameter, accompanied by an increase in pore volume above 30 Å diameter. This porosity redistribution however does not affect the apparent specific surface area calculated by the BET method since the BET method utilizes a higher relative pressure region of an isotherm. The loss of micropore volume below 20 Å diameter is consistent with the extensive destruction of the nanotube walls by etching with O_3.

VI-6. Summary

The following results were obtained in this study:

The large initial specific surface area observed for the nanotubes prior to O_3-etching indicates that purification with HF(aq) and HCl(aq) accompanied by oxidation in air/Ar mixtures opens a substantial fraction of the nanotubes for N_2 adsorption.

1. Electron microscopy studies indicate that SWNT bundles are morphologically modified by O_3-induced etching.
2. O_3-induced oxidation occurs preferentially on the exposed geometrical outer surface of nanotube conglomerates due to the high reactivity of the O_3 molecule at the sample surface.
3. The localization of oxidation at the outer geometric surface of nanotube conglomerates is accompanied by little or no reduction in the specific surface area of the underlying nanotubes.
4. Extensive O_3-induced etching of nanotube conglomerates results in loss of pore volume in pores below 20 Å diameter as nanotube walls are destroyed.
5. Oxygenated functional groups produced on nanotubes by O_3 treatment and heating only to 523 K cause a small reduction in specific surface area, as measured by N_2 adsorption.

VI-7. Acknowledgements

We gratefully acknowledge the Army Research Office for the support of this work. We also acknowledge the interest and support from Dr. Chris Karwacki at the Aberdeen Proving Ground, and the loan of the Quantachrome Autosorb instrument.

VII. POROSITY CHARACTERIZATION OF SWNTS BY NONANE PREADSORPTION

VII-1. Abstract

The preferential blocking of the interior adsorption sites of single walled carbon nanotubes (SWNTs) by n-nonane is demonstrated. Following adsorption of n-nonane and evacuation for 24 hours at 323 K, it was found that interior sites with diameters less than ~14 Å remained filled with n-nonane, blocking the physical adsorption of N_2 on these sites at 77.3 K. We demonstrate that "nonane blocking" is a very useful technique for nanotube porosity characterization.

VII-2. Introduction

Recently much attention has been directed to single wall carbon nanotubes (SWNTs) as potential adsorbents. Carbon nanotubes have tubular structures formed by graphene sheets rolled into seamless cylinders with diameters of a few nanometers and lengths that can reach micrometers. Adsorption in the nanotube interior can provide a significant advantage over adsorption on other forms of carbon used today. A molecule adsorbed in the nanotube interior is bound more strongly to the concave walls than to a flat carbon surface.

Nitrogen adsorption at 77 K has been used over decades for sorbent characterization. A number of methods have been developed for N_2 isotherm analysis to obtain specific surface area, external and internal surface areas, microporosity and mesoporosity volumes, pore size distribution etc. There are several reports on N_2 adsorption studies on nanotubes *(149, 163-166, 169, 170, 173-181)*. Both theoretical calculations *(149, 169, 174, 179)* and experimental estimations *(180, 181, 279, 388)* give the binding energy for nitrogen adsorbed in nanotubes at zero coverage within the range of 12-18 kJ/mol. This binding energy is greater by about 50% than on planar graphite *(388)*. The adsorption energy of the outer convex surface is the same or less than that for graphite. Theoretical local adsorption isotherms calculated for nitrogen adsorption in the interior of small nanotubes belong to type I in the IUPAC classification *(171, 174, 179)*, and are characteristic for microporous materials *(383)*. If the nanotube diameter is larger than 2 nm then this type of condensation can be referred to as classic capillary condensation described by the Kelvin equation. For smaller nanotubes the concept of capillary condensation can not be applied due to the lack of precise definition of the meniscus in such small pores *(200)*.

The complexity of nanotube materials requires a reliable way of porosity and surface area characterization. One widely used parameter to characterize N_2 adsorption is $\alpha_S = n/n_{0.4}$, where n= number of molecules adsorbed at some equilibrium relative pressure, and $n_{0.4}$= number of molecules adsorbed at $P/P_0 = 0.4$. Traditionally α_S plots, n-nonane preadsorption and Deryagin-Radushkevich (DR) methods were used for characterization of microporous materials *(383)*. The recent development of high resolution α_S plots makes this method very useful for discrimination of overlapping micro- and mesoporosities *(389-391)*.

In this paper we report the result of our study of nitrogen adsorption on single walled carbon nanotubes where the interior sites have been blocked by the preadsorption of n-nonane.

VII-3. Experimental section

A. Single Walled Carbon Nanotubes

Single walled carbon nanotubes were obtained from the Liu group, Duke University, and were prepared by a CVD method with a Fe/Mo catalyst supported on alumina aerogel. Briefly, an alumina boat which was loaded with a certain amount of catalyst was placed into a quartz tube. The tube was heated to 850ºC under Ar flow; then the Ar flow was shut off and CO was introduced at 850ºC. After 40 minutes growth time the gas was switched back to Ar and the system was cooled to room temperature.

The product (100 mg) was mixed with 5 mL of HF(aq) (52%) and 15 mL of distilled water to dissolve the alumina support. It was stirred for 18 h and then HF was removed. The sample still contained many metal particles coated by carbon layers. To further purify the product, the sample was heated in a 15% air/Ar mixture at 440ºC for 1 h, and then washed in 5 mL of concentrated HCl(aq) (37%) to dissolve the metal particles formed during the oxidation process. The final purified product consists mainly of SWNTs in bundle form, which

agglomerate into adherent sheets of material. TEM images show that the sample still contains a small amount of amorphous carbon. The nanotube diameter distribution is broad ranging from 0.9 nm to 2.5 nm as shown in Figure 51. Thermogravimetric studies indicate that the purified SWNTs also contain a small amount of metal oxide. The material remaining after full combustion in air is less than 5% of the original weight. We estimate that the purity of the SWNT sample is over 90%.

B. Nitrogen Adsorption

Nitrogen adsorption isotherms were measured by the conventional volumetric method on a 15 mg sample. Nanotubes in the form of compact buckypaper were weighed and stored through the whole experiment in a small quartz thimble used to achieve high accuracy in sample weighing. The thimble with a known amount nanotubes was inserted into a 12 mm OD quartz adsorption tube and annealed at 1073 K for 3 h to remove carbon-oxygen functionalities from the nanotubes *(46, 47, 156, 157, 172, 191, 195, 197, 243)*. Upon annealing, the sample was repeatedly weighed and returned to the tube for immediate initial isotherm measurement. A filler rod was utilized to decrease the dead volume of the adsorption tube and to enhance the accuracy of defining of the adsorbed amount of nitrogen. The isotherm measurements were carried out on a Quantachrome Autosorb 1 MP instrument equipped with 1 mTorr pressure transducer. In total, 132 points were recorded starting at 10^{-6} relative pressure. The temperature transpiration effect was accounted for automatically by the instrument.

C. Nonane Preadsorption

N-nonane (99+% purity) was purchased from Aldrich. An aliquot of nonane was placed into a small bulb and several freeze-pump-thaw cycles were used to remove air from the liquid.

After that nonane was distilled under vacuum into a bulb with zeolite to remove possible traces of water. An IR spectrum of the vapor taken after this purification did not show any impurities.

The adsorption tube containing nanotubes in the thimble was connected to the gas handling system and outgased at 573 K for more than 12 h. After cooling to room temperature the sample was exposed to the vapor of n-nonane at about 4.7 Torr for 30 min. After this the tube was immersed into ℓ-N_2 for a moment to condense n-nonane on the wall of the adsorption tube. As the tube warmed the condensed n-nonane melted and filled the thimble. The nanotubes were left for 10 min in ℓ-nonane and after this the n-nonane was desorbed at chosen temperatures for more that 24 h. The n-nonane desorption was carried at 298 K, 323 K, 348 K, 373 K and 523 K. Following n-nonane desorption, the adsorption tube with the sample was purged with dry nitrogen and immediately connected to the measuring port of the Quantachrome Autosorb 1 MP instrument for N_2 adsorption.

D. High Resolution α_S Plots

High resolution α_S-plots were obtained by plotting the measured amount of nitrogen adsorbed on the nanotubes versus the corresponding α_S. We used the values of α_S from ref. *(391)* where a standard adsorption isotherm was measured on a Cabot BP 280 nongraphitazed carbon black over a relative pressure range from 10^{-6} to 0.99 resulting in 104 points. The α_S at a particular relative pressure was obtained according to the formula $\alpha_S = n/n_{0.4}$, where n and $n_{0.4}$ are the amounts of adsorbed nitrogen from the isotherm of the standard Cabot BP 280 carbon sample at this relative pressure and at P/P_0=0.4, respectively. A more detailed explanation about the application of the α_S-plot method in N_2 adsorption studies can be found elsewhere *(238, 383, 389, 390)*.

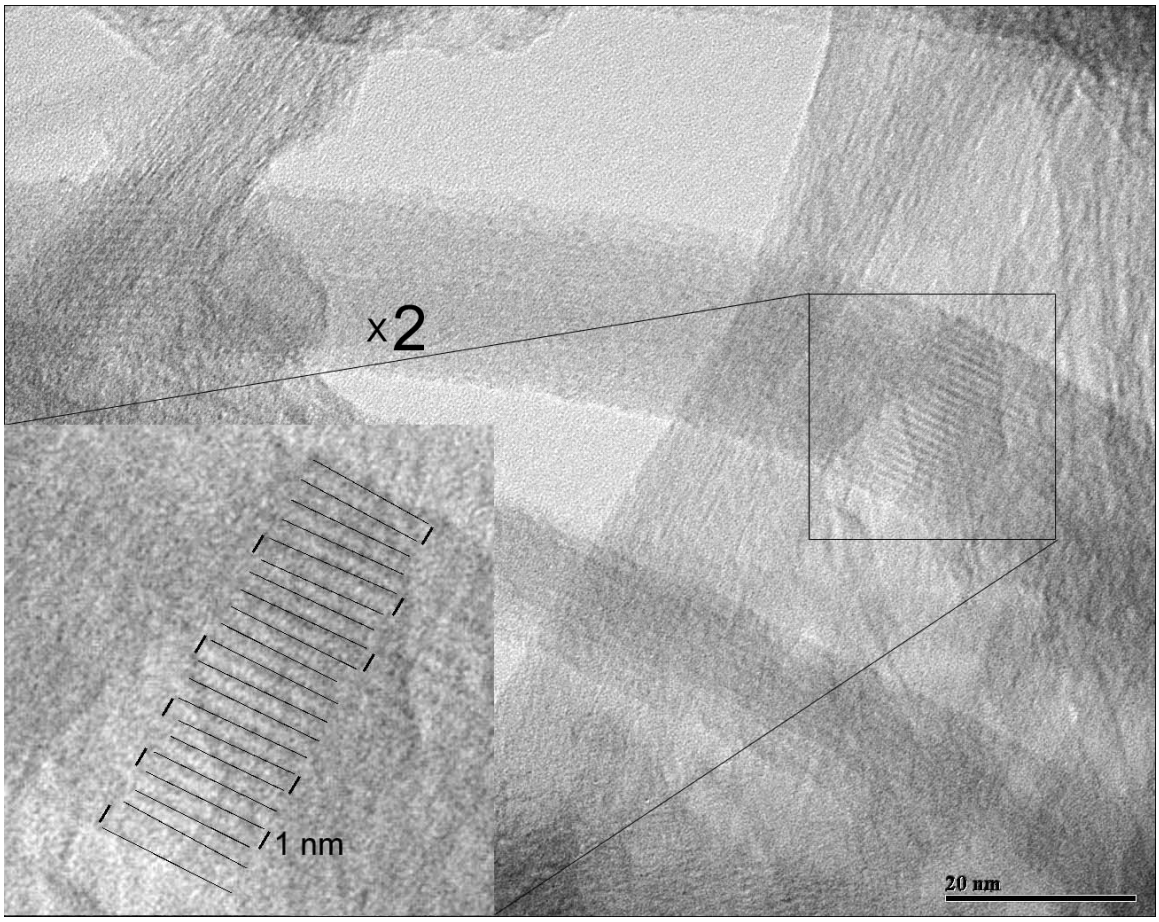

Figure 51. TEM image of single wall carbon nanotube. The nanotube bundled into ropes of various sizes. Nanotube diameters vary from in the 0.9 – 2.5 nm range. A small bar in the inset in the left corner is 1 nm long on the inset scale.

E. DFT Pore Size Distribution

The pore size distribution was estimated applying a Nonlinear Density Functional Theory (NDFT) kernel supplied by Quantachrome as a part of their software package. The distribution was calculated by fitting the experimental isotherm with a sum of theoretical isotherms that were computed for the carbon slit pore model. The details of this computation are described elsewhere *(232, 385, 386)*. In this paper we present the pore volume histograms and cumulative pore volumes versus pore sizes.

VII-4. Results

Figure 51 shows a TEM image of nanotubes. Nanotubes diameters vary in the 0.9 – 2.5 nm range however nanotubes with ~1.0 – 1.6 make the main fraction. Nanotubes are bundled into ropes of different diameters.

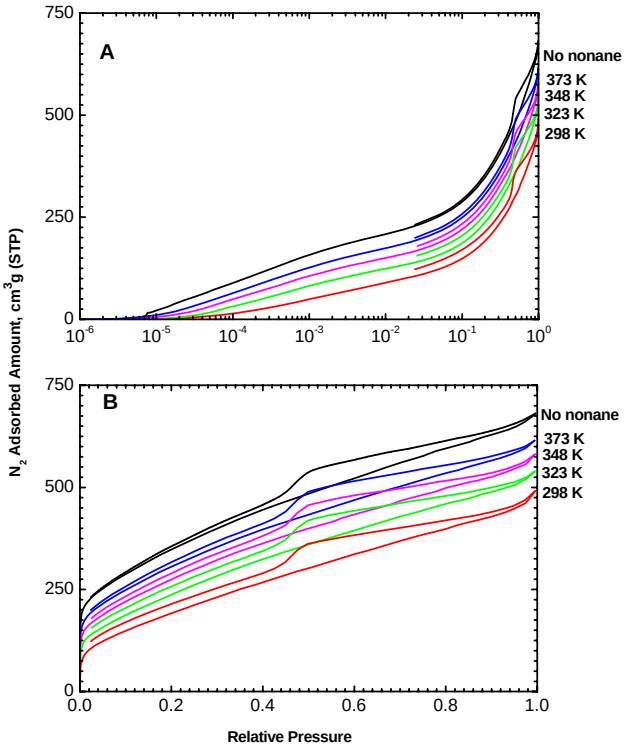

Figure 52. Representative nitrogen adsorption-desorption isotherms for nanotubes at different stages of n-nonane preadsorption. A. semilog scale; B. normal scale.

Figure 52 shows nitrogen adsorption isotherms on SWNTs measured at different stages of n-nonane preadsorption. For convenience, labels No nonane-, 298-, 323-, 348- and 373- are used on the plots to indicate SWNTs which are unfilled or filled with n-nonane and outgased at various temperatures. Figure 52A shows the isotherms on a semilog relative pressure scale to expand the low pressure area of the isotherms. As can be seen, N_2 adsorption starts at $P/P_0 \approx$

2×10^{-6} for the No nonane-isotherm whereas the beginning of the 298-isotherm is delayed to $P/P_0 \approx 2\times10^{-5}$. The amount of adsorbed nitrogen at relative pressures below 0.01, i.e. in the microporous regime, is several times higher for the No nonane-isotherm than that for the 298-isotherm. All isotherms have a similar hysteresis loop in the 0.4 - 1.0 relative pressure range on the adsorption branch of the isotherm, as seen from Figure 52B. Desorption branches increase their deviations from the adsorption lines from $P/P_0 = 1.0$ down to $P/P_0 \approx 0.44$ then sharply approach the adsorption branches. For the No nonane-isotherm the hysteresis completely closes around $P/P_0 \approx 3\times10^{-2}$ whereas desorption and adsorption lines run almost in parallel for 298- and 323-isotherms in Figure 52A down to $P/P_0 \approx 0.05$. The mismatch of adsorption and desorption branches below $P/P_0 \approx 0.44$ can be explained by partial trapping of nitrogen at higher relative pressures either in the interstitial channels of nanotube bundles or inside nanotubes when filled with n-nonane. In the first case a swelling of nanotube bundles may occur which allows N_2 molecules into the enlarged interstitial channels. In the second case in addition to bundle swelling, nitrogen can mix with n-nonane inside nanotubes. In both cases nitrogen trapping is a kinetic effect related to a potential barrier a molecule needs to overcome in order to desorb; this barrier is higher for nitrogen trapped by mixing with n-nonane. All the N_2 isotherms presented in Figure 52 can be classified as type VI according to the IUPAC classification.

Figure 53 shows the high resolution α_S-plots for the sample at different levels of n-nonane preadsorption. An upward swing below $\alpha_S \approx 0.2$ is observed for No nonane-, 373-, and 348-α_S-plots with the highest value for the No nonane-α_S-plot. This swing originates from the N_2 monolayer adsorption enhanced by the micropore field and is called the "filling swing" *(389)*. There is no filling swing in the 298- and 323-α_S-plots. Straight line sections of No nonane-, 373-, 348-, and 323-α_S-plots in the 0.2 - 0.55 region of α_S correspond to monolayer filling in

mesopores and macropores and can be used for apparent specific surface area calculations. The slope of this straight line is proportional to the external specific surface area and the intercept is equal to the micropore volume. The next upward swing observed for all α_S-plots above $\alpha_S = 0.6$ is called the "cooperative swing" and corresponds to filling of residual pore volumes left upon N_2 monolayer completion *(389)*. This process can not be considered as classic capillary condensation due to the uncertainty of the definition of the meniscus for very narrow pores. In all α_S-plots presented here the increase of the cooperative swing slows after $\alpha_S = 1.6$.

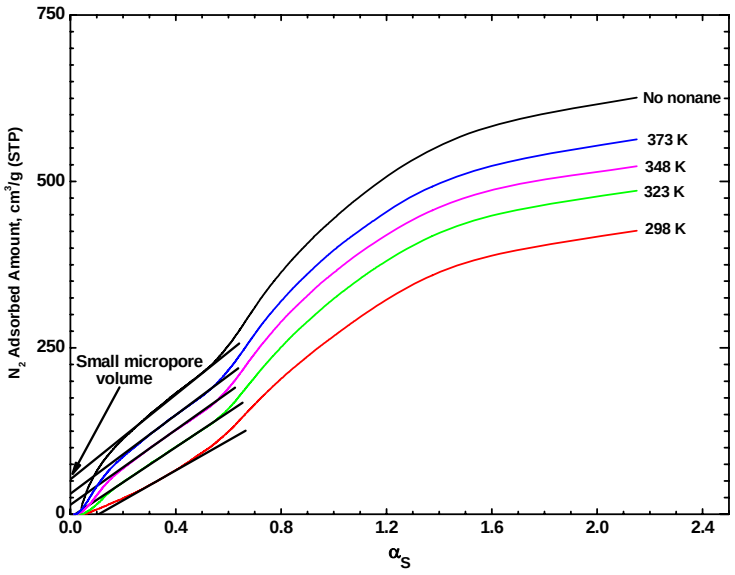

Figure 53. High resolution α_S-plots obtained for the sample at different stages of nonane preadsorption. The intercepts of the dashed and straight lines give the total pore volume and micropore volumes.

Figure 54A and Figure 54B show the cumulative pore volume (CPV) plots and pore size distribution (PSD) histograms, respectively, for adsorption isotherms on SWNTs measured at different stages of n-nonane preadsorption. The 298- and 323-CPV plots as well as correspondent PSD histograms start above ~10 Å indicating that n-nonane is retained by 10 Å micropores up to 323 K. The other regions of the CPV plots and PSD histograms have very

similar profiles for all stages of n-nonane preadsorption. This corroborates the previous conclusion that n-nonane is retained only by small micropores with diameters no more than 10 Å. There are two families of peaks observed in the PSD histograms corresponding to large micropores with 10-20 Å and mesopores with 20-50 Å diameters. The volume of the 20-50 Å mesopores is approximately three times larger than that of 10-20 Å mesopores.

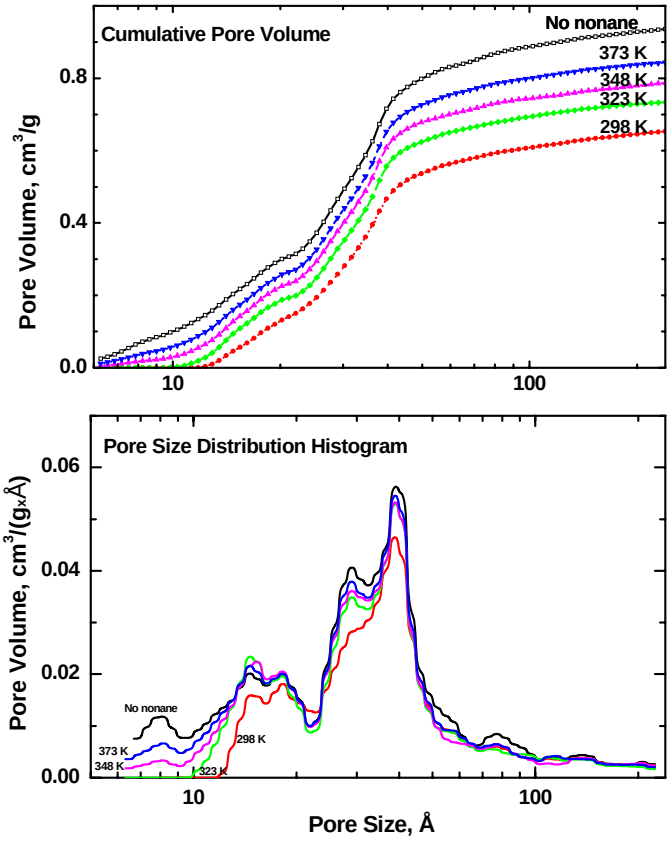

Figure 54. A. Density Functional Theory cumulative pore volume plots; B. Pore size distribution histograms.

Table 9 summarizes the characteristics of the nanotube material studied. The total α_S surface area of the sample was obtained from the slope of the line drawn from the origin and tangent to the No nonane-α_S-plot at $\alpha_S = 0.55$. The total α_S volume was calculated from the amount of adsorbed N_2 at $P/P_0 = 0.98$ of the No nonane-isotherm. The DFT small micropore and

total pore volume were obtained from the No nonane-CPV plots for 10 Å and 200 Å pores respectively. The BET specific surface area was calculated in the 0.05-0.3 region of the No nonane-isotherm. The external BET surface area was assumed to be equal to the surface area obtained from the 323-isotherm. The small micropore volume was calculated from the difference of nitrogen amounts for the No nonane-isotherm and 323-isotherm at $P/P_0 = 3 \times 10^{-4}$ where all nanotubes with diameters below 14 Å should be filled *(171)*.

Table 9. Summarized Characteristic of Studied Nanotube Material.

Method	Pore Volumes, cm^3/g		Specific Surface Area, m^2/g	
	Small micropores (nanotube diameters ≤ 14 Å)	Total	External	Total
α_S	0.08	1.02	718	1127
DFT	0.09	0.93	-	-
BET + nonane	0.10	-	911	1262

VII-5. Discussion

Nonane blocking of micropores has been extensively used for porosity characterization of different carbons *(238, 383)*. It was shown that nonane, if subjected to pumping below 323 K, is retained in different carbons containing micropores narrower than ~7 Å or ~10-11 Å when π-orbitals are taken into account *(392)*. Temperature programmed desorption (TDP) studies of n-nonane adsorption on SWNTs conducted by Kondratyuk et al. *(194)* indicate that nonane can be retained in nanotubes with a mean diameter of 13.6 Å upon outgasing at 323 K. N-nonane blocking is a kinetic effect so n-nonane can be eventually desorbed; however, N_2 adsorption

isotherms were measured at 77 K, and at this temperature the residence time for n-nonane inside carbon nanotubes is infinite on the time scale of the experiment. Figure 54 presents pore size distributions for carbon nanotubes calculated employing the slit-pore model. Surprisingly, the 323-PSD shows that nonane is retained by ~10 Å pores (or 13-14 Å diameter nanotubes) that corroborates the TPD experiment. It is known that adsorption in a cylindrical pore occurs at lower pressures relative to a slit pore of comparable size *(393)*. Therefore a nanotube size distribution calculated adopting the slit-pore model should underestimate nanotube diameters. The origin of this coincidence is not clear and the results obtained from slit-pore DFT pore size distribution are included here only for comparison with other micropore estimation methods.

Figure 54B shows that there are three pore size regions in PSD histograms. The first region is below 10 Å and covers small micropores that can be assigned mostly to the interior of small diameter (< 14 Å) nanotubes. A rough estimate of the volume of these nanotubes is specified in the Table 9 and is not larger than 0.1 cm^3/g constituting only 10% of the total pore volume. The reduced contribution of small diameter nanotubes to the total pore volume is corroborated by low nitrogen uptake at $P/P_0 < 10^{-5}$. Below this value of relative pressure nanotubes with diameters below ~14 Å should be filled with N_2 at 77 K whereas a 15.2 Å nanotube is only ~50 % filled at $P/P_0 \approx 10^{-5}$ *(171)*.

The second region covers ~10-20 Å pores or the interior of nanotubes with ~14-23 Å diameters and has ~ 0.2 cm^3/g volume. Our TEM studies (Figure 51) show that the fraction of ~14-23 Å nanotubes is lower relative to the nanotubes with diameters below ~14 Å. The higher volume of the second region is explained by larger volume of bigger diameter nanotubes, for instance, a 20 Å tube is 2.5 or 6.3 times more capacious than 14 or 10 Å one.

The third region encompasses ~20 - 50 Å mesopores exhibiting ~0.5 cm^3/g volume. A TEM study indicates that the fraction of nanotubes with diameters above ~25 Å is not significant. This mesoporosity may result from the voids in the complex net structure formed by nanotube bundles and individual nanotubes. All together nanotubes form only 30 % of the total pore volume that, when the higher capacity of larger diameter nanotubes taken into account, indicate that the mild air oxidation is not sufficient to open the majority of nanotube in the sample. This contradicts with the assumption we made in our earlier study *(172)* that due to a high BET surface area the main fraction of nanotubes is open. This study shows that adsorption sites other than nanotube interior may contribute to the BET surface area and n-nonane blocking can be very helpful in determining the fraction of opened nanotubes.

VII-6. Summary

The following conclusions were made from the study of nitrogen adsorption on SWNTs containing preadsorbed n-nonane:

1. Adsorbed n-nonane is retained only on small diameter (< 14 Å) nanotubes after desorption at 323 K for 24 hours.
2. The nanotube interior forms only ~30% of the total pore volume indicating that mild air oxidation at 400° C for 1 hour is not sufficient for opening the majority of carbon nanotubes.
3. The external surface area constitutes ~63-72% of the total area demonstrating that sites other than nanotube interior adsorption sites may substantially contribute to the total surface area of carbon nanotube materials and that the sorption properties may strongly depend on the material morphology.

VII-7. Acknowledgements

We gratefully acknowledge the Army Research Office for the support of this work. We also acknowledge the interest and support from Dr. Chris Karwacki at the Aberdeen Proving Ground, and the loan of the Quantachrome Autosorb instrument.

PART III

DESIGN, CONSTRUCTION AND TESTING OF A VACUUM SYSTEM – IR SPECTROMETR FOR STUDIES OF ADSORPTION ON HIGH AREA SOLID SURFACES

PREFACE

In this section I describe my activities in the design, construction, and testing of a system for IR spectroscopy investigations on high area surfaces. This supplements my experience on an existing vacuum-IR system which had been built before my arrival at the University of Pittsburgh. I gained new experience for the designing and construction and testing of this new equipment.

SYSTEM DESIGN

A. Vacuum System and IR Cell Design

A new vacuum system for transmission IR measurement on high surface area powder has been built based on the experience gained while working with the IR system described in the Part I. Since the methodology and investigated materials were similar to those used in previous studies, the new system was designed integrating the advantages of the one in use, but in addition some improvements were also introduced. The approach used for IR studies of adsorption and reaction on high surface area powder by Basu and Yates *(244)* has been proven to be very successful and has the following advantages: excellent sample temperature control, high speed of sample temperature change, wide pressure (10^{-7} – 10^{3} Torr) and temperature (90 – 1000 K) ranges, low thermal gradients across the sample, small volume of the IR cell, small spectrometer purging volume (to remove atmospheric CO_2 and H_2O), and automated sample positioning. However, the hardware that incorporated this approach lacked some very helpful features which were included in the new system design. The new system is equipped with pressure gauges (cold cathode and capacitance manometer) directly in the IR cell, its pumping speed is increased by using high diameter tubing, and a sample can be moved independently of the IR cell. In addition the QMS is connected directly to the cell and the cell is provided with a heated doser which allows exposing the sample to chemicals with limited volatility.

Taking into account both positive and negative experiences the new system was designed according the following concepts:

- Excellent sample temperature control
- Excellent IR cell pressure measurements
- Availability of chemical analysis of the gases in the IR cell

- Precise and easy sample and IR beam alignment
- High pumping speed
- Availability of direct dosing onto the sample
- IR cell versatility and replacement simplicity

The detailed description of the new system is given in the following text.

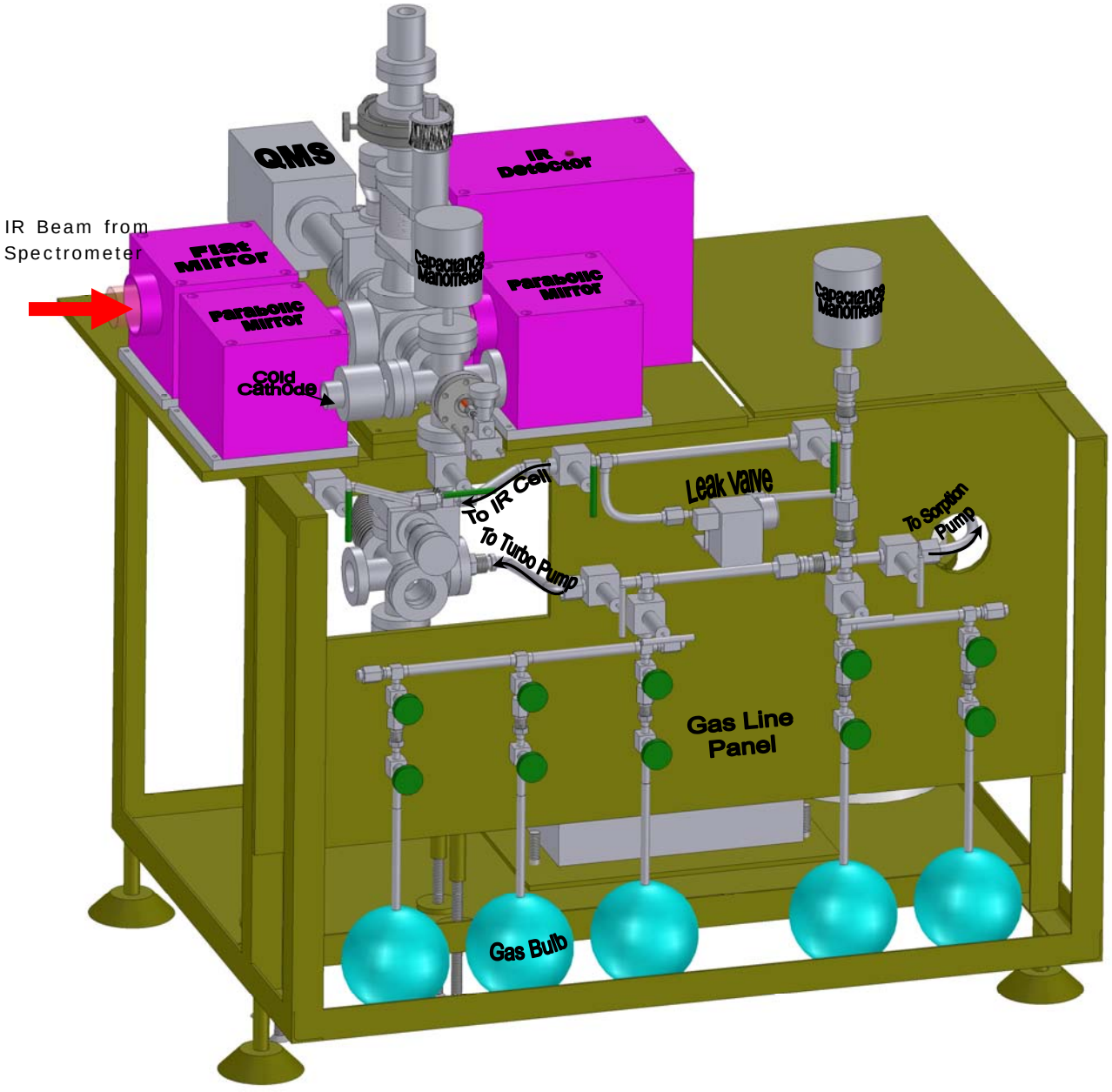

Figure 55. General view of the transmission IR system.

Figure 55 shows the general view of the vacuum system for transmission IR studies of gas adsorption and reaction on high surface area powders. The system consists of the following parts: 1) IR cell with sample holder and manipulator; 2) pressure gauges and QMS for gas chemical composition; 3) gas dosing part; 4) gas handling line; 4) vacuum generation part; and 5) optical bench. All these parts are fixed on a mobile support rack and can be easily disconnected and replaced.

The sample holder and manipulator are shown in Figure 56. A sample of high surface powder can be pressed or sprayed onto a piece of tungsten grid stretched between two Ni clamps. The clamps are connected to copper power leads that serve for current conductance and heat exchange with the refrigerant in the metal dewar. The grid can be resistively heated to ~1500 K and cooled to ~83 K when liquid nitrogen used as a refrigerant. Due to the absence of any isolation between the sample and ℓ-N_2 bath and because of small thickness (0.002") of the W grid the sample temperature and be easily and quickly changed which allows temperature programmed studies. The sample temperature is measured by a K type (alumel-chromel) thermocouple spot-welded at the top of the grid. Temperature control is achieved by means of a Lab View program which adjusts the power supplied to the grid according to a preset temperature-time profile by using feedback signal from the thermocouple. The thermocouple wires and power leads are sealed in and go through a feedthrough that is connected to a metal dewar where a refrigerant is stored. Sample position can be vertically adjusted by means of the Z-stage which allows a 2" travel. In that way three or four samples (a 7 mm diameter disk pressed into the grid) can be easily studied at the same conditions. Moreover the sample can be azimuthally adjusted by means of the differentially pumped rotatable manipulator placed on top

on the Z-stage. This option greatly facilitate temperature programmed desorption studies as well as direct dosing of weakly volatile chemicals.

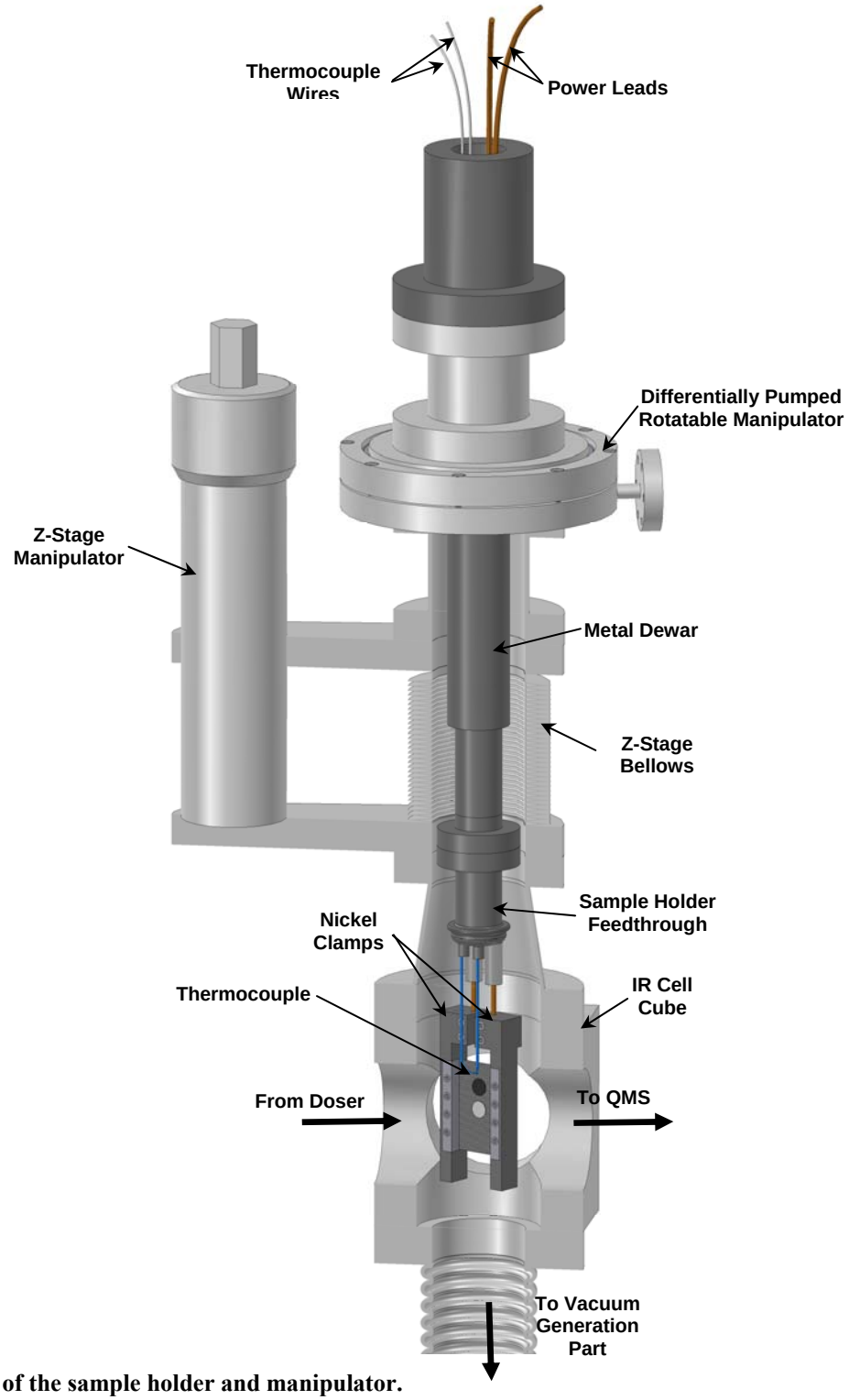

Figure 56. View of the sample holder and manipulator.

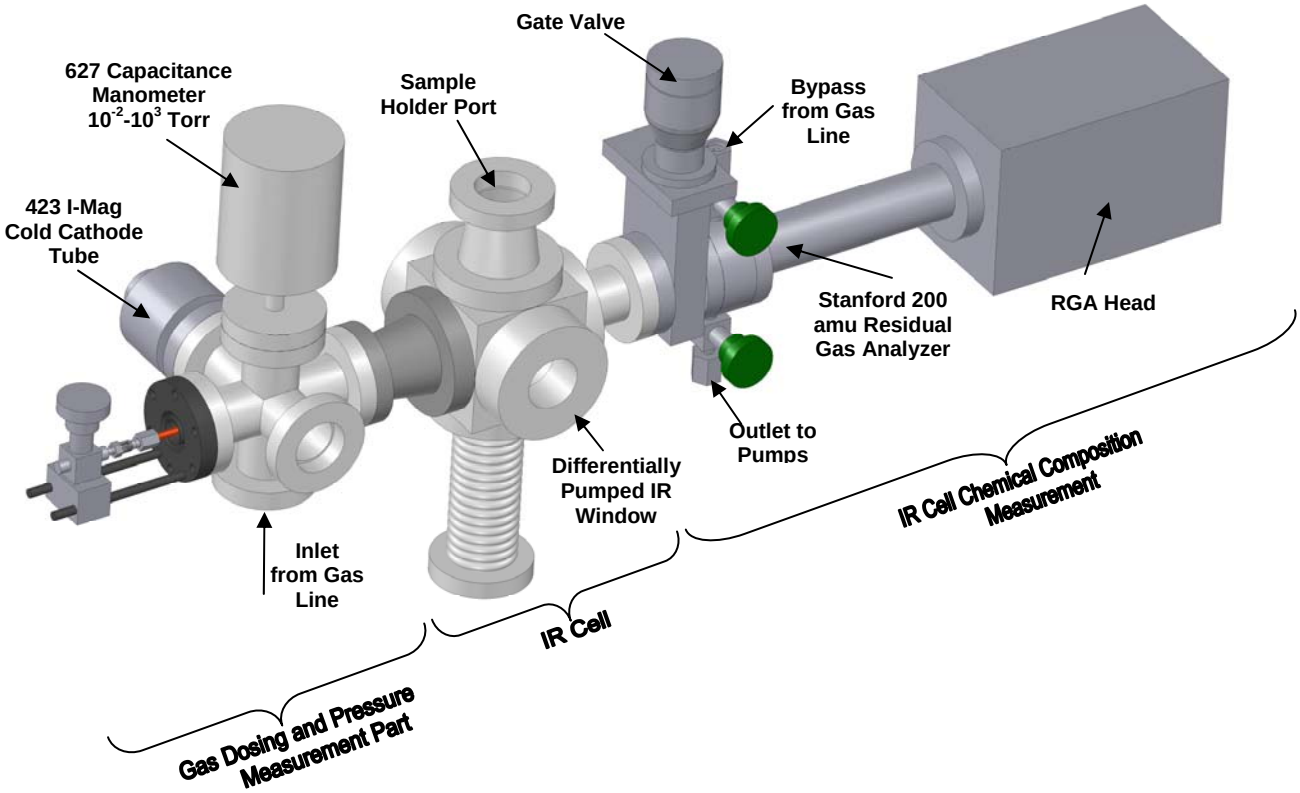

Figure 57. View of the pressure measurement and chemical composition detection parts.

Figure 57 shows the assembly of the IR cell with the residual gas analyzer and the gas dosing and pressure measurement part. The IR cell is made of a 3 3/8" six way stainless steel cube. The sample manipulator is positioned on top of the cube via a cone adapter. Two KBr windows are sandwiched with rubber O-rings between two stacked metal plates which are also separated by a larger concentric O-ring. The space between the KBr window and the plates is confined by the concentric O-ring and is constantly pumped allowing one to maintain $\leq 10^{-8}$ Torr base pressure. The front part of the IR cell is connected to the gas dosing and pressure measurement part. Two pressure transducers, a cold cathode and a capacitance manometer, are used to cover the 10^{-9} – 10^{-2} and 10^{-3} – 10^{2} Torr pressure ranges respectively. The choice for a cold cathode is dictated by the desire to sudy organic molecules, which would be easily decomposed by a hot ionization gauge. During the experiments the cold cathode gauge is shut

down. The residual gas analyzer (RGA) is connected to the back of the IR cell and used for monitoring gas chemical composition in the cell and also for system leak checking. In addition by turning the manipulator by 90° relative to the IR beam one can orient the sample so the desorbing species would be in line of sight to the mass spectrometer. This configuration is useful for temperature programmed studies as shown in the following chapter. The RGA is equipped with a spacer with two valve isolated ports. One port is connected to the gas line and the other to the vacuum generation part of the system. This is done for testing gases for purity bypassing the IR cell if a sample can not be exposed to the gas. When the IR cell is pressurized the RGA is isolated by a gate valve and the bypass line, connected to the vacuum generation part, is used for keeping the sensitive QMS elements in vacuum.

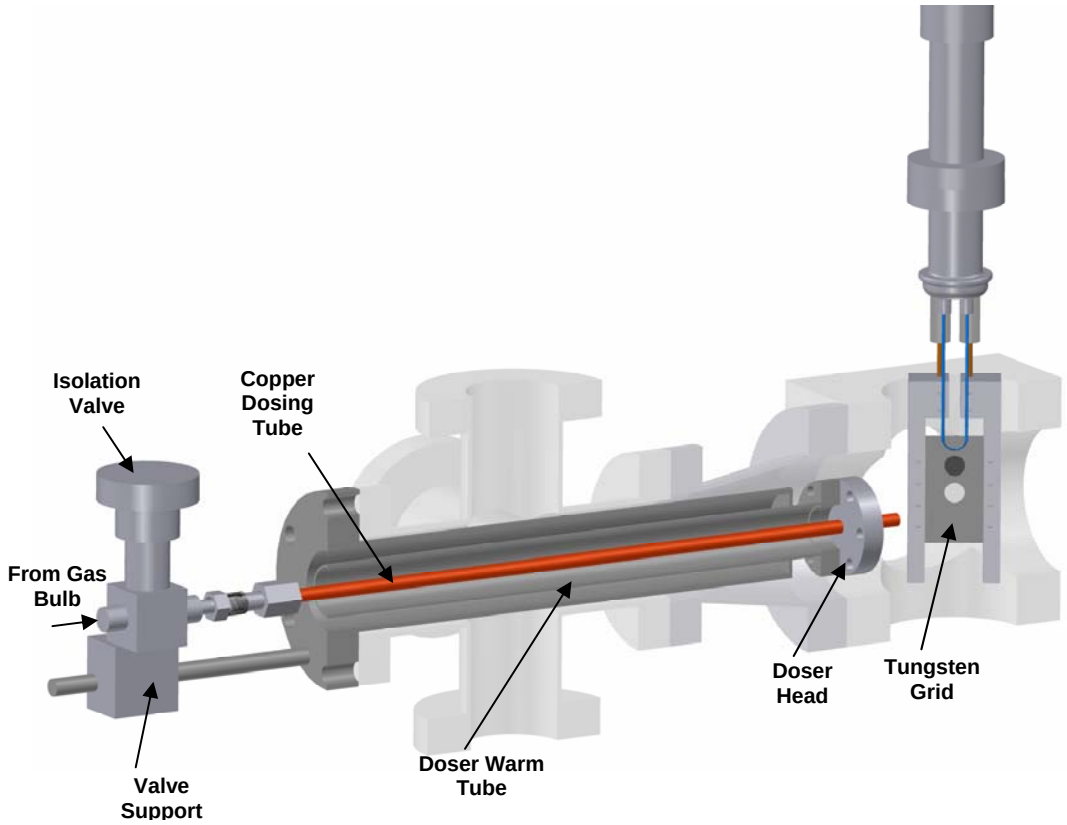

Figure 58. The high temperature doser. The cube of the IR cell and doser connectors are made semitransparent for better view.

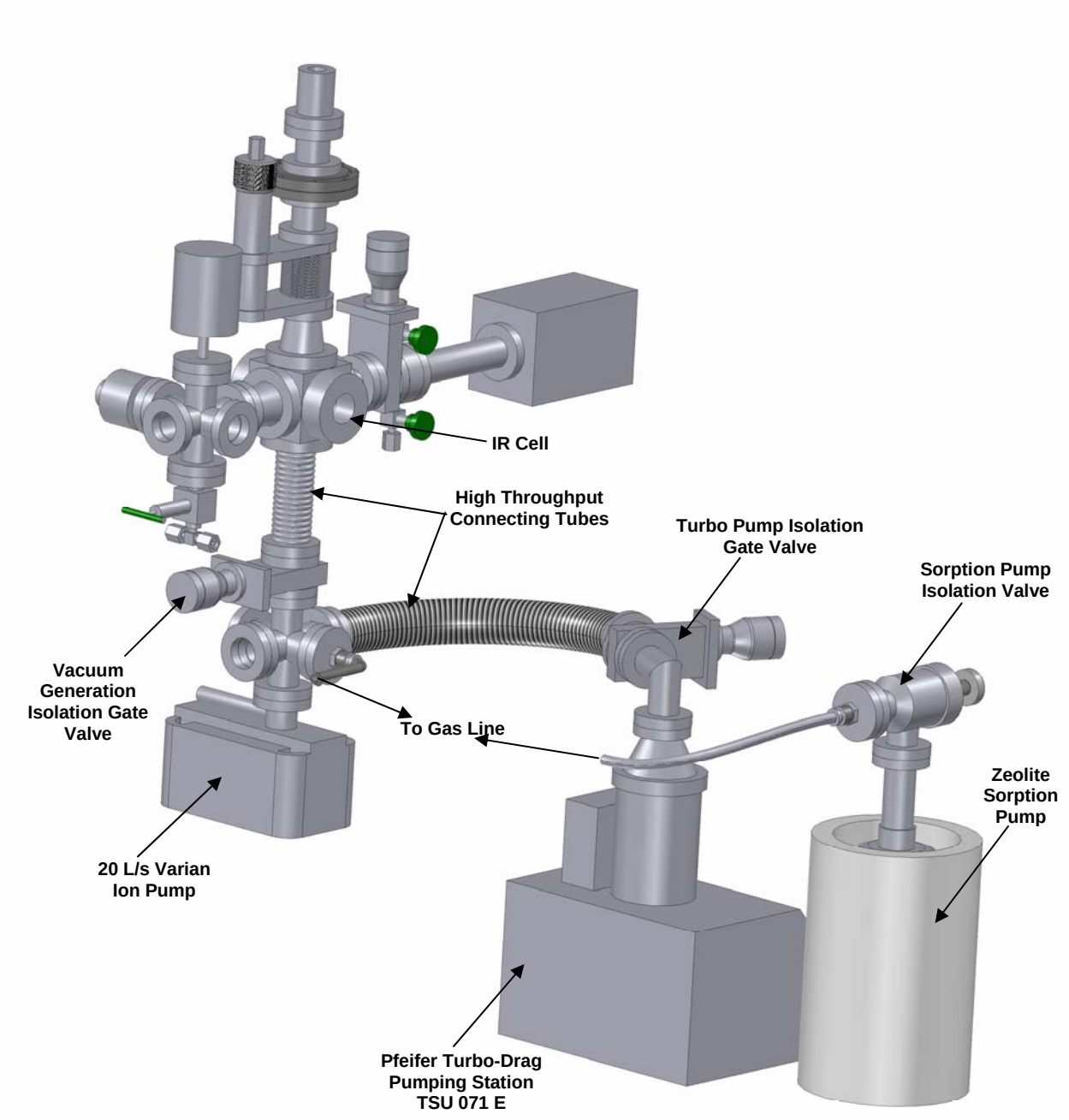

Figure 59. View of the system vacuum generation part.

Figure 58 shows the cross-section of a high temperature doser. The doser is built to introduce low volatility chemicals directly onto the sample. It consists of a copper tube soldered into a 0.33" flange from one side and connected to a VCR joint on the other side. The copper

tube can be heated by a heating tape to increase the vapor pressure of the weakly volatile chemical. The copper gas delivery tube and the heating element are encased in a stainless tube labeled in Figure 58 as “Doser Warm Tube”. This assembly in enclosed in a second stainless tube and air may be drawn through this annular space for cooling if necessary.

Figure 59 shows the system vacuum generation part along with the IR cell assembly. The requirement for low cell volume does not allow using a large chamber with all parts attached directly to it. On the other hand utilizing of very small connectors decreases the pumping efficiency. In this design the IR cell is connected to the vacuum generation part via connector tubes with internal diameters of 1.3” or larger. After purging, the system is first pumped by the sorption zeolites pump down to ~10^{-3} Torr and then pumping is continued by the Turbo-Drag pumping station (a turbomolecular pump coupled with an oil free mechanical pump) which can produce ~10^{-8} Torr vacuum. Even deeper vacuum can be reached by using the 20 l/s ion pump located directly under the IR cell. The pressure at the turbomolecular pump is monitored by a hot ionization gauge. The Turbo-Drug pumping station is set on an independent platform to decrease vibration of the whole system.

B. Optical Design

Figure 60 show the top view of the optical bench used for measuring transmission IR spectra. An IR beams is directed from a Bruker Tensor 27 FTIR spectrometer via the side port onto a flat mirror, then the beam is reflected by a gold plated parabolic mirror and focused onto the sample. Another gold plated parabolic mirror is used to collect the transmitted IR light, collimate it and redirect onto a collecting mirror that reflects the beam onto the detector. All four mirrors are equipped with position, tilt and angle adjustment gears for precise focusing of the IR beam. The alignment of the IR beam onto the sample can be done by observation of the diffuse

light scattered by the powder pressed into the grid. The external optical bench allows fast and facile beam and sample alignments due to easy access to the scattered light from all angles. The mirrors and detector are encased into containers which are connected by rubber sleeves. This assembly is constantly purged with water- and carbon dioxide-free nitrogen gas.

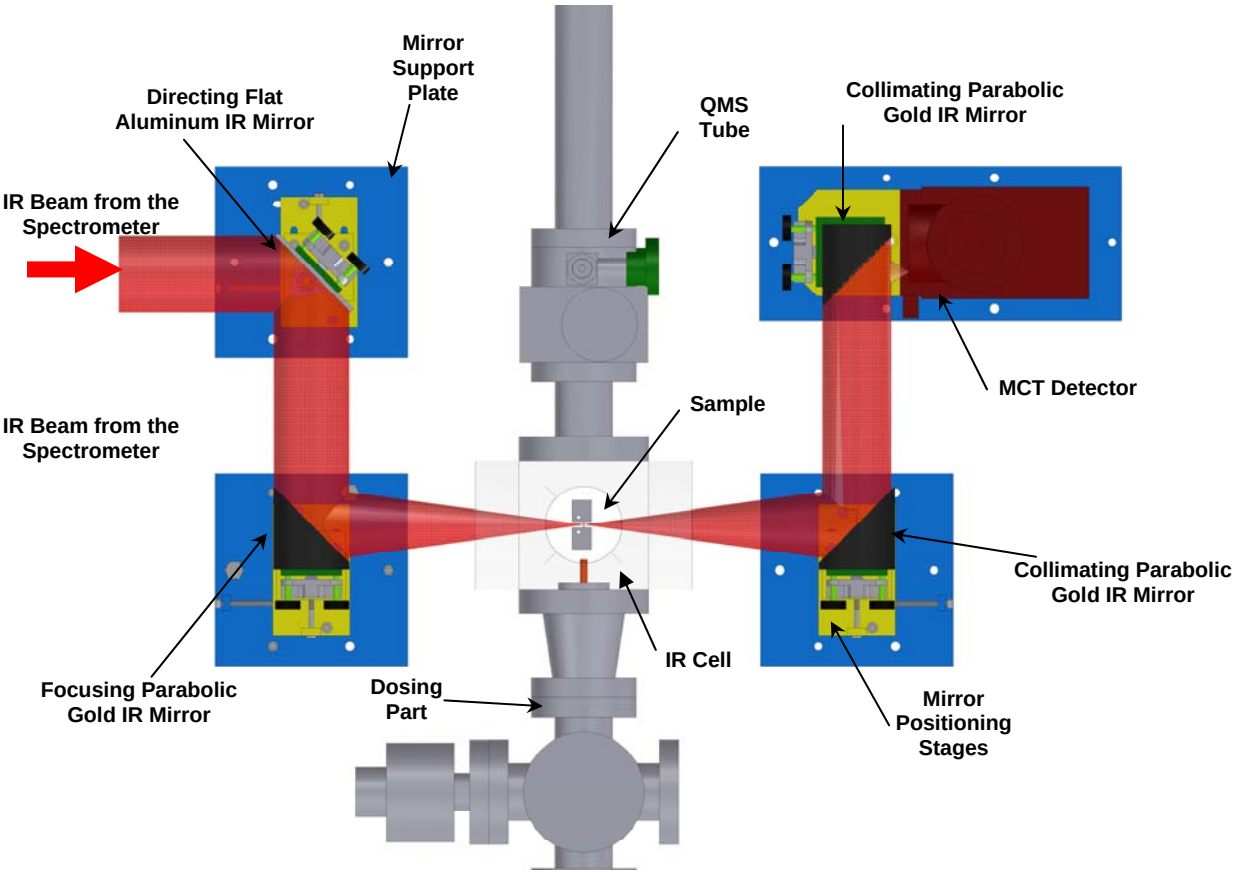

Figure 60. Top view of the system optical bench.

In general this design has been proven to be very useful and versatile. The system allows for many modifications and add-in components. The following work is included in this chapter to demonstrate the performance of this system.

VIII. TRIETHYLENDIAMINE ADSORPTION ON Al_2O_3*

VIII-1.Abstract

The adsorption of triethylenediamine (TEDA) at 300 K is observed to occur via hydrogen bonding to isolated Al-OH groups on the surface of partially dehydroxylated high area γ-Al_2O_3 powder. This form of bonding results in +0.3 to +0.4% blue shifts in the CH_2 scissor modes at 1455 cm^{-1} and a -0.4% red shift in the CN skeletal mode at 1060 cm^{-1}, compared to the gas-phase frequencies. Other modes are red shifted less than 0.1%. The isolated OH modes are red shifted by -200 to -1000 cm^{-1} due to the strong hydrogen bonding association of Al-OH groups with an N atom in TEDA. Thermal desorption of adsorbed TEDA from the surface occurs in the range 300-700 K. Mass spectral and infrared studies indicate that the decomposition of TEDA occurs on Al_2O_3 above 725 K, and that C-H bonds are broken, forming adsorbed species with N-H bonds which are stable to 1000 K or above. In contrast to adsorption at 300 K, adsorption of TEDA at 85 K results in the formation of a condensed ice of TEDA, which covers the outer surface of the porous Al_2O_3 and which does not interact with Al-OH groups inside the porous powder due to immobility.

* Reproduced with permission from S. Kim, O. Byl, J. T. Yates, Jr.; Adsorption of Triethylendiamine on Al_2O_3 – I: a Vibrational Spectroscopic and Desorption Kinetic Study of Surface Bonding. Journal of Physical Chemistry B 109(8), 3507-3511 (2005). Copywrigh 2005 American Chemical Society.

VIII-2.Introduction

The adsorption of triethylenediamine (TEDA) [systematic name: 1,4-diazabicyclo[2.2.2]octane (DABCO)] has not been studied using infrared spectroscopy. Because of its highly symmetrical structure, exposing two tertiary amine moieties at its two vertices, adsorption would be expected to occur at one end of the molecule, leaving exposed the other reactive amine group. Surface functionalization by adsorbed TEDA could therefore result in the production of strong electron donor surface properties. It is reported that TEDA is adsorbed on a silica surface via one nitrogen atom with the other nitrogen free at high coverage of TEDA *(394)*. In addition, two nitrogen atoms in a single TEDA molecule may bind with neighboring OH groups on silica surfaces. TEDA binds to the nitrile group or to the methyl group in methyl iodide via its nitrogen atom. In environmental and military applications, TEDA has been impregnated on various supports in order to adsorb toxic gases (HCN, CNCl, SO_2, CH_3I, etc.) or as a sensor to detect these gases *(395-398)*. Despite many applications, there is a dearth of basic information about TEDA adsorption on surfaces. In the present paper, the chemical behavior of TEDA adsorbed on high surface area Al_2O_3 is investigated by transmission infrared spectroscopy and temperature programmed desorption techniques.

VIII-3.Experimental methods

The stainless steel ultrahigh vacuum (UHV) infrared cell and portions of the vacuum system are shown in Figure 61. The system was designed to provide temperature control of a porous solid adsorbent from 83 K to above 1400 K. The cell may be rapidly pumped and has provision for gas-phase analysis with a quadrupole mass spectrometer (QMS) during temperature programmed desorption (TPD). Compared to a similar previous design *(244)*, this cell features excellent conductance between the sample and the QMS, and also has higher pumping speed.

The cell has two differentially pumped KBr windows for the IR beam to pass and the cell itself is pumped with a turbomolecular pump (Pfeiffer Corp., model TMU 071P) to maintain a base pressure $P \leq 1.0 - 10^{-8}$ Torr after system bakeout at 400 K. The QMS (SRS, model RGA 200) is connected to the cell by a high conductance connection. The temperature of the sample can be varied with resistive heating and is controlled and linearly programmed by temperature control software. The lowest temperature obtained with liquid N_2 cooling of the reentrant Dewar is 83 K.

The γ-aluminum oxide powder was obtained from Guild Associates. The N_2 BET surface area is 250 m^2/g. The powder is pressed into a tungsten grid (0.002" thickness) using a hydraulic press *(399, 400)*. The applied pressure is about 7000 $lb/inch^2$. A type K thermocouple is welded on the upper edge of the tungsten grid. The grid is tightly clamped into Ni cooling bars which are bolted onto Cu electrical leads which also conduct heat from the grid + clamps into the reentrant Dewar. The Al_2O_3 is annealed in vacuum at 1200 K for 1 min to produce a highly dehydroxylated surface *(400-403)*. The treatment also removes traces of organic contaminants.

The triethylenediamine (TEDA) was obtained from Aldrich (98% purity) and was used without further purification. TEDA is dosed into the chamber through the gas line by sublimation at room temperature. The vapor pressure of TEDA at 297 K is 0.59 Torr. The pressure of the TEDA is measured by a Bayard-Alpert type ionization gauge (BAG) (Kurt J. Lesker Corp., model IG 2200) in the pressure range of $1.0 \times 10^{-3} - 2.0 \times 10^{-9}$ Torr and by a capacitance manometer (MKS Corp., model 627B) which has range of $1 \times 10^{-2} - 1 \times 10^{2}$ Torr. Care was taken not to use the BAG during actual TEDA dosing experiments in order to avoid decomposition by electron impact or by the hot filament.

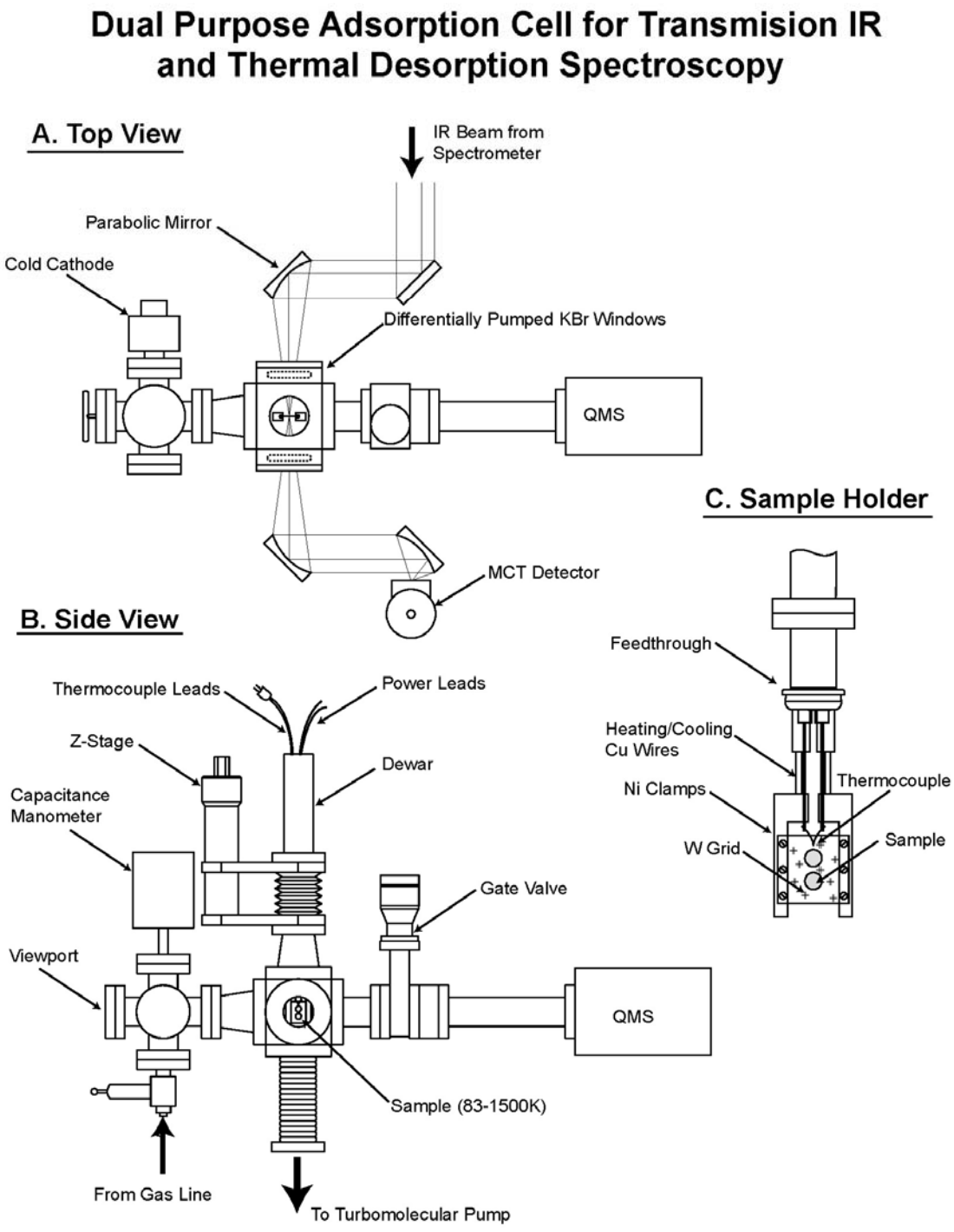

Figure 61. Schematic diagram of IR and temperature programmed desorption apparatus.

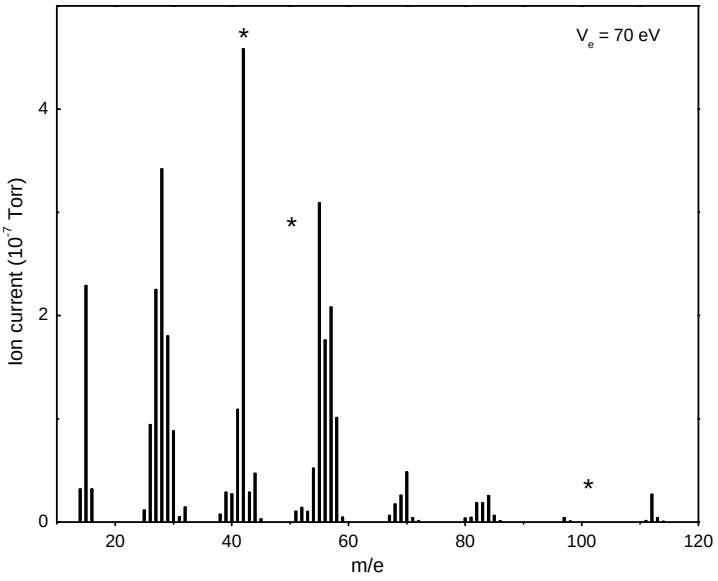

Figure 62. Mass spectrum of triethylenediamine (TEDA) gas phase. * = ion fragments used in temperature programmed desorption experiment.

The infrared spectra are collected with a Bruker TENSOR 27 FT-IR spectrometer by the transmission method. The spectrometer and the custom cell enclosure are purged continuously with gaseous N_2. The IR detector is a liquid N_2-cooled MCT detector manufactured by Bruker. Each spectrum is obtained by averaging 500 interferograms at 2 cm^{-1} resolution. The background spectra are taken through the empty grid region just before taking each spectrum of the Al_2O_3 sample. Spectral subtraction is used to eliminate the effect of any gas-phase contribution as well as other effects in the infrared cell.

TEDA coverages at 300 K are adjusted by controlling the equilibrium pressure of TEDA admitted to the cell. Coverages at 85 K are controlled by the admission of a known number of molecules to the cell. When the Dewar is at 77 K, an unknown fraction of the admitted TEDA condensed on the outer surface of the Dewar.

The mass spectrum of gas-phase TEDA was measured at an electron energy of 70 eV. Three prominent mass spectral peaks are characteristic of TEDA at m/e) 112 (parent), m/e) 55, and m/e) 42. A bar graph of the mass spectral cracking pattern is shown in Figure 62, where corrections for small quantities of residual gases present in the vacuum system have been made.

VIII-4.Experimental Results

VIII-4A. Transmission IR Studies of TEDA Adsorption on Hydroxylated Al_2O_3.

To interpret the spectra of adsorbed TEDA, the spectrum of TEDA in the gas phase was measured at 300 K. Figure 63 shows the infrared spectrum of: (a) gasphase TEDA; (b) condensed TEDA at 85 K on the outer surface of an Al_2O_3 sample; and (c) adsorbed TEDA at 300 K on Al_2O_3. The vibrational modes have been assigned into general categories as shown. The frequency and assignments of the vibrational modes for the gas-phase TEDA molecule, and for the adsorbed and condensed phases of TEDA from our studies are given in Table 10 *(404, 405)*. In subsequent work, we will use the fractional shifts of the infrared frequencies of the adsorbed TEDA (compared to TEDA (g)) as a means of qualitatively understanding the surface bonding. Table 11 lists the red and blue shifts for the various vibrational modes of the adsorbed TEDA molecules.

Several general features of the three phases of TEDA may be seen qualitatively from the spectral comparison. (1) The spectral line shapes for the vibrational modes of the gas-phase TEDA differ from that of both condensed and adsorbed TEDA. This is due to vibration-rotation structure in the gas-phase spectrum which does not exist for the condensed or adsorbed molecules. (2) The absorption bands are both broad and overlapped in the adsorbed TEDA phase. In contrast, in the condensed TEDA phase the absorption bands are sharper and some of the bands present in gas phase are absent. Compared to the previous results *(404)*, which are

given in parentheses in Table 10, there is little difference in the observed frequencies of vibrational modes for the condensed TEDA ice film. (3) Even though the modes below 1000 cm^{-1} are not seen for TEDA on Al_2O_3 as a result of the cutoff band due to lattice modes in the Al_2O_3, the informative CN skeletal deformation mode at 1060 cm^{-1} can be accurately observed in the presence of the oxide cutoff band. (4) The isolated Al-OH modes near 3700 cm^{-1} are observed in the condensed TEDA spectrum at 85 K but disappear for TEDA adsorbed at 300 K. This means that diffusion of TEDA into the internal pore structure of the Al_2O_3 does not occur at 85 K. TEDA is expected to adsorb on Al_2O_3 with hydrogen bonding via the N atom by interaction with isolated Al-OH groups at 300 K.

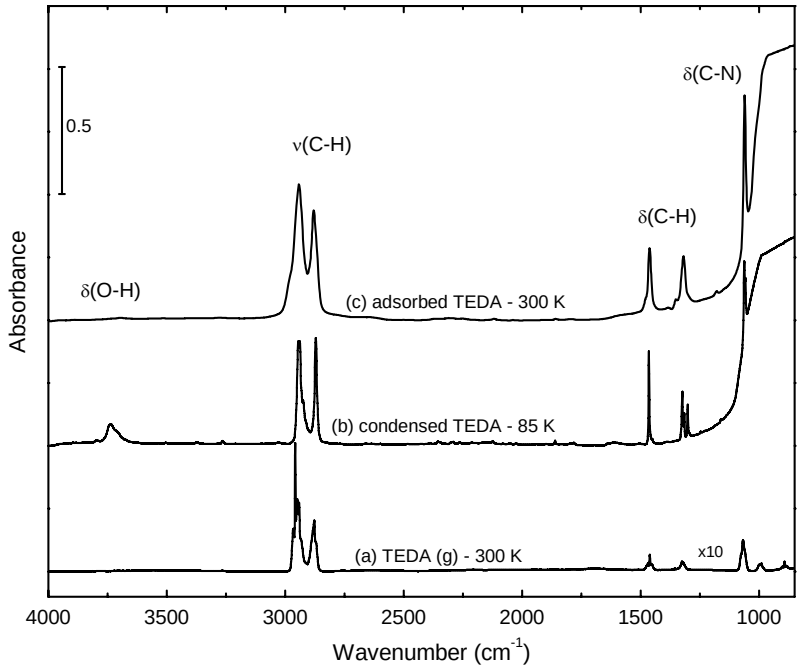

Figure 63. FTIR spectra of TEDA: (a) in gas phase at 300 K; (b) in condensed phase on Al_2O_3 at 85 K; (c) in adsorbed phase on Al_2O_3 at 300 K.

Table 10. FT-IR spectral data and vibrational assignment for TEDA.

Gas Phase 300 K [260 mTorr] (cm^{-1})	Adsorbed Phase on Al_2O_3			Assignment
	300 K [260 mTorr] (cm^{-1})	300 K [5 mTorr] (cm^{-1})	85 K [a] (cm^{-1})	
2964 (s)				CH_2 sym.str. [b, c]
2954 (s)	2954	2955		
2946 (s)	2946	2943	2945 (2945)	
2938 (s)	2938		2938 (2937)	
2929 (sh)	2928	2930	2924 (2923)	
2880 (sh)	2880	2882		CH_2 asym.str. [b, c]
2874 (s)	2873		2871(2870)	
2866 (s)	2866	2868		
1465 (m)	1465	1466	1465 (1464)	CH_2 sci. [b c]
1458 (m)	1461	1461		
1450 (w)	1455	1456	1450 (1451)	CH_2 sci. [b, c]
1352 (w)	1352	1351		CH_2 wag. [c]
1323 (m)	1322	1324	1324 (1323)	CH_2 twist .[b]
1317 (m)	1316	1316	1316 (1315)	CH_2 twist. [b]
1295 (w)	1294	1294	1302 (1302)	CH_2 wag. [c]
1072 (s)				
1064 (s)	1060	1060	1062 (1062)	CN skel. [b, c]
1056 (s)			1057 (1052)	
995 (m)				
988 (m)	987		990 (991)	CC skel. [b, c]

[a] Frequency in parentheses is from ref. *(404)*, where IR spectrum is obtained from TEDA polycrystalline film deposited on KBr window at 83 K. [b] This assignment is based on ref. *(404)*. [c] This assignment is based on ref. *(405)*.

At sufficiently low temperature, TEDA is frozen as an ice on the outer surface of the Al_2O_3. The development of the condensed TEDA layer on the Al_2O_3 surface as a function of increasing dosage at 85 K is shown in Figure 64. It may be seen that condensation occurs monotonically without any change of the pattern of the vibrational modes of TEDA as dosage increases, and that the isolated Al-OH stretching modes are not influenced at any coverage of

condensed TEDA. In contrast to the experiment at 85 K, Figure 65 shows the spectral developments for the vibrational modes of TEDA during adsorption at 300 K. Each spectrum is taken when the pressure of TEDA has reached equilibrium at 300 K. As will be shown below, TEDA bonds to Al-OH groups by hydrogen bonding. TEDA would be also expected to adsorb at Lewis acid (Al^{3+}) sites on Al_2O_3.

Table 11. Mode shifts of adsorbed TEDA /Al_2O_3 vs. TEDA in gas phase.

Frequency [a] (cm^{-1})	Red Shift		Blue Shift		% shift [b]	Mode
	260 mTorr	5 mTorr	260 mTorr	5 mTorr		
2964 (s)						CH_2 sym.str. [c, d]
2955 (s)	-	-			- -0.03	
2946 (s)	-	-3			- -0.12	
2938 (s)						
2928 (sh)						
2880 (sh)			-	+2	- +0.07	CH_2 asym.str. [c, d]
2874 (s)			-			
2866 (s)			-	+2	- +0.07	
1465 (m)						CH_2 sci. [c, d]
1458 (m)			+3	+3	+0.21 +0.21	
1450 (w)			+5	+6	+0.34 +0.41	CH_2 sci. [c, d]
1352 (w)						CH_2 wag. [d]
1323 (m)						CH_2 twist. [c]
1317 (m)	-1	-1			-0.08 -0.08	CH_2 twist. [c]
1295 (w)	-1	-1			-0.08 -0.08	CH_2 wag. [d]
1064 (m)	-4	-4			-0.38 -0.38	CN skel. [c, d]
988 (m)	-1				-0.10	CC skel. [c, d]

[a] Frequency of TEDA vibrational mode in gas phase. [b] percentage of the mode shifts vs. frequency in gas phase of TEDA (see 1st column in Table 10). [c] This assignment is based on ref. *(404)*. [d] This assignment is based on ref. *(405)*.

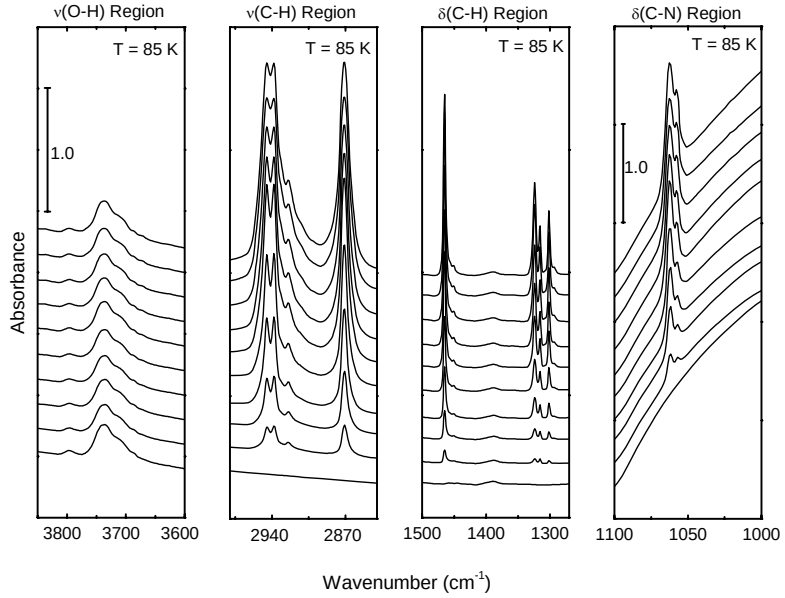

Figure 64. FTIR spectra of Al-OH modes and condensed TEDA ice on Al_2O_3 at 85 K with increasing dose of TEDA.

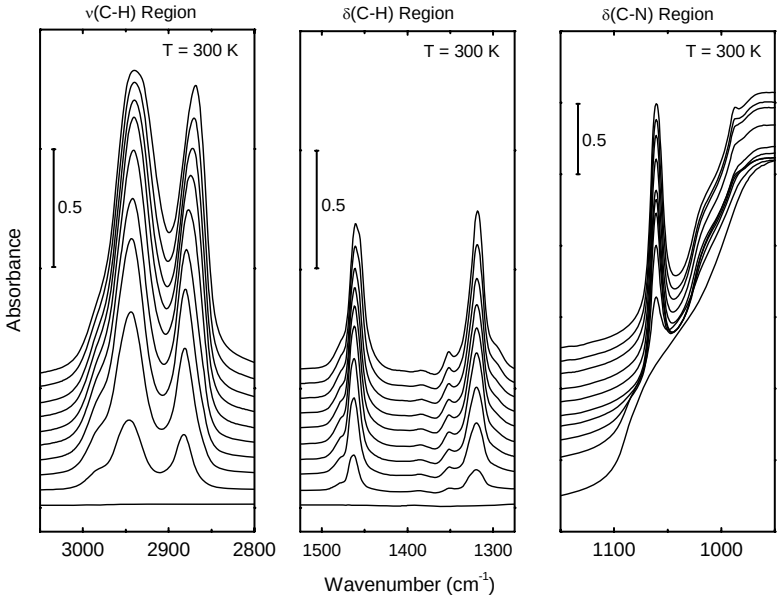

Figure 65. FTIR spectra of adsorbed TEDA on Al_2O_3 at 300 K with increasing equilibrium pressure of TEDA. P) 0, 1, 2, 3, 5, 18, 44, 82, 135, 246 mTorr.

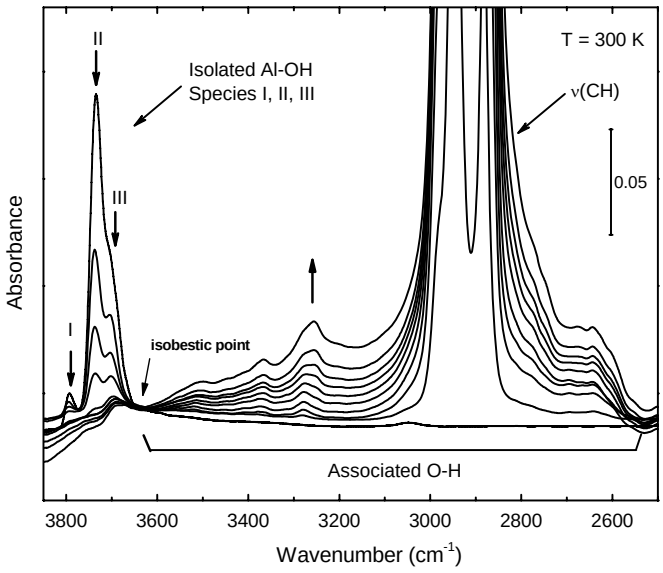

Figure 66. FTIR spectra of adsorbed TEDA on Al_2O_3 at 300 K with increasing pressure of TEDA. P) 0, 1, 2, 3, 5, 18, 44, 82, 135, 246 mTorr. An isosbestic point is observed at 3640 cm^{-1}. The ν(CH) modes due to adsorbed TEDA are seen in the 3000 cm^{-1} region.

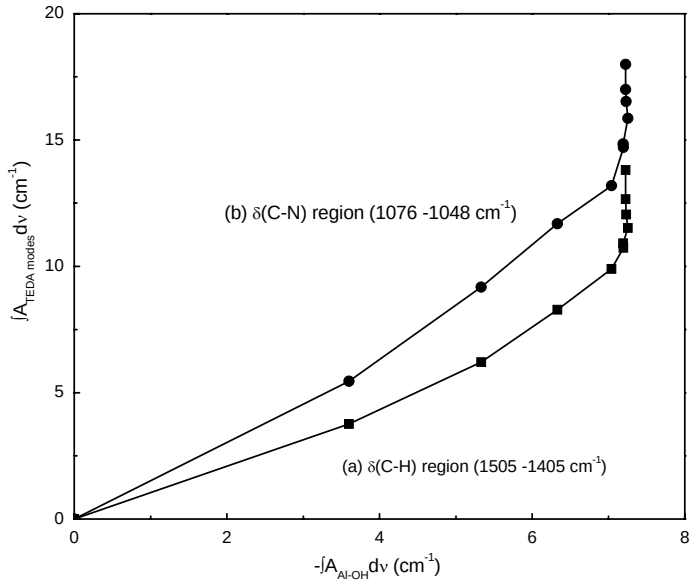

Figure 67. Relationship between the integrated absorbance of the several TEDA modes and the decreased isolated Al-OH integrated intensity with increasing dose of TEDA at 300 K: (a) in *ν*(C-H) region (1505 - 1405 cm^{-1}); (b) in *ν*(C-N) region (1076 - 1048 cm^{-1}).

The behavior of the isolated Al-OH surface species as a function of the pressure of TEDA in a sequence of adsorption experiments at 300 K is shown in Figure 66. The isolated Al-OH species exhibit different OH vibrational frequencies in accordance with previous assignments and are due to different degrees of coordination of Al^{3+} ions to O^{2-} ions in the solid *(402)*. As TEDA is adsorbed, both of the basic (~3800 cm^{-1}) and acidic (~3740 and ~3700 cm^{-1}) isolated Al-OH species are simultaneously converted to associated Al-OH•••TEDA modes with red-shifted frequencies spread over a wide frequency range below 3640 cm^{-1}. Superimposed on the broad associated Al-OH bonds is the ν(CH) region due to adsorbed TEDA. An isosbestic point near 3640 cm^{-1} indicates a stoichiometric conversion of isolated Al-OH species to Al-OH•••TEDA species. The extreme peak broadness of the band due to associated Al-OH•••TEDA species as well as the enhancement of the integrated absorbance of the associated OH stretching modes is characteristic of hydrogen bonding. In normal cases of hydrogen bonding the integrated absorption due to hydrogen bonding may increase by as much as an order of magnitude *(366)*. In the case shown here, a factor of ~4 increase in integrated absorbance is observed in the wavenumber range shown in Figure 66.

Figure 67 shows the relationship between the integrated absorption of two TEDA modes and the decrease of isolated Al-OH integrated intensity as TEDA is adsorbed to full coverage at 300 K. Figure 67 clearly shows that a highly nonlinear relationship exists between the consumption of isolated Al-OH species as hydrogen bonding occurs and the increase in TEDA coverage as the equilibrium pressure increases at 300 K. In particular, after the isolated Al-OH species have been completely complexed with TEDA, a large increase in TEDA coverage continues to occur. This means that TEDA adsorbs in two or more stages on the hydroxylated

Al_2O_3 surface. It is likely that TEDA adsorption occurs on Al^{3+} Lewis acid sites together with hydrogen bonding to Brønsted Al-OH sites.

The specific interaction of TEDA molecules with isolated Al-OH sites may be monitored by observing the integrated absorbance of the isolated Al-OH species as a function of the equilibrium pressure of TEDA. This procedure clearly separates the Al-OH bonded TEDA from adsorbed TEDA species at other sites. We assume that the decrease in integrated absorbance of the isolated Al-OH species is proportional to the coverage of Al-OH···TEDA complexes.

The Langmuir adsorption kinetic model can be applied to TEDA adsorption on Al-OH sites as follows:

$$\frac{d\theta}{dt} = k_a P(1-\theta) - k_d \theta \tag{5}$$

where θ is the fractional surface coverage of the adsorbate on the Al-OH sites, P is the equilibrium pressure of TEDA and k_a and k_d are the adsorption and desorption rate constants, respectively. This equation reduces to the Langmuir adsorption isotherm at equilibrium:

$$P/\theta = P + 1/K_{eq} \quad \left(K_{eq} = k_a/k_d\right) \tag{6}$$

The isotherm at 300 K is plotted as shown in Figure 68. The lower equilibrium pressure region below 44 mTorr is mainly characteristic of the first stage of TEDA adsorption on Al_2O_3 at 300 K. The fractional coverage of TEDA hydrogen bonded to Al-OH groups is obtained by subtracting the integrated intensity of the isolated Al-OH modes before and after TEDA dosing at each equilibrium pressure. The inset to Figure 68 shows the initial part of the adsorption data replotted according to eq. 6. The linearity of the plot in Figure 68 shows that complexing Al-OH groups with TEDA is an equilibrium process strictly following Langmurian kinetics, up to ~44 mTorr at 300 K.

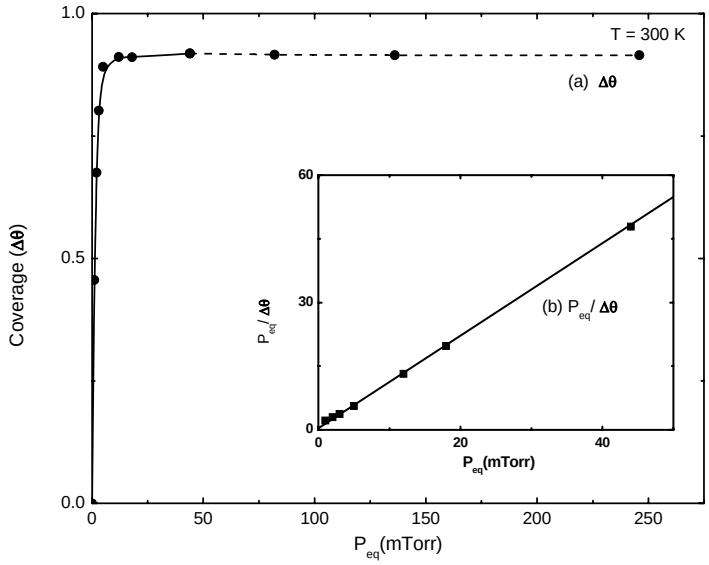

Figure 68. Langmuir isotherm plot of TEDA adsorption on Al-OH groups at 300 K: (a) Coverage of adsorbed TEDA on Al-OH species (Δθ) vs equilibrium pressure (P_{eq}). (b) $P_{eq}/\Delta\theta$ vs Peq, where Δθ is obtained from $-\int A_{OH}\, d\nu$ for isolated Al-OH species. The dashed line in the isotherm above 44 mTorr indicates that the fit to Langmuir behavior is not to be expected.

VIII-4B. Thermal Desorption of TEDA from Hydroxylated Al_2O_3.

The temperature programmed desorption spectra from the Al_2O_3 surface following condensation of a thick layer of TEDA at 85 K is shown in Figure 69. Thermal desorption at m/e = 42, m/e = 55, and m/e = 112 (parent) are recorded. The main desorption feature at 238 K is due to free sublimation of TEDA into the gas phase. A leading edge analysis of the temperature dependence of desorption rate for the condensed TEDA layer was performed. A plot of ln *P* vs 1/T is shown in the left insert to Figure 69, monitoring m/e = 42 and m/e = 55. A linear regression analysis yields ΔH_{sub} (TEDA) = 65.4 ± 0.6 kJ/mol as an average of the two measurements. This agrees favorably with ΔH_{sub} for TEDA (61.9 ± 3.3 kJ/mol), which was measured by Wada et al. *(406)*. Thus, near 200 K a condensed layer of TEDA sublimes from the outer geometrical surface of the powdered and compressed disk of Al_2O_3.

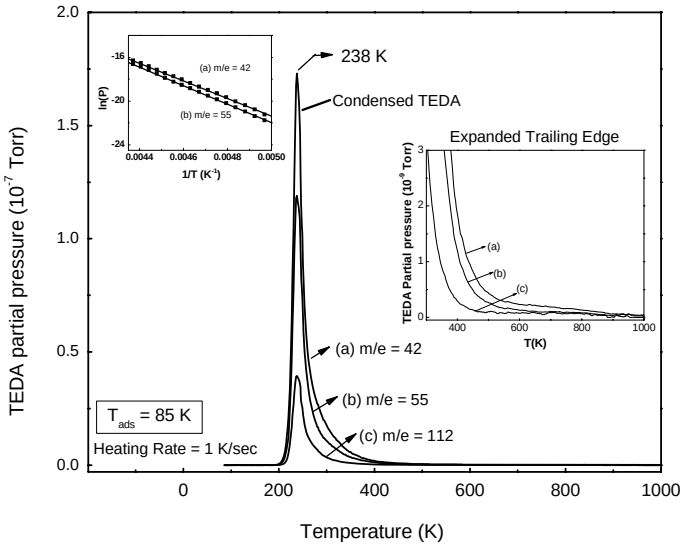

Figure 69. Temperature programmed desorption of condensed TEDA on Al_2O_3 for: (a) m/e = 42; (b) m/e = 55; (c) m/e = 112. The adsorption temperature was 85 K. The kinetic plot in the left insert yields ΔH_{sub} for condensed TEDA ice on the outer surface of the Al_2O_3. The right insert shows the trailing edge region above 300 K with a magnified vertical scale.

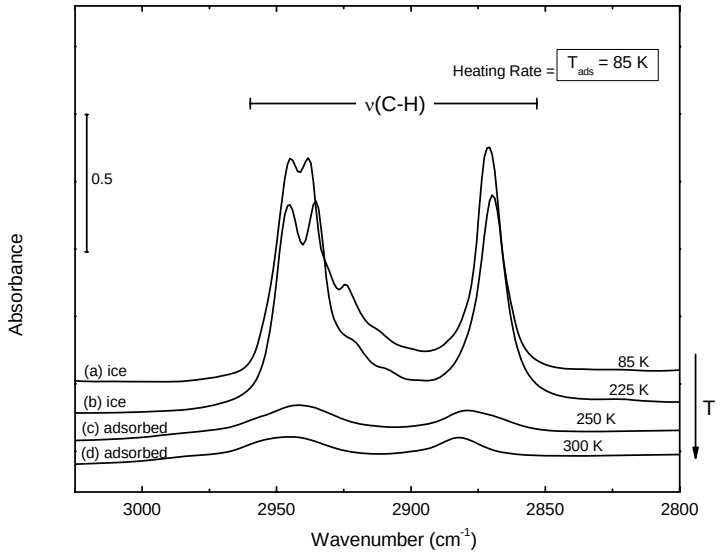

Figure 70. FT-IR spectra of condensed TEDA on Al_2O_3 during TPD experiment (heating rate = 1 K/s). Each spectrum is obtained by averaging 16 scans.

The right-hand inset to Figure 69 showing the trailing edge of the TEDA sublimation process is informative. If substantial amounts of the chemisorbed condensed outer film of TEDA had diffused into the inner pore structure of the compressed Al_2O_3 sample, where stronger chemisorption could occur, then a thermal desorption peak in the 400-500 K temperature range would have been observed, as will be shown later (See Figure 71). The absence of a discernible desorption process in this temperature range indicates that the condensed TEDA layer mainly vaporizes and does not deliver TEDA adsorbate by migration to the powdered Al_2O_3 interior when the heating rate is 1 K/s.

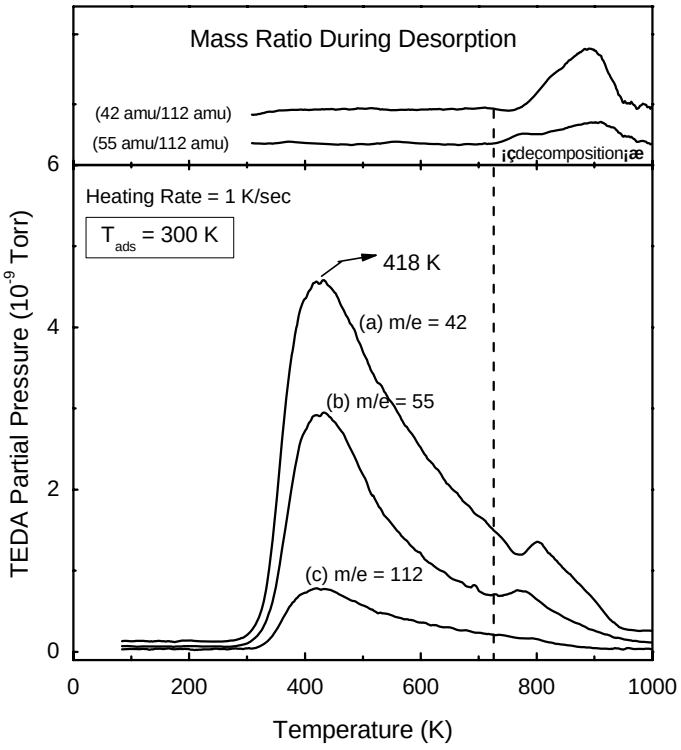

Figure 71. TPD spectra of adsorbed TEDA on Al_2O_3 for: (a) m/e = 42; (b) m/e = 55; (c) m/e = 112. The adsorption temperature was 300 K. The plots of the mass ratio of m/e) 42 and m/e = 55 to m/e = 112 are shown at top and indicate TEDA decomposition on Al_2O_3 above ~725 K.

During the temperature programmed desorption experiment when free sublimation of the condensed TEDA is being observed, IR spectra were also taken at every 25 K temperature increment as sublimation takes place, and selected examples of the spectra are shown in Figure 70. Each spectrum was obtained by averaging only 16 interferograms taking only 7 - 8 s. The IR absorbance from condensed TEDA on Al_2O_3 is observed to decrease up to 238 K as sublimation occurs. After that point (238 K) a relatively small amount of adsorbed TEDA is produced on the Al_2O_3. Two broad spectral features in the ν(CH) region are shown. These features in the ν(CH) region are very similar to the spectral feature shown for TEDA adsorbed from gas phase at 300 K in Figure 65, except their integrated absorbance is below 10% of the integrated absorbance which can be achieved by adsorption of gaseous TEDA at 300 K. This observation combined with the thermal desorption results (right inset, Figure 69) indicate that free sublimation of TEDA is the primary process being observed with only a small fractional filling of interior sites in the Al_2O_3 powder.

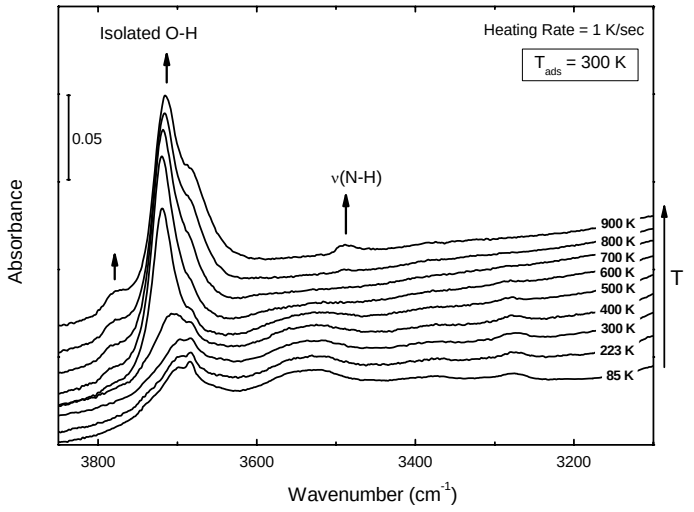

Figure 72. FT-IR spectra of adsorbed TEDA on Al_2O_3 during the TPD experiment (heating rate = 1 K/s). Each spectrum is obtained by averaging 16 scans, and is measured at the temperature shown.

Figure 71 shows the TEDA desorption experiment carried out after TEDA adsorption from the gas phase at 300 K. Here, a larger quantity of TEDA desorbs above 300 K than was observed in Figure 69. This is a result of adsorption at 300 K, where the temperature and time at this temperature favor diffusion of TEDA into the interior of the powder. Up to ~725 K, desorption of TEDA occurs without the evolution of observable decomposition products and the mass ratio 42/112 and 55/112 remains almost constant as shown at the top of Figure 71. However, above 725 K, the three mass spectral features at m/e) 42, 55, and 112 do not behave in the same manner and the 42/112 and 55/112 ratios increase substantially. This suggests that TEDA begins to dissociate on Al_2O_3 at 725 K, yielding other thermal desorption products which also have mass spectrometer cracking products at m/e = 42 and m/e = 55. In Figure 72, studies of the infrared spectrum of the Al_2O_3 containing adsorbed TEDA reveal that a new spectral feature at 3485 cm^{-1} begins to develop near 800 K. This feature is due to an N-H stretching mode which develops as C-H bonds dissociate, likely resulting in self-hydrogenation of N-containing cracking products of TEDA decomposition on the Al_2O_3 surface. This N-H containing surface species is observable to temperatures >1000 K. It is also seen that the desorption of TEDA is accompanied by the regeneration of isolated Al-OH modes.

VIII-5.Discussion

The major finding from this work is that TEDA binds via hydrogen bonding to isolated Al-OH groups on the surface of γ-alumina. It is observed that -OH groups with various frequencies, corresponding to different acidities, are all able to hydrogen bond to the nitrogen lone pair in the TEDA molecule. A wide range of associated Al-OH•••TEDA species, having a wide range of -OH frequencies shifted up to -1000 cm^{-1} or more from the isolated Al-OH mode frequencies, are produced. The observation of an isosbestic point at 3640 cm^{-1} indicates that a

stoichiometric conversion process occurs, i.e., that all types of Al-OH groups are complexed by hydrogen bonding to TEDA. Similar observations of an isosbestic point have been made in IR studies of the physical adsorption of both CO and N_2 on isolated Si-OH groups on SiO_2 *(331, 407)*, where hydrogen bonding also occurs at low temperatures. The adsorption of TEDA by hydrogen bonding to Al-OH groups occurs reversibly at 300 K, and accurately follows the Langmuir isotherm.

The electronic and geometrical nature of the Al-OH···TEDA hydrogen bond dictates the ratio of the integrated ν(OH) absorbance of the Al-OH···TEDA species to that of the isolated species. Issues such as the static dipole moment and the polarizability of the complexing species participating in hydrogen bonding are involved *(366)*. Ultimately the magnitude of $\partial\mu/\partial q$, the dynamic dipole associated with the normal coordinate displacement, ∂q, determines the intensity of the IR transition. In the case of hydrogen bonding to OH groups for molecules in solution, an enhancement of the ν(OH) integrated absorbance upon hydrogen bonding by a factor of 10 or more is often found.14 The relatively low intensity ratio observed here (~4) may be due to a number of features of the O-H···N interaction in the complex, as mentioned above. An additional effect may be the strong dielectric screening of $\partial\mu/\partial q$ by the Al_2O_3, occasioned by the attraction of the TEDA molecule to the surface, causing the O-H bond to be twisted more parallel to the surface. In this inclined geometry, the dynamic dipole will induce a strong antiparallel image dynamic dipole in the Al_2O_3, leading to depolarization and reduction of absorbance for the associated Al-OH···TEDA mode *(408)*. Such image effects would also contribute to a slight decrease of the -OH vibrational frequency. For the Al-OH···TEDA species,

large shifts of î(OH) of many hundreds of wavenumbers are seen (Figure 66) masking any image effects.

In addition to reversible adsorption of TEDA on isolated Al-OH groups, a second stage of TEDA absorption is detected in this work, as shown in Figure 67. After complete complexation of TEDA with all available Al-OH groups, significant additional adsorption of TEDA occurs. It is likely that additional TEDA adsorption occurs with Al^{3+} Lewis acid sites, but a clear spectral signature for TEDA adsorption in these sites has not been seen in this work.

The thermal desorption experiments shown here sample TEDA molecules adsorbed in two stages as indicated in Figure 67. A detailed analysis of the desorption kinetics is not warranted because of the mix of binding types, and also because of the involvement of surface diffusion processes from the interior of the Al_2O_3 to vacuum as desorption occurs from the porous oxide. Interestingly, the chemical decomposition of TEDA on the surface at temperatures of about 725 K and above is observed by both mass spectroscopy and IR spectroscopy. The development of an N-H stretching mode at above 800 K indicates that C-H bond scission has occurred, and that self-hydrogenation processes occur on a surface species containing a N atom. The experiments carried out here were not designed to investigate the thermal decomposition of TEDA on Al_2O_3 in detail.

Finally, the observations of a +0.3 to +0.4% blue shift in the CH2 scissor mode at 1455 cm^{-1} for adsorbed TEDA, and a -0.4% red shift in the CN skeletal mode at 1060 cm^{-1}, compared to gas phase frequencies, are indicative of the nature of the surface bonding of TEDA. The direction and magnitude of the shifts of these two modes supply experimental information which may be useful for modeling of the surface bonding of TEDA.

VIII-6.Summary

The adsorption of triethylenediamine (TEDA) on highly hydroxylated γ-Al_2O_3 has been studied using transmission infrared spectroscopy and thermal desorption methods. The following results have been obtained: (1) TEDA has been found to adsorb on Al-OH groups by hydrogen bond formation, resulting is red shifts to the ν(OH) frequency by up to 1000 cm^{-1} or more. In addition, evidence for a second stage of TEDA adsorption is observed, and this likely involves attachment of the TEDA molecules to Lewis acid Al^{3+} sites. (2) TEDA adsorbs reversibly on the Al-OH sites, accurately obeying the Langmuir isotherm at 300 K. The observation of an isosbestic point in the spectral region between the isolated Al-OH modes and the associated Al-OH modes indicates that a stoichiometric conversion process is being observed. (3) Desorption of TEDA occurs in the range 300-725 K without dissociation of the TEDA molecule on the Al_2O_3. Above 725 K, mass spectrometric and IR evidence indicates TEDA dissociation, and a surface species containing an N-H bond is formed probably as a result of self-hydrogenation resulting from C-H bond scission. (4) Characteristic blue shifts of +0.3 to +0.4% are observed for the CH_2 scissor mode of TEDA when it is bound to the surface. The C-N skeletal mode exhibits a -0.4% red shift for the adsorbed molecule. (5) At 85 K, TEDA adsorbs as an ice on the outer geometric surface of the powdered Al_2O_3 sample and does not penetrate into the powder interior. Free sublimation of this condensed film of TEDA occurs with only minor entry into the pore structure of the Al_2O_3 when the temperature is programmed upward at 1 K/s. In contrast, at 300 K, mobility of TEDA throughout the compressed Al_2O_3 powder is observed.

VIII-7.Acknowledgment.

We acknowledge with thanks the support of this work by The Army Research Office, and discussion with Dr. Alex Balboa of Aberdeen Proving Ground and with Dr. Joseph Rossin of Guild Associates.

PART IV

APPENDICES

APPENDIX A

Adsorption of Hydrogen on Carbon Nanotubes

The extreme significance of the topic of H_2 adsorption in nanotubes stems from the view of hydrogen as a prominent candidate for the fuel of future *(409)*. One gram of hydrogen is three times more energetic then a gram of gasoline; the exhaust of a hydrogen-based engine is harmless; and water, a possible supply for hydrogen production, is abundant. However, hydrogen is a gas with its boiling point at 20.28 K. Handling ℓ-H_2 requires cryogenic temperatures and high pressures, and H_2 is flammable. In order to overcome these difficulties a compact and safe medium for hydrogen transportation and transferring is required *(409)*. The US Department of Energy 2010 has set a target of 6 wt % of hydrogen for hydrogen-storage systems *(122)*. Adsorption in carbon nanotubes may offer a solution to the problem of safe and compact on-board storage of hydrogen fuel. In the past decade many publications appeared reporting different hydrogen uptakes by carbon nanotubes. More detailed literature reviews can be found elsewhere *(410-413)*. The intense research in this area was stimulated by an article by Dillon et al. in 1997 *(414)*. The authors have reported 5-15 wt % H_2 uptake at 133 K by SWNTs with 0.1-0.2 mass% purity assuming that all H_2 is adsorbed on nanotubes only *(414)*. However it turned out that a great amount of H_2 originated not from nanotubes but from Ti alloy particles as was shown later by Hirscher et al. *(415)*. Ye et al. measured adsorption of H_2 on ropes of SWNTs at 40 atm and 80 K and estimated hydrogen adsorption to be 8% *(416)*. An investigation of

hydrogen adsorption on 50% pure SWNTs at room temperature and 10 MPa by Liu et al. *(417)* indicates that hydrogen storage capacity of SWNTs may reach 4.2 wt %. Nonetheless the initial excitement from these findings has not found confirmation in the later reports *(15, 122)*. Grand canonical Monte Carlo calculations by Wand et al. *(418)* indicate that the DOE's target can be achieved only if the following becomes possible: H_2-nanotube wall interaction is doubled, the arrangement of nanotubes in a bundle is optimized, and adsorption is carried out at 77K. Recent comparative studies of H_2 adsorption on different carbon nanostructures by Panella et al. *(419)* indicate that the best material for hydrogen storage should possess high surface area and micropore density. In their study activated carbon excels carbon nanotubes in this respect. Moreover Zuttel et al. it have been fount no evidence to support the possibility of hydrogen storage in carbon nanotubes based on physical adsorption on perfect nanotubes *(15)*. On the other hand the recent Monte Carlo simulations of Hu et al. *(420)* indicate that hydrogen adsorption at room temperature and 100 atm can be enhanced to ~ 4 wt % level by doping SWNTs with alkali metals. This theoretical study corroborates previous experimental tests of H_2 adsorption on alkali-doped carbon nanotubes *(421)* but in this case physisorption may be accompanied by chemisorption phenomena. In addition, Levesque et al. *(422)* in the recent Monte Carlo simulations of H_2 storage in carbon nanotube bundles composed of 13.3 Å tubes have concluded that SWNTs can be used as a hydrogen storage medium only at cryogenic temperatures but not at room temperature. Overall there is no general agreement of whether carbon nanotubes can hold the initial promise for H_2 storage medium but a substantial advancement is expected when more pure and uniform nanotube samples in large quantities become available. However a low polarizibility of a H_2 molecule induces low binding energies of hydrogen to the surface of carbon nanotubes. Due to this hydrogen storage in carbon

nanotubes by physisorption may not be feasible. Binding energy enhancement can be reached by nanotube doping with active metals *(421)* which will result in H_2 chemisorption.

APPENDIX B

Appendix High Purity Ozone Generation – IR Study of O_3 Concentration

A separate glass system was constructed to study the behavior of ozone during O_3-induced oxidation of nanotubes. The system, described in Section VI-3, consists of the ozone generator, connection lines and the IR glass cell. The homemade cell is a glass cylinder covered from both sides with KBr windows and aligned in the IR spectrometer sample compartment. A constant flow of the gas mixture (for instance, oxygen and ozone) from the ozone generator can be studied by means of IR spectroscopy.

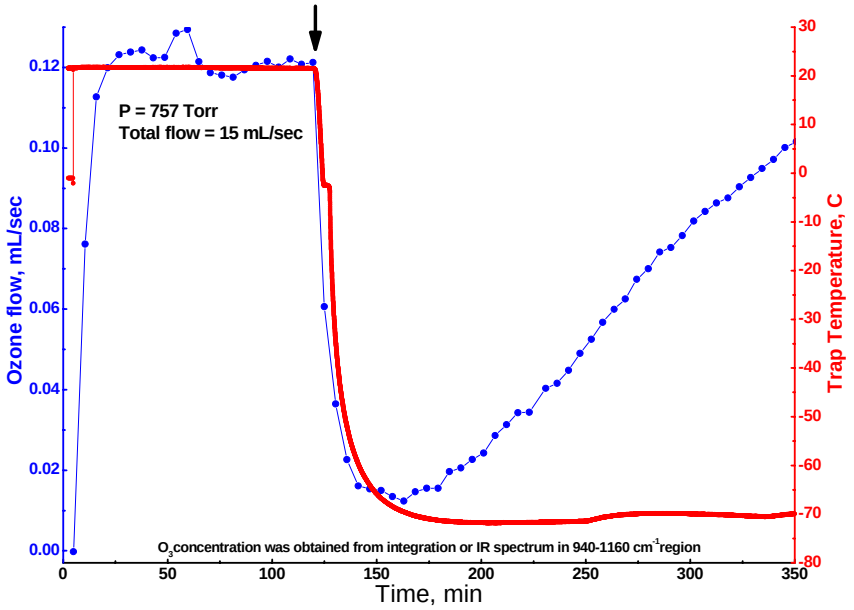

Figure 73. O_3 generation process. The red line depicts temperature of the SiO_2 trap; the blue line describes the O_3 flow versus time. The arrow point the time when the trap was cooled down with dry ice.

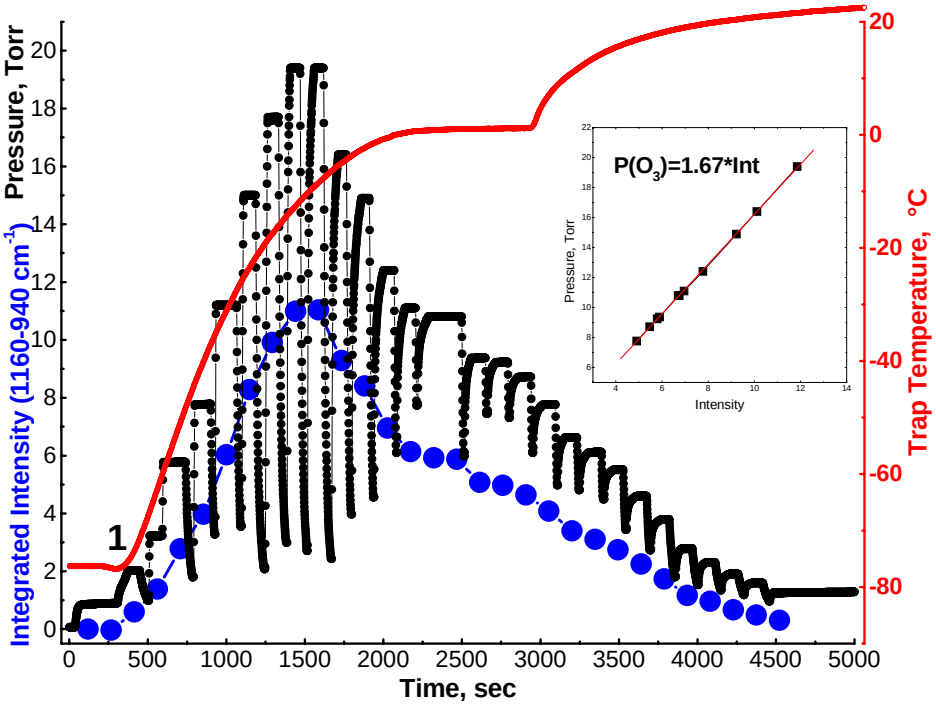

Figure 74. Ozone desorption IR studies. The red line – temperature of the SiO_2 trap. The blue line – the integrated intensity of O_3 spectrum in the 940 – 1160 cm^{-1} region. The black line – the pressure in the IR cell.

Ozone is produced form 99.994% pure oxygen in the constant flow ozone generator described elsewhere *(251)*. A generation process consists of ozone making in the corona discharge transformer and collecting it in the dry ice cooled SiO_2 trap. Previously, it was proved that initially 96% pure O_3 can be obtained. Here we present IR studies that confirm our earlier results. Figure 73 shows the plot of O_3 flow from the ozone generator versus time. At the beginning the transformer was off, so no ozone was produced – the first point in Figure 73. After the first scan the transformer was switched on and ozone started to be generated. After a few minutes a steady state was reached signifying the maximum ozone generating capacity of the transformer. At the time pointed by the arrow the SiO_2 trap was cooled down to about 196 K with dry ice. It is seen that the ozone concentration dropped dramatically indicating that O_3 was

been collected in the trap. As the trap loads with ozone its adsorption capability decreases and eventually the ozone flow have to reach its initial value after some time. Indeed the ozone concentration after the trap saturation is slightly higher but in the experiment shown in Figure 73 the saturation condition has not yet been reached. This must be due to the adsorption of ozone by the trap at room temperature. This is confirmed by the observation of the bluish color of the silica as the trap was warmed up to room temperature. This experiment provides information about the length of the ozone production cycle which is about 3 hours in all experiments.

Figure 74 shows ozone desorption IR studies carried out to obtain, firstly, the coefficient k in the equation:

$$P_{O_3} = k \cdot \int_{940cm^{-1}}^{1160cm^{-1}} \upsilon \cdot d\upsilon \qquad (7)$$

where the integral is the integrated intensity of O_3 IR band in the region 940 to 1160 cm^{-1} and P is the partial pressure of ozone in the cell. It also was used to calculate O_3 flow from the ozone generator in ozone making studies, see Figure 73. And secondly, to optimize ozone collecting technique in order to achieve the maximum amount of ozone at its highest purity. The experiment was performed as following. Ozone was collected in the trap and stored there at 196 K. The oxygen left after ozone preparation was pumped out to ~ 0.4 Torr while the trap was kept at 196 K. The trap temperature was monitored through the experiment with a K type thermocouple immersed in the center of the trap via a glass capillary. At the point "1" the cooler was removed and the trap warmed up without additional heating. As the trap temperature rises ozone starts to desorb from the trap and every 2 minutes a sample of gas was taken to the IR cell and the infrared spectrum was measured. After that the gas was pumped out from the cell. The oscillatory profile of the pressure curve – the black line in Figure 74 – is explained by this

technique. This method was employed to obtain O_3 as pure as possible since it decomposes quickly and it is difficult to obtain 100% pure ozone even in the absence of metal surfaces.

As it is seen from the pressure and IR integrated intensity profiles in Figure 74 ozone desorption rate gives rise to a peak in the -30-10° C range. This temperature range is used for further experiments.

To obtain the coefficient k in the eqn. (7) 10 points (11^{th} through the 21^{st} in the integrated intensity versus time profile) were used for the pressure against integrated intensity plot depicted in the inset of Figure 74. On the basis of the previous studies we assumed that in the chosen region only ozone desorbs from the trap. We also checked this assumption in a separate experiment carried out as following: some amount of ozone was collected in the 2 liter generator accumulating bulb at pressures from 15 to 40 Torr. The pressure was constantly read by the MKS 10^{-3}-10^{3} range capacitance manometer connected to the bulb and recorded by the computer. The bulb then was heated to about 150°C and as the pressure increase leveled up indicating the end of the ozone decomposition reaction it was cooled down to room temperature. The experiment was performed with different amounts of ozone at different stages of ozone desorption from the silica trap. The linear character of the pressure – intensity plot as it is shown in the inset of Figure 74 is in agreement with our assumption giving the coefficient value 1.67.

APPENDIX C

List of Publications

1. O. Byl, J. Liu, W. Yang, W.-L. Yim, J. K. Johnson, J. T. Yates, Jr.; **Unusual Hydrogen Bonding in Water-Filled Carbon Nanotubes**. Submitted to the Journal of American Chemical Society.
2. O. Byl, J. Liu, J. T. Yates, Jr.; **Porosity Characterization of Single Wall Carbon Nanotubes by Nonane Preadsorption.** Submitted to Carbon.
3. S. Kim, D. C. Sorescu, O. Byl, J. T. Yates, Jr.; **The Perturbation of Adsorbed CO by Amine Derivatives Coadsorbed on the γ-Al_2O_3 Surface – FTIR First Principles Studies.** Submitted to Journal of Physical Chemistry.
4. O. Byl, J. Liu, J. T. Yates, Jr.; **Etching of Carbon Nanotubes by Ozone – a Surface Area Study.** Langmuir 21(9), 4200-4204 (2005).
5. S. Kim, O. Byl, J. T. Yates, Jr.; **Adsorption of Triethylendiamine on Al_2O_3 – III: Bonding to Lewis Acid Al^{3+} Sites.** Journal of Physical Chemistry B 109(13), 6331-6333 (2005).
6. S. Kim, O. Byl, J. T. Yates, Jr.; **Adsorption of Triethylendiamine on Al_2O_3 – II: Hydrogen Bonding to Al-OH Groups.** Journal of Physical Chemistry B 109(8), 3499-3506 (2005).
7. S. Kim, O. Byl, J. T. Yates, Jr.; **Adsorption of Triethylendiamine on Al_2O_3 – I: a Vibrational Spectroscopic and Desorption Kinetic Study of Surface Bonding.** Journal of Physical Chemistry B 109(8), 3507-3511 (2005).
8. W.-L. Yim, O. Byl, J. T. Yates, Jr., J. K. Johnson; **Dimensional Effects on the LO-TO Splitting in CF_4: First-Principles and Infrared Absorption Studies.** Journal of the American Chemical Society 127(9), 3198-3206 (2005).

9. W.-L. Yim, O. Byl, J. T. Yates, Jr., J. K. Johnson; **Vibrational Behavior of Adsorbed CO_2 on Single-Walled Carbon Nanotubes**. Journal of Chemical Physics 120(11), 5377-5386 (2004).
10. O. Byl, P. Kondratyuk, J. T. Yates, Jr.; **Adsorption and Dimerization of NO Inside Single-Walled Carbon Nanotubes – an Infrared Spectroscopic Study.** Journal of Physical Chemistry B 107(18), 4277-4279 (2003).
11. O. Byl, P. Kondratyuk, S. T. Forth, S. A. FitzGerald, L. Chen, J. K. Johnson, J. T. Yates, Jr.; **Adsorption of CF_4 on the Internal and External Surfaces of Opened Single-Walled Carbon Nanotubes: a Vibrational Spectroscopy Study.** Journal of the American Chemical Society 125(19), 5889-5896 (2003).

BIBLIOGRAPHY

1. S. Iijima; *Nature* 354, 56 (1991).
2. Y. L. Li, I. A. Kinloch, A. H. Windle; *Science* 304, 276 (2004).
3. A. D. Migone, S. Talapatra; in **Encyclopedia of Nanoscience and Nanotechnology.** H. S. Nalwas, Ed. American Scientific Publishers, Stevenson Ranch, Calif., 2004, vol. 3, 749-767.
4. R. H. Baughman, A. A. Zakhidov, W. A. de Heer; *Science* 297, 787 (2002).
5. M. S. Dresselhaus, G. Dresselhaus, P. C. Eklund; **Science of Fullerenes and Carbon Nanotubes.** Academic Press, San Diego, 1996.
6. M. S. Dresselhaus, G. Dresselhaus, P. Avouris; Eds., **Carbon Nanotubes: Synthesis, Structure, Properties, and Applications.** Springer-Verlag, Berlin, 2001.
7. H. J. Dai; *Surf. Sci.* 500, 218 (2002).
8. T. W. Ebbesen; Ed., **Carbon Nanotubes: Preparation and Properties.** CRC, Boca Raton, Fla., 1997.
9. K. Tanaka, T. Yamabe, K. Fukui; Eds., **The Science and Technology of Carbon Nanotubes.** Elsevier, Oxford, UK, 1999.
10. A. Kukovecz, Z. Konya, I. Kiricsi; in **Encyclopedia of Nanoscience and Nanotechnology.** H. S. Nalwas, Ed. American Scientific Publishers, Stevenson Ranch, Calif., 2004, vol. 9, 923-946.
11. M. S. Dresselhaus, P. C. Eklund, G. Dresselhaus; in **Carbon Materials for Advanced Technologies.** T. D. Burchells, Ed. Pergamon, Amsterdam ; New York, 1999, 35-94.
12. P. J. F. Harris; **Carbon Nanotubes and Related Structures: New Materials for the Twenty-first Century**. Cambridge University Press, Cambridge, UK, 1999.
13. S. Reich, C. Thomsen, J. Maultzsch; **Carbon nanotubes : basic concepts and physical properties**. Wiley-VCH, Weinheim ; Cambridge, 2004.
14. M. Meyyappan; **Carbon Nanotubes: Science and Applications**. CRC Press, Boca Raton, FL, 2005.
15. A. Zuttel, S. Orimo; *MRS Bull.* 27, 705 (2002).
16. T. Belin, R. Epron; *Mat. Sci. Eng. B* 119, 105 (2005).
17. S. M. Huang, X. Y. Cai, J. Liu; *J. Am. Chem. Soc.* 125, 5636 (2003).
18. L. X. Zheng, M. J. O'Connell, S. K. Doorn, X. Z. Liao, Y. H. Zhao, E. A. Akhadov, M. A. Hoffbauer, B. J. Roop, Q. X. Jia, R. C. Dye, D. E. Peterson, S. M. Huang, J. Liu, Y. T. Zhu; *Nat. Mater.* 3, 673 (2004).
19. S. Iijima, T. Ichihashi; *Nature* 363, 603 (1993).
20. D. S. Bethune, C. H. Kiang, M. S. Devries, G. Gorman, R. Savoy, J. Vazquez, R. Beyers; *Nature* 363, 605 (1993).
21. C. Journet, W. K. Maser, P. Bernier, A. Loiseau, M. L. delaChapelle, S. Lefrant, P. Deniard, R. Lee, J. E. Fischer; *Nature* 388, 756 (1997).

22. A. Thess, R. Lee, P. Nikolaev, H. J. Dai, P. Petit, J. Robert, C. H. Xu, Y. H. Lee, S. G. Kim, A. G. Rinzler, D. T. Colbert, G. E. Scuseria, D. Tomanek, J. E. Fischer, R. E. Smalley; *Science* 273, 483 (1996).
23. H. Kataura, Y. Kumazawa, Y. Maniwa, Y. Ohtsuka, R. Sen, S. Suzuki, Y. Achiba; *Carbon* 38, 1691 (2000).
24. J. C. Bae, Y. J. Yoon, S. J. Lee, K. M. Song, H. K. Baik; *Carbon* 40, 2905 (2002).
25. D. H. Robertson, D. W. Brenner, J. W. Mintmire; *Phys. Rev. B* 45, 12592 (1992).
26. D. H. Oh, Y. H. Lee; *Phys. Rev. B* 58, 7407 (1998).
27. P. Nikolaev, A. Thess, A. G. Rinzler, D. T. Colbert, R. E. Smalley; *Chem. Phys. Lett.* 266, 422 (1997).
28. A. A. Lucas, P. H. Lambin, R. E. Smalley; *J. Phys. Chem. Solids* 54, 587 (1993).
29. Z. K. Tang, N. Wang, X. X. Zhang, J. N. Wang, C. T. Chan, P. Sheng; *New J. Phys.* 5, 146 (2003).
30. N. Wang, Z. K. Tang, G. D. Li, J. S. Chen; *Nature* 408, 50 (2000).
31. F. Lupo, J. A. Rodriguez-Manzo, A. Zamudio, A. L. Elias, Y. A. Kim, T. Hayashi, M. Muramatsu, R. Kamalakaran, H. Terrones, M. Endo, M. Ruhle, M. Terrones; *Chem. Phys. Lett.* 410, 384 (2005).
32. C. H. Kiang; *J. Phys. Chem. A* 104, 2454 (2000).
33. R. Saito, G. Dresselhaus, M. S. Dresselhaus; Eds., **Physics of Carbon Nanotube.** World Sci, Singapore, Singapore, 1998.
34. W. E. Alvarez, F. Pompeo, J. E. Herrera, L. Balzano, D. E. Resasco; *Abstr. Pap. Am. Chem. Soc.* 223, U630 (2002).
35. A. Okamoto, H. Shinohara; *Carbon* 43, 431 (2005).
36. S. Bandow, S. Asaka, Y. Saito, A. M. Rao, L. Grigorian, E. Richter, P. C. Eklund; *Phys. Rev. Lett.* 80, 3779 (1998).
37. M. F. Zhang, M. Yudasaka, S. Iijima; *J. Phys. Chem. B* 108, 12757 (2004).
38. A. R. Harutyunyan, G. Chen, P. C. Eklund; *Appl. Phys. Lett.* 82, 4794 (2003).
39. M. Takizawa, S. Bandow, M. Yudasaka, Y. Ando, H. Shimoyama, S. Iijima; *Chem. Phys. Lett.* 326, 351 (2000).
40. S. Farhat, M. L. de La Chapelle, A. Loiseau, C. D. Scott, S. Lefrant, C. Journet, P. Bernier; *J. Chem. Phys.* 115, 6752 (2001).
41. S. M. Bachilo, L. Balzano, J. E. Herrera, F. Pompeo, D. E. Resasco, R. B. Weisman; *J. Am. Chem. Soc.* 125, 11186 (2003).
42. H. Ago, S. Imamura, T. Okazaki, T. Saitoj, M. Yumura, M. Tsuji; *J. Phys. Chem. B* 109, 10035 (2005).
43. H. J. Jeong, K. H. An, S. C. Lim, M. S. Park, J. S. Chang, S. E. Park, S. J. Eum, C. W. Yang, C. Y. Park, Y. H. Lee; *Chem. Phys. Lett.* 380, 263 (2003).
44. S. Maruyama, Y. Miyauchi, T. Edamura, Y. Igarashi, S. Chiashi, Y. Murakami; *Chem. Phys. Lett.* 375, 553 (2003).
45. E. Borowiak-Palen, T. Pichler, X. Liu, M. Knupfer, A. Graff, O. Jost, W. Pompe, R. J. Kalenczuk, J. Fink; *Chem. Phys. Lett.* 363, 567 (2002).
46. D. B. Mawhinney, V. Naumenko, A. Kuznetsova, J. T. Yates, Jr., J. Liu, R. E. Smalley; *Chem. Phys. Lett.* 324, 213 (2000).
47. A. Kuznetsova, J. T. Yates, Jr., J. Liu, R. E. Smalley; *J. Chem. Phys.* 112, 9590 (2000).
48. D. Ciuparu, Y. Chen, S. Lim, G. L. Haller, L. Pfefferle; *J. Phys. Chem. B* 108, 503 (2004).

49. E. Gregan, S. M. Keogh, A. Maguire, T. G. Hedderman, L. O. Neill, G. Chambers, H. J. Byrne; *Carbon* 42, 1031 (2004).
50. A. B. Dalton, C. Stephan, J. N. Coleman, B. McCarthy, P. M. Ajayan, S. Lefrant, P. Bernier, W. J. Blau, H. J. Byrne; *J. Phys. Chem. B* 104, 10012 (2000).
51. M. Yudasaka, M. Zhang, S. Iijima; *Chem. Phys. Lett.* 374, 132 (2003).
52. T. W. Odom, J. L. Huang, P. Kim, C. M. Lieber; *Nature* 391, 62 (1998).
53. J. W. G. Wildoer, L. C. Venema, A. G. Rinzler, R. E. Smalley, C. Dekker; *Nature* 391, 59 (1998).
54. D. Bernaerts, A. Zettl, N. G. Chopra, A. Thess, R. E. Smalley; *Solid State Commun.* 105, 145 (1998).
55. C. A. Dyke, J. M. Tour; *J. Phys. Chem. A* 108, 11151 (2004).
56. H. Park, J. J. Zhao, J. P. Lu; *Nanotechnology* 16, 635 (2005).
57. K. H. An, J. S. Park, C. M. Yang, S. Y. Jeong, S. C. Lim, C. Kang, J. H. Son, M. S. Jeong, Y. H. Lee; *J. Am. Chem. Soc.* 127, 5196 (2005).
58. K. Shen, S. Curran, H. F. Xu, S. Rogelj, Y. B. Jiang, J. Dewald, T. Pietrass; *J. Phys. Chem. B* 109, 4455 (2005).
59. Z. H. Chen, X. Du, M. H. Du, C. D. Rancken, H. P. Cheng, A. G. Rinzler; *Nano Lett.* 3, 1245 (2003).
60. R. Krupke, F. Hennrich, H. von Lohneysen, M. M. Kappes; *Science* 301, 344 (2003).
61. P. C. Collins, M. S. Arnold, P. Avouris; *Science* 292, 706 (2001).
62. J. Liu, A. G. Rinzler, H. J. Dai, J. H. Hafner, R. K. Bradley, P. J. Boul, A. Lu, T. Iverson, K. Shelimov, C. B. Huffman, F. Rodriguez-Macias, Y. S. Shon, T. R. Lee, D. T. Colbert, R. E. Smalley; *Science* 280, 1253 (1998).
63. K. J. Ziegler, Z. N. Gu, J. Shaver, Z. Y. Chen, E. L. Flor, D. J. Schmidt, C. Chan, R. H. Hauge, R. E. Smalley; *Nanotechnology* 16, S539 (2005).
64. K. J. Ziegler, Z. N. Gu, H. Q. Peng, E. L. Flor, R. H. Hauge, R. E. Smalley; *J. Am. Chem. Soc.* 127, 1541 (2005).
65. Z. Gu, H. Peng, R. H. Hauge, R. E. Smalley, J. L. Margrave; *Nano Lett.* 2, 1009 (2002).
66. L. C. Venema, J. W. G. Wildoer, H. L. J. T. Tuinstra, C. Dekker, A. G. Rinzler, R. E. Smalley; *Appl. Phys. Lett.* 71, 2629 (1997).
67. S. R. Lustig, E. D. Boyes, R. H. French, T. D. Gierke, M. A. Harmer, P. B. Hietpas, A. Jagota, R. S. McLean, G. P. Mitchell, G. B. Onoa, K. D. Sams; *Nano Lett.* 3, 1007 (2003).
68. S. Iijima, C. Brabec, A. Maiti, J. Bernholc; *J. Chem. Phys.* 104, 2089 (1996).
69. R. Martel, H. R. Shea, P. Avouris; *Nature* 398, 299 (1999).
70. M. Sano, A. Kamino, J. Okamura, S. Shinkai; *Science* 293, 1299 (2001).
71. B. Q. Wei, R. Vajtai, Y. Y. Choi, P. M. Ajayan, H. W. Zhu, C. L. Xu, D. H. Wu; *Nano Lett.* 2, 1105 (2002).
72. Y. H. Li, C. L. Xu, B. Q. Wei, X. F. Zhang, M. X. Zheng, D. H. Wu, P. M. Ajayan; *Chem. Mater.* 14, 483 (2002).
73. P. Bernier, W. Maser, C. Jouret, A. Loiseau, M. L. de la Chapelle, S. Lefrant, R. Lee, J. E. Fischer; *Carbon* 36, 675 (1998).
74. D. Nepal, D. S. Kim, K. E. Geckeler; *Carbon* 43, 660 (2005).
75. M. J. O'Connell, P. Boul, L. M. Ericson, C. Huffman, Y. H. Wang, E. Haroz, C. Kuper, J. Tour, K. D. Ausman, R. E. Smalley; *Chem. Phys. Lett.* 342, 265 (2001).

76. V. A. Davis, L. M. Ericson, A. N. G. Parra-Vasquez, H. Fan, Y. H. Wang, V. Prieto, J. A. Longoria, S. Ramesh, R. K. Saini, C. Kittrell, W. E. Billups, W. W. Adams, R. H. Hauge, R. E. Smalley, M. Pasquali; *Macromolecules* 37, 154 (2004).
77. S. Maruyama, E. Einarsson, Y. Murakami, T. Edamura; *Chem. Phys. Lett.* 403, 320 (2005).
78. L. M. Ericson, H. Fan, H. Q. Peng, V. A. Davis, W. Zhou, J. Sulpizio, Y. H. Wang, R. Booker, J. Vavro, C. Guthy, A. N. G. Parra-Vasquez, M. J. Kim, S. Ramesh, R. K. Saini, C. Kittrell, G. Lavin, H. Schmidt, W. W. Adams, W. E. Billups, M. Pasquali, W. F. Hwang, R. H. Hauge, J. E. Fischer, R. E. Smalley; *Science* 305, 1447 (2004).
79. P. V. Kamat, K. G. Thomas, S. Barazzouk, G. Girishkumar, K. Vinodgopal, D. Meisel; *J. Am. Chem. Soc.* 126, 10757 (2004).
80. X. Q. Chen, T. Saito, H. Yamada, K. Matsushige; *Appl. Phys. Lett.* 78, 3714 (2001).
81. B. W. Smith, Z. Benes, D. E. Luzzi, J. E. Fischer, D. A. Walters, M. J. Casavant, J. Schmidt, R. E. Smalley; *Appl. Phys. Lett.* 77, 663 (2000).
82. H. J. Huang, H. Kajiura, A. Yamada, M. Ata; *Chem. Phys. Lett.* 356, 567 (2002).
83. K. Tohji, H. Takahashi, Y. Shinoda, N. Shimizu, B. Jeyadevan, I. Matsuoka, Y. Saito, A. Kasuya, S. Ito, Y. Nishina; *J. Phys. Chem. B* 101, 1974 (1997).
84. C. N. R. Rao, A. Govindaraj, G. Gundiah, S. R. C. Vivekchand; *Chem. Eng. Sci.* 59, 4665 (2004).
85. S. R. C. Vivekchang, A. Govindaraj; *Proc. Ind. Academ. Sci. Chem. Sci.* 115, 509 (2003).
86. S. R. C. Vivekchand, A. Govindaraj, M. M. Seikh, C. N. R. Rao; *J. Phys. Chem. B* 108, 6935 (2004).
87. Y. Kim, D. E. Luzzi; *J. Phys. Chem. B* ASAP Article, 10.1021/jp0522359 S1089 (2005).
88. J. Y. Li, J. F. Zhang; *Physica E* 28, 309 (2005).
89. Y. Lian, Y. Maeda, T. Wakahara, T. Akasaka, S. Kazaoui, N. Minami, T. Shimizu, N. Choi, H. Tokumoto; *J. Phys. Chem. B* 108, 8848 (2004).
90. Y. S. Min, E. J. Bae, W. Park; *J. Am. Chem. Soc.* 127, 8300 (2005).
91. H. Hu, A. P. Yu, E. Kim, B. Zhao, M. E. Itkis, E. Bekyarova, R. C. Haddon; *J. Phys. Chem. B* 109, 11520 (2005).
92. Y. Q. Xu, H. Q. Peng, R. H. Hauge, R. E. Smalley; *Nano Lett.* 5, 163 (2005).
93. A. Dailly, J. W. L. Yim, C. C. Ahn, E. Miura, R. Yazami, B. Fultz; *Appl. Phys. A* 80, 717 (2005).
94. G. S. Duesberg, W. Blau, H. J. Byrne, J. Muster, M. Burghard, S. Roth; *Synth. Met.* 103, 2484 (1999).
95. M. Holzinger, A. Hirsch, P. Bernier, G. S. Duesberg, M. Burghard; *Appl. Phys. A* 70, 599 (2000).
96. X. Y. Xu, R. Ray, Y. L. Gu, H. J. Ploehn, L. Gearheart, K. Raker, W. A. Scrivens; *J. Am. Chem. Soc.* 126, 12736 (2004).
97. S. K. Doorn, R. E. Fields, H. Hu, M. A. Hamon, R. C. Haddon, J. P. Selegue, V. Majidi; *J. Am. Chem. Soc.* 124, 3169 (2002).
98. S. Maruyama, R. Kojima, Y. Miyauchi, S. Chiashi, M. Kohno; *Chem. Phys. Lett.* 360, 229 (2002).
99. S. Arepalli, P. Nikolaev, O. Gorelik, V. G. Hadjiev, H. A. Bradlev, W. Holmes, B. Files, L. Yowell; *Carbon* 42, 1783 (2004).
100. J. Zhang, H. L. Zou, Q. Qing, Y. L. Yang, Q. W. Li, Z. F. Liu, X. Y. Guo, Z. L. Du; *J. Phys. Chem. B* 107, 3712 (2003).

101. J. G. Wiltshire, A. N. Khlobystov, L. J. Li, S. G. Lyapin, G. A. D. Briggs, R. J. Nicholas; *Chem. Phys. Lett.* 386, 239 (2004).
102. C. A. Furtado, U. J. Kim, H. R. Gutierrez, L. Pan, E. C. Dickey, P. C. Eklund; *J. Am. Chem. Soc.* 126, 6095 (2004).
103. A. Hashimoto, K. Suenaga, A. Gloter, K. Urita, S. Iijima; *Nature* 430, 870 (2004).
104. L. Valentini, C. Cantalini, L. Lozzi, S. Picozzi, I. Armentano, J. M. Kenny, S. Santucci; *Sens. Actuators B* 100, 33 (2004).
105. Z. Yao, H. W. C. Postma, L. Balents, C. Dekker; *Nature* 402, 273 (1999).
106. A. Kis, G. Csanyi, J. P. Salvetat, T. N. Lee, E. Couteau, A. J. Kulik, W. Benoit, J. Brugger, L. Forro; *Nat. Mater.* 3, 153 (2004).
107. M. Terrones, F. Banhart, N. Grobert, J. C. Charlier, H. Terrones, P. M. Ajayan; *Phys. Rev. Lett.* 89, 075505 (2002).
108. S. M. Chen, W. M. Shen, G. Z. Wu, D. Y. Chen, M. Jiang; *Chem. Phys. Lett.* 402, 312 (2005).
109. U. Dettlaff-Weglikowska, V. Skakalova, R. Graupner, S. H. Jhang, B. H. Kim, H. J. Lee, L. Ley, Y. W. Park, S. Berber, D. Tomanek, S. Roth; *J. Am. Chem. Soc.* 127, 5125 (2005).
110. V. N. Khabashesku, W. E. Billups, J. L. Margrave; *Acc. Chem. Res.* 35, 1087 (2002).
111. K. F. Kelly, I. W. Chiang, E. T. Mickelson, R. H. Hauge, J. L. Margrave, X. Wang, G. E. Scuseria, C. Radloff, N. J. Halas; *Chem. Phys. Lett.* 313, 445 (1999).
112. R. Barthos, D. Mehn, A. Demortier, N. Pierard, Y. Morciaux, G. Demortier, A. Fonseca, J. B. Nagy; *Carbon* 43, 321 (2005).
113. J. K. Lim, W. S. Yun, M. H. Yoon, S. K. Lee, C. H. Kim, K. Kim, S. K. Kim; *Synth. Met.* 139, 521 (2003).
114. Y. M. Ying, R. K. Saini, F. Liang, A. K. Sadana, W. E. Billups; *Org. Lett.* 5, 1471 (2003).
115. T. Ramanathan, F. T. Fisher, R. S. Ruoff, L. C. Brinson; *Chem. Mater.* 17, 1290 (2005).
116. A. Gromov, S. Dittmer, J. Svensson, O. A. Nerushev, S. A. Perez-Garcia, L. Licea-Jimenez, R. Rychwalski, E. E. B. Campbell; *J. Mater. Chem.* 15, 3334 (2005).
117. S. Pekker, J. P. Salvetat, E. Jakab, J. M. Bonard, L. Forro; *J. Phys. Chem. B* 105, 7938 (2001).
118. L. Zhang, J. Z. Yang, C. L. Edwards, L. B. Alemany, V. N. Khabashesku, A. R. Barron; *Chem. Commun.*, 3265 (2005).
119. M. E. Itkis, S. Niyogi, M. E. Meng, M. A. Hamon, H. Hu, R. C. Haddon; *Nano Lett.* 2, 155 (2002).
120. C. N. R. Rao, B. C. Satishkumar, A. Govindaraj, M. Nath; *ChemPhysChem* 2, 78 (2001).
121. M. S. Dresselhaus, K. A. Williams, P. C. Eklund; *MRS Bull.* 24, 45 (1999).
122. A. C. Dillon, M. J. Heben; *Appl. Phys. A* 72, 133 (2001).
123. S. R. Challa, D. S. Sholl, J. K. Johnson; *J. Chem. Phys.* 116, 814 (2002).
124. G. Arora, S. I. Sandler; *J. Chem. Phys.* 123, 044705 (2005).
125. Z. G. Mao, S. B. Sinnott; *J. Phys. Chem. B* 105, 6916 (2001).
126. S. M. Gatica, M. J. Bojan, G. Stan, M. W. Cole; *J. Chem. Phys.* 114, 3765 (2001).
127. K. Koga, G. T. Gao, H. Tanaka, X. C. Zeng; *Nature* 412, 802 (2001).
128. M. M. Calbi, F. Toigo, M. W. Cole; *Phys. Rev. Lett.* 86, 5062 (2001).
129. M. M. Calbi, F. Toigo, M. W. Cole; *J. Low Temp. Phys.* 126, 179 (2002).

130. M. W. Cole, V. H. Crespi, G. Stan, C. Ebner, J. M. Hartman, S. Moroni, M. Boninsegni; *Phys. Rev. Lett.* 84, 3883 (2000).
131. L. Firlej, B. Kuchta; *Colloid Surface A* 241, 149 (2004).
132. S. M. Gatica, G. Stan, M. M. Calbi, J. K. Johnson, M. W. Cole; *J. Low Temp. Phys.* 120, 337 (2000).
133. R. B. Hallock, Y. H. Kahng; *J. Low Temp. Phys.* 134, 21 (2004).
134. J. C. Lasjaunias, K. Biljakovic, J. L. Sauvajol, P. Monceau; *Phys. Rev. Lett.* 91, 025901 (2003).
135. G. Stan, M. J. Bojan, S. Curtarolo, S. M. Gatica, M. W. Cole; *Phys. Rev. B* 62, 2173 (2000).
136. G. Stan, M. W. Cole; *Surf. Sci.* 395, 280 (1998).
137. G. Stan, V. H. Crespi, M. W. Cole, M. Boninsegni; *J. Low Temp. Phys.* 113, 447 (1998).
138. W. Teizer, R. B. Hallock, E. Dujardin, T. W. Ebbesen; *Phys. Rev. Lett.* 82, 5305 (1999).
139. W. Teizer, R. B. Hallock, E. Dujardin, T. W. Ebbesen; *Phys. Rev. Lett.* 84, 1844 (2000).
140. D. M. Ackerman, A. I. Skoulidas, D. S. Sholl, J. K. Johnson; *Mol Simulat* 29, 677 (2003).
141. M. M. Calbi, M. W. Cole; *Phys. Rev. B* 66, 115413 (2002).
142. M. M. Calbi, S. M. Gatica, M. J. Bojan, M. W. Cole; *J. Chem. Phys.* 115, 9975 (2001).
143. V. Krungleviciute, L. Heroux, S. Talapatra, A. D. Migone; *Nano Lett.* 4, 1133 (2004).
144. S. Talapatra, V. Krungleviciute, A. D. Migone; *Phys. Rev. Lett.* 89, 246106 (2002).
145. S. Talapatra, A. Z. Zambano, S. E. Weber, A. D. Migone; *Phys. Rev. Lett.* 85, 138 (2000).
146. M. Bienfait, P. Zeppenfeld, N. Dupont-Pavlovsky, M. Muris, M. R. Johnson, T. Wilson, M. DePies, O. E. Vilches; *Phys. Rev. B* 70, 035410 (2004).
147. Z. J. Jakubek, B. Simard; *Langmuir* 20, 5940 (2004).
148. V. Krungleviciute, L. Heroux, A. D. Migone, C. T. Kingston, B. Simard; *J. Phys. Chem. B* 109, 9317 (2005).
149. M. W. Maddox, K. E. Gubbins; *Langmuir* 11, 3988 (1995).
150. S. Rols, M. R. Johnson, P. Zeppenfeld, M. Bienfait, O. E. Vilches, J. Schneble; *Phys. Rev. B* 71, 155411 (2005).
151. W. Shi, J. K. Johnson; *Phys. Rev. Lett.* 91, 015504 (2003).
152. W. A. Steele, M. J. Bojan; *Adv. Colloid Interface Sci.* 77, 153 (1998).
153. S. Talapatra, A. D. Migone; *Phys. Rev. Lett.* 87, 206106 (2001).
154. N. M. Urban, S. M. Gatica, M. W. Cole, J. L. Riccardo; *Phys. Rev. B* 71, 245410 (2005).
155. M. Muris, N. Dufau, M. Bienfait, N. Dupont-Pavlovsky, Y. Grillet, J. P. Palmari; *Langmuir* 16, 7019 (2000).
156. A. Kuznetsova, D. B. Mawhinney, V. Naumenko, J. T. Yates, Jr., J. Liu, R. E. Smalley; *Chem. Phys. Lett.* 321, 292 (2000).
157. A. Kuznetsova, J. T. Yates, Jr., V. V. Simonyan, J. K. Johnson, C. B. Huffman, R. E. Smalley; *J. Chem. Phys.* 115, 6691 (2001).
158. C. Matranga, L. Chen, B. Bockrath, J. K. Johnson; *Phys. Rev. B* 70, 165416 (2004).
159. M. Muris, N. Dupont-Pavlovsky, M. Bienfait, P. Zeppenfeld; *Surf. Sci.* 492, 67 (2001).
160. V. V. Simonyan, J. K. Johnson, A. Kuznetsova, J. T. Yates, Jr.; *J. Chem. Phys.* 114, 4180 (2001).
161. H. Ulbricht, J. Kriebel, G. Moos, T. Hertel; *Chem. Phys. Lett.* 363, 252 (2002).
162. A. J. Zambano, S. Talapatra, A. D. Migone; *Phys. Rev. B* 64, 075415 (2001).

163. M. Cinke, J. Li, B. Chen, A. Cassell, L. Delzeit, J. Han, M. Meyyappan; *Chem. Phys. Lett.* 365, 69 (2002).
164. M. Eswaramoorthy, R. Sen, C. N. R. Rao; *Chem. Phys. Lett.* 304, 207 (1999).
165. A. Fujiwara, K. Ishii, H. Suematsu, H. Kataura, Y. Maniwa, S. Suzuki, Y. Achiba; *Chem. Phys. Lett.* 336, 205 (2001).
166. C. M. Yang, K. Kaneko, M. Yudasaka, S. Iijima; *Nano Lett.* 2, 385 (2002).
167. C. M. Yang, K. Kaneko, M. Yudasaka, S. Iijima; *Physica B* 323, 140 (2002).
168. Y. F. Yin, T. Mays, B. McEnaney; *Langmuir* 15, 8714 (1999).
169. M. Arab, F. Picaud, M. Devel, C. Ramseyer, C. Girardet; *Phys. Rev. B* 69, 165401 (2004).
170. F. X. Li, Y. Wang, D. Z. Wang, F. Wei; *Carbon* 42, 2375 (2004).
171. S. Agnihotri, J. P. B. Mota, M. Rostam-Abadi, M. J. Rood; *Langmuir* 21, 896 (2005).
172. O. Byl, J. Liu, J. T. Yates, Jr.; *Langmuir* 21, 4200 (2005).
173. S. Inoue, N. Ichikuni, T. Suzuki, T. Uematsu, K. Kaneko; *J. Phys. Chem. B* 102, 4689 (1998).
174. J. I. Paredes, F. Suarez-Garcia, S. Villar-Rodil, A. Martinez-Alonso, J. M. D. Tascon, E. J. Bottani; *J. Phys. Chem. B* 107, 8905 (2003).
175. M. T. Martinez, M. A. Callejas, A. M. Benito, M. Cochet, T. Seeger, A. Anson, J. Schreiber, C. Gordon, C. Marhic, O. Chauvet, J. L. G. Fierro, W. K. Maser; *Carbon* 41, 2247 (2003).
176. Y. H. Hu, E. Ruckenstein; *Ind. Eng. Chem. Res.* 43, 708 (2004).
177. C. Bossuot, G. Bister, A. Fonseca, J. B. Nagy, J.-P. Pirard;AIP Conf. Proc. (Electronic Properties of Molecular Nanostructures) 591, 393-396 (2001).
178. W. F. Du, L. Wilson, J. Ripmeester, R. Dutrisac, B. Simard, S. Denommee; *Nano Lett.* 2, 343 (2002).
179. T. Ohba, K. Kaneko; *J. Phys. Chem. B* 106, 7171 (2002).
180. D. H. Yoo, G. H. Rue, M. H. W. Chan, Y. H. Hwang, H. K. Kim; *J. Phys. Chem. B* 107, 1540 (2003).
181. D. H. Yoo, G. H. Rue, Y. H. Hwang, H. K. Kim; *J. Phys. Chem. B* 106, 3371 (2002).
182. C. Matranga, B. Bockrath; *J. Phys. Chem. B* 109, 4853 (2005).
183. C. Matranga, B. Bockrath; *J. Phys. Chem. B* 108, 6170 (2004).
184. C. Matranga, B. Bockrath; *J. Phys. Chem. B* 109, 9209 (2005).
185. W. L. Yim, O. Byl, J. T. Yates, Jr., J. K. Johnson; *J. Chem. Phys.* 120, 5377 (2004).
186. T. Duren, F. J. Keil; *Chem Eng Technol* 24, 698 (2001).
187. M. R. Johnson, S. Rols, P. Wass, M. Muris, M. Bienfait, P. Zeppenfeld, N. Dupont-Pavlovsky; *Chem. Phys.* 293, 217 (2003).
188. Z. G. Mao, S. B. Sinnott; *J. Phys. Chem. B* 104, 4618 (2000).
189. S. Talapatra, A. D. Migone; *Phys. Rev. B* 65, 045416 (2002).
190. S. E. Weber, S. Talapatra, C. Journet, Z. Zambano, A. D. Migone; *Phys. Rev. B* 61, 13150 (2000).
191. O. Byl, P. Kondratyuk, S. T. Forth, S. A. FitzGerald, L. Chen, J. K. Johnson, J. T. Yates, Jr.; *J. Am. Chem. Soc.* 125, 5889 (2003).
192. W. L. Yim, O. Byl, J. T. Yates, Jr., J. K. Johnson; *J. Am. Chem. Soc.* 127, 3198 (2005).
193. M. R. Babaa, N. Dupont-Pavlovsky, E. McRae, K. Masenelli-Varlot; *Carbon* 42, 1549 (2004).
194. P. Kondratyuk, J. T. Yates, Jr.; *Chem. Phys. Lett.* 410, 324 (2005).

195. P. Kondratyuk, J. T. Yates, Jr.; *Chem. Phys. Lett.* 383, 314 (2004).
196. R. Q. Long, R. T. Yang; *Ind. Eng. Chem. Res.* 40, 4288 (2001).
197. O. Byl, P. Kondratyuk, J. T. Yates, Jr.; *J. Phys. Chem. B* 107, 4277 (2003).
198. A. Heyden, T. Duren, F. J. Keil; *Chem. Eng. Sci.* 57, 2439 (2002).
199. E. Dujardin, T. W. Ebbesen, H. Hiura, K. Tanigaki; *Science* 265, 1850 (1994).
200. N. Naguib, H. H. Ye, Y. Gogotsi, A. G. Yazicioglu, C. M. Megaridis, M. Yoshimura; *Nano Lett.* 4, 2237 (2004).
201. M. P. Rossi, H. H. Ye, Y. Gogotsi, S. Babu, P. Ndungu, J. C. Bradley; *Nano Lett.* 4, 989 (2004).
202. K. Koga, R. D. Parra, H. Tanaka, X. C. Zeng; *J. Chem. Phys.* 113, 5037 (2000).
203. K. Koga, G. T. Gao, H. Tanaka, X. C. Zeng; *Physica A* 314, 462 (2002).
204. J. Bai, C. R. Su, R. D. Parra, X. C. Zeng, H. Tanaka, K. Koga, J. M. Li; *J. Chem. Phys.* 118, 3913 (2003).
205. H. Tanaka, K. Koga; in **Water in Confining Geometries** V. Buch and J. P. Devlins, Eds. Springer, Berlin; New York, 2003, 151-177.
206. Y. Maniwa, H. Kataura, M. Abe, A. Udaka, S. Suzuki, Y. Achiba, H. Kira, K. Matsuda, H. Kadowaki, Y. Okabe; *Chem. Phys. Lett.* 401, 534 (2005).
207. Y. Maniwa, H. Kataura, M. Abe, S. Suzuki, Y. Achiba, H. Kira, K. Matsuda; *J. Phys. Soc. Jpn.* 71, 2863 (2002).
208. S. Ghosh, K. V. Ramanathan, A. K. Sood; *Europhys. Lett.* 65, 678 (2004).
209. A. I. Kolesnikov, J. M. Zanotti, C. K. Loong, P. Thiyagarajan, A. P. Moravsky, R. O. Loutfy, C. J. Burnham; *Phys. Rev. Lett.* 93, 035503 (2004).
210. J. Marti, J. A. Padro, E. Guardia; *J. Mol. Liq.* 62, 17 (1994).
211. J. Marti, M. C. Gordillo; *J. Chem. Phys.* 114, 10486 (2001).
212. J. Marti, M. C. Gordillo; *Phys. Rev. E* 64, 021504 (2001).
213. J. Marti, M. C. Gordillo; *Phys. Rev. B* 63, 165430 (2001).
214. J. Marti, M. C. Gordillo; *Chem. Phys. Lett.* 354, 227 (2002).
215. J. Marti, M. C. Gordillo; *J. Chem. Phys.* 119, 12540 (2003).
216. J. Marti, E. Guardia, M. C. Gordillo; *Chem. Phys. Lett.* 365, 536 (2002).
217. J. Marti, E. Guardia, J. A. Padro; *J. Chem. Phys.* 101, 10883 (1994).
218. M. C. Gordillo, G. Nagy, J. Marti; *J. Chem. Phys.* 123, 054707 (2005).
219. M. C. Gordillo, J. Marti; *Chem. Phys. Lett.* 329, 341 (2000).
220. M. C. Gordillo, J. Marti; *Chem. Phys. Lett.* 341, 250 (2001).
221. M. C. Gordillo, J. Marti; *Phys. Rev. B* 67, 205425 (2003).
222. M. D. Ellison, A. P. Good, C. S. Kinnaman, N. E. Padgett; *J. Phys. Chem. B* 109, 10640 (2005).
223. O. Byl, J. Liu, Y. Wang, W.-L. Yim, J. K. Johnson, J. T. Yates, Jr.; *J. Am. Ceram. Soc.*, submitted (2005).
224. B. W. Smith, M. Monthioux, D. E. Luzzi; *Nature* 396, 323 (1998).
225. S. Bandow, M. Takizawa, H. Kato, T. Okazaki, H. Shinohara, S. Iijima; *Chem. Phys. Lett.* 347, 23 (2001).
226. L. J. Li, A. N. Khlobystov, J. G. Wiltshire, G. A. D. Briggs, R. J. Nicholas; *Nat. Mater.* 4, 481 (2005).
227. M. Hodak, L. A. Girifalco; *Phys. Rev. B* 67, 075419 (2003).
228. X. Fan, E. C. Dickey, P. C. Eklund, K. A. Williams, L. Grigorian, R. Buczko, S. T. Pantelides, S. J. Pennycook; *Phys. Rev. Lett.* 84, 4621 (2000).

229. D. Green, C. Chamon; *Phys. Rev. Lett.* 85, 4128 (2000).
230. M. M. Calbi, M. W. Cole, S. M. Gatica, M. J. Bojan, G. Stan; *Rev Mod Phys* 73, 857 (2001).
231. A. I. Skoulidas, D. M. Ackerman, J. K. Johnson, D. S. Sholl; *Phys. Rev. Lett.* 89, 185901 (2002).
232. L. D. Gelb, K. E. Gubbins, R. Radhakrishnan, M. Sliwinska-Bartkowiak; *Rep. Prog. Phys.* 62, 1573 (1999).
233. S. Rols, R. Almairac, L. Henrard, E. Anglaret, J. L. Sauvajol; *Eur Phys J B* 10, 263 (1999).
234. C. Carraro; *Phys. Rev. B* 61, R16351 (2000).
235. K. A. Williams, P. C. Eklund; *Chem. Phys. Lett.* 320, 352 (2000).
236. C. Matranga, L. Chen, M. Smith, E. Bittner, J. K. Johnson, B. Bockrath; *J. Phys. Chem. B* 107, 12930 (2003).
237. P. Kondratyuk, Y. Wang, J. K. Johnson, J. T. Yates, Jr.; *J. Phys. Chem. B* 109, 20999 (2005).
238. F. Rouquerol, J. Rouquerol, K. S. W. Sing; **Adsorption by Powders and Porous Solids: Principles, Methodology, and Applications**. Academic Press, San Diego, 1999.
239. A. Peigney, C. Laurent, E. Flahaut, R. R. Bacsa, A. Rousset; *Carbon* 39, 507 (2001).
240. N. Pierard, A. Fonseca, J. F. Colomer, C. Bossuot, J. M. Benoit, G. Van Tendeloo, J. P. Pirard, J. B. Nagy; *Carbon* 42, 1691 (2004).
241. I. Stepanek, G. Maurin, P. Bernier, J. Gavillet, A. Loiseau, R. Edwards, O. Jaschinski; *Chem. Phys. Lett.* 331, 125 (2000).
242. A. Kuznetsova, I. Popova, J. T. Yates, Jr., M. J. Bronikowski, C. B. Huffman, J. Liu, R. E. Smalley, H. H. Hwu, J. G. G. Chen; *J. Am. Chem. Soc.* 123, 10699 (2001).
243. D. B. Mawhinney, V. Naumenko, A. Kuznetsova, J. T. Yates, Jr., J. Liu, R. E. Smalley; *J. Am. Chem. Soc.* 122, 2383 (2000).
244. P. Basu, T. H. Ballinger, J. T. Yates, Jr.; *Rev. Sci. Instrum.* 59, 1321 (1988).
245. J. L. Zimmerman, R. K. Bradley, C. B. Huffman, R. H. Hauge, J. L. Margrave; *Chem. Mater.* 12, 1361 (2000).
246. D. B. Mawhinney, J. T. Yates, Jr.; *Carbon* 39, 1167 (2001).
247. M. K. Kostov, M. W. Cole, J. C. Lewis, P. Diep, J. K. Johnson; *Chem. Phys. Lett.* 332, 26 (2000).
248. R. P. Fournier, S. Savoie, F. Bessette, A. Cabana; *J. Chem. Phys.* 49, 1159 (1968).
249. J. H. Yang, L. A. Clark, G. J. Ray, Y. J. Kim, H. Du, R. Q. Snurr; *J. Phys. Chem. B* 105, 4698 (2001).
250. A. G. Rinzler, J. Liu, H. Dai, P. Nikolaev, C. B. Huffman, F. J. Rodriguez-Macias, P. J. Boul, A. H. Lu, D. Heymann, D. T. Colbert, R. S. Lee, J. E. Fischer, A. M. Rao, P. C. Eklund, R. E. Smalley; *Appl. Phys. A* 67, 29 (1998).
251. V. Zhukov, I. Popova, J. T. Yates, Jr.; *J. Vac. Sci. Technol. A* 18, 992 (2000).
252. Gaussian 98, Revision A.11: M. J. Frisch, G. W. Trucks, H. B. Schlegel, G. E. Scuseria, M. A. Robb, J. R. Cheeseman, V. G. Zakrzewski, J. A. Montgomery, Jr., R. E. Stratmann, J. C. Burant, S. Dapprich, J. M. Millam, A. D. Daniels, K. N. Kudin, M. C. Strain, O. Farkas, J. Tomasi, V. Barone, M. Cossi, R. Cammi, B. Mennucci, C. Pomelli, C. Adamo, S. Clifford, J. Ochterski, G. A. Petersson, P. Y. Ayala, Q. Cui, K. Morokuma, P. Salvador, J. J. Dannenberg, D. K. Malick, A. D. Rabuck, K. Raghavachari, J. B. Foresman, J. Cioslowski, J. V. Ortiz, A. G. Baboul, B. B. Stefanov, G. Liu, A. Liashenko,

P. Piskorz, I. Komaromi, R. Gomperts, R. L. Martin, D. J. Fox, T. Keith, M. A. Al-Laham, C. Y. Peng, A. Nanayakkara, M. Challacombe, P. M. W. Gill, B. Johnson, W. Chen, M. W. Wong, J. L. Andres, C. Gonzalez, M. Head-Gordon, E. S. Replogle, J. A. Pople. Gaussian, Inc., Pittsburgh PA, 2001.
253. M. P. Allen, D. J. Tildesley; **Computer Simulation of Liquids**. Clarendon Press, Oxford, New York, 1987.
254. R. L. Rowley; **Statistical Mechanics for Thermophysical Property Calculations**. Prentice Hall, Englewood Cliffs, NJ, 1994.
255. B. E. Poling, J. M. Prausnitz, J. P. O'Connell; **The Properties of Gases and Liquids**. McGraw-Hill, New York, ed. 5th, 2001.
256. R. Q. Snurr, J. Karger; *J. Phys. Chem. B* 101, 6469 (1997).
257. A. I. Skoulidas, D. S. Sholl; *J. Phys. Chem. B* 105, 3151 (2001).
258. W. A. Steele; *Surf. Sci.* 36, 317 (1973).
259. P. Nectoux, M. Drifford, L. Belloni, A. Vinit; *Mol. Phys.* 49, 1375 (1983).
260. B. Rowland, N. S. Kadagathur, J. P. Devlin; *J. Chem. Phys.* 102, 13 (1995).
261. V. Buch, L. Delzeit, C. Blackledge, J. P. Devlin; *J. Phys. Chem.* 100, 3732 (1996).
262. L. Delzeit, M. S. Devlin, B. Rowland, J. P. Devlin, V. Buch; *J. Phys. Chem.* 100, 10076 (1996).
263. L. H. Jones, B. I. Swanson; *J. Phys. Chem.* 95, 2701 (1991).
264. M. Gilbert, M. Drifford; *J. Chem. Phys.* 66, 3205 (1977).
265. F. P. Daly, A. G. Hopkins, C. W. Brown; *Spectrochim. Acta A* 30A, 2159 (1974).
266. J. R. Scherer; in **Advances in Infrared and Raman Spectroscopy** R. J. H. Clark and R. E. Hesters, Eds. Heyden, London ; New York, 1975, vol. 5, 149-216.
267. J. C. Evans, N. Wright; *Spectrochim. Acta* 16, 352 (1960).
268. J. C. Evans; *Spectrochim. Acta* 16, 994 (1960).
269. J. Bertie, J. P. Devlin; *J. Chem. Phys.* 79, 2092 (1983).
270. J. P. Devlin, P. J. Wooldridge, G. Ritzhaupt; *J. Chem. Phys.* 84, 6095 (1984).
271. J. R. Scherer, M. K. Go, S. Kint; *J. Phys. Chem.* 77, 2108 (1973).
272. T. Graim, D. P. Landau; *Phys. Rev. B* 24, 5156 (1980).
273. S. M. Gatica, M. J. Bojan, G. Stan, M. W. Cole; *J. Chem. Phys.* 114, 3765 (2001).
274. R. C. Gordillo, J. Boronat, J. Casulleras; *Phys. Rev. Lett.* 85, 2348 (2000).
275. M. C. Gordillo, J. Boronat, J. Casulleras; *Phys. Rev. B* 61, R878 (2000).
276. T. Wilson, O. E. Vilches; *Low Temp. Phys.* 29, 732 (2003).
277. H. J. Dai, J. H. Hafner, A. G. Rinzler, D. T. Colbert, R. E. Smalley; *Nature* 384, 147 (1996).
278. J. Kong, H. T. Soh, A. M. Cassell, C. F. Quate, H. J. Dai; *Nature* 395, 878 (1998).
279. T. Wilson, A. Tyburski, M. R. DePies, O. E. Vilches, D. Becquet, M. Bienfait; *J. Low Temp. Phys.* 126, 403 (2002).
280. S. E. Weber, S. Talapatra, C. Journet, A. Zambano, A. D. Migone; *Phys. Rev. B* 66, 049901 (2002).
281. T. Wilson, O. E. Vilches; *Physica B* 329, 278 (2003).
282. S. Ramachandran, T. A. Wilson, D. Vandervelde, D. K. Holmes, O. E. Vilches; *J. Low Temp. Phys.* 134, 115 (2004).
283. M. Yvinec, R. M. Pick; *J. Chem. Phys.* 71, 3440 (1979).
284. G. Kresse, J. Hafner; *Phys. Rev. B* 47, 558 (1993).
285. G. Kresse, J. Hafner; *Phys. Rev. B* 49, 14251 (1994).

286. G. Kresse, J. Furthmueller; *Phys. Rev. B* 54, 11169 (1996).
287. S. Baroni, A. D. Corso, S. d. Gironcoli, P. Giannozzi; http://www.pwscf.org,
288. E. Balan, A. M. Saitta, F. Mauri, G. Calas; *Am. Mineral.* 86, 1321 (2001).
289. D. Vanderbilt; *Phys. Rev. B* 41, 7892 (1990).
290. I. Morrison, J. C. Li, S. Jenkins, S. S. Xantheas, M. C. Payne; *J. Phys. Chem. B* 101, 6146 (1997).
291. N. Troullier, J. L. Martins; *Phys. Rev. B* 43, 1993 (1991).
292. M. Fuchs, M. Scheffler; *Comput. Phys. Commun.* 119, 67 (1999).
293. Y. A. Sataty, A. Ron, F. H. Herbstein; *J. Chem. Phys.* 62, 1094 (1975).
294. J. K. Dewhurst, R. Ahuja, S. Li, B. Johansson; *Phys. Rev. Lett.* 88, 075504 (2002).
295. W. Kohn, Y. Meir, D. E. Makarov; *Phys. Rev. Lett.* 80, 4153 (1998).
296. A. Milet, T. Korona, R. Moszynski, E. Kochanski; *J. Chem. Phys.* 111, 7727 (1999).
297. X. Wu, M. C. Vargas, S. Nayak, V. Lotrich, G. Scoles; *J. Chem. Phys.* 115, 8748 (2001).
298. T. van Mourik, R. J. Gdanitz; *J. Chem. Phys.* 116, 9620 (2002).
299. M. Kamiya, T. Tsuneda, K. Hirao; *J. Chem. Phys.* 117, 6010 (2002).
300. T. A. Wesolowski; *J. Chem. Phys.* 113, 1666 (2000).
301. H. Rydberg, N. Jacobson, P. Hyldgaard, S. I. Simak, B. I. Lundqvist, D. C. Langreth; *Surf. Sci.* 532-535, 606 (2003).
302. A. Heßelmann, G. Jansen; *Chem. Phys. Lett.* 367, 778 (2003).
303. A. J. Misquitta, B. Jeziorski, K. Szalewicz; *Phys. Rev. Lett.* 91, 033201 (2003).
304. X. Xu, W. A. Goddard; *J. Chem. Phys.* 121, 4068 (2004).
305. X. Xu, W. A. Goddard; *Proc. Natl. Acad. Sci. U. S. A.* 101, 2673 (2004).
306. L. A. Girifalco, M. Hodak; *Physical Review B* 65, 125404 (2002).
307. J. J. Zhao, A. Buldum, J. Han, J. P. Lu; *Nanotechnology* 13, 195 (2002).
308. R. W. G. Wyckoff; **Crystal Structures**. John Wiley & Sons, New York, London, 1963, vol. 1.
309. R. W. G. Wyckoff; **Crystal Structures**. John Wiley & Sons, New York, London, 1964, vol. 2.
310. X. Gonze, C. Lee; *Phys. Rev. B* 55, 10355 (1997).
311. J. P. Perdew, K. Burke, M. Ernzerhof; *Phys. Rev. Lett.* 77, 3865 (1996).
312. J. P. Perdew; in **Electronic Structure of Solids** H. Eschrigs, Ed. Akademie Verlag, Berlin, 1991, 11.
313. B. Muller, H. D. Lutz, J. Hermeling, E. Knozinger; *Spectrochim. Acta A* 49, 191 (1993).
314. K. Aoki, B. J. Baer, H. C. Cynn, M. Nicol; *Phys. Rev. B* 42, 4298 (1990).
315. M. M. Szostak, N. Lecalve, F. Romain, B. Pasquier; *Chem. Phys.* 187, 373 (1994).
316. C. H. Turner, J. K. Johnson, K. E. Gubbins; *J. Chem. Phys.* 114, 1851 (2001).
317. K. Kaneko, N. Fukuzaki, K. Kakei, T. Suzuki, S. Ozeki; *Langmuir* 5, 960 (1989).
318. A. L. Smith, H. L. Johnson; *J. Am. Chem. Soc.* 74, 4696 (1952).
319. C. E. Dinerman, G. E. Ewing; *J. Chem. Phys.* 53, 626 (1970).
320. C. E. Dinerman; **Low Temperature Spectroscopic Study of the Vibrational and Electronic Bands of Nitric Oxide Dimer.** PhD Thesis, Indiana University, 1971.
321. J. K. Park, H. Sun; *Chem. Phys.* 263, 61 (2001).
322. C. D. Valentin, G. Pacchioni, M. Chiesa, E. Giamello, S. Abbet, U. Heiz; *J. Phys. Chem. B* 106, 1637 (2002).
323. J. T. Yates, Jr., T. E. Madey; *J. Chem. Phys.* 45, 1623 (1966).

324. J. T. Yates, Jr.; **Experimental Innovations in Surface Science: a Guide to Practical Laboratory Methods and Instruments**. AIP Press: Springer, New York, 1998.
325. E. Tsidoni, Y. Kozirovski, M. Folman, J. Heidbergh; *J. Electron Spectrosc. Relat. Phenom.* 44, 98 (1987).
326. M. Fastow, Y. Kozirovski, M. Folman, J. Heidberg; *J. Phys. Chem.* 96, 6126 (1992).
327. E. M. Nour, L. H. Chen, M. M. Strube, J. Laane; *J. Phys. Chem.* 88, 756 (1984).
328. B. J. Howard, A. R. W. Mckellar; *Mol. Phys.* 78, 55 (1993).
329. R. Kometer, F. Legay, N. Legaysommaire, N. Schwentner; *J. Chem. Phys.* 100, 8737 (1994).
330. L. Krim; *J. Mol. Struct.* 471, 267 (1998).
331. T. R. Beebe, Jr., J. T. Yates, Jr.; *Surf. Sci.* 159, 369 (1985).
332. H. Ulbricht, G. Moos, T. Hertel; *Phys. Rev. B* 66, 252 (2002).
333. Y. H. Kahng, R. B. Hallock, E. Dujardin, T. W. Ebbesen; *J. Low Temp. Phys.* 126, 223 (2002).
334. A. Modi, N. Koratkar, E. Lass, B. Q. Wei, P. M. Ajayan; *Nature* 424, 171 (2003).
335. J. Li, Y. J. Lu, Q. Ye, M. Cinke, J. Han, M. Meyyappan; *Nano Lett.* 3, 929 (2003).
336. R. J. Chen, S. Bangsaruntip, K. A. Drouvalakis, N. W. S. Kam, M. Shim, Y. M. Li, W. Kim, P. J. Utz, H. J. Dai; *Proc. Natl. Acad. Sci. U. S. A.* 100, 4984 (2003).
337. Q. F. Pengfei, O. Vermesh, M. Grecu, A. Javey, O. Wang, H. J. Dai, S. Peng, K. J. Cho; *Nano Lett.* 3, 347 (2003).
338. C. K. W. Adu, G. U. Sumanasekera, B. K. Pradhan, H. E. Romero, P. C. Eklund; *Chem. Phys. Lett.* 337, 31 (2001).
339. P. G. Collins, K. Bradley, M. Ishigami, A. Zettl; *Science* 287, 1801 (2000).
340. J. Kong, N. R. Franklin, C. W. Zhou, M. G. Chapline, S. Peng, K. J. Cho, H. J. Dai; *Science* 287, 622 (2000).
341. R. Q. Long, R. T. Yang; *J. Am. Chem. Soc.* 123, 2058 (2001).
342. J. L. Rivera, C. McCabe, P. T. Cummings; *Nano Lett.* 2, 1427 (2002).
343. M. Cinke, J. Li, C. W. Bauschlicher, A. Ricca, M. Meyyappan; *Chem. Phys. Lett.* 376, 761 (2003).
344. M. Kamiya, T. Tsuneda, K. Hirao; *J. Chem. Phys.* 117, 6010 (2002).
345. M. C. Schabel, J. L. Martins; *Phys. Rev. B* 46, 7185 (1992).
346. L. A. Girifalco, M. Hodak; *Phys. Rev. B* 65, 125404 (2002).
347. G. Kresse, J. Furthmuller; *Comp. Mater. Sci.* 6, 15 (1996).
348. H. J. Monkhorst, J. D. Pack; *Phys. Rev. B* 13, 5188 (1976).
349. K. B. Shelimov, R. O. Esenaliev, A. G. Rinzler, C. B. Huffman, R. E. Smalley; *Chem. Phys. Lett.* 282, 429 (1998).
350. N. N. Avgul, A. V. Kiselev; in **Chemistry and Physics of Carbon** P. L. Walkers, Ed. Dekker, New York, 1970, vol. 6.
351. M. Fastow, Y. Kozirovski, M. Folman; *J. Electron Spectrosc. Relat. Phenom.* 64-5, 843 (1993).
352. G. Hummer, J. C. Rasaiah, J. P. Noworyta; *Nature* 414, 188 (2001).
353. W. H. Noon, K. D. Ausman, R. E. Smalley, J. P. Ma; *Chem. Phys. Lett.* 355, 445 (2002).
354. R. J. Mashl, S. Joseph, N. R. Aluru, E. Jakobsson; *Nano Lett.* 3, 589 (2003).
355. V. Buch, J. P. Devlin; Eds., **Water in confining geometries** Springer, Berlin; New York, 2003.
356. M. C. Bellissent-Funel; *Eur. Phys. J. E* 12, 83 (2003).

357. J. Wang, Y. Zhu, J. Zhou, X. H. Lu; *Phys. Chem. Chem. Phys.* 6, 829 (2004).
358. D. J. Mann, M. D. Halls; *Phys. Rev. Lett.* 90, 195503 (2003).
359. C. Dellago, M. M. Naor, G. Hummer; *Phys. Rev. Lett.* 90, 105902 (2003).
360. N. E. Levinger; *Science* 298, 1722 (2002).
361. H. Yui, Y. Guo, K. Koyama, T. Sawada, G. John, B. Yang, M. Masuda, T. Shimizu; *Langmuir* 21, 721 (2005).
362. S. Vaitheeswaran, J. C. Rasaiah, G. Hummer; *J. Chem. Phys.* 121, 7955 (2004).
363. A. Waghe, J. C. Rasaiah, G. Hummer; *J. Chem. Phys.* 117, 10789 (2002).
364. A. Berezhkovskii, G. Hummer; *Phys. Rev. Lett.* 89, 064503 (2002).
365. X. Zhou, C. Q. Li, M. Iwamoto; *J. Chem. Phys.* 121, 7996 (2004).
366. G. C. Pimentel, A. L. McClellan; **The Hydrogen Bond**. W.H. Freeman, San Francisco,, 1960.
367. C. J. Gruenloh, J. R. Carney, C. A. Arrington, T. S. Zwier, S. Y. Fredericks, K. D. Jordan; *Science* 276, 1678 (1997).
368. C. J. Tsai, K. D. Jordan; *J. Phys. Chem.* 97, 5208 (1993).
369. R. N. Pribble, T. S. Zwier; *Faraday Discuss.*, 229 (1994).
370. R. N. Pribble, T. S. Zwier; *Science* 265, 75 (1994).
371. J. Sadlej, V. Buch, J. K. Kazimirski, U. Buck; *J. Phys. Chem. A* 103, 4933 (1999).
372. P. Andersson, C. Steinbach, U. Buck; *Eur Phys J D* 24, 53 (2003).
373. J. P. Devlin, V. Buch; *J. Phys. Chem.* 99, 16534 (1995).
374. B. Rowland, N. S. Kadagathur, J. P. Devlin, V. Buch, T. Feldman, M. J. Wojcik; *J. Chem. Phys.* 102, 8328 (1995).
375. J. P. Devlin, V. Buch; *J. Phys. Chem. B* 101, 6095 (1997).
376. J. Hernandez, N. Uras, J. P. Devlin; *J. Chem. Phys.* 108, 4525 (1998).
377. H. M. Lee, S. B. Suh, K. S. Kim; *J. Chem. Phys.* 114, 10749 (2001).
378. G. S. Fanourgakis, E. Apra, W. A. de Jong, S. S. Xantheas; *J. Chem. Phys.* 122, 134304 (2005).
379. K. Nauta, R. E. Miller; *Science* 287, 293 (2000).
380. J. P. Devlin, V. Buch; *Journal of Physical Chemistry* 99, 16534 (1995).
381. H. J. C. Berendsen, J. R. Grigera, T. P. Straatsma; *J. Phys. Chem.* 91, 6269 (1987).
382. H. Z. Geng, X. B. Zhang, S. H. Mao, A. Kleinhammes, H. Shimoda, Y. Wu, O. Zhou; *Chem. Phys. Lett.* 399, 109 (2004).
383. S. J. Gregg, K. S. W. Sing; **Adsorption, Surface Area, and Porosity**. Academic Press, London ; New York, ed. 2nd, 1982.
384. D. J. McCaa, J. H. Shaw; *J. Mol. Spectrosc.* 25, 374 (1968).
385. N. A. Seaton, J. P. R. B. Walton, N. Quirke; *Carbon* 27, 853 (1989).
386. P. I. Ravikovitch, A. Vishnyakov, R. Russo, A. V. Neimark; *Langmuir* 16, 2311 (2000).
387. M. S. P. Shaffer, X. Fan, A. H. Windle; *Carbon* 36, 1603 (1998).
388. B. Y. Wei, M. C. Hsu, Y. S. Yang, S. H. Chien, H. M. Lin; *Mater. Chem. Phys.* 81, 126 (2003).
389. K. Kaneko, C. Ishii, H. Kanoh, Y. Hanzawa, N. Setoyama, T. Suzuki; *Adv. Colloid Interface Sci.* 77, 295 (1998).
390. M. Jaroniec, K. Kaneko; *Langmuir* 13, 6589 (1997).
391. M. Kruk, M. Jaroniec, K. P. Gadkaree; *J. Colloid Interface Sci.* 192, 250 (1997).
392. P. J. M. Carrott, F. C. Drummond, M. B. Kenny, R. A. Roberts, K. S. W. Sing; *Colloids Surf.* 37, 1 (1989).

393. P. B. Balbuena, K. E. Gubbins; in **Characterization of porous solids III: proceedings of the IUPAC Symposium (COPS III), Marseille, France, May 9-12, 1993** J. Rouquâerol, F. Rodriguez-Reinoso, K. S. W. Sing and K. K. Ungers, Eds. Elsevier, Amsterdam ; New York, 1994, vol. 87, 41-49.
394. K. K. Iu, J. K. Thomas; *J. Photoch. Photobio. A* 71, 55 (1993).
395. J. A. Rossin, R. W. Morrison; *Carbon* 29, 887 (1991).
396. C. R. Hall, K. S. W. Sing; *Chem. Br.* 24, 670 (1988).
397. J. L. Pickett, M. Naderi, M. J. Chinn, D. R. Brown; *Sep. Sci. Technol.* 37, 1079 (2002).
398. J. C. Wren, W. Long, C. J. Moore, K. R. Weaver; *Nucl. Technol.* 125, 13 (1999).
399. T. H. Ballinger, J. T. Yates, Jr.; *Langmuir* 7, 3041 (1991).
400. T. H. Ballinger, J. C. S. Wong, J. T. Yates, Jr.; *Langmuir* 8, 1676 (1992).
401. E. B. Cornelius, T. H. Milliken, G. A. Mills, A. G. Oblad; *J. Phys. Chem.* 59, 809 (1955).
402. H. Knozinger, P. Ratnasamy; *Catal. Rev. Sci. Eng.* 17, 31 (1978).
403. J. B. Peri, R. B. Hannan; *J. Phys. Chem.* 64, 1526 (1960).
404. G. S. Weiss, A. S. Parkes, E. R. Nixon, R. E. Hughes; *J. Chem. Phys.* 41, 3759 (1964).
405. M. P. Marzocchi, G. Sbrana, G. Zerbi; *J. Am. Chem. Soc.* 87, 1429 (1965).
406. T. Wada, E. Kishida, Y. Tomiie, H. Suga, S. Seki, I. Nitta; *Bull. Chem. Soc. Jpn.* 33, 1317 (1960).
407. T. P. Beebe, P. Gelin, J. T. Yates, Jr.; *Surf. Sci.* 148, 526 (1984).
408. P. R. Antoniewicz, R. R. Cavanagh, J. T. Yates, Jr.; *J. Chem. Phys.* 73, 3456 (1980).
409. L. Schlapbach, A. Zuttel; *Nature* 414, 353 (2001).
410. A. Zuttel; *Naturwissenschaften* 91, 157 (2004).
411. M. Hirscher, M. Becher; *J. Nanosci. Nanotechno.* 3, 3 (2003).
412. V. V. Simonyan, J. K. Johnson; *J. Alloys Compd.* 330, 659 (2002).
413. R. G. Ding, J. J. Finnerty, Z. H. Zhu, Z. F. Yan, G. Q. Lu; in **Encyclopedia of Nanoscience and Nanotechnology.** H. S. Nalwas, Ed. American Scientific Publishers, Stevenson Ranch, Calif., 2004, vol. 4, 13-33.
414. A. C. Dillon, K. M. Jones, T. A. Bekkedahl, C. H. Kiang, D. S. Bethune, M. J. Heben; *Nature* 386, 377 (1997).
415. M. Hirscher, M. Becher, M. Haluska, U. Dettlaff-Weglikowska, A. Quintel, G. S. Duesberg, Y. M. Choi, P. Downes, M. Hulman, S. Roth, I. Stepanek, P. Bernier; *Appl. Phys. A* 72, 129 (2001).
416. Y. Ye, C. C. Ahn, C. Witham, B. Fultz, J. Liu, A. G. Rinzler, D. Colbert, K. A. Smith, R. E. Smalley; *Appl. Phys. Lett.* 74, 2307 (1999).
417. C. Liu, Y. Y. Fan, M. Liu, H. T. Cong, H. M. Cheng, M. S. Dresselhaus; *Science* 286, 1127 (1999).
418. Q. Y. Wang, J. K. Johnson; *J. Phys. Chem. B* 103, 4809 (1999).
419. B. Panella, M. Hirscher, S. Roth; *Carbon* 43, 2209 (2005).
420. N. P. Hu, X. Y. Sun, A. Hsu; *J. Chem. Phys.* 123, 044708 (2005).
421. R. T. Yang; *Carbon* 38, 623 (2000).
422. D. Levesque, A. Gicquel, F. L. Darkrim, S. B. Kayiran; *J. Phys.: Condens. Matter* 14, 9285 (2002).